FEDERATED LEARNING-BASED RECURRENT DYNAMIC NETWORK FOR FREQUENCY CONTROL OF NETWORKED MICROGRID SYSTEM

By

ANDREW XAVIER RAJ

Thesis Submitted to the School of Graduate Studies, Universiti Putra Malaysia, in Fulfilment of the Requirements for the Degree of Doctor of Philosophy

December 2023

FK 2023 25

DEDICATION

This thesis is gratefully dedicated to:

My beloved wife Sonia Princy Arockiasamy for her continued support, patience and understanding and to my beloved parents.

&

My beloved brother.

Abstract **of** thesis presented to the Senate of Universiti Putra Malaysia in fulfilment of the requirement for the degree of Doctor of Philosophy

FEDERATED LEARNING-BASED RECURRENT DYNAMIC NETWORK FOR FREQUENCY CONTROL OF NETWORKED MICROGRID SYSTEM

By

ANDREW XAVIER RAJ

December 2023

Chairman : Associate Professor Ir. Noor Izzri bin Abdul Wahab, PEng, PhD
Faculty : Engineering

An essential goal within power system operations is to ensure reliability, safe and high standard of power supply. A pivotal measure for achieving this goal is through the implementation of load frequency control (LFC). Essentially, LFC is an automated process designed to regulate the system frequency and net tie line power between a control area and its neighboring areas to align with their predetermined values of ±0.2 Hz as per the IEEE Standard 1547. Nowadays, the power systems are becoming more complex due to the increasing penetration of renewable energy sources (RES) and the transition of the conventional unilateral system to digitization through communication systems leading to the development of Microgrids and Networked Microgrids system. This transition leads to frequency instability due to the intermittent nature of RES. Any fluctuations in the load frequency that occur without a clear direction can cause damage to distributed generators, auxiliary engines, and other hardware equipment. In severe cases, such fluctuations can even pose a threat to the safety of the power grid itself. The primary focus of this thesis centers on addressing the issue of frequency deviation in a highly RE dominated power network and proposes a suitable control scheme with an appropriate control technique. Initially, the study is made considering a fractional-order proportional-integral-derivative (FOPID) controller designed in a centralized fashion, whose parameters are tuned using a proposed chaotic atom search optimization (CASO) for a RE integrated multi-area power system. However, this approach is deemed unsuitable for ensuring the necessary flexibility for a stable network operation in the event of an increase in Distributed Energy Resources (DERs) penetration. Furthermore, this scheme is susceptible to a single-point failure. To address the limitation of centralized control, a decentralized control strategy is employed using an improved version of FOPID controller called nonlinear FOPID (NLFOPID) controller. During this case, a hybrid atom search–particle swarm optimization (AS-PSO) approach is proposed to tune the parameters of the NLFOPID controller. However, a coordinated operation is impossible for a decentralized control scheme. This problem is addressed using distributed control strategy (DCS) based on a leader-follower framework for the coordination of multiple distributed energy resources (DERs) in NMGs. A chaotic hybrid AS-PSO optimized federated average learning of recurrent zeroing neural dynamics designed self-adaptive FOPID (FAL-ZND FOPID) controller is proposed for frequency regulation of NMG using DCS. Furthermore, the LFC is studied for prosumer and consumer-based P2P energy markets considering the proposed adaptive control technique. Finally, the real power system validation is carried out by utilizing a New England IEEE-39 test bus system. The results obtained proves that the proposed distributed adaptive controller improves the frequency response of the system by 65 %, 54 %, 45 % and 42 % in terms of settling time, peak overshoot and undershoot and also controller effort, respectively compared to decentralized and centralized control schemes.

Abstrak tesis yang dikemukakan kepada Senat Universiti Putra Malaysia sebagai memenuhi keperluan untuk ijazah Doktor Falsafah

RANGKAIAN DINAMIK BERULANG BERASASKAN PEMBELAJARAN BERSEKUTU UNTUK KAWALAN FREKUENSI SISTEM RANGKAIAN MICROGRID

Oleh

ANDREW XAVIER RAJ

Disember 2023

Pengerusi : Profesor Madya Ir. Noor Izzri bin Abdul Wahab, PEng, PhD
Fakulti : Kejuruteraan

Matlamat penting dalam operasi sistem kuasa adalah untuk memastikan kebolehpercayaan, serta piawaian bekalan kuasa yang selamat dan tinggi. Langkah pangsi untuk mencapai matlamat ini adalah melalui pelaksanaan kawalan frekuensi beban (load frequency control, LFC). Pada asasnya, LFC adalah proses automatik yang direka untuk mengawal frekuensi sistem dan kuasa garis sambungan bersih antara kawasan kawalan dan kawasan-kawasan yang berdekatan untuk menyesuaikan dengan nilai-nilai yang telah ditentukan ±0,2 Hz menurut IEEE Standard 1547. Terkini, sistem-sistem kuasa menjadi semakin kompleks disebabkan oleh peningkatan penembusan sumber tenaga boleh diperbaharui (renewable energy sources, RES) dan peralihan daripada sistem unilateral konvensional kepada pendigitalan melalui sistem komunikasi yang membawa kepada pembangunan sistem Mikrogrid dan Mikrogrid Terangkai. Peralihan ini mengakibatkan ketidakstabilan frekuensi yang berpunca daripada sifat RES yang berjeda. Sebarang turun naik dalam frekuensi beban yang berlaku tanpa arah yang jelas boleh merosakkan penjana teragih, enjin tambahan dan peralatan perkakasan lain. Bagi kes yang teruk, keadaan turun naik sebegini boleh mengancam keselamatan grid kuasa itu sendiri. Fokus utama kajian ini adalah untuk menangani isu sisihan frekuensi dalam rangkaian kuasa sumber tenaga boleh diperbaharui dan mencadangkan satu skim kawalan dengan teknik kawalan yang sesuai. Pada mulanya, kajian ini mempertimbangkan pengawal tertib pecahan berkadar-integer-terbitan (fractional order proportional-integral-derivative (FOPID)) yang direka bentuk secara berpusat dengan parameter yang ditala menggunakan cadangan pengoptimuman carian atom berkecamuk (chaotic atom search optimization, CASO) untuk sistem kuasa bersepadu pelbagai kawasan tenaga boleh diperbaharui. Walau bagaimanapun, pendekatan ini dianggap tidak sesuai untuk memastikan kebolehubahan yang diperlukan untuk operasi rangkaian yang stabil sekiranya berlaku peningkatan penembusan Sumber Tenaga Teragih (distributed energy resources, DERs). Tambahan pula, skim ini mudah terdedah kepada kegagalan titik tunggal. Untuk menangani batasan kawalan berpusat, strategi kawalan ternyahpusat digunakan menggunakan versi pengawal FOPID diperbaik yang

dinamakan pengawal FOPID tak linear (NLFOPID). Dalam kes ini, pendekatan hibrid pengoptimuman kerumunan zarah dan carian atom (atom search–particle swarm optimization, AS-PSO) dicadangkan untuk menala parameter pengawal NLFOPID. Walau bagaimanapun, operasi yang terselaras adalah mustahil untuk skim kawalan ternyahpusat. Masalah ini ditangani menggunakan strategi kawalan teragih (distributed control strategy, DCS) berdasarkan rangka kerja pengikut-pemimpin untuk penyelarasan pelbagai sumber tenaga teragih (DERs) dalam NMGs. Sebuah kaotika hibrid AS-PSO dioptimalkan belajar rata-rata persekutuan dinamik saraf berulang nol yang direka FOPID adaptif diri (FAL-ZND FOPID) pengawal telah dicadangkan untuk pengaturan frekuensi NMG menggunakan DCS. Tambahan pula, LFC dikaji untuk pasaran tenaga pengeluar swaguna dan P2P berasaskan pengguna yang bergantung kepada teknik kawalan suai yang dicadangkan. Akhir sekali, pengesahan sistem kuasa sebenar dilakukan dengan menggunakan sistem bas ujian IEEE-39 New England. Keputusan yang diperoleh membuktikan bahawa pengawal suai teragih yang dicadangkan mampu meningkatkan tindak balas frekuensi sistem sebanyak 65%, 54%, 45% dan 42% masing-masing dari segi masa penyelesaian, puncak terlajak dan lajak bawah, dan juga usaha pengawal berbanding dengan skim kawalan ternyahpusat dan terpusat.

ACKNOWLEDGEMENTS

Firstly, I would like to express my sincere gratitude to my thesis advisor Assoc. Prof. Ir. Dr. Noor Izzri bin Abdul Wahab, for his immense support and supervision throughout my PhD program and would like to express my deepest gratitude to my beloved mentor Dr. Veerapandiyan Veerasamy for her enlightening guidance and inspiring instruction in every stage of my PhD.

Besides, I would like to express my appreciation for the guidance and coaching of co-supervisors, Prof Dr. Mohd Amran b. Mohd Radzi, and Assoc. Prof. Dr. Nasri b. Sulaiman for their profound and carefully aimed comments and suggestions of this study.

I am incredibly grateful to all staff members of Department of Electrical and Electronics Engineering and Faculty of Engineering (Electrical), especially many thanks also extended to my colleagues in the Advanced Lightning Power and Energy Research (ALPER) group for their companionship, helpful insights, and friendly working environment.

Last but not the least, I would like to thank my family and friends for supporting me spiritually throughout writing this thesis.

This thesis was submitted to the Senate of Universiti Putra Malaysia and has accepted as fulfilment of the requirement for the degree of Doctor of Philosophy. The Members of the Supervisory Committee were as follows:

Noor Izzri bin Abdul Wahab, PEng, PhD
Associate Professor Ir.
Faculty of Engineering
Universiti Putra Malaysia
(Chairman)

Mohd Amran bin Mohd Radzi, PhD
Professor
Faculty of Engineering
Universiti Putra Malaysia
(Member)

Nasri bin Sulaiman, PhD
Associate Professor
Faculty of Engineering
Universiti Putra Malaysia
(Member)

Veerapandiyan Veerasamy, PhD
Research Fellow
School of Electrical and Electronics Engineering
Nanyang Technological University
Singapore
(External Member)

____
ZALILAH MOHD SHARIFF, PhD
Professor and Dean
School of Graduate Studies
Universiti Putra Malaysia

Date: 14 March 2024

TABLE OF CONTENTS

LIST OF TABLES

LIST OF FIGURES

LIST OF ABBREVIATIONS

ABC	Artificial Bee Colony
ACE	Area Control Error
AE	Aqua Electrolyzer
ALO	Ant Lion Optimization
ANN	Artificial Neural Network
apf	area participation factor
ASO	Atom Search optimization
AS-PSO	Atom Search Particle Swarm Optimization
AVR	Automatic Voltage Regulator
BA	Bat Algorithm
BD	Boiler Dynamics
BESS	Battery Energy Storage System
CASO	Chaotic Atom Search Optimization
CAS-PSO	Chaotic Atom Search Particle Swarm Optimization
CE	Control Effort
cpf	Contract participation factor
CPM	Contract Participation Matrix
CSTP	Concentrated Solar Thermal Power
DAI	Distributed Averaging based Integral
DC	Distributed Control
DCS	Distributed Control Strategy
DDES	Decentralized Deregulated Energy System
DE	Differential Evolution
DEG	Diesel Engine Generator
DERs	Distributed Energy Resources

DGs	Distributed Generations
DISCOs	Distribution Companies
DPM	Distribution Participation Matrix
ESS	Energy Storage System
EVs	Electric Vehicles
FA	Firefly Algorithm
FAL	Federated Average Learning
FC	Fuel Cell
FDI	False Data Injection
FESS	Flywheel Energy Storage
FLC	Fuzzy Logic Control
FO	Fractional Order
FOPID	Fractional Order Proportional Integral Derivative
GA	Genetic Algorithm
GDB	Governor Dead Band
GES	Geothermal Energy System
GENCOs	Generation Companies
GHNN	Generalized Hopfield Neural Network
GPP	Geothermal Power Plant
GRC	Generation Rate Constraint
gRPC	Google Remote Procedure Call
GWO	Grey Wolf Optimization
HNN	Hopfield Neural Network
HPS	Hybrid Power System
I	Integral
IAE	Integral Absolute Error
ICA	Imperialist Competitive Algorithm

IMC	Internal Model Control
IO	Integer Order
IPPs	Independent Power Producers
ISE	Integral Square Error
ISO	Independent System Operator
ITAE	Integral Time Absolute Error
ITSE	Integral Time Square Error
LFC	Load Frequency Control
LQR	Linear Quadratic Regulator
MFO	Moth Flame Optimization
MGs	Microgrids
MOs	Market Operators
MPC	Model Predictive Control
NMGs	Networked Microgrids
NLFOPID	Nonlinear FOPID
OTEC	Ocean Thermal Energy Conversion
P2P	Peer to Peer
PD	Proportional Derivative
PI	Proportional Integral
PID	Proportional Integral Derivative
PO	Peak Overshoot
PoA	Proof of Authority
PoW	Proof of Work
PSO	Particle Swarm Optimization
PSS	Power System Stabilizers
PU	Peak Undershoot
PV	Photo Voltaic

RNN	Recurrent Neural Network
RPis	Raspberry Pis
RT-LAB	Real Time Laboratory
SC-OTEC	Solar Concentrated Ocean thermal Energy Conversion
SD	Standard Deviation
SE	Steady state Error
SG	Synchronous Generator
SGD	Stochastic Gradient Descent
SLP	Step Load Perturbation
SMC	Sliding Mode Control
SOs	System Operators
SPG	Solar Power Generation
ST	Settling Time
STES	Solar Thermal Energy System
STPG	Solar Thermal Power Generation
TCP/IP	Transmission Control Protocol/Internet Protocol
TLBO	Teaching Learning Based Optimization
TRANSCOs	Transmission Companies
TSO	Transmission System Operator
UDP	Universal Datagram Protocol
VSG	Virtual Synchronous Generator
WPG	Wind Power Generation
WTPG	Wind Turbine Power Generation
ZNN	Zhang Neural Network
ZND	Zeroing Neural Dynamics

CHAPTER 1

INTRODUCTION

1.1 Background

Renewable energy sources (RES), such as solar and wind, are becoming the primary options for integration into power networks in the form of Microgrids (MGs). Factors like environmental considerations, economic considerations, and the growing integration of small-scale renewables are rendering the traditional centralized power generation concept obsolete, steering the energy landscape towards a more decentralized future. MGs, which operate at the low voltage (LV) electrical distribution level, consist of distributed energy resources (DERs) including Distributed Generations (DGs), Energy storage units and loads (Xia et al., 2022). However, due to the limited capacity of an individual MG, the concept of Networked Microgrid (NMG) systems has emerged. These involves clustering multiple adjacent MGs together to enhance the power supply flexibility (Liu et al., 2023).

The increasing integration of power electronics interfaced RE sources and DERs lead to significant reduction in stored energy capacity and the ability to regulate system frequency (Bevrani 2014). Frequency is a critical factor in maintaining the stability and security of the power system. Hierarchical control approaches are generally employed to regulate the frequency of the power, involving three levels of control tasks: Primary (decentralized droop control), secondary (load frequency control (LFC)), and tertiary (optimal power flow) control (Li et al., 2023).

Secondary frequency control, also known as LFC plays a crucial role in maintaining the frequency stability and reliability of power systems. The control of secondary frequency can be achieved through three schemes: centralized, decentralized, and distributed control (Yang et al., 2022).

In this research, the three secondary frequency control schemes are investigated for various power network to evaluate the effectiveness and test the suitability of proposed scheme for NMG. A novel adaptive recurrent fractional order secondary frequency controller is proposed in this research work by adopting the most suitable control scheme by including all the control hierarchy for NMG with peer to peer (P2P) energy trading. The robustness of the proposed controller is validated at various conditions. The models and codes presented in this thesis are supported with simulation results using MATLAB/Simulink.

1.2 Problem statement

The interconnection of RES into the electric power networks facilitates the decarbonization of electricity system by effectively harnessing and distributing substantial quantities of RE. (Arya et al., 2021). However, the RES like solar and wind power leads to uncertain variation in power generation due to meteorological conditions which introduces frequency oscillation that need to be controlled else resulting in damage of equipment's and blackout. To cater this issue, the secondary layer of the hierarchical control generally employs centralized control scheme by incorporating proportional integral (PI)/Proportional Integral Derivative (PID) control loops and bandwidth communication systems to monitor real time frequency variations in the network (Arya et al., 2017a).

On the other hand, tuning the gain parameters of the controller for RE incorporated power system is a crucial task. Traditionally, tuning the gain parameters of these controllers is done using established methods like Ziegler and Nichols (Z-N), Cohen-Coon's Astrom, Hagglund, and other conventional approaches. However, these techniques design the gain parameters for a specific set of operating conditions and may prove ineffective for a broader operating range in real power system (Ziegler et al., 1942, Das et al., 2014). To resolve this, heuristic-based stochastic optimization techniques like genetic algorithm (GA) (Daneshfar et al., 2012), sine cosine algorithm (Rajesh et al., 2019a) and imperialist competitive algorithm (ICA) (Arya et al., 2023) are used to optimize the controller's gain parameters for LFC application. However, the convergence properties of the stochastic optimization algorithms are strongly connected to the random numbers generated by the random number generator (RNG) in each algorithm (Yang et al., 2007). Because of this RNG, the solutions generated by the optimization algorithms are not diversified to hit every mode in the multi-modal objective landscape in search space. Therefore, it is crucial to explore and identify the appropriate type and design of controller parameters, as they significantly impact the performance and stability of the system which needs to be explored further.

In the period from mid-1980s, the electric power industry is undergoing a transition from a model of vertically integrated utilities, where a single entity managed generation, transmission, and distribution, providing power at regulated prices. This model is evolving into a deregulated framework, where competitive companies offer unbundled power to customers at reduced rates (Fathy et al., 2020). This transformation has sparked a competitive environment in power generation, facilitating an open access policy for transmission, and promoting competition at the distribution level. LFC is an important ancillary service in the deregulated energy market for regulating the frequency to the nominal value and minimizing the tie-line power deviations between control areas (Jin et al., 2022). Conventionally, centralized control scheme is employed in the literature by integrating numerous controllers for frequency regulation of deregulated system (Shayeghi et al., 2021, Mohanty et al., 2020, Sasaki et al., 2003). However, adopting centralized control has certain limitations such as its uni-directional, centralized design leads to cascading failures resulting in blackout of the entire system. The lack of data and control hinders modern demands and consumer participation (Gupta et al., 2022). Therefore, a control scheme which solely provides benefits related to resilience, flexibility, security, market dynamics and consumer engagement is necessary.

In the last decade, technological advancements in power electronics, energy storage technologies, and communication systems have made it more feasible to integrate and control distributed generation (DG) units into the grid systems. Further, the high penetration of RES and the existence of several DG units in close electrical proximity to one another have led to the development of the MGs.

Nowadays, the RES located in a distributed manner as opposed to the conventional large, centralized power plants are connected to a larger and more complex NMGs (Li et al., 2017). NMGs is a large nonlinear highly structured network consisting of several interconnected distributed DGs or subsystems. The literature references (Xia et al., 2022, Kamal et al., 2022) highlight two main approaches for controlling the frequency of large-scale systems like NMGs: centralized and decentralized control. However, these control schemes face difficulties in coordinating efficiently among DERs based on their own information (Ding et al., 2019). Therefore, an efficient control scheme is required for effective coordination of DERs.

Moreover, commonly used controllers in these schemes are conventionally tuned PI/PID. However, its effectiveness diminishes under diverse operating condition and susceptible to uncertain disturbances in practical scenarios. Moreover, employing the PID controller as a secondary frequency control may not provide sufficient damping of frequency oscillations at a faster rate. While the PID controller is a simple and widely used industrial controller, it may not be able to effectively dampen oscillations as compared to more advanced controller like fractional order PID (FOPID) controller.

On the other hand, numerous adaptive control strategies are utilized as LFC in the literature. Model predictive control (MPC) (Jayachandran et al., 2019) is employed for maintaining the balance between generation and demand, ensuring the system operates at a stable frequency. Moreover, MPC offers advantages in terms of adaptability and robustness, as it considers future system behavior during the optimization process. However, MPC involves solving optimization problems at each time step, leading to high computational demands. Implementing MPC requires a great understanding of the system dynamics and accurate modelling. Deviations between the model and the actual system can affect performance. Similarly, sliding mode control (SMC) (Li et al., 2019), had been extensively utilized as secondary frequency controller in the literature. Nevertheless, SMC can exhibit chattering, which is a high-frequency oscillation in the control signal. This can lead to wear and tear on mechanical components and is undesirable in practical applications. H_2/H_∞ control (Zhang et al., 2020a) are also employed to regulate the frequency of the power network. However, in certain cases, H_∞ controllers may be conservative, leading to overestimation of uncertainties and suboptimal performance. Therefore, a control technique with appropriate control scheme is essential to coordinate the widely dispersed DERs in the NMG system.

On the other hand, the bi-directional power flow caused by DERs, along with the intermittency and randomness of RES, introduces challenges in planning, operating, and protecting power systems. Furthermore, the traditional retail market structure is no longer suitable for the evolving energy landscape (Almasalma et al., 2017). To address the technical challenges posed by DERs, innovative market schemes are being explored to incentivize DERs in utilizing their flexibility effectively.

In response to these developments, the concept of peer to peer (P2P) energy trading has emerged and is rapidly gaining traction worldwide. P2P energy trading markets enable prosumers, market operators (MOs), and system operators (SOs) to establish bilateral communication channels, facilitating efficient information exchange. However, the high-frequency transmission of information in P2P energy trading also introduces new possibilities and vulnerabilities for cyber-attacks (Ali et al., 2023). As a result, ensuring the security of personal information and data becomes a critical concern in P2P energy trading. Protecting personal information and data security is paramount in P2P energy trading systems. Safeguarding the privacy of prosumers personal information, such as their identities, contact details, and energy consumption patterns, is crucial. Additionally, ensuring the security and integrity of data exchanged during P2P energy trading is essential to prevent unauthorized access, tampering, or data breaches (Dinesha et al., 2022). Furthermore, the controller deployed to regulate the frequency of the energy trading systems are susceptible to deception attacks, particularly false data injection (FDI). The FDI attack into the control process can lead to incorrect feedback values of electrical data which potentially causing severe damage to the energy system (Yang et al., 2022a). Therefore, a technology that can safeguard the trading and control action against cyberattacks are needed.

The above problem statements can be summarized as follows:

1. The need to develop an optimization technique to optimize the fractional order controller in centralized control scheme to overcome the drawback of conventional optimization techniques of reaching local minima.
2. An efficient independent control scheme is essential for the fractional order controller in deregulated power systems to address drawbacks like single points of failure, low reliability, and instability.
3. An effective control scheme is vital for coordinating geographically dispersed DERs. A novel adaptive recurrent fractional order controller is necessary to counteract frequency oscillations caused by high-penetration inertia-less renewable energy sources. Also, a technology must be adopted to address the security concerns against FDI attacks by the eavesdropper on the controller which may lead to grid instability.

1.3 Objectives

The aim of this research is to develop an adaptive controller to regulate the frequency of RE dominated system and to facilitate the P2P energy trading. For this, the research considers a NMG model that can enable the P2P energy trading with an adaptive controller operating in distributed manner. To secure the P2P trading and control actions, a blockchain technology is utilized. The objectives of this research are:

1. To develop a chaotic version of atom search optimization technique to optimize the parameters of fractional order controller in a centralized scheme to regulate the frequency of RE integrated power network.

2. To propose and develop a decentralized fractional order controller for deregulated system which consists of RE sources for greater competition and market forces.
3. To develop a distributed leader-follower-based federated average learning of recurrent zeroing neural dynamics designed self-adaptive fractional-order PID (FAL-ZND FOPID) to achieve successful coordination of MGs in the NMGs. Further, to implement a blockchain technology to secure the controller and P2P energy trading in the NMG system against FDI attack.

1.4 Scope of the study

The scope and limitations of this research work are as follows:

1. The study uses linearized small-signal transfer function models for system analysis, despite the inherent complexity and uncertainties in real-world nonlinear systems. This simplification of nonlinear and uncertain systems into linear mathematical models aims to reduce control efforts without compromising performance.
2. The controller designed for this study are limited to fractional order PID controllers. Further, the study involves designing the FOPID controller using a recurrent based Zeroing Neural Dynamics (ZND) network also called as Zhang neural network (ZNN).
3. The proposed secondary control is capable of regulating both the active and reactive power. But, the investigation in this study is limited to regulate only active power of the network as it control the frequency component of the system.
4. The NMG model for P2P energy trading can operate independently or stay connected to the main utility grid. However, the study focuses solely on the islanded operation of NMG, allowing peers to engage in trading either within or between microgrids.
5. For distributed frequency control against FDI attack, the blockchain requires heavy computation and communication in short-time scales. So most of the work is still at the concept of product stage because of the difficulty of the practical blockchain implementation, the computational capability limited by the blockchain itself.

1.5 Thesis outline

This thesis is organized into 5 chapters according to thesis format of Universiti Putra Malaysia (UPM). Each chapter consists of key sections including introduction, literature review, methodology, results and discussion, and conclusions.

In Chapter 1, the research work is introduced with a focus on providing a brief discussion of the background, problem statement, objectives, scope, and research contributions.

After that, Chapter 2 begins with a detailed comprehensive literature review on existing system model studied for LFC application, the hierarchical control architecture and control schemes, and the various secondary control techniques implemented. Throughout this review, the gaps in the current research of LFC problem are significantly identified, which will be addressed in subsequent chapters.

Next, Chapter 3 provides a concise overview of the methodology employed to accomplish the research objectives. The investigation focuses on optimizing the control parameters using artificial intelligence (AI) techniques. The design and optimization of FOPID controllers for LFC applications are explained, followed by the design of an adaptive FOPID controller using federated learning-based ZND for addressing the frequency control issues in a blockchain-based P2P energy trading framework.

In Chapter 4, the results obtained based on the methodology in chapter 3 is clearly illustrated. Initially, a control technique is proposed to optimize the gain values of centralized secondary FOPID controller for a RE integrated power network. The simulation and quantitative results are compared with the existing techniques and real-time variations of RES. Then, a decentralized control scheme is proposed to overcome the limitations of conventional scheme. A new technique is proposed, and the simulation results are validated in hardware in loop (HIL). Finally, a distributed control framework is proposed for NMG system. An FOPID controller is designed using ZND concept. The proposed control scheme performance is compared with the centralized and decentralized control schemes for a New England IEEE-39 bus system to study its effectiveness for a large-scale test system.

Finally, Chapter 5 presents a conclusion of the research study's findings, along with suggestions for future work.

CHAPTER 2

LITERATURE REVIEW

2.1 Introduction

Power system stability is the ability of the system, under a given initial operating state, to maintain a state of operational equilibrium following exposure to a physical disruption (Kundur et al., 2004). Throughout this process, most system variables remain within the defined bounds, ensuring the integrity of the overall system remains intact. When delving into the concept of power system stability, it is customary to categorize into three facets: rotor angle stability, frequency stability, and voltage stability, as depicted in Figure 2.1. Rotor angle stability refers to the system's capability to uphold synchronization among generators following significant (transient angle stability) or minor (small disturbance angle stability) transient disturbances. Such disruptions often stem from short circuits in the transmission network and are frequently resolved without affecting the mechanical power output from prime movers. Techniques like power system stabilizers (PSS), thyristor exciters, and swift fault clearing mechanisms contribute to maintaining rotor angle stability (Bevrani et al., 2011).

Voltage stability is the ability to sustain acceptable voltage levels post-disturbance. The stability of voltages in the system is linked to the reactive power equilibrium in the power system. The automatic voltage regulator (AVR) plays a pivotal role in stabilizing voltage by regulating the internal voltage of the generators (Kumari et al., 2023).

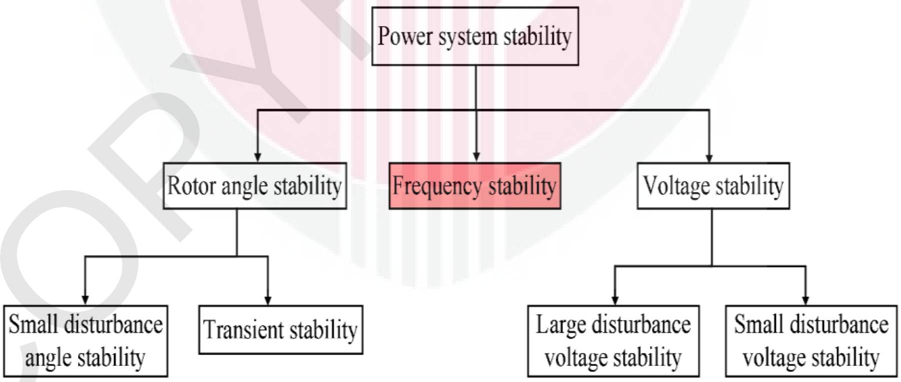

Figure 2.1 : Types of power system stability (Kundur et al., 2004)

In contrast to rotor angle stability, the concept of frequency stability revolves around the prolonged mismatch between active power generation and consumption. Initially, this active power imbalance is absorbed by the kinetic energy of rotating system components (such as turbines, generators, and motors), leading to change in frequency. This is similar to water level fluctuations in a tank, due to surplus or shortage of water supply. However, the solution is temporary, necessitating a corrective action to align mechanical input from the prime movers with network loads. This realignment restores the frequency to the desired level and is known as load frequency control (Naderi et al., 2023), the fundamental theme of this thesis. Given that this thesis concentrates on frequency stability rather than voltage stability and rotor angle stability. As, the voltage and rotor angle perturbations are often localized and can be remedied without affecting the entirety of the grid, frequency deviations are typically systemic, potentially jeopardizing the operational integrity of the entire network. Moreover, with the increasing integration of renewable energy sources (RES) and the evolving load profiles, maintaining a steadfast frequency has become even more exigent (Bevrani, 2014). This underscores the importance of load frequency control (LFC). LFC not only ensures that generators and loads are in equilibrium but also that the system operates within a permissible frequency range, thus safeguarding the grid from the ramifications of frequency excursions. To achieve this, hierarchical control strategies are commonly employed to control the system.

The hierarchical control upholds the frequency stability, which involves maintaining the system frequency at a desired level despite variations in consumption or generation. This is accomplished by continuously adjusting the power production to match the consumption throughout operation. Because storing substantial amount of power is generally inefficient (Machowski, 2020), as it need to be consumed. In addition, another goal is to minimize the operating costs. The control hierarchy usually consists of three levels: primary, secondary, and tertiary control (Li et al., 2023). Figure 2.2 illustrates how these levels collaborate to address the power imbalances in power system, along with the timescales when each level is activated.

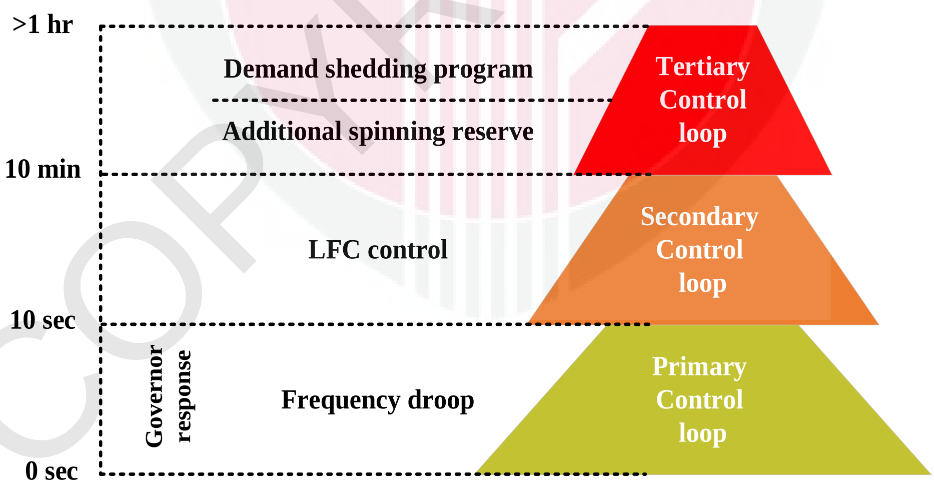

Figure 2.2 : Hierarchical frequency control loop in power system

Firstly, the primary controllers, known as governors, are local automatic controllers situated at generating units. Generally, a proportional controller that adjust the mechanical input power from the turbine based on the deviation in angular speed from a nominal speed. These controllers need to respond instantaneously. To maintain stability, governors ensure that an increase in shaft speed reduces turbine mechanical output and vice versa. In steady state, the desirable relationship is given by,

$$\frac{\Delta c}{\Delta \omega_m} = -\frac{1}{\rho} \tag{2.1}$$

where Δc is the change in valve positioning, $\Delta\omega_m$ is the deviation in generator angular speed from the nominal angular speed, and ρ is a positive constant known as the speed-droop coefficient.

Next, the secondary control in which when a long-term power imbalance occurs, primary controllers alone might not fully restore the frequency to its initial state. Secondary control (also called LFC) comes into play to alter the governor's set point, thus, adjusting the power output even when $\Delta\omega_m = 0$. It is slower than the primary control, and often automated.

In many systems, LFC uses PI based controller to generate inputs for each area, which are then distributed to generating units using participation factor (Bevrani, 2014). Finally, the tertiary control in which it operates manually by the Transmission System Operator (TSO) which is slower than other control levels. Its objectives are to ensure adequate LFC spinning reserves, optimal dispatch of LFC-participating units, and restoration of LFC bandwidth.

2.2 Frequency Response Modeling

The system frequency relies on the equilibrium of real power. A modification in real power requirement at a specific network location impacts the entire system by causing a frequency adjustment. Thus, the system frequency serves as a valuable gauge for demonstrating imbalances in system load and generation (Weedy, 2012). Any momentary disparity in energy causes an immediate frequency shift due to the initial counteraction by the kinetic energy of the rotating machinery. If there is a substantial decrease in generation without an appropriate system reaction, it can result in severe frequency deviations beyond the operational capacity of the machinery (Glover, 2007). Apart from the primary frequency regulation, the majority of sizable synchronous generators come with an additional secondary frequency control mechanism. A diagram illustrating the configuration of a synchronous generator incorporating frequency control loops as presented in Figure 2.3.

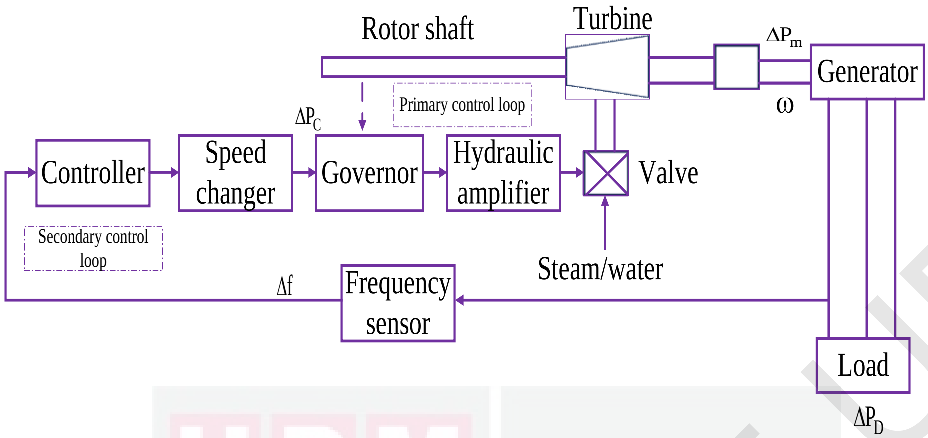

Figure 2.3 : Schematic representation of synchronous generator with frequency control loops (Bevrani, 2014)

Figure 2.3 illustrates the speed governor role in maintaining the system frequency. It detects speed changes through primary and secondary control loops. The hydraulic amplifier positions the main valve against the water pressure, and the speed changer maintains its output. Each unit's speed governor contributes to overall generation shift, with secondary control adjusting the load reference via a speed changer motor. Feedback integrates the frequency deviation into the primary control loop via a dynamic controller, regulating using the outcome signal (ΔP_C). In Figure 2.3, load changes lead to transient frequency shift (Δf). The feedback mechanism triggers, aligning the turbine generation (ΔPm) with load to restore frequency after a load perturbation (ΔP_D) (Bevrani, 2014).

To study this effect, a linearized model describing the frequency response of the block diagram depicted in Figure 2.3 for a single generator unit is presented in Figure 2.4. This model is then extended to encompass an interconnected multi area power system. The overall dynamic relationship between the incremental mismatch power (ΔP_m - ΔP_D) and the frequency deviation (Δf) can be succinctly captured by a swing equation:

$$\Delta P_m(t) - \Delta P_D(t) = 2H_{eq}\frac{d\Delta f(t)}{dt} + D\Delta f(t) \tag{2.2}$$

where, Δf signifies the frequency deviation, ΔP_m represents the alteration in mechanical power, ΔP_D denotes the load change, H_{eq} symbolizes the inertia constant, and D stands for the load damping coefficient. Typically, the damping coefficient is expressed as the percentage change in load for a 1% shift in frequency. For instance, a customary value of 1.5 for D indicates that a 1% frequency change would correspond to a 1.5% load change (Elgerd, 1982). By utilizing the Laplace transform, the above Equation can be expressed as follows:

$$\Delta P_m(s) - \Delta P_D(s) = 2H_{eq}\, s\,\Delta f(s) + D\Delta f(s) \tag{2.3}$$

The representation of Equation (2.3) can be depicted in a block diagram format, illustrated in Figure 2.4.

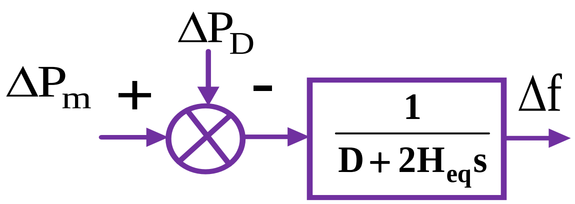

Figure 2.4 : Transfer function representation of generator-load model (Elgerd, 1982)

A simplified model of the governor-generator system is developed in previous works (Kundur, 1994, Obaid et al., 2016) and is illustrated in Figure 2.5. This model serves as the basis for power system frequency analysis and control design. The governor-turbine dynamics are represented using first-order transfer functions. The time constants of the governor and turbine (T_g, T_t, T_{tr}, and T_r) are provided in Table 2.1 (Obaid et al., 2016). The droop gain (R) is determined by the ratio of frequency change Δf to the change in generator power output ΔP, as depicted in Figure 2.5. The objective of the turbine-governor control system is to maintain the desired system frequency by adjusting the mechanical power output of the turbine, denoted as ΔP_m. The relationship between frequency and power for turbine-governor control is described by Equation (2.4),

$$\Delta P_C = \Delta P_{ref} - \frac{1}{R} \times \Delta f \tag{2.4}$$

In Equation (2.4), the term $\Delta P_C - \Delta P_{ref}$ is represented by ΔP, and the droop gain is defined as,

$$-R = \text{Slope} = \Delta f \,/\, \Delta P \tag{2.5}$$

The governors employ a droop control to regulate the generator power output in response to deviations in frequency. This mechanism constitutes the primary frequency control, which is automatically administered by the governors. For instance, if demand power increases (or generation power decreases) leading to a frequency decrease, the governors respond by providing a low-frequency service and vice versa. (Mohanty et al., 2014).

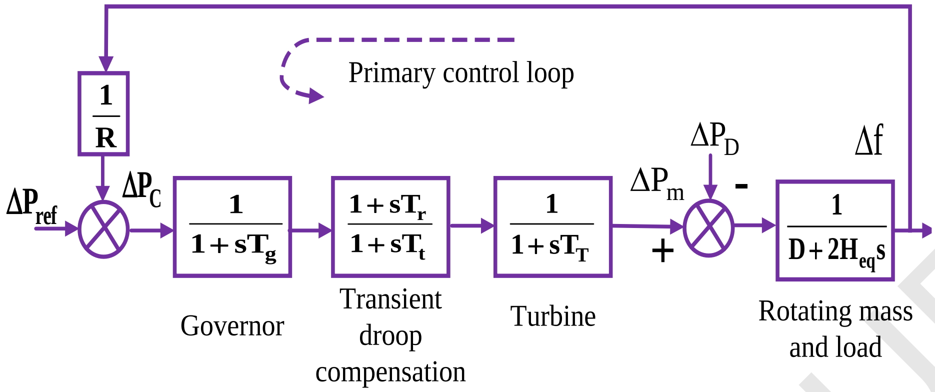

Figure 2.5 : Primary frequency control model (Elgerd, 1982)

Table 2.1 : Values of the simplified power system

T_g	T_t	T_{tr}	T_r	1/R	H_{eq}	D
0.2 s	12 s	2 s	0.3 s	-0.09 p.u.,	4.44 s	1 p.u.,

(Elgerd, 1982)

2.2.1 Transfer Function Model of ith Area System

A multiarea power system is composed of interconnected tie-lines to connect various control areas to balance the power. The variation in frequency recorded within each control area serves as an indicator of the mismatch power trend across the interconnections, encompassing more than just the local control area (Bevrani, 2014). The secondary LFC system within each control area of an interconnected power system is responsible for managing the exchange of power with other control areas alongside maintaining its own local frequency. The power transmission through the tie-line from area i to area j can be mathematically expressed as:

$$P_{tie,ij} = \frac{V_i V_j}{X_{ij}} \sin\left(\delta_i - \delta_j\right) \tag{2.6}$$

where, V_i and V_j represent the voltage (in p.u.,) at the terminals of equivalent machines in area i and area j, respectively. δ_i and δ_j denotes the power angle of the equivalent machines in areas i and j, and X_{ij} stands for the reactance of the tie line connecting area i and area j.

Linearizing Equation (2.6) around an equilibrium point yield

$$\Delta P_{tie,ij} = T_{ij}(\Delta\delta_i - \Delta\delta_j) \tag{2.7}$$

where, T_{ij} represents the synchronizing torque coefficient defined as:

$$T_{ij} = \frac{|V_i||V_j|}{X_{ij}} \cos(\delta_i^0 - \Delta\delta_j^0) \qquad (2.8)$$

By substituting Equation (2.8) in (2.7) and applying Laplace transforms results:

$$\Delta P_{tie,i} = \sum_{\substack{j=1 \\ j\neq i}}^{i} \Delta P_{tie,ij} = \frac{2\Pi}{s}\left[\sum_{\substack{j=1 \\ j\neq i}}^{i} T_{ij}\Delta f_i - \sum_{\substack{j=1 \\ j\neq i}}^{i} T_{ij}\Delta f_j\right] \qquad (2.9)$$

The expression in Equation (2.9) can be depicted in the form of block diagram. When integrated with the mechanical power mismatch (ΔP_m - ΔP_D) as described in Figure 2.5, it results in the simplified interconnected power system block diagram as shown in Figure 2.6.

In Figure 2.6, the shaded block represents the LFC loop introduced by the presence of a tie-line. The change in tie-line power flow ($\Delta P_{tie,\,i}$) is fed back to influence the frequency change (Δf_i) through this secondary feedback loop. Subsequently, the Area Control Error (ACE_i) signal is calculated according to Equation (2.10) and applied to the controller.

$$ACE_i = \Delta P_{tie,i} + B_i \Delta f_i \qquad (2.10)$$

where, B_i is a bias factor, which can be determined using Equation (2.11):

$$B_i = \frac{1}{(R_i + D_i)} \qquad (2.11)$$

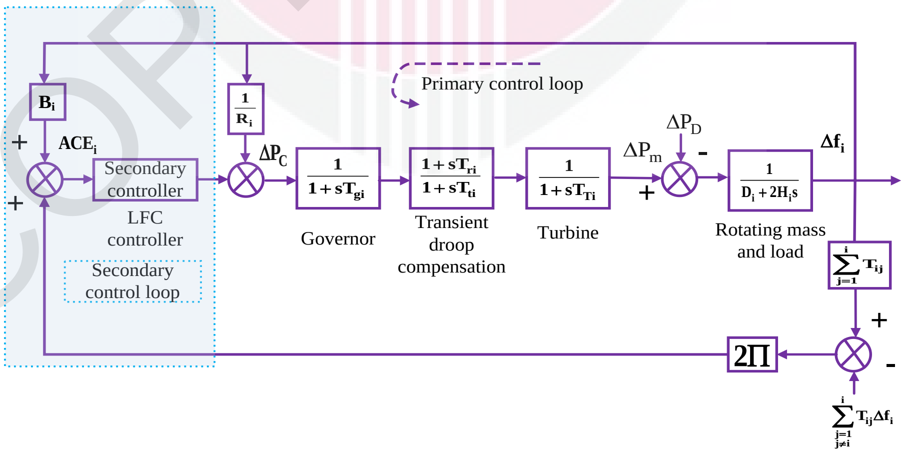

Figure 2.6 : Linearized transfer function model of ith area system
(Bevrani et al., 2011)

2.3 Diverse Power System Models Utilizing LFC

The evolution of power system models has been a continuous process driven by technological advancements, changing energy landscapes, regulatory developments, and the need for more efficient, reliable, and sustainable electricity generation and distribution. This section discusses, various system model that have been studied in the literature from the conventional thermal power generation model to modern power systems like smart grids, microgrids, and deregulation. To navigate the uncertainties and complexities of these systems, various new control techniques have been proposed. This section delves into the issues tied to traditional and modern power systems, highlighting their transformation and the challenges they pose.

2.3.1 Traditional Power Systems

For decades, the traditional generating models that has been widely used in power systems are thermal, hydro, and nuclear power resources. These systems are categorized into separate groups based on their scale and control area: single-area, two-area (the most extensively studied), three-area, and four-area power systems. While a few studies have explored larger power systems with more than four control areas, such investigations remain limited.

Researchers have extensively examined LFC in single-area power systems. For instance, a study (Ismayil et al., 2014) investigates LFC in a single-area power model incorporating thermal power plants. Another study (Doolla et al., 2006) evaluates a single-area hydropower system and proposes a novel LFC technique utilizing an ON/OFF control valve to reduce the size of the dump load. Frequency control of a single-area multi-source power system using classical controllers is explored by Mohanty et al., (2014).

In the context of two-area power systems, challenges related to LFC are widely discussed. Rahim et al., (2018) introduces Fuzzy Logic Control (FLC) based LFC and Integral (I) control for a two-area interconnected system. Different optimization techniques are utilized (Mostafa et al., 2018) to optimize the PID controller parameters for a two-area power system. Additionally, the performance of LFC is studied (Mohanty et al., 2014) for a dual-area interconnected power network with nonlinearities using Differential Evolution (DE) algorithm-based PI and PID controllers.

LFC issues in three-area power systems are reviewed extensively. Fractional-order PID controller design is explored for LFC in a three-area reheat thermal power system (Delassi et al., 2018). A neuro-fuzzy controller-based LFC is evaluated in a three-area hydrothermal system under varying load conditions (Saikia et al., 2014). An efficient Model Predictive Control (MPC) design is proposed to regulate the frequency in a three-area power system comprising nine power plants (Shiroei et al., 2013).

To keep frequency fluctuations within the permissible limits, large power systems interconnected by tie lines are often partitioned into multiple areas. Malik et al., (1988) proposes the first LFC approach for a four-area hydropower system using a generalized approach that combines dual-mode control, discontinuous control, and variable structure systems, while considering system nonlinearities. Another study employs a modified version of Bat Algorithm (BA) combined with fuzzy logic is implemented to optimize PI controller gains for LFC in a four-area power network (Khooban et al., 2015).

2.3.2 Deregulated Power Systems

In the context of an open energy market, LFC plays a crucial role in regulating the frequency to its nominal value and minimizing the tie-line power deviations between control areas. The evolution of the electricity market, including privatization, the establishment of free markets, and the pursuit of economic efficiency and reliability, has led to the deregulation of power system regulatory structures. This transformation has disintegrated the traditional vertical utility structure into distinct entities: Generation Companies (GENCOs), Transmission Companies (TRANSCOs), Distribution Companies (DISCOs), and Independent System Operators (ISOs), fundamentally altering the operation and configuration of electric energy networks (Abazari et al., 2019).

In a deregulated electricity market, LFC must account for various transaction types, including bilateral transactions and poolco-based transactions. DISCOs can enter into contracts with GENCOs or Independent Power Producers (IPPs) in bilateral transactions. Within the same area, DISCOs contracting with GENCOs is referred to as a poolco-based transaction. If a DISCO's demand exceeds the contracted power, it is considered as contract violation. The incremental power production of an area is influenced by its ACE, and each GENCO's is determined by its ACE participation factor (apf) (Christie et al., 1996).

The concept of Distribution Participation Matrix (DPM) is introduced by Donde et al., (2001) to explore the interactions between GENCOs and DISCOs. Each element in DPM is termed as contract participation factor (cpfs). Deregulated environment analysis of a thermal generating unit in two areas is conducted using DPM. Mohanty et al., (2020) extended the LFC analysis to multi-source power systems incorporating hydro, gas, nuclear, and thermal components. Sasaki and Enomoto et al., (2002) adapt the North American Electric Reliability Corporation standard to the Japanese energy system and assess the compliance of their LFC scheme with these standards. A comparative analysis of LFC in traditional and deregulated power environments is discussed elaborately by Kumar et al., (2021). A performance comparison of various controllers and optimization techniques in a deregulated environment is presented (Kumar et al., 2023). Another study (Prajapati et al., 2020) provides an overview of Electric Vehicles (EVs) technologies. Battery Energy Storage Systems (BESS) find widespread applications in mitigating frequency deviation caused by unexpected demand variations, with economic and operational advantages.

Many investigations are carried-out in deregulated power system without the incorporation of RES (Meliopoulos et al., 1999, Kumar et al., 2022, Latif et al., 2019). Limited studies are only available in the literature integrating large scale RES in realistic deregulated power system (Parmar et al., 2014, Kumari et al., 2020). An unequal three-area deregulated system with realistic dish Stirling solar thermal system and non-conventional sources in each area is studied by Babu et al., (2022). Another study considered a two-area multi source power system having a geothermal, dish Stirling power plant in each area with thermal power system (Tasnin et al., 2018). A three-area power system with wind, Geothermal power plant (GPP) and PV plant in each area is studied under various deregulated scenarios (Mishra et al., 2022). Similarly, a three-area deregulated model comprising thermal system, wind energy system and super magnetic energy storage device in each area is investigated by Das et al., (2021).

2.3.3 Microgrids

The rapid advancement of DGs have contributed to the widespread integration of DG units into grid systems. Additionally, the significant penetration of RES and the presence of multiple DG units in close electrical proximity have given rise to the emergence of MGs. An MG is a segment of the grid encompassing DERs, including DGs, RES, ESS, and load demands. MGs can operate in both autonomous/islanded and grid-connected modes. To the best of the author's knowledge, LFC has been applied on islanded MG system only. LFC strategies in grid connected MG system is found nowhere in the literature. The summary of literature works on islanded MG are listed in Table 2.2.

Table 2.2 : Summary on literature reviews on MG

System investigated	Concluding remarks	References
Islanded MG	1. RES such as wind power generation (WPG) and photo voltaic (PV) plants are considered as uncontrolled sources and diesel engine generator (DEG) as controlled source. 2. To provide frequency stability, battery energy storage system (BESS) and fuel cell (FC) are used. 3. An anti-windup PID controller is employed to regulate the frequency.	(Khaleel et al., 2023)
	1. RES such as wind and PV are considered as uncontrolled sources and DEG as controlled source. 2. ESS) such as such as AE, FC and flywheel energy storage (FESS) are used. 3. Conventional PI controller is utilized to regulate the frequency of MG.	(Naderipour et al., 2023)
	1. RES such as wind and PV are considered as controlled sources. 2. To provide frequency stability, BESS and FC are used. 3. An anti-windup PID controller is employed to regulate the frequency.	(Mansour et al., 2022)

Table 2.2 : Continued

	1. PV, wind and thermal systems are considered. 2. FC and BESS are used as energy storage system. 3. Fuzzy tuned MPC is utilized to regulate the frequency of isolated MG system.	(Kayalvizhi et al., 2017)
	1. RES such as PV and wind model are considered. 2. ESS such as BESS, FC are employed	(Khalghani et al., 2016)
	1. DEG and plugin electric vehicle (PEV) is used as controllable sources 2. Wind and PV sources are uncontrollable 2. FESS and BESS are used as ESS. 3. Fuzzy tuned FOPID controller is used to eliminate the frequency oscillations in MG.	(Khooban et al., 2017)
Shipboard MG	1. Ship DEG, ocean wave energy and PV are used as controllable sources 2. FESS and BESS are used as ESS. 3. Fractional order PID controller is used to eliminate the frequency oscillations in the MG.	(Kamal et al., 2022)
	1. Ship DEG, ocean wave energy and wind are used as controllable sources 2. FESS and BESS are used as ESS. 3. SMC controller is used to eliminate the frequency oscillations in the MG.	(Khooban et al., 2018)

2.3.4 Networked Microgrids

MGs plays a significant role in advancing the deployment of DERs by integrating them into the low or medium voltage distribution network. This integration not only improves network reliability but also enhances controllability (Bandeiras et al., 2020). Meanwhile, the increasing integration of distributed RES with unpredictable features poses challenges to the operation of MGs. Nowadays, parallel advancements in technology, smart meters, communication, and management have empowered individuals to play a more proactive role. This progress has made P2P energy trading among MGs feasible. Geographically proximate MGs can be interconnected in a cyber-physical sense, forming the NMGs system (Zhang et al., 2020a). In this system, multiple MGs are collectively managed to coordinate the inherent multiparty energy flow, information flow, and cash flow. The networking of autonomous MGs is emerging as a strategic initiative, aiming to provide high-quality and environmentally friendly energy and information services to local end-users. This is achieved by maximizing the utilization of limited resources shared among NMGs (Liu et al., 2018a). The summary of literature works on NMG are listed in Table 2.3.

Table 2.3 : Summary on literature reviews on NMG

System investigated	Concluding remarks	References
Islanded NMG	1. A three-area MG cluster with DEG, wind and FC in each area. 2. A distributed reconfigured model predictive control is used as a frequency controller.	(Yang et al 2023)
	1. Three-area NMG with wind, PV, EV aggregators and FC. 2. A linear active disturbance rejection controller is employed as a controller and state observer.	(Taghizadegan et al., 2023)
	1. Two-area model with SG, wind, PV and BESS are adopted in each area. 2. The optimal frequency deviation in each area is solved using MPC.	(Siti et al., 2022)
	1. Two-area model with thermal, PV, EV and BESS in area-1 and hydro, wind, EV, and FESS in area-2. 2. A 3-degree of freedom FOPI controller is employed to regulate the frequency of the NMG.	(Aly et al., 2023)
	1. Two-area model with DEG, PV, wind and BESS in each area. 2. An adaptive event triggered sliding mode controller is used to regulate the frequency.	(Luo et al., 2020)
NMG with DC link	1. A three-area interconnected multi microgrid network with biodiesel generator in each area and PV, wave and geothermal energy sources in area-1,2 and 3. 2. BESS such as redox flow battery, capacitive, solar oxide are employed to improve the frequency stability. 3. Proportional FOPID controller is employed to supress the frequency oscillations.	(Latif et al., 2019)
Shipboard NMG	1. A three-area consisting micro gas turbine, EV aggregators, and wind energy system. 2. A deep deterministic multi agent algorithm is employed to control the networked microgrid.	(Fan et al., 2023)

2.3.5 LFC for P2P Energy Market

The rapid expansion of RES, such as PV, WPG, and PEVs, has paved the way for the rise of small-scale energy producers known as prosumers. These prosumers can sell their surplus energy to neighbouring peers, utility companies, or even directly to the power grid through a mechanism known as P2P Energy Trading. The active involvement of prosumers, who are both consumers and producers of energy, is crucial for the success of P2P trading. A comprehensive overview of motivational psychology is provided to support P2P trading by enhancing user participation (Tushar et al., 2019). Broadly, the P2P sharing market is categorized into three types based on the trading method and information exchange among participants: coordinated market, decentralized market, and community market (Hu et al., 2021). Notably, there has been a growing number of studies integrating P2P trading mechanisms into the MG energy market. The determination of P2P trading prices in the MG market with the market structure in south Korea has been analyzed by An et al., (2020). Considering the seasonal factors and uncertainties in RES, a novel P2P trading framework is introduced (Tushar et al., 2019). For P2P trading in NMGs, Nasiri et al. (2022) introduces a novel bi-level hybrid robust-stochastic framework to analyze the strategic market behaviour of NMG that are interconnected and incorporate a high penetration of EV fleets. Similarly, a two-stage aggregated control in community MG to realize P2P energy trading is investigated (Long et al., 2018).

It is found that most existing studies only consider 'energy' as the main transactive commodity in the P2P energy market. In fact, the coalitions of small-scale prosumers can provide flexible ancillary service, which means the transactive commodities should not be only limited to energy (Hu et al., 2021). It is worth studying how both energy and ancillary can be co-ordinately traded. Ancillary services in the context of P2P energy trading refer to additional functions and support services that are essential for maintaining the stability, reliability, and efficiency of the electrical grid. Ancillary services typically include frequency regulation, voltage control, black start capability and demand response (Zhang et al., 2020b). According to the report of National Grid, UK, the frequency response can be categorized into two types of service: dynamic and non- dynamic. Dynamic frequency response is a continuously provided service to control the normal second by second changes, whilst non-dynamic frequency response is usually referred to the discrete service triggered at a defined frequency deviation (Siano et al., 2021). In the MG, entities such as dispatchable generation units, ESS and demand responsible loads can adjust their power generation or demand to flexibly offer the frequency response service. A comprehensive P2P trading mechanism for the MG should include ancillary service as a critical part of the entire trading process.

Several research works have attempted to integrate ancillary services into energy markets at both the distribution and transmission levels. Du et al., (2020) used NMGs, functioning as balancing service providers to the transmission system, participate in real-time balancing markets by submitting bids. A day-ahead scheduling strategy is proposed (Zhou et al., 2018) for integrated community energy systems to engage in joint energy and ancillary service markets. However, these joint markets are typically situated within the realm of wholesale markets. MGs are considered active prosumers that offer both energy and ancillary services to the distribution network (Siano et al., 2021). While the concept of joint energy and ancillary service exchanges is explored, the primary emphasis of this research centres on the optimal management of the distribution system. Additionally, an incentive contract between the independent system operator and providers of frequency regulation services is formulated (Rayati et al., 2019), enabling the simultaneous purchase of energy and ancillary services. An islanded MG with four prosumers and three consumers simultaneously participating in P2P energy trading and frequency ancillary services using LFC (Veerasamy et al., 2023). Further, the authors adopted blockchain technology to secure the P2P trading in MG. From the above literature studies, the crucial aspect of frequency regulation using LFC, which serves as a tradable ancillary service within the context of NMG has not been thoroughly examined. Furthermore, securing the P2P energy trading and the control signals from cyberattacks is not considered in the literature.

2.4 Control Strategies

The secondary frequency can be controlled via different schemes, such as centralized, decentralized, and distributed control. The following subsections describe in detail each control strategy.

2.4.1 Centralized Control

Centralized control strategies have been extensively studied for frequency regulation in high-voltage conventional synchronous generation systems, encompassing various power sources such as thermal, hydro, nuclear, and RES like micro-hydro and pumped storage. Several type of controllers, including linear, nonlinear, adaptive, and intelligent techniques, have been employed within the framework of centralized control. Research articles often emphasize computational intelligence methods to optimize integer order controllers. Notably, these studies are primarily concerned with optimizing centralized control strategies as depicted in Figure 2.7.

For instance, a centralized PID controller is utilized to control a two-area multi-source power system consisting of thermal, hydro, and gas units in each area. The PID controller gain values are optimized using a class topper optimization technique (Rai et al., 2020). A hybrid particle swarm optimization-gravitational search algorithm (PSO-GSA) is applied to tune PID controller gains, and its performance is compared with classical controllers such as I and PI controllers for a two-area conventional reheat thermal power network (Veerasamy et al., 2019). A novel adaptive SMC to regulate the frequency of a two-area thermal system, with sliding surface coefficients optimized using grey wolf optimization (GWO) algorithm (Guo et al., 2021). Peng et al., (2017) investigates an H_∞ control approach with event-triggered communication for a multi-area system with BESS.

Neural network-based control strategies are also integrated into frequency regulation. For instance, a generalized Hopfield neural network (GHNN) based adaptive PID controller for the frequency stabilization of a two-area conventional reheat thermal system, accounting for system non-linearities (Ramacandran et al., 2018). A neuro fuzzy-based PID controller is employed for LFC strategy (Jood et al., 2019). While many studies focus on single-loop control, there is a recent shift towards improving closed-loop performance by utilizing multi-loop/cascade combinations of PID and its modified forms. The strategies are often combined with optimization algorithms. PSO-GSA optimized cascaded PI-PD controller is applied to a two-unequal area system with various generation units and RE sources (Veerasamy et al., 2020). Abou El-Ela et al., (2022) studied a cascaded proportional-derivative with filter and proportional-integral (PDn-PI) control approach with gains obtained through a coyote optimization algorithm for a two-area thermal PV-wind energy system. Celik et al., (2021) employs a dragon fly algorithm to obtain gain values for a (1 + PD)-PID controller in a multi-area multi-source power system.

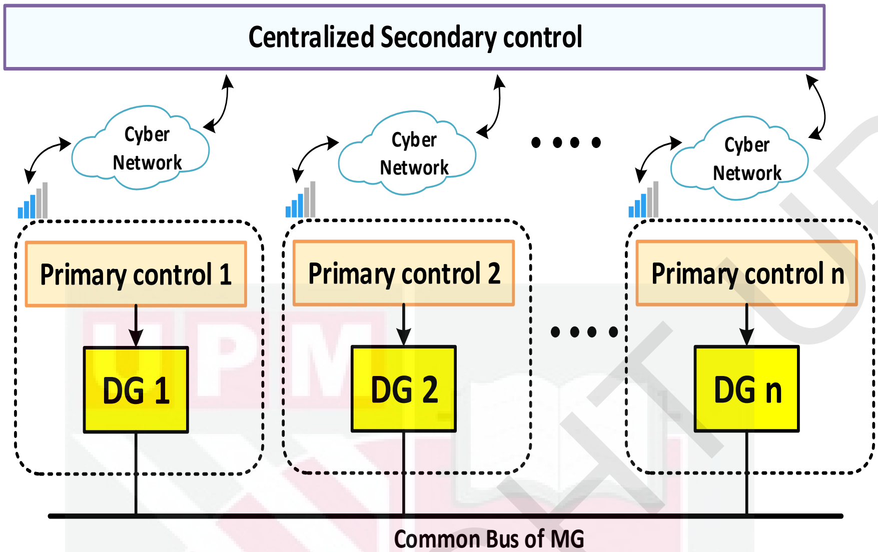

Figure 2.7 : Centralized control of the MG system

2.4.2 Decentralized Control

In contrast to a centralized approach, decentralized control is more favourable for large-scale interconnected systems (Veerasamy et al., 2023). It offers advantages over traditional centralized control methods by lessening computational demands and simplifying control processes. Furthermore, it demonstrates greater resilience against communication challenges and structural changes within the system (Pandey et al., 2013). In terms of control, each DG within the system possesses its individual local frequency information, contributing to the overall system frequency regulation, as depicted in Figure 2.8. In a study by authors in (Magdy et al., 2019), a decentralized PID controller, enhanced by PSO technique is introduced. This methodology is applied to an Egyptian power system encompassing several types of power plants and addressing communication delays.

Similarly, in a multi-area power system (Ebrahim et al., 2009) the authors employed PID control coupled with a stochastic PSO technique, separately within each control area. Another approach involves a Type-2 fuzzy-tuned PI controller implemented for a two-area reheat thermal unit (Sudha et al., 2011). This decentralized control concept is validated against both a Type-1 fuzzy PI and a conventional PI controller. An Internal Model Control (IMC) technique is proposed to adjust gain values of a decentralized PID controller specifically for a three-area reheat thermal system (Tan et al., 2011). For a multi-area power system with various power sources, including non-reheat, reheat, and hydropower networks (Fu et al., 2018), an active disturbance rejection controller is developed for each area to regulate the ACE of the power network.

Additionally, non-linear controllers such as SMC, H_∞ control, event-triggered integral SMC, and MPC are harnessed for managing the frequency of multi-area power systems. Mi et al., (2013) employed SMC for a multi-area multi-source power system. Similarly, an event-triggered integral SMC-based disturbance observer is adopted for a two-area non-reheat thermal power system (Shangguan et al., 2022). A novel decentralized control strategy is explored using switching control theory, addressing time delays and packet losses. This strategy's performance is evaluated against H_∞ and linear matrix inequality-Linear quadratic regulator (LMI-LQR) controllers (Zhang et al., 2020c). Shojaee et al., (2022) outlines a decentralized MPC design for regulating the system frequency with a wind turbine generation unit and a diesel engine generator. The efficiency of MPC is contrasted with the linear quadratic gaussian (LQG) controller and verified through simulation.

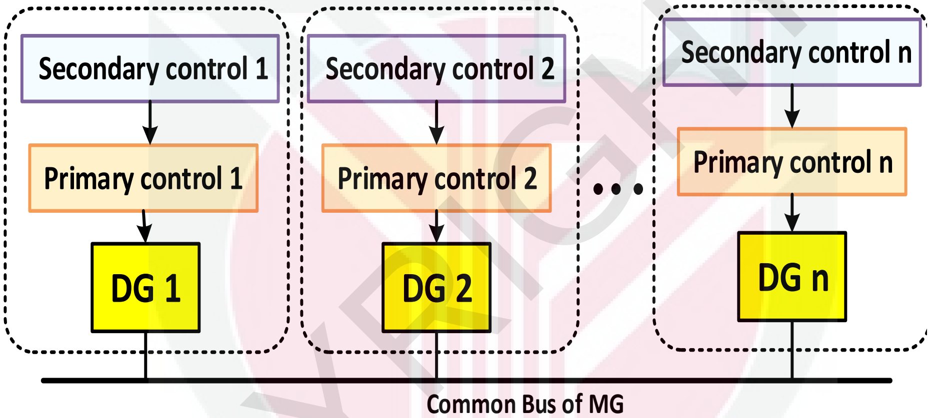

Figure 2.8 : Decentralized control of the MG system

2.4.3 Distributed Control

The distributed control (DC) is a coordinated control of multiple generating units or plants to be controlled through proper communication channel within the system. In the case of LFC, it has a secondary control as distributed to each unit and these controllers communicate with its neighbors for coordinate operation. This scheme is more advantageous, as it has the ability to operate even under uncertain disturbances. The fully distributed data updating of the DC structure results in efficient data sharing that helps in fast decision-making. Figure 2.9 shows the DC of the MG system and communication among each interconnected MG system in the cluster. Several types of DC have been carried out in distributed consensus-based control, leader-follower control, two-layered consensus algorithm, pinning gain-based distributed control, and distributed consensus cost minimization (Liu et al., 2018b). However, among these techniques, only a limited control structure is studied for secondary frequency control applications.

A distributed LFC scheme is proposed for a conventional power system by Andrade et al., (2020), which feedback the rotor angle deviation internally to the generator governor that acts as a distributed controller based on the control law. The developed control scheme is tested on the IEEE 39-bus system. A randomized distributed demand response algorithm is developed to stabilize the frequencies during contingencies (Vedady moghadam et al., 2014). Smart appliances are considered as load aggregators connected via a sparse communication network. The proposed control is validated on IEEE 9-bus system, revealing that the demand side response algorithm has successfully minimized the frequency deviation with minimum overshoots and undershoots.

A distributed averaging-based integral (DAI) control, also known as a consensus algorithm, is developed for the frequency regulation of a four-machine two-area test system (Schiffer et al., 2017). The robustness of the proposed distributed control is tested by applying constant and time-varying delays and link losses. The authors developed a distributed frequency regulation algorithm for a prosumer-based power grid. The communication network between the prosumer regulates the system-wide frequency by exchanging the frequency information (Honarvar Nazari et al., 2014). For ESSs in MG, a distributed frequency control strategy is developed to adjust the power output of ESSs and turbines by adaptive dynamic programming (ADP) control (Mu et al., 2019). The proposed method adjusts the frequency deviations better than fuzzy, LQR, and PID control. A leader-follower control strategy is employed for inverter-based cascaded parallel MG (Bidram et al., 2013). Similarly, a co-operative secondary frequency control for inverter-based MGs is proposed (Ding et al., 2019).

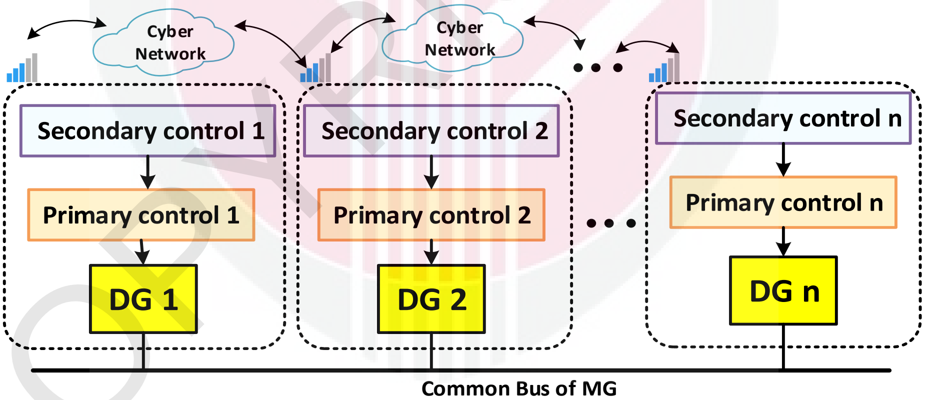

Figure 2.9 : Distributed control of MG system

2.5 Control Techniques

Over the past few decades, a multitude of sophisticated intelligence-based control techniques and approaches have been emerged in the context of LFC for modern power systems. These methodologies encompass various areas of interest, and their applications are closely scrutinized to achieve specific performance objectives. To succinctly outline the range of existing control methods in LFC, an overview is presented in Figure. 2.10.

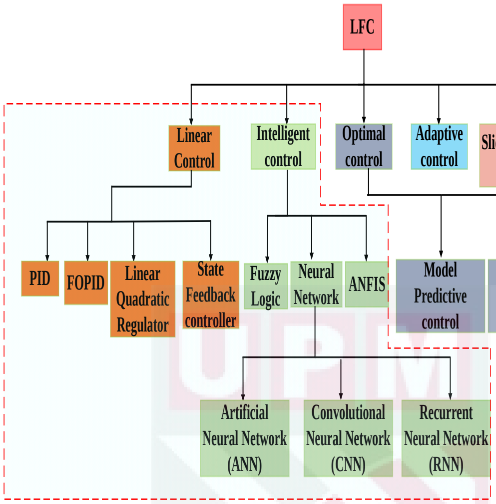

Figure 2.10 : General control techniques used by researchers for LFC of power system

2.5.1 Linear Control

The majority of research efforts within the realm of LFC predominantly focus on linear control strategies. Classical control methods, such as Bode, Nyquist, and root locus techniques, are commonly employed to derive optimal gains and phase margins. A brief overview of these methods is presented in the following subsections.

a. PID Control

The PID approach stands as the most prevalent, forming the basis for over 90% of industrial control loops (Kozak et al., 2014). In the context of LFC, the classical PI controller is proposed for a single-area electrical power system facing communication delays. The stability boundary locus, analyzed through an analytic-graphical framework is used to determine the appropriate PI parameters (Saxena et al., 2018). Two area thermal system considering generation rate constraints (GRC) and governor dead band (GDB) are studied with the application of PID controller (Veerasamay et al., 2020). The controller gain values are optimized using hybrid PSO algorithm. A PID controller is employed for a two equal area multi source system consisting of WPG, PV, wave and thermal power plant incorporating GRC in area −1 and WPG, PV and Thermal plant with GRC in area-2 (Hasanien et al., 2018). The initial gain values of the controller are optimized using whale optimization algorithm. Another study presents the design and implementation of PID control tuned using the PSO algorithm, to manage LFC in a standalone microgrid power network (Dhanasekaran et al., 2023). Despite the numerous advantages it offers, the PID controller performance is ineffective for uncertain, coupled, and nonlinear systems. Furthermore, for integrating processes, an excessive overshoot occurs due to a derivative kick.

b. FOPID control

A common fractional order (FO) controller based on FO calculus is FOPID. The difference between integer order (IO) and FO calculus is the FO controller, based on the extension of differentiation and integration to any order, which can be rational, irrational, or complex (Celik et al., 2019). Over the last few decades, fractional-order calculus plays a significant role in designing various controllers by expanding the fractional integrals and derivatives to fractional orders to achieve robustness and superior performance (Podlubny et al., 1999). FOPID controller is the generalization of traditional PID controller which has two additional tuning parameters offering great flexibility to the plant to be controlled. The unique features of FOPID controller are attaining a excellent response to a minimum phase system, controlling of nonlinear system without linearization, and less sensitive to system parameter variations (Cao et al., 2005). In the investigation of LFC strategies, both traditional PID and fractional-order Proportional Integral Derivative ($PI^{\lambda}D^{\mu}$, where λ represents the order of integration and μ is the order of differentiation) controllers, tuned using moth flame optimization (MFO) are explored for single and dual-area power systems (Saurabh et al., 2020). The results indicate that $PI^{\lambda}D^{\mu}$ outperforms PID in damping frequency oscillations and managing tie line power fluctuations.

The influence of employing a fractional-order proportional-integral (PI^{λ}) controller in a single-area-delayed LFC system is explored by Celik et al., (2019), with a particular focus on its impact on delay margin improvement. Optimization techniques are employed to fine-tune PI controller parameters for LFC in a three-area interconnected system (Kumari et al., 2017). This study highlights the importance of precise tuning of integral gain to strike a balance between desired transient response and minimal overshoot in dynamic system performance. In the context of a hybrid energy distributed power system, an FOPID controller is proposed with an effective biogeography-based krill herd optimization technique (Daraz et al., 2023). The effectiveness of the controller is tested on a three-area hybrid power system model.

c. Nonlinear FOPID control

The linear FOPID controller discussed above cannot maintain a reliable control performance as the LFC of a power system usually operates at a wide range in real time because of its associated uncertainties (Elyaalaoui et al., 2021). Furthermore, the linear FOPID controller may cause instability if the operation condition varies significantly. To counteract such complexities, a nonlinear function is inserted with the linear FOPID control and termed as nonlinear FOPID (NLFOPID) controller. The NLFOPID controller has been proven to be effective in various domains like control of highly nonlinear redundant robotic systems (Kumar et al., 2017), hypersonic vehicle attitude control (Song et al., 2015), underwater vehicle control (Hasan et al., 2020), and control of wind turbines (Pathak et al., 2020). In LFC, a hyperbolic tangential function is incorporated in to a linear FOPID controller of deregulated power system in presence of EVs and RES (Fathy et al., 2022). A nonlinear FOPI controller is employed for primary frequency control application of two area power system model (Elyaalaoui et al., 2021). Similarly, a hyperbolic secant function is embedded to improve the performance of the FOPID controller for islanded MG network comprising WTPG, PV and DEG (Athira et al., 2023). The hyperbolic functions used in the literatures are not as smooth or bounded over their entire domain. For designing nonlinear controllers for control systems with nonlinear behavior smooth and bounded saturation properties make it a versatile function for limiting the control signal and ensuring stability and performance in control systems. Therefore, a smooth and bounded hyperbolic function is needed to enhance the robustness of the linear FOPID controller.

d. Approximation Techniques

For practical and simulation implementation of the FOPID and NLFOPID controller the fractional order transfer function of the controller should be approximated to integer order. Numerous strategies are available in the literature for approximating the FO transfer function model. The most commonly used techniques are oustaloup, improved oustaloup and Matsuda approximation techniques (Deniz et al., 2020). The oustaloup approximation (Baranowski et al., 2015) that relies on recursive distribution of zeros and poles in a selected frequency band has been used to convert the non-integer order transfer function to integer order transfer function. The mathematical formulation of rational oustaloup filter is described as (Deniz et al., 2016):

$$G(s)=k\prod_{i=-N}^{N}\frac{s+\omega'_i}{s+\omega_i} \tag{2.12}$$

$$\omega'_i=\left(\frac{\omega_h}{\omega_b}\right)^{\frac{i+N+\frac{1}{2}(1+q)}{2N+1}} \tag{2.13}$$

$$\omega_i=\left(\frac{\omega_h}{\omega_b}\right)^{\frac{i+N+\frac{1}{2}(1-q)}{2N+1}} \tag{2.14}$$

where N is defined as an order of approximation, ω_h and ω_b are the higher and lower bound of the selected frequency band, ω'_i and ω_i are the zeroes and poles of the filter by dividing the frequency range into 2N+1 intervals. However, the oustaloup technique has a poor approximation effect in the frequency band near the lower bound and higher bound (Gao et al., 2012).

To overcome the boundary fitting issue of oustaloup approximation, an improved oustaloup approximation is proposed by Gao et al., (2012), which incorporates the appropriate weight coefficients b and d in the approximation process to overcome the boundary fitting problem. The fitting frequency range for improved oustaloup approximation is specified at [ω_b, ω_h], and the order is N. For simulation, ω_b = 0.01

rad/sec, ω_h = 1000 rad/sec and N=5 is considered. The fractional-order operator s^α is approximated as:

$$s^{\alpha}=\left(\frac{d\omega_b}{b}\right)^{\alpha}\left(\frac{ds^2+bs\omega_h}{d(1-\alpha)s^2+bs\omega_h+d\alpha}\right)\left[\frac{1+\dfrac{s}{d\omega_b/b}}{1+\dfrac{s}{d\omega_h/b}}\right]^{\alpha} \tag{2.15}$$

where, b>0, d>0, 0< α <1, and s=jω, the fractional component K(s) can be expressed as a rational transfer function in the form of poles and zeros:

$$K(s)=\lim_{N\to\infty}K_N(s)=\lim_{N\to\infty}\prod_{k=-N}^{N}\frac{1+s/\omega'_k}{1+s/\omega_k} \tag{2.16}$$

The zero and pole of k are defined below:

$$\omega'_k=\left(\frac{b}{d}\right)^{\frac{2k-\alpha}{2N+1}}\omega_h^{\frac{N+k+\frac{1}{2}(1-\alpha)}{2N+1}}\omega_b^{\frac{N-k+\frac{1}{2}(1+\alpha)}{2N+1}} \tag{2.17}$$

$$\omega_k=\left(\frac{b}{d}\right)^{\frac{2k+\alpha}{2N+1}}\omega_h^{\frac{N+k+\frac{1}{2}(1+\alpha)}{2N+1}}\omega_b^{\frac{N-k+\frac{1}{2}(1-\alpha)}{2N+1}} \tag{2.18}$$

A continuous rational transfer function model is obtained by approximating the irrational fractional part of Equation (3.29)

$$G(s)=K\left(\frac{ds^2+b\omega_h s}{d(1-\alpha)s^2+b\omega_h s+d\alpha}\right)\prod_{k=-N}^{N}\frac{1+s/\omega'_k}{1+s/\omega_k} \tag{2.19}$$

where, $K=(\omega_b\omega_h)^{\alpha}$.

2.5.2 Intelligent Control

In the recent years, the integration of RES has led to increasing the size and the structural complexity of power systems. The linear controllers are not sufficient to achieve the desired level of accurate operation. To address this issue, intelligent techniques such as artificial neural network (ANN), fuzzy logic, and meta-heuristic based optimization algorithms have been used to solve this problem to a great extent. A concise review of these approaches is provided in the following paragraphs.

a. ANN Control

ANN is a concept motivated by biological nervous systems. The implementation of the ANN controller to enhance the dynamic performance of LFC in a three-area interconnected power system. ANN is utilized to tune the gains of PI controller (Kumar et al., 2016). ANN observer-based nonlinear sliding mode control (SMC) designed for LFC in a dual-area power system is presented (Prasad et al., 2020); ANN observer is employed to estimate the power plant unmeasured states and unmatched perturbations. A layered recurrent ANN based LFC is studied fora dual-area interconnected power system with WPG (Sharma et al., 2020).

b. RNN Control

Recurrent Neural Network (RNN) a type of ANN which is used to design the dynamic controller for LFC applications to deal with the system dynamics and uncertainties. For instance, Hopfield neural network (HNN) is a subset of RNN which is applied for a two-area thermal power system model. The control performance is compared with the linear controllers (Ramachandran et al., 2018). The same authors used HNN as an adaptive FOPID controller for multi-area RE integrated power network. The controller performance is compared with HNN PID controller (Ramachandran et al., 2021). Veerasamy et al., (2022) modifies the HNN as cascaded PID controller to regulate the frequency of complex RE integrated system with EV aggregators. However, only limited studies are available in the literature employing RNN-based dynamic control.

c. Fuzzy Logic Control

Due to its robustness and reliability, fuzzy logic control approach is applied to deal with complex and nonlinear control problems that cannot be addressed efficiently by traditional control methods. FLCs can be designed and implemented without modelling the controlled process. This approach has widely been used for various LFC challenges in power systems. Design and implementation of fuzzy-based hierarchical approach to improve the frequency control performance in the Great Britain power system is investigated by Sharma et al., (2020). Hence, the proposed design asserts its robustness against different load conditions and parameters uncertainty of the investigated system. A PI controller incorporated with fuzzy logic gain scheduling technique based on two-level control strategy has been successfully employed for LFC for a dual-area power system (Hussein et al., 2019). Using fuzzy self-tuning PID controller based on Tribe-DE algorithm, LFC for an interconnected two-area power system is proposed (Jalali et al., 2020).

2.6 Optimization Techniques

To guarantee reliable control and desirable dynamic system performances, optimization algorithms have been considerably used by the researchers for LFC study to tune the controller parameters. In the last decade, researchers have investigated the control and stability of power systems using different algorithms such as genetic algorithm (GA), PSO, firefly algorithm (FA), Teaching learning-based optimization (TLBO), and so on based on ‘No free lunch’ theory. GA and PSO are the most widely utilized algorithms to address different issues in the field of power systems. The successful implementation of these algorithms later is used to optimize the parameters of a fuzzy controller for LFC in a dual-area power system with PV Plant (Cam et al., 2017). The decentralized LFC synthesis is formulated as a multi-objective optimization problem and is solved using GA to design well-tuned PI controllers in multi-area power system (Daneshfar et al., 2012).

FA tuned Fuzzy logic based on Two-Degree of freedom PID controller is employed to damp the frequency fluctuations and control the tie line power flow in an interconnected diverse-sourced multi-area power system (Raju et al., 2020). FA tuned PI controller-based LFC is investigated for a two-area system comprises PV system (Abd-Elazim et al., 2018). An improved version of FA and pattern search tuned optimal gains of fuzzy aided PID controller to damp out the frequency deviation is studied considering the nonlinearity constraints (Rajesh et al., 2019b). In addition to the approved superiority of the proposed design over other previous techniques, there is no need to retune the parameters of the proposed controller when the system experiences different load conditions or parameters uncertainties.

Besides all these techniques, recently numerous algorithms had been proposed and implemented for LFC applications. An artificial rabbit’s algorithm is proposed for optimal tuning of a PID controller in a three-area HPS. The performance of the proffered control technique is compared with PSO, DE and JAYA algorithms. In terms of ST, PO and PU, the artificial rabbit algorithm tuned PID controller outperforms than other optimization technique (El-sehiemy et al., 2023). For a three degree of freedom PID controller, a novel meta-heuristic technique namely equilibrium optimizer has been developed for a two-area multi source power system model (Guha et al., 2021). The outcomes have been evaluated with GA, PSO and GWO techniques. Similarly, for a two-area interconnected power system Archimedes optimization algorithm is developed to optimize the gain values of tilt integral derivative controller (Ahmed et al., 2022). The simulation results reveals that the proposed control technique outdoes PSO, WOA and GWO algorithms.

2.6.1 Atom Search Optimization

Numerous heuristic techniques have been employed to fine-tune controller parameters for LFC applications. Nonetheless, optimizing the controller's gain values remains a significant challenge for researchers, given the increasing uncertainties in power system generation and load. Due to these challenges, researchers are actively exploring novel optimization techniques to enhance system performance by optimizing controller gain values. In this context, ASO a recent population-based metaheuristic optimization algorithm inspired by physical theory of molecular dynamics, which describes the structure of matter and how atoms interact at the micro level (Zhao et al., 2019a). ASO's efficacy has been validated in various real-time engineering applications, such as parameter estimation for hydrogeologic problems (Zhao et al., 2019a), Polymer

Exchange Membrane (PEM) fuel cells (Mossa et al., 2021), feature selection (Too et al., 2020), dispersion coefficient in ground water (Zhao et al., 2019b), power system stabilizer (Izci et al., 2022) and many engineering problems (Sun et al., 2021).

The attractive feature of using ASO is the interaction force from the potential energy expressed by Lennard-jones potential and the geometric constraint force between two atoms are used to perform a search. The interaction force between atoms has two main properties. The first is the repulsion to compression, which repels the atom when crowdedness is within a certain range. The second is the attraction between atoms. Constraint forces are employed to keep the bond length and angle between any two atoms at the desired levels. During early iterations of ASO, an individual atom interacts with other atoms through attraction or repulsion, and repulsion can prevent over accumulation of atoms and premature convergence of the algorithm improving the exploration ability across the whole search space. As iterations progress, the repulsion steadily weakens and the attraction gradually strengthens, indicating that exploration is decreasing, and exploitation is increasing. During the final iterations, each atom interacts with others simply by attraction, ensuring that the algorithm has a better exploitation capability. Throughout the iterative process, constraint force between each atom and the atom with the best fitness always exists (Zhao et al., 2019b).

In LFC, ASO has been implemented to optimize the gain values of PID controller of HPS. The effectiveness of the proposed optimization technique is compared with other well-established techniques like GA, PSO, ALO and BA (Khokhar et al., 2020). The proposed ASO tuned PID controller outperforms other techniques in terms of settling time (ST) by 72 %, Peak overshoot (PO) by 56 %, Peak undershoot by 41 %. However, ASO like other stochastic optimization algorithms rely on RNG to explore the search space, make decisions, and guide the search toward optimal solutions. The convergence properties of ASO are closely tied to the random numbers generated by the RNGs utilized in each algorithm. The use of RNGs can sometimes limit the diversity of solutions generated by optimization algorithms, preventing them from exploring all the modes in a multi-modal objective landscape within the search space (Hekimoglu et al., 2019). This limitation can particularly impact the exploration phase during the early iterations, potentially leading to premature convergence and trapping in local optima.

2.6.2 Chaos based Optimization Techniques

To address the issues of poor convergence rate and pre-empt from being confined to local optima in traditional RNGs based optimization techniques chaos functions is introduced into the optimization algorithms. Chaos exhibits properties such as ergodicity, dynamics, and non-repetitiveness (Barshandeh et al., 2021). These properties are valuable in optimization as they contribute to a more diverse search. Chaos introduces dynamism, enabling the algorithm to produce a wide range of solutions and explore different landscapes within the search space. These characteristics of chaos accelerate the search process by avoiding repetition and ensuring that the algorithm explores various regions of the search space (Mundra et al., 2023). To incorporate chaos into metaheuristic algorithms, chaotic maps are used to generate chaotic sequences instead of relying solely on RNGs.

The most widely used chaotic maps are one dimensional (1D) chaotic map due to their simple structure and easy implementation (Zhang et al., 2023a). The various 1D chaotic maps are circle map, cubic map, Gauss map, iterative chaotic map with infinite collapses, logistic map, sine map, tent map, Chebyshev map, piecewise map, and singer map. Out of all these, the logistic map, sine map, and tent map are the most popular 1D chaotic maps used in optimization techniques to improve the convergence speed and search capability (Singh et al., 2022). The chaotic maps studied in the literature works are detailed as follows:

a. Logistic Map

The logistic map is widely used second-order, simple, nonlinear, and dynamic polynomial map. This map's equation generally appears in biological population of nonlinear dynamics exhibiting chaotic behaviour (Demir et al., 2020). Mathematically the logistic map can be expressed as:

$$x_{k+1} = rx_k \left(1-x_k\right) \tag{2.20}$$

where k defines the number of iterations, x_k signifies the chaotic variable, and r is the control parameter lies in the interval (0, 4). In most of the literature work, the value of r is chosen between 1 to 4 to generate the chaotic sequence (Tian et al., 2017, Zhang et al., 2023b). Since, the value of r between 1 to 3 gives poor chaotic behaviour as inferred from Figure 2.11. But the chaotic sequence is exhibited in the range of $3 \le r \le 4$ with certain selection of parameters.

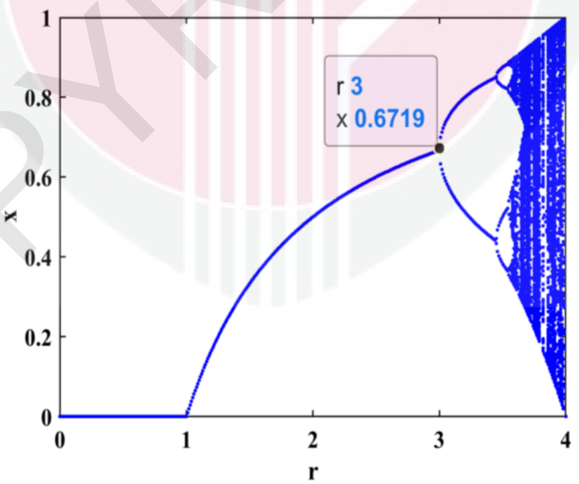

Figure 2.11 : Bifurcation diagram of logistic map

b. Sine Map

Sine map is one of the simple 1D chaotic maps that generates similar chaotic sequences as logistic map (Demir et al., 2020). However, the mathematical expression of the sine map is totally different from the logistic map and is given as:

$$x_{k+1} = r\sin\left(\pi x_k\right) \tag{2.21}$$

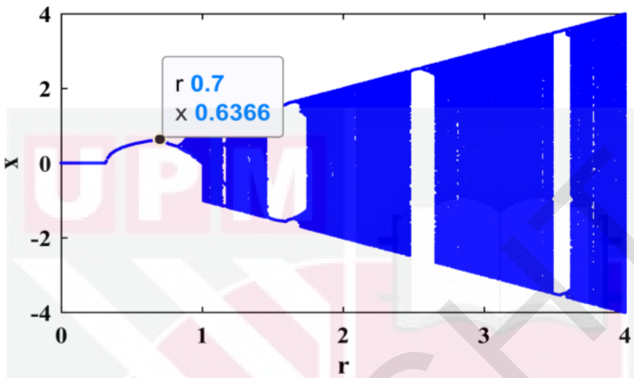

Figure 2.12 : Bifurcation diagram of sine map

Equation (2.21) describes the sine function, which maps the input angle in the range of [0,4], where r is the bifurcation parameter, x_k and x_{k+1} denotes the current and next iterative sequence between 0 and 1, respectively. The sine map shows satisfactory chaotic behaviour when r ∈ [0.7, 4]. Moreover, it is substantially revealed from Figure 2.12, that there is some correlation between the sine and logistic maps at the initial stage.

c. Tent Map

A tent map is a discrete-time, piecewise, linear chaotic map with some unique attributes like simple shape, chaotic orbits, etc (Li et al., 2021). The mathematical formulation of the tent map is given by

$$x_{k+1} = \begin{cases} r\dfrac{x_k}{2} & x_i < 2 \\ r\dfrac{(1-x_k)}{2} & x_i > 2 \end{cases} \qquad 0 < r \le 4;\ x_k \in [0,1] \tag{2.22}$$

The dynamic behaviour of the tent map depends on the control parameter r which varying from predictable to chaotic. The bifurcation diagram of the tent map is illustrated in Figure 2.13. The tent map has distinctive advantages of higher iterative speed than logistic map, and the probability density function is uniform compared with the logistic and sine map (Fan et al., 2020).

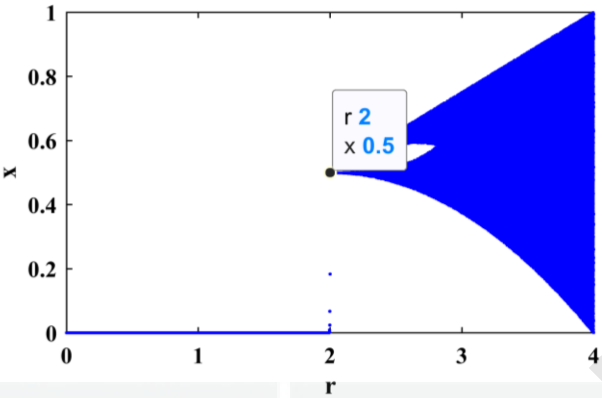

Figure 2.13 : Bifurcation diagram of tent map

2.7 Summary

This chapter provides a literature survey on LFC for power systems which covers a wide range of topic, including, a conventional power system models, recent developments in LFC methodologies for various aspects of modern power systems (deregulated systems, MGs, NMGs and P2P market), and a concise overview of different control strategies. Based on the literature survey, the following research gaps have been identified as addressed:

Numerous researchers have investigated several control frameworks for deregulated system. However, only few studies are conducted by considering suitable control strategy with an optimum controller. Several studies have been explored to design the gain parameters of FOPID controller with a control strategy used in LFC applications for NMG system. However, there is a lack of research that considers the dynamic variation of these controller gain parameters with a suitable control strategy in response to changes in system parameters, RE power generation and loading condition. Various researchers have adopted blockchain technology to secure the P2P transactions in energy markets. However, limited research is available in the literature in order to secure the controller and P2P energy trading in the NMG system against cyber threats.

CHAPTER 3

METHODOLOGY

3.1 Introduction

This chapter outlines the overall structure of methodology employed in this research. Figure 3.1 provides an overview of the framework for the research work. The methodology is applied to achieve three distinct objectives. The first objective focuses solely on developing an improved form of ASO called chaotic ASO (CASO) algorithm. An RE integrated two-area power system is developed in MATLAB/Simulink to examine the robustness of the proposed technique. A centralized FOPID controller is employed in this case, and the gain values of the controller are optimized using the proposed CASO algorithm. Then, to further improve the performance of the algorithm, a hybrid AS-PSO algorithm is proposed as the second objective. The effectiveness of the proffered control technique is assessed to optimize the gain values of the controller in regulating the frequency of a RE integrated multi-area power network developed in a deregulated environment. To regulate the frequency of the network, a deregulated robust NLFOPID controller is proposed, and the parameters are adjusted using the propounded control technique. Finally, the third objective involves the development of a new algorithm by combining CASO (objective 1) and AS-PSO (objective 2) called CAS-PSO algorithm. The efficacy of the algorithm is further improved by modifying the constant gain values of the algorithm into an adaptive one using the ZND based FOPID controller. Further, the initial bias values of ZND-FOPID are obtained using the proposed CAS-PSO algorithm. To evaluate the effectiveness of the proffered control technique, a NMG power network is developed. Consequently, the robustness is exhibited for the real-time P2P energy trading between the MGs in the NMG implemented using blockchain. Additionally, the controller is also implemented in the blockchain environment to make it more resilient against the attack. The implementation is carried out using a real-time digital simulator called OPAL-RT simulator interfaced with Raspberry Pis (RPis) via transfer control protocol/internet protocol (TCP/IP).

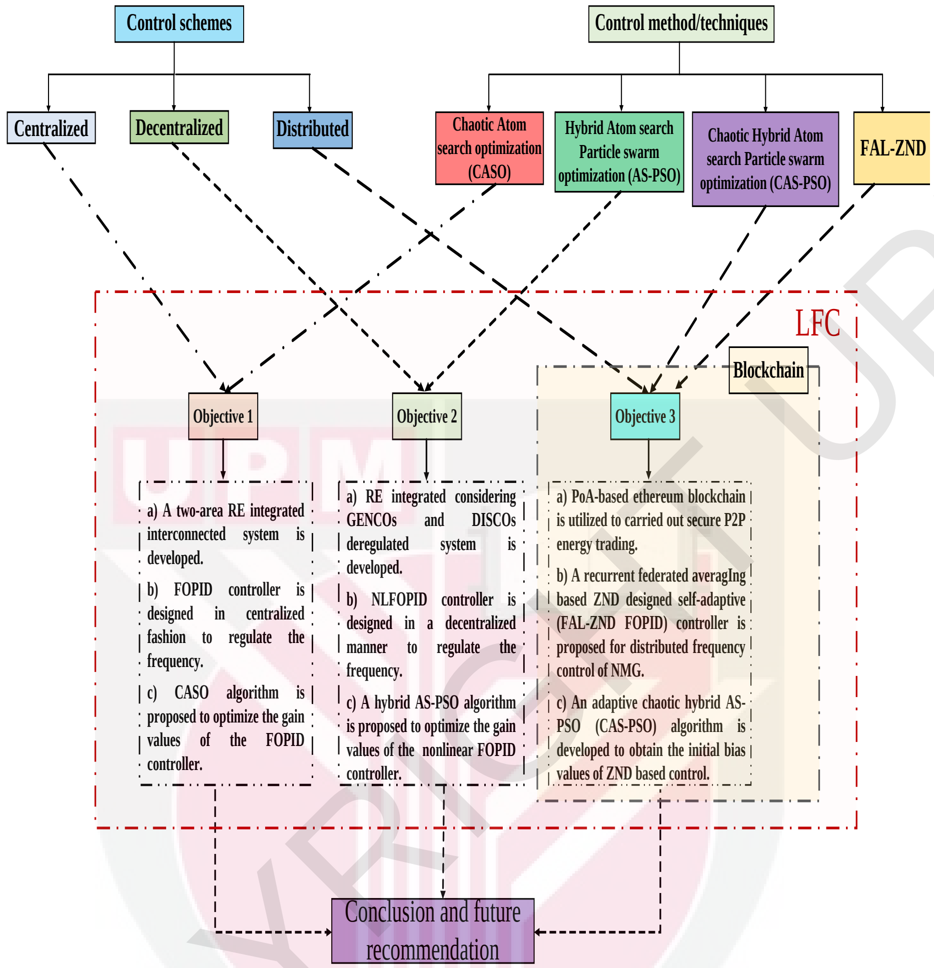

Figure 3.1 : Flowchart representing the overall research

3.2 The Design of Centralized FOPID Controller

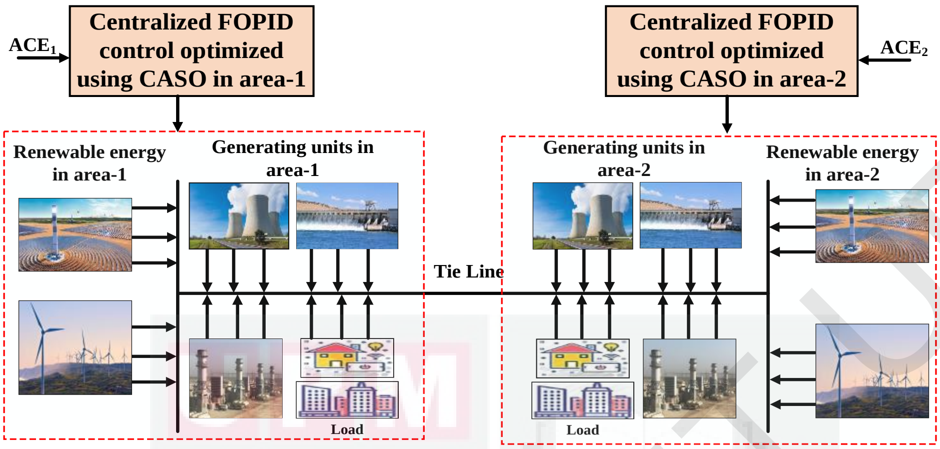

Figure 3.2 : Schematic representation of centralized control in LFC

In the first objective, FOPID controller is employed as a centralized control. Figure 3.2 depicts the schematic representation of centralized control scheme in LFC. Figure 3.3 depicts the proposed CASO optimized centralized FOPID controller approach for LFC of power system. The transfer function and control output of centralized FOPID controller are given as:

$$K(t)=K_p+K_i\frac{d^{-\lambda}}{dt^{-\lambda}}+K_d\frac{d^{\mu}}{dt^{\mu}} \tag{3.1}$$

$$u(t)=(K_p+K_i\frac{d^{-\lambda}}{dt^{-\lambda}}+K_d\frac{d^{\mu}}{dt^{\mu}})\times e(t) \tag{3.2}$$

where, $e(t)=\Delta f_i+\Delta P_{tie,i\,j}$. Δf_i signifies the change in frequency of i^{th} area. $\Delta P_{tie,ij}$ defines the change in tie line power between i^{th} and j^{th} area. K_p, K_i, and K_d are the proportional, integral, and derivative gains of the controller, λ and μ represents the integral and differential operators, which takes the values of arbitrary any real number. In this work, the integral time absolute error (ITAE) is chosen as an objective function (J) to tune parameters of FOPID controller by minimizing the ACE as it provides the superior performance by reducing the settling time and undershoots of the plant to be controlled. The objective function can be defined as (Sondhi et al., 2014),

$$J=ITAE=\int_0^T\left[\left|\Delta f_i+\Delta P_{tie,i\,j}\right|\right].tdt \quad \because i,j=1,2,3\,\&\,j\neq i \tag{3.3}$$

Subjected to the following boundary constraints:

$$K_p^{min} \le K_{pi} \le K_p^{max}, K_d^{min} \le K_{di} \le K_d^{max}, \mu^{min} \le \mu_i \le \mu^{max},$$
$$K_i^{min} \le K_{ii} \le K_i^{max}, \lambda^{min} \le \lambda_i \le \lambda^{max} \tag{3.4}$$

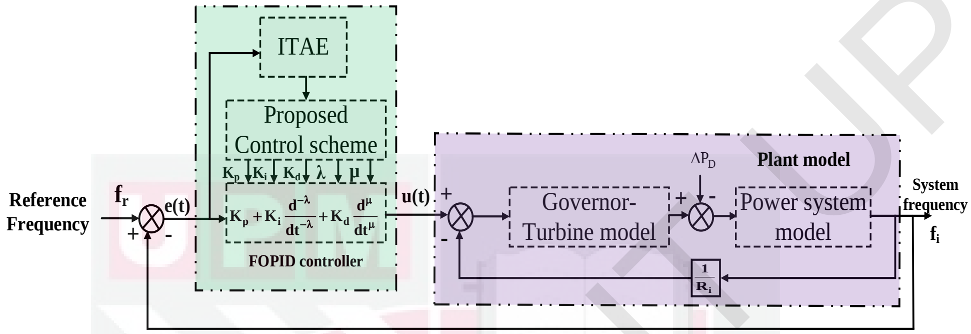

Figure 3.3 : Closed-loop feedback control of power system with CASO-FOPID controller

3.2.1 CASO for Tuning of FOPID Controller

The steps for tuning the FOPID controller using CASO are detailed as follows:

Step 1: Initialize the gain and fractional order terms randomly, and its positions are described as $X_i = (xi^1, ...x_i^d, ...x_i^n)$, where i denotes an atom in the population (i=1,2, ...N), and d denotes the dimension (d=1,2, …D) of the search space.

Step 2: Define the values of initial parameters such as depth weight (α), multiplier weight (β), and a maximum number of iterations (T) and initialize the number of atoms (N), its position, and velocity. For the given parameters, calculate the fitness function defined in Equation (3.3) for each atom.

Step 3: Calculate the mass $m_i(t)$ of i^{th} atom using the equation defined below,

$$m_i(t) = \frac{M_i(t)}{\sum_{j=1}^{N} M_i(t)}, \quad M_i(t) = e^{-\frac{Fit_i(t) - Fit_{best}(t)}{Fit_{worst}(t) - Fit_{best}(t)}} \tag{3.5}$$

where $Fit_i(t)$ is the i^{th} atom fitness value at t^{th} iteration and $Fit_{best}(t)$ and $Fit_{worst}(t)$ are the atom best and worst fitness value at t^{th} iteration which can be defined as

$$Fit_{best}(t) = \min_{i \in \{1,2,\ldots,N\}} Fit_i(t) \tag{3.6}$$

$$Fit_{worst}(t) = \max_{i \in \{1,2,\ldots,N\}} Fit_i(t) \tag{3.7}$$

Step-4: To intensify the exploration phase in the early stage of iterations, each atom must interact with as many neighbourhood atoms with better fitness values as possible, where the K neighbour atom performs to improve the exploitation during the final iterations. Thus, each atom must interact with few atoms with better fitness values as possible as its K neighbours. As a result, K decreases with progress in iteration number corresponding to function of time as follows.

$$K(t) = N - (N-2) \times \sqrt{\frac{t}{T}} \tag{3.8}$$

Step 5: Compute the total interaction force $F_i^d(t)$ exerted by other atoms on the i^{th} atom in the d^{th} dimension space that can be expressed as sum of the forces with random weights as follows.

$$F_i^d(t) = \sum_{j \in Kbest} rand_j F_{ij}^d(t) \tag{3.9}$$

where $rand_j$ is a random number ranging between 0 and 1. The constraint force $G_i^d(t)$ is expressed as a force-controlled by the best atom on each atom. Therefore, the constraint force can be calculated as

$$G_i^d(t) = \lambda(t)\left(x_{best}^d(t) - x_i^d(t)\right) \tag{3.10}$$

where λ is the Lagrangian multiplier expressed as $\lambda(t) = \beta e^{\frac{-20t}{T}}$, $x^d_{best}(t)$ defines the best atom found at t^{th} iteration in d^{th} position, $x^d_i(t)$ depicts the best atom attained at t^{th} iteration in i^{th} position. Finally, the resultant force is obtained by adding constraint force and interaction force.

$$F_r^d(t) = F_i^d(t) + G_i^d(t) \tag{3.11}$$

Step 6: Determine the acceleration of each atom through interaction and constraint force of atom as below,

$$
a_i^d(t) = \frac{F_i^d(t)}{m_i^d(t)} + \frac{G_i^d(t)}{m_i^d(t)} = -\alpha\left(1-\frac{t-1}{T}\right)^3 e^{\frac{-20t}{T}}
\sum_{j\in Kbest} \frac{rand_j\left[2\times\left(h_{ij}(t)\right)^{13} - h_{ij}{}^{7}\right]}{m_i(t)}
\frac{\left(x_j^d(t)-x_i^d(t)\right)}{\left\|X_i(t),X_j(t)\right\|_2} + \beta e^{\frac{-20t}{T}} \frac{x_{best}^d(t)-x_i^d(t)}{m_i(t)} \tag{3.12}
$$

In case of ASO algorithm, the velocity of each atom is calculated using Equation (3.13) defined as,

$$
v_i^d(t+1) = rand_i^d v_i^d(t) + a_i^d(t) \tag{3.13}
$$

In Equation (3.13), $v_i^d(t)$ and $a_i^d(t)$ denote the current velocity and acceleration vectors of i^{th} atom in d^{th} dimension in search space, respectively, where $v_i^d(t+1)$ signifies the new velocity values, and $rand_i^d$ generates a random number in the range (0,1).

In case of CASO, the chaotic sequences created by the chaotic map (logistic, sine, and tent) replace the random parameter $rand_i^d$ of ASO which improves the flexibility of the atom in each iteration and convergence rate. The velocity updating equation of CASO is defined in Equation (3.14), and the corresponding position of each atom is updated at iteration t is formulated as given in Equation (3.15).

$$
v_i^d(t+1) = x_k v_i^d(t) + a_i^d(t) \tag{3.14}
$$

$$
x_i^d(t+1) = x_i^d(t) + v_i^d(t+1) \tag{3.15}
$$

Step 7: Check maximum number of iterations is reached and obtain the optimized controller parameters as x_{best}. If not, repeat from step 2 through 7 until the stopping criterion is reached.

As a result, the optimized FOPID control parameters are obtained by reducing the ACE of interconnected HPS by reaching the global minima with the atoms' location providing the best optimal solution. The initialized parameters of CASO are T=100, N=50, α=50, and β =0.2. The above steps are summarized in the form of flowchart for optimizing the parameters of FOPID controller as depicted in Figure 3.4. The boundaries for tuning the parameters of FOPID controller such as k_p, k_i and k_d [$k_{pi,\,min}$, $k_{pi,\,max}$, $k_{ii,\,min}$, $k_{ii,\,max}$, $k_{di,\,min}$, $k_{di,\,max}$] are bounded between [-3, 3], λ and μ is selected between [0,1].

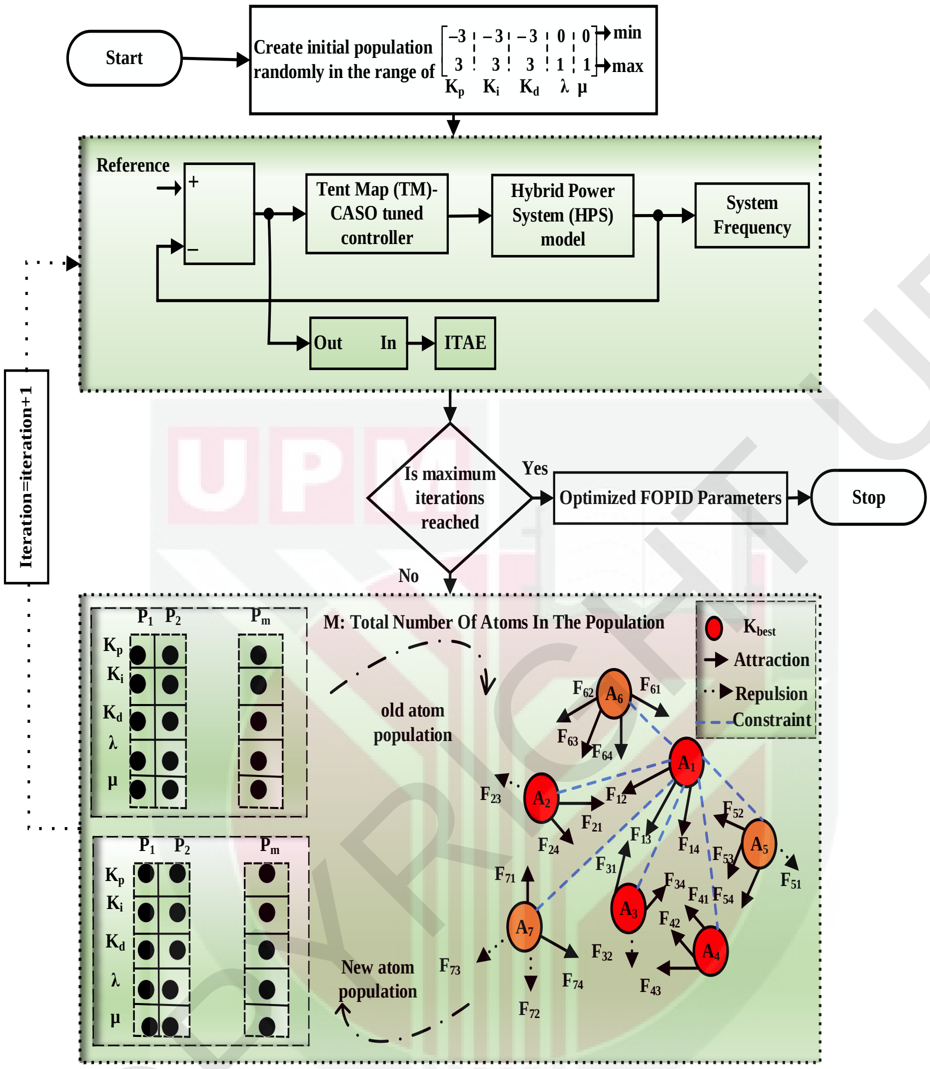

Figure 3.4 : Proposed CASO algorithm to optimize FOPID controller for LFC

3.2.2 LFC Model Studied for Centralized Control Strategy

The developed centralized FOPID controller is tested on i^{th} area hybrid power system (HPS) with reheat thermal, gas, and hydro unit, and RES like solar thermal and wind power generation with energy storage devices as shown in Figure 3.5. In worldwide, most of the base load demand is met by the above-mentioned conventional plants. Countries like Malaysia where the major power generations are from thermal, hydro, and gas power plants to meet the base load demand with the installed capacity of thermal, hydro, and gas generation units in Malaysia being 13.5 GW, 6.7 GW and 42.3 GW, respectively which supplying 62.78% of total load demand (Ali Kadhem et al., 2019). Further, the remaining part of load demand is met by RES like solar, wind, biogas, and biodiesel, etc. Considering these aspects, the proposed study incorporates solar thermal power generation (STPG) and wind turbine power generation (WTPG) with energy storage devices such as AE and FC in the HPS model for LFC operation. In the case of thermal unit, the non-linearities namely boiler dynamics (BD), generation rate constraints (GRC), and governor dead band (GDB) are considered for realistic analysis of the system.

In conventional steam plants, the change in generation is actuated by turbine control valves, and boiler controls respond instantly to changes in steam flow and pressure deviation. As the boiler dynamics generate steam under pressure, the pressure effects of a drum type boiler are taken into consideration in this study. The primary reason to consider GRC in this study is to simulate the practical constraints on the sensitivity of the turbine. The value of GRC considered in this work is 0.0005 p.u.MW/s (Morsali et al., 2014). On the other hand, the dead band in thermal steam units is induced by backlash in the linkage that connects the servo pistons to the camshaft. Therefore, in this study, the limiting value of dead band is set at 0.05 % (Tripathy et al., 1992). The nonlinearity associated with the reheat thermal system, Gas, hydro, and RES generation unit is mathematically linearized around certain operating points, resulting in a first-order transfer function is described as follows:

Solar thermal power plants use the sun as a heat source to generate electricity. Concentrating solar power is essential for reaching high enough temperatures for a power plant to operate effectively. A thermodynamic cycle which converts the useful heat received from concentrated solar thermal power into electricity (Boretti et al., 2021). The solar collectors and working fluid are the two most important components of the STPG system. Solar collectors with parabolic troughs are commonly used in the solar field to collect solar energy, which is focused onto a tube filled with working fluid (oil, air, or water) and circulates. When the working fluid is heated, it is used by the power cycle to generate high-pressure steam in a boiler and then to generate electricity by expanding it in a turbogenerator. For small-signal analysis, the STPG plant can be linearized with a few approximations, and the transfer function model is described as below (Kler et al., 2019):

$$G_s(s) = \frac{\Delta P_{STPG}}{\Delta P_{solar}} = \frac{K_s}{1+sT_s}\frac{K_T}{1+sT_T} \tag{3.16}$$

where K_S and K_T signify the gain constant, T_S and T_T indicate the time constant of solar collector and steam turbine, respectively.

Wind power has been steadily increased in recent years as a mature form of renewable energy power generation, and its penetration into the electrical grid keeps rising. In this study a double fed induction generator based WTPG is employed. Although wind power has benefits in terms of environmental impact and supply, its intermittent nature in power output causes overburdening of interconnected tie-lines, resulting in frequency deviation of the power system. As the wind speed changes, a pitch control mechanism is activated, which changes the pitch of the rotor in order to keep the power produced by the wind energy conversion system constant. As shown in Figure 3.5, three WTPG are considered and represented by first order lag-based transfer function as (Kler et al., 2019):

$$G_{WTPG}(s) = \frac{\Delta P_{WTPG}}{\Delta P_{wind}} = \frac{K_{WTPG}}{1+sT_{WTPG}} \tag{3.17}$$

where K_{WTPG} and T_{WTPG} denote the gain and time constant of WTPG.

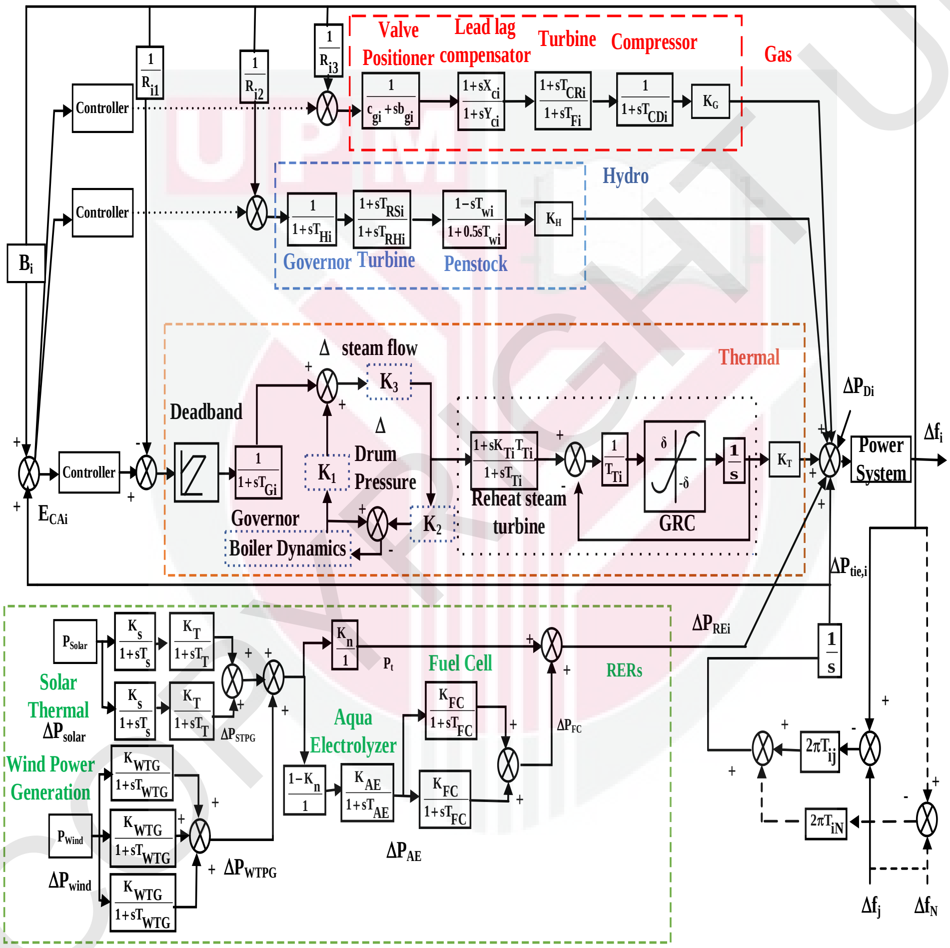

Figure 3.5 : Transfer function model of multi-area multi-source HPS

The STPG/WTPG system with an abundantly clean power generation can meet the load demand. However, the STPG/WTPG output power is not constant and varies with the intensity of solar radiation and wind speed (Lee et al., 2008). Moreover, these fluctuations result in variations in frequency. To overcome these issues, AE were used to absorb and produce hydrogen from the rapidly varying output power of STPG/WTPG. The hydrogen produced is kept in a hydrogen tank and utilised to power fuel cells. The total output power from STPG, WTPG and FC is supplied to meet the load demand (Lee et al., 2008). Figure 3.6 depicts the energy exchange process of AE and FC. The linearized transfer function model of AE and FC is expressed as:

$$G_{AE}(s) = \frac{K_{AE}}{1+sT_{AE}} = \frac{\Delta P_{AE}}{(\Delta P_{WTG} + \Delta P_{STPG})(1-K_n)} \tag{3.18}$$

where K_{AE} and T_{AE} represents the gain and time constant of AE, respectively. $K_n = \frac{P_t}{(P_{WTG} + P_{STPG})}$ is presumed as 60%.

$$G_{FC}(s) = \frac{K_{FC}}{1+sT_{FC}} \tag{3.19}$$

where K_{FC} and T_{FC} denote the gain and time constant of FC, respectively.

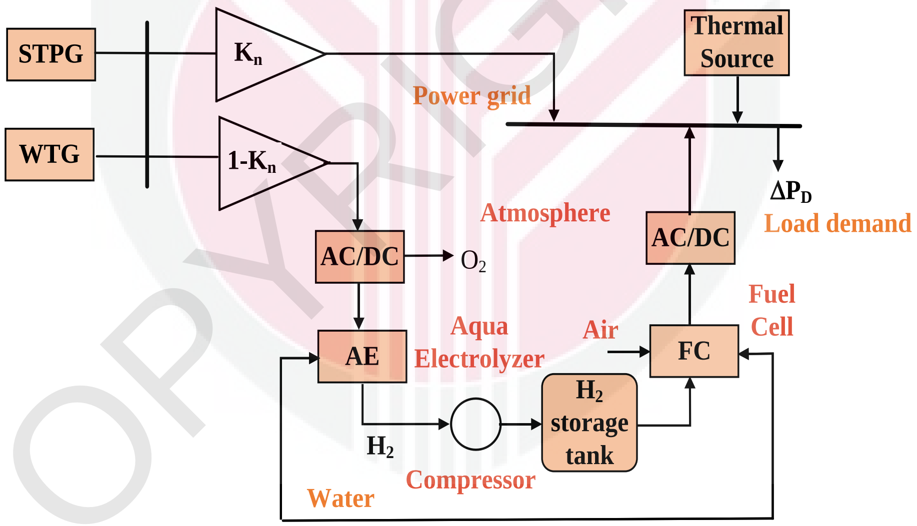

Figure 3.6 : Processes of energy exchange in AE-FC (Arya et al., 2017b)

3.3 Design of Decentralized NLFOPID Controller

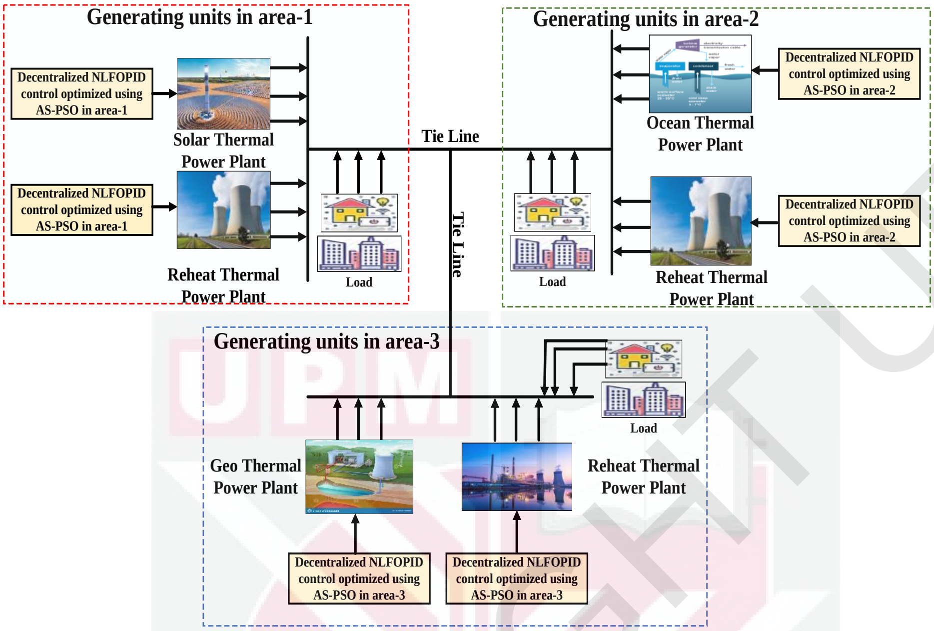

Figure 3.7 : Schematic representation of decentralized control in LFC

In this section, the concept of NLFOPID control designed in a decentralized manner is discussed in detail. The schematic diagram of decentralized control in LFC system is depicted in Figure 3.7. As discussed in Section 3.2, the linear FOPID controller represents a relative differential representation of fractional order $PI^{\lambda}D^{\mu}$ with two additional tunable parameters, namely the integer-order λ and differential order μ, which makes the controller more robust and adaptable. However, a linear FOPID controller cannot maintain a reliable control performance as the LFC of a power system usually operates at a wide operating range. To counteract this, a hyperbolic cosine function of instantaneous error is cascaded into the linear FOPID controller transfer function equation as expressed in Equation (3.1) allowing the controller to behave as NLFOPID. The schematic figure of the NLFOPID controller is illustrated in Figure 3.8. The control law of the NLFOPID controller is given by Equation (3.20)

$$u(t) = K_p e'(t) + K_i \frac{d^{-\lambda}}{dt^{-\lambda}} e'(t) + K_d \frac{d^{\mu}}{dt^{\mu}} e'(t) \tag{3.20}$$

where $e'(t)$ is the output of nonlinear hyperbolic function defined as:

$$e'(t) = e(t) \times y(t) \tag{3.21}$$

where y is the nonlinear hyperbolic function defined mathematically by Equation (3.25)

$$y(t) = \cosh(A_n e(t)) \tag{3.22}$$

$$e(t) = \begin{cases} e(t) & ; |e(t)| \leq e_{max}(t) \\ e_{max}(t)\,\mathrm{sgn}(e(t)) & ; |e(t)| > e_{max}(t) \end{cases} \tag{3.23}$$

where, A_n is a user-tuned positive constant. The hyperbolic cosine function is even, smooth and bound, which means that it can be used as a saturation function to limit the control signal in control systems. This property is particularly useful in nonlinear control design. The variation in the nonlinear function y is confined to $y_{min} \leq y \leq y_{max}$. When e(t) = 0, the lower bound of y(t) will be 1. Here, A_n is optimized using the proposed AS-PSO algorithm through the minimization of the ITAE objective function, in addition to the FOPID controller parameters. The ITAE is considered as ACE, which accelerates the frequency deviation and tie-line power deviation of the system. Hence, the objective function is defined as:

$$J=\mathrm{ITAE}=\int_0^T \left[|e(t)| \right] \cdot t \cdot dt \tag{3.24}$$

with the boundary constraints:

$$K_p^{min} \leq K_{pi} \leq K_p^{max},\ K_d^{min} \leq K_{di} \leq K_d^{max},\ \mu^{min} \leq \mu_i \leq \mu^{max},$$
$$K_i^{min} \leq K_{ii} \leq K_i^{max},\ \lambda^{min} \leq \lambda_i \leq \lambda^{max}, A_n^{min} \leq A_i \leq A_n^{max} \tag{3.25}$$

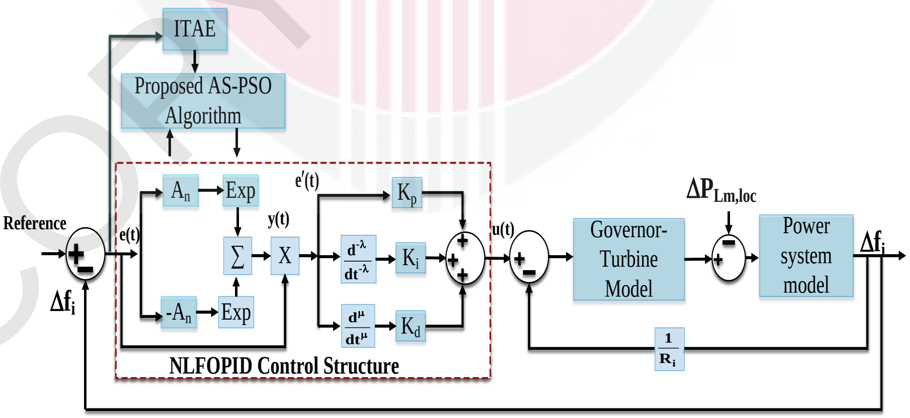

Figure 3.8 : Closed-loop control structure of NLFOPID controller for LFC

To implement FO transfer function model in simulation, generally oustaloup approximation technique is employed as discussed in section 2.5.1. Nevertheless, it has poor approximation which leads to poor accuracy and performance of the controller. Therefore, in this objective improved oustaloup approximation approach is applied to implement the NLFOPID controller for the LFC of the deregulated energy system.

3.3.1 Hybrid Atom Search Particle Swarm Optimization

In this work, a maiden attempt is made to combine the non-swarm intelligence (i.e., physics-inspired) optimization-based ASO algorithm with the swarm-based PSO technique. The physics-based intelligence technique is based on imprecise physical systems and is often subjected to disturbances governed by physical laws. Thus, the solutions obtained from these imperfect physical systems-based optimization techniques possess better global search ability and robustness, but it is globally optimal. On the flip side, the swarm-based intelligence technique possesses exploration characteristic that makes the optimization problem to reach the local optimum but not robust. This paves the way to incorporate the swarm-based technique into the physics-based optimization methods.

As a result, it enhances the search and convergence ability of the method by deriving the advantages of the collective behaviour of the swarm and attractive forces of the particle in the nature of physics. This property makes the swarm of matter particles which are subjected to forces. Thus, it has the characteristics of both exploration and exploitation. Hence, it enhances the efficacy in obtaining the global optimal solution. Because of this reason, a parallel hybrid AS-PSO technique has been used for tuning the parameters of the NLFOPID controller for frequency regulation of deregulated multi-area energy systems. A description of ASO can be found in section 2.6.1. In ASO, each atom is updated by its velocity equation to obtain the optimal solution as expressed in Equation (3.13). To improve the search ability of ASO and to enhance the exploration characteristics, the acceleration of the atom in Equation (3.13) is modified with the flocking behaviour of PSO. The process of convergence by the PSO algorithm is presented by Kennedy et al., (1995). The velocity updating of each particle in the search space is defined as:

$$v_i^d\left(t+1\right)=\omega\cdot v_i^d\left(t\right)+c_1\cdot r_1(x_{pbest,i}-x_i^d(t))+c_2\cdot r_2(x_{gbest}-x_i^d(t)) \tag{3.26}$$

where r_1 and r_2 are the distinct random numbers ranging between 0 and 1. ω is the linearly decreasing inertia weight, c_1 and c_2 are the social and cognitive coefficients take the value of 0.9 and 0.4, $x_{pbest,i}$ is the personal best position of the i^{th} particle, x_{gbest} is the global best position particle attained so far, $x_i(t)$ and $v_i(t)$ are the current position and velocity of the i^{th} particle at t^{th} iteration, respectively. The first term in Equation (3.26) represents the current velocity of the particle, the term $c_1\cdot r_1(x_{pbest,i}-x_i^d(t))$ associated with cognition behaviour, and $c_2\cdot r_2(x_{gbest}-x_i^d(t))$ depicts the social behaviour of particles which helps to enhance the exploration behaviour. These behaviours are incorporated into the velocity updating of atoms in ASO, which intensify the search behaviour to reach the global optimum. The modified form of Equation (3.26) can be defined as:

$$v_i^d(t+1)=\omega\cdot v_i^d(t)+\text{randn}\cdot a_i^d(t)+c_1\cdot r_1\cdot(x_{p_{best,i}}-x_i^d(t))+c_2\cdot r_2\cdot(x_{g_{best}}-x_i^d(t)) \qquad (3.27)$$

where randn denotes the normalized random number between [0,1], c_1 and c_2 denote the cognitive and social coefficients of the particle, r_1 and r_2 denotes the uniform random number between [0,1], ω denotes the weight factor. T and t denote the current iteration number and the maximum number of iterations. In Equation (3.27), the first and second terms correspond to the velocity and acceleration of i^{th} atom, and the third and fourth terms represent the atom's cognitive and social behaviour, respectively. Thus, the proposed heterogenous hybridization method helps to enhance the atom's search capability and reaches the optimum solution with the minimum number of iterations. The detailed steps of the AS-PSO technique for tuning the control parameters to maintain the system frequency under deregulated environment are discussed as follows:

Step-1: Initialization - Set the parameters of AS-PSO like total number of atoms (N), multiplier weight (β), number of iterations (T), and depth weight (α), etc. Randomly initialize the parameters of the controller and its positions which are specified as $X_i = (x_i^1,...x_i^d,....x_i^n)$, i =1, 2…., N, where i and d specify the atom and its dimension of the search region (d=1, 2, …, D). Also, initialize the minimum and maximum boundary of gain and fractional terms of the NLFOPID controller.

Step-2: Evaluation of fitness function - Compute the fitness function as defined in Equation (3.24) for each atom to minimize the frequency error of the system and obtain the optimal parameters of the NLFOPID controller.

Step-3: Computation of Mass - At the moment t, a selection process is performed to choose the best atom based on their best fitness evaluation to compute the normalized mass of the atom. The atom with heavier mass will take part in the consecutive iterations and delivers a global optimum solution as it has the best fitness value. The mass of the i^{th} atom, m_i is evaluated as given in Equation (3.5).

Step-4: Computation of resultant force - In this step, the resultant force F_r is calculated by adding the interaction force and constraint forces from Equation (3.11).

Step-5: Updating of acceleration - The acceleration of the i^{th} atom in the d^{th} dimension space at the moment t is updated according to newton's second law of motion as given in Equation (3.12).

Step-6: Velocity Updating - The velocity of each atom is updated by combining the global search ability of ASO and the local search capability of PSO using the mathematical model described in Equation (3.27). g_{best} refers to the global best position particle attained so far, and $p_{best,i}$ implies the personal best location of the i[th] atom. In Equation (3.27), the primary portion of the equation $\{\omega \cdot v_i^d(t)+c_1 \cdot randn \cdot a_i^d(t)\}$ depicts the velocity updating equation of ASO, which is predominantly dedicated to exploration; and the second half $c_2 \cdot r_1 \cdot (x_{pbest,i}-x_i^d(t))+c_3 \cdot r_2 \cdot (x_{gbest}-x_i^d(t))$ is the cognitive and social behaviour derived from PSO, which is used to attract the atoms in the direction of the resultant force that emphasizes exploitation.

For instance, Figure 3.9 depicts an atom population of seven atoms, with the first four atoms with the best fitness values indicated as the K_{best} atoms and the forced condition of atom x_1 with x_2, x_3 and x_4 are shown. Atom x_1 in the population search space has attraction forces from atoms x_2, x_3 and x_4, the repulsive force from s_5, and constraint force from x_{gbest}, the best atom obtained so far. Moreover, the atom x_1 contains PSO-like attraction forces, which helps to obtain the best atom x_{gbest}, and its personal best atom, $x_{1,\ pbest}$.

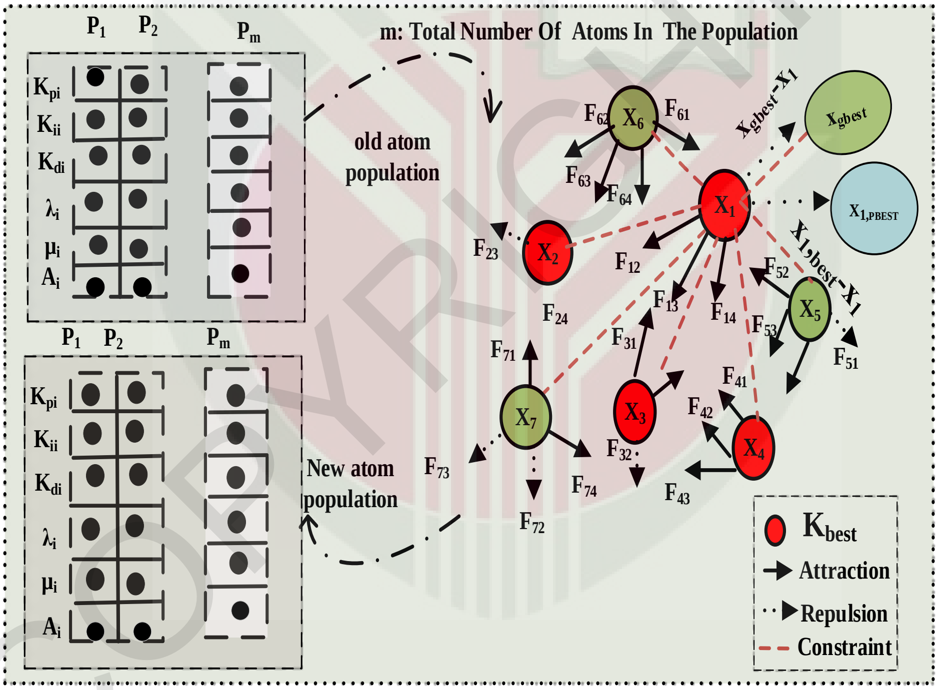

Figure 3.9 : Forces of atoms in AS-PSO

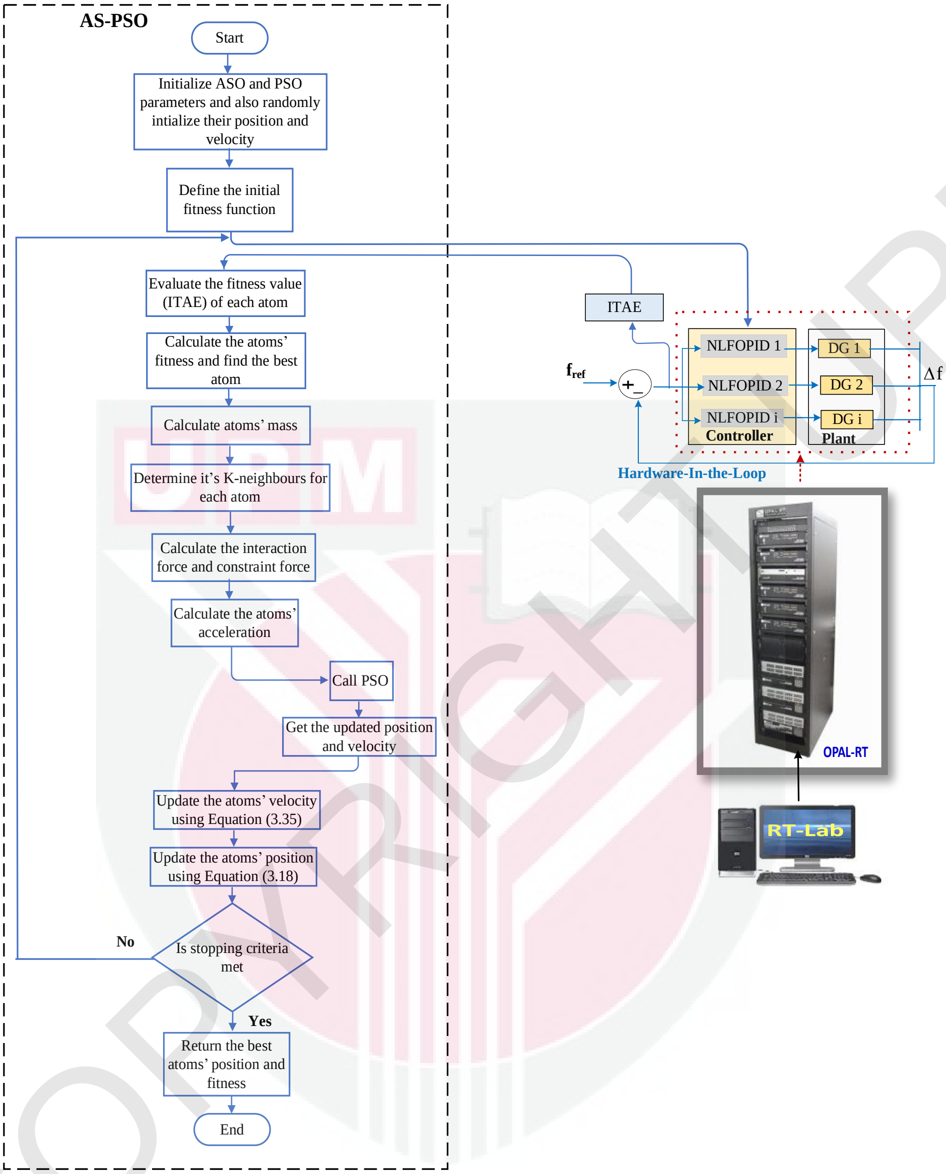

Figure 3.10 : Flowchart of AS-PSO for tuning the parameters of NLFOPID controller

Step-7: Position updating – The position of each atom is updated based on its updated velocity as defined in Equation (3.15).

Step-8: Check the Convergence - The proposed hybrid AS-PSO technique converges with the assumed maximum number of iterations, and the tuned controller parameters corresponding to the gbest are obtained. If the number of iterations is not reached, repeat steps 2 through 8 until the terminating condition is reached. The various parameters assumed for simulating the AS-PSO are N=50, T=100, α=50, and β=0.2 for tuning the controller gain parameters of the NLFOPID controller. The detailed steps of AS-PSO implementation are presented as a flowchart, as illustrated in Figure 3.10. To further prove the robustness of the proposed technique, the developed deregulated Simulink model is deployed in OPAL-RT 5600 system. This may involve selecting appropriate solver settings and configuring communication interfaces between the simulation model and the OPAL-RT system. The Simulink model with the integrated hybrid AS-PSO algorithm and NLFOPID controller is compiled. The performance of the proposed NLFOPID controller with optimized parameters obtained using the proffered AS-PSO is analyzed under various scenarios to ensure that the controller meets the specified optimization objectives.

3.3.2 LFC Model Studied for Decentralized Control Strategy

The deregulated energy system under investigation comprises three unequal areas with a capacity of 2000 MW, 4000 MW, and 8000 MW, respectively. The reheat thermal energy system (RTES) is considered as base load power generation in all areas with RE sources of solar thermal energy system (STES), ocean thermal energy conversion (OTEC), and geothermal energy system (GES) in area-1, area-2, and area-3, respectively. In this study, a total of six DISCOs and GENCOs are participating in the trading of energy via contracts. Each area of deregulated system has RTES (GENCO-2, GENCO-4, and GENCO-6), and either of the RE sources such as STES (GENCO-1), OTEC plant (GENCO-3), and GES (GENCO-5). The detailed transfer function modelling of RES is described as follows:

a. STES Model

Solar energy is used as a heat source in solar thermal systems. The energy from the sun is concentrated through a parabolic collector to achieve a high temperature for power generation. The useful heat obtained using concentrated solar thermal power (CSTP) is then converted into electricity through the expansion of steam following a thermodynamic cycle (Rahman et al., 2022). In STES, the fundamental components are solar collectors and working fluid. The parabolic trough solar collector is widely used to collect solar radiation and guide it into a tube that is circulated with a working fluid (water, oil, or air). A boiler produces high-pressure steam when a working fluid is heated, which expands in a turbogenerator to create electricity (El haj Assad et al., 2021). Thus, the process of STES is linearized with few approximations for small-signal analysis, and the transfer function model obtained of solar field (G_{SS}), governor (G_{GS}), and turbine (G_{TS}) is given below,

$$G_{SS}(s) = \frac{K_{SS}}{1+sT_{SS}} e^{-sT_D}, \; G_{GS}(s) = \frac{1}{1+sT_{GS}} \text{ and } G_{TS}(s) = \frac{K_{TS}}{1+sT_{TS}} \tag{3.28}$$

where T_{SS}, $T_{GS,}$ and T_{TS} are the solar field, governor, and turbine time constants. K_{SS} and K_{TS} define the gain constant of the solar field and turbine, and T_D denotes the transport delay of the solar field. The detailed transfer function diagram of STES is given in Figure 3.11.

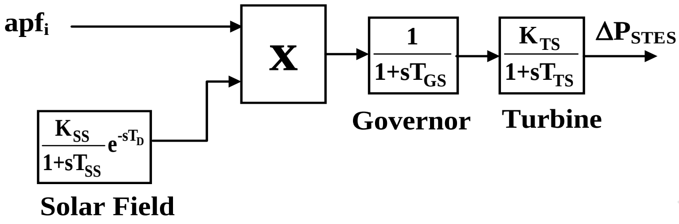

Figure 3.11 : LFC model of STES

b. OTEC Model

Ocean thermal energy conversion systems use the temperature difference between the surface and deep ocean water to generate electricity. The temperature difference is employed to vaporize and condense a working fluid alternately. The corresponding changes in volume and pressure are used to operate a turbine, which in turn generates electricity. The OTEC mechanism can be an open or closed cycle (Yang et al., 2022b). An open-cycle OTEC system uses warm seawater as the working fluid, whereas the closed cycle uses ammonia as a working fluid. The supremacy of using closed-cycle OTEC over open-cycle OTEC is that the working fluid has been condensed and recirculated back to the evaporator to repeat the cycle. The working fluid continues to circulate in a closed system which significantly increases the efficiency of a closed-cycle OTEC system than an open-cycle (Rahman et al., 2022). However, the temperature difference between the surface and deep seawater is just 20-25^{o}c, resulting in poor thermal efficiency. To improve efficiency, an SC-OTEC plant is considered (Wang et al., 2010). Hence, in this work, an SC-OTEC system is considered as one of the RE generation systems, whose schematic representation is depicted in Figure 3.12. Thus, the governor and turbine model of SC-OTEC is linearized into first-order transfer function as:

$$G_{OG}(s) = \frac{K(1+sT_{OG2})}{1+sT_{OG1}} \;,\; G_{OT}(s) = \frac{K_{OT}}{1+sT_{OT}} \tag{3.29}$$

where K and K_{OT} are the speed droop and gain constant of the governor and turbine, and T_{OG1} and T_{OT} are the time constant of the governor and turbine, respectively. The transfer function model is employed in the OTEC system of Figure, in which T_{OG2} is the time delay. P_{net} is the net power in W.

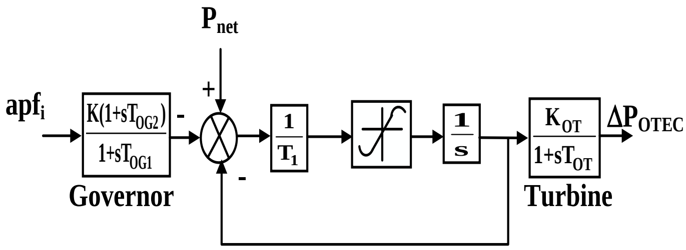

Figure 3.12 : LFC model of OTEC

c. GES Model

Currently, 86% of the world's energies are generated from finite energy sources buried deep within the Earth's crust (Coal, oil, gas, and uranium). Geothermal energy is the only form of RE in the Earth's crust. Recent studies have shown that geothermal energy is used in 82 countries for power generation, with the United States being ranked as one of the top 10 countries generating electrical power of ~3.45 GWe from installed geothermal power plants (Rahman et al., 2022). To generate electricity, GES uses heat energy beneath the earth's surface. The hot water with a temperature of 50-400°C is piped to the power plant from 1000-2000 m deep boreholes (El haj Assad et al., 2021). Then, it is connected to two or more separators to convert into steam to produce electricity. As the operation of GES is similar to a conventional non-reheat thermal power plant. Hence, the transfer function of the governor and turbine can be represented as:

$$G_{GGE}(s) = \frac{K_{GGE}}{1+sT_{GGE}}, \; G_{TGE}(s) = \frac{K_{TGE}}{1+sT_{TGE}} \tag{3.30}$$

where T_{GGE} and T_{TGE} are the governor and turbine time constants, respectively. K_{GGE} and K_{TGE} define the gain constant of the governor and turbine, respectively. The detailed transfer function diagram of GES is given in Figure 3.13.

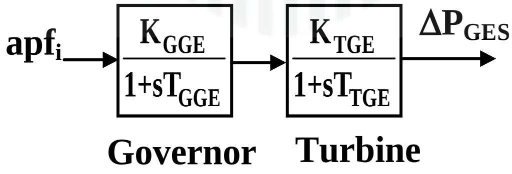

Figure 3.13 : LFC model of GES

d. RTES Model

In the case of RTES model, the non-linearities namely BD, GRC, and GDB are considered for realistic analysis of the system. In conventional steam plants, the change in generation is actuated by turbine control valves, and boiler controls respond instantly to changes in steam flow and pressure deviation. As the boiler dynamics generate steam under pressure, the pressure effects of a drum type boiler are taken into consideration in this study as shown in Figure 3.14. The primary reason to consider GRC in this study is to simulate the practical constraints on the sensitivity of the turbine. The value of GRC considered in this work is 0.0005 p.u.MW/s (Ramachandran et al., 2018). On the other hand, the dead band in thermal steam units is induced by backlash in the linkage that connects the servo pistons to the camshaft. Therefore, in this study, the limiting value of dead band is set at 0.05 % (Arya et al., 2021).

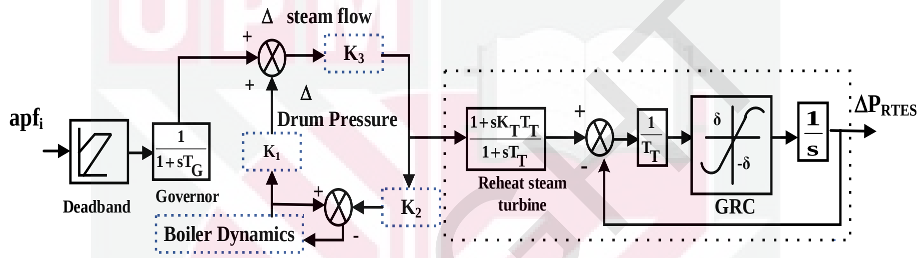

Figure 3.14 : LFC model of RTES

e. DPM Computation

The DISCO participation Matrix (DPM) is used for trading the energy in the energy pool using the contracts between DISCOs and GENCOs of control area (Donde et al., 2001). A typical description of DPM for the system model considered is expressed in Equation (3.31).

$$\text{DPM}=\begin{bmatrix} cpf_{11} & cpf_{12} & cpf_{13} & cpf_{14} & cpf_{15} & cpf_{16} \\ cpf_{21} & cpf_{22} & cpf_{23} & cpf_{24} & cpf_{25} & cpf_{26} \\ cpf_{31} & cpf_{32} & cpf_{33} & cpf_{34} & cpf_{35} & cpf_{36} \\ cpf_{41} & cpf_{42} & cpf_{43} & cpf_{44} & cpf_{45} & cpf_{46} \\ cpf_{51} & cpf_{52} & cpf_{53} & cpf_{54} & cpf_{55} & cpf_{56} \\ cpf_{61} & cpf_{62} & cpf_{63} & cpf_{64} & cpf_{65} & cpf_{66} \end{bmatrix} \tag{3.31}$$

Each element in DPM, say cpf_{mn} represents the fraction of the total load demand contracted by DISCO 'n' from GENCO 'm'. The amount of power generated by each GENCO should be equal to the sum of the demands by all DISCOs with which a contract of power is made. Therefore, the contracted power of m^{th} GENCO with the DISCOs is given as follows:

$$\Delta P_{gc,m} = \sum_{n=1}^{N_d} cpf_{mn} \Delta P_{L,n} ; m=1,2,....N_k \tag{3.32}$$

where N_k is the number of GENCOs and N_l is the number of DISCOs. In a deregulated energy sector, DISCOs may have contracts with GENCOs in the same area as well as other areas. Thus, the scheduled tie-line power of any area will vary as the DISCOs demand varies. Hence, the net planned steady-state power flow from an area is written as:

$$\Delta P_{tie12,scheduled} = \sum_{m=1}^{2}\sum_{n=3}^{4} cpf_{mn}\Delta P_{L,n} - \sum_{m=3}^{4}\sum_{n=1}^{2} cpf_{mn}\Delta P_{L,n} \tag{3.33}$$

The tie-line power error is defined as:

$$\Delta P_{tie12,error} = \Delta P_{tie12,actual} - \Delta P_{tie12,scheduled} \tag{3.34}$$

The total load of the m^{th} control area is calculated by adding the contracted and uncontracted load demand of the k^{th} control area DISCOs.

$$\Delta P_{dm} = \sum_{n=1}^{d} \Delta P_{L,n} + \Delta P_{Lm,loc} \tag{3.35}$$

where 'd' signifies the number of DISCOs in the m^{th} area. $\Delta P_{L,n}$ represent the contracted load demand of DISCOs in the n^{th} area and $\Delta P_{Lm,loc}$ is the uncontracted or local load demand of DISCOs in the m^{th} area. The schematic representation of deregulated energy system under investigation is depicted in Figure 3.15.

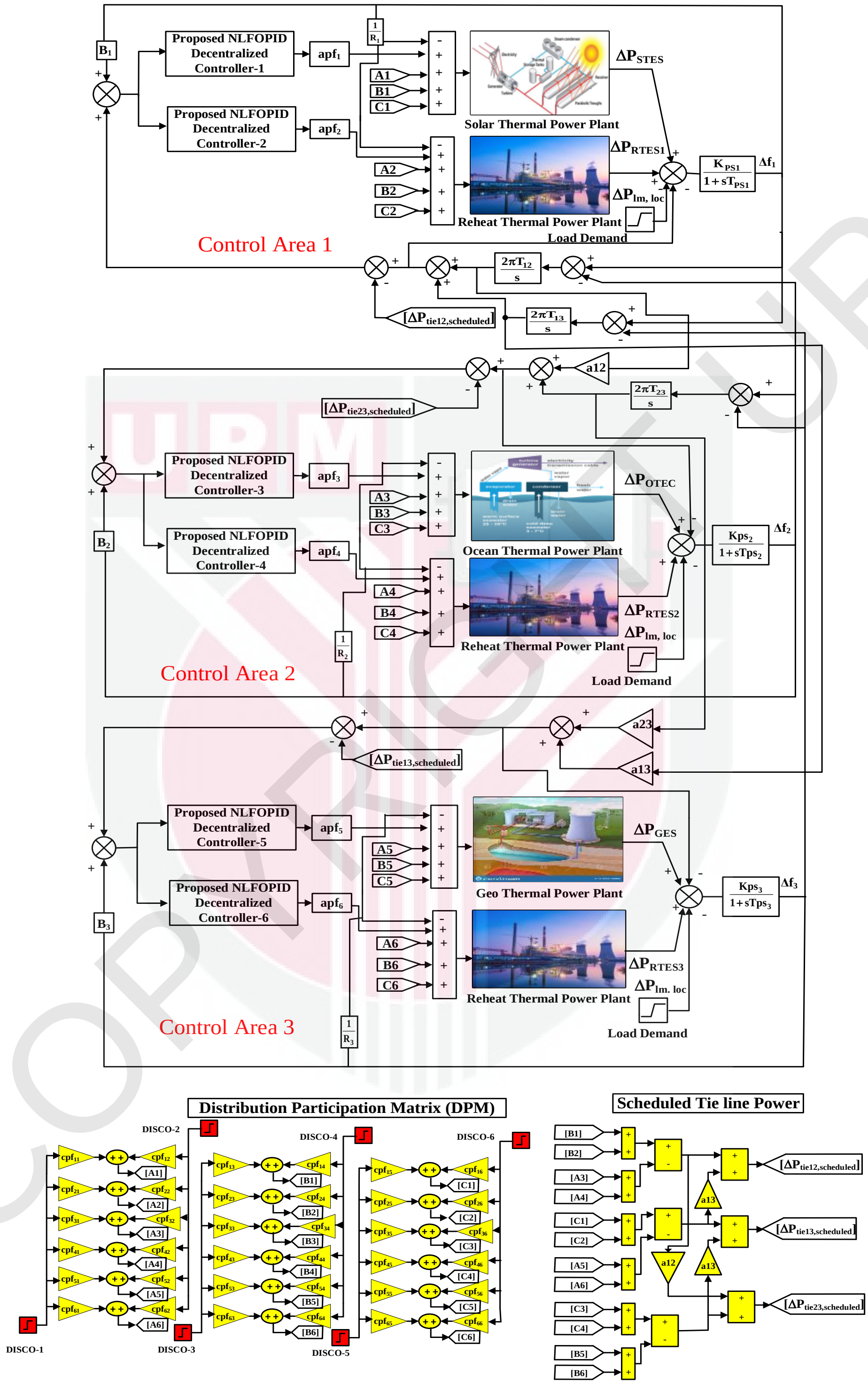

Figure 3.15 : Block diagram of three unequal areas deregulated energy system

3.4 Distributed Control Framework

The proposed control scheme allows local controllers in each MG to communicate with neighbouring controllers and adjust the frequency based on a reference value. The schematic representation of distributed control in LFC framework is shown in Figure 3.16. The consensus-based distributed control framework aims to maintain the MG system at a nominal frequency within an acceptable range (Liu et al., 2018b). Controllers are interconnected through a communication network, enabling data transfer among MG networks. When connecting with other MG networks, the controller follows the frequency reference of the leading MG network. Additionally, in cases of frequency imbalances, power is transferred through tie-lines to balance the demand. An interconnection graph is a representation that specifies the topology or structure through which MGs can access information about each other's state (Wen et al., 2015). This graph outlines the connectivity and relationships between various MGs in a network, providing a framework for information exchange and communication among them. The following subsections briefly discusses about the graph topology and the proposed adaptive distributed controller.

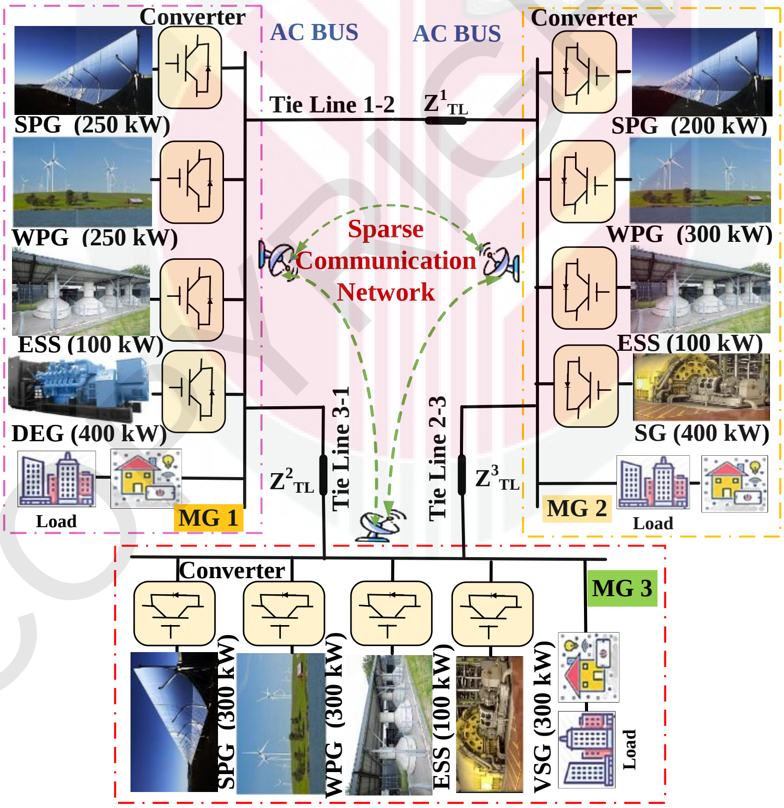

Figure 3.16 : Distributed control framework in LFC

3.4.1 Graph Topology

Graph topology provides a clear and intuitive way to represent the physical and operational connectivity of MGs in NMG. Nodes in the graph represent the components, while edges represent the connections and interactions between these components. Figure 3.17 shows the representation of NMG in the sense of graph topology. The following lemmas gives a clear understanding of the communication network of NMG considered.

Lemma 1: The communication network for controlling the distributed NMG is depicted as an undirected graph $G=(N,E,A)$, with $N=\{N_1,.....N_n\}$ is a set of n nodes representing the MGs involved and edges $E \subseteq N \times N$ connecting adjacent MGs to form tie-lines (Wen et al., 2015).

Lemma 2: The connectivity of the nodes is defined by the weighted adjacency matrix G is $A=[p_{ij}] \in \mathbb{R}^{n \times n}$, where p_{ij} represents the weight for information transmitted between agents i and j (Liu et al., 2018b). if

$$p_{ij} = \begin{cases} 1 & i \neq j \,\&\, i, j \text{ are directly connected} \\ 0 & i = j \,|\, i, j \text{ are not directly connected} \end{cases}$$

The communication link between MGs is bidirectional in this study $(N_i, N_j) \in E \Rightarrow (N_j, N_i) \in E \forall i, j$.

Lemma 3: The communication links between MGs can be represented using the Laplacian matrix, which is defined as

$$L = D - A \Rightarrow \begin{cases} l_{ij} = -p_{ij}, & i \neq j \\ l_{ij} = \sum_{i=1}^{n} p_{ij}, & i = j \end{cases}$$

where l_{ij} represents the element in the L and is equal to $-p_{ij}$ when i is not equal to j, and when i is equal to j, l_{ij} equals the sum of p_{ij} over all n DGs. Here, D is a diagonal matrix, referred to as the degree matrix, and is defined as diag(d_1, d_2, ..., d_n), where d_i represents the number of MGs that have communication connections to the i^{th} MG (Bidram et al., 2013).

Lemma 4: If G is an undirected graph and L represents its Laplacian matrix, then L is both symmetrical and positive semi-definite. Additionally, the eigenvalues of L satisfy the inequality $0 = \lambda_1 \leq \lambda_1 \leq .... \leq \lambda_n$. If the communication network satisfies the spanning tree condition (also known as the pinning condition), a path connects every pair of MGs in the network.

To maintain system frequency, a fundamental consensus procedure can be employed to reach an agreement among MGs with dynamics $\dot{x}_i = u_i$. This algorithm is represented as (Yang et al., 2023):

$$\dot{x}_i = \sum_{j=1}^{N_i} p_{ij}(f_{mi} - f_{mj}) \tag{3.36}$$

Here, f_{mi} and f_{mj} represent the frequency of the i[th] and j[th] MGs in the cluster. The overall dynamics of the group of agents can be described by:

$$\dot{x}_i = -Lx \tag{3.37}$$

The convergence rate of the controller is determined by the matrix L and the weight that need to be well-designed for faster convergence. The communication topology is depicted in Figure 3.17.

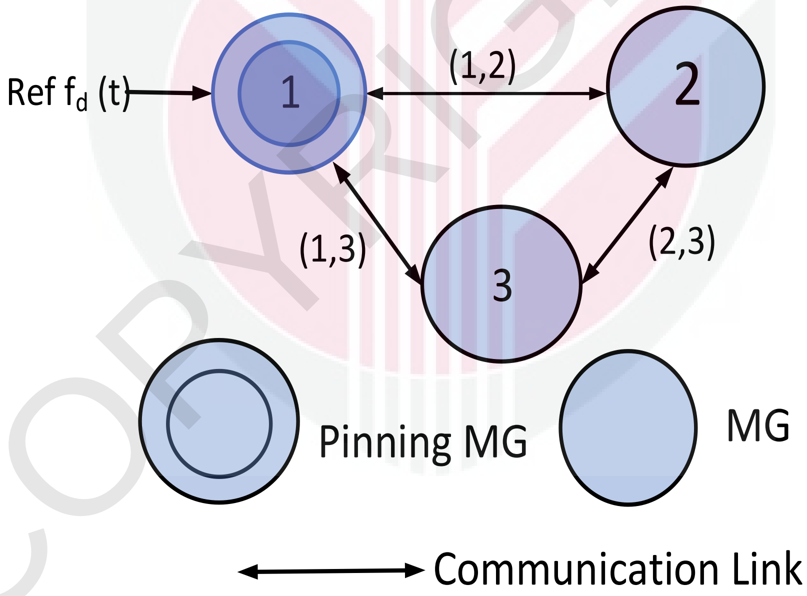

Figure 3.17 : Communication Topology

3.4.2 ZND-based Adaptive FOPID for DCS

In this section, ZND based FOPID controller is designed based on a leader-follower consensus protocol to regulate the frequency of the NMG. The ZND model is a type of recurrent neural network that is employed to solve equations and address dynamic problems. These networks have the unique characteristic of having zero residual error. The main concept behind ZND control involves constructing an error function and monitoring the time-varying solution by utilizing the time derivative of the time-varying parameter. The process of building DCS-based ZND FOPID control involves the following steps.

Step-1: Define an error function – First, an error function is constructed as

$$e(t) = f_d(t) - f_m(t) \tag{3.38}$$

where $f_d(t)$ is the reference frequency, and $f_m(t)$ is the actual or measured frequency of the plant.

Step-2: Defining an objective function – Using the Lyapunov theory and the frequency error of the NMG system as the error signal e(t), define a positive value energy function to be minimized as given in Equation (3.39).

$$J = \frac{1}{2} e^2(t) \tag{3.39}$$

Substituting Equation (3.38) in Equation (3.39) results in,

$$J = \frac{1}{2}\left(f_d(t) - f_m(t)\right)^2 \tag{3.40}$$

In frequency regulation, the controller regulates the frequency (f_m) of the plant to achieve a balanced steady state. The output of the plant f_m= T[u(t)], hence Equation (3.40) can be changed as follows:

$$J = \frac{1}{2}\left(f_d(t) - T[u(t)]\right)^2 \tag{3.41}$$

To define an error function based on the leader-follower consensus protocol with the tracking frequency error of the local neighbourhood as

$$e_i = \sum_{j \in N_i} p_{ij}(f_{mi}(t) - f_{mj}(t)) + a_i(f_{mi}(t) - f_d(t)) \tag{3.42}$$

where a_i is the pinning gain. f_{mi} and f_{mj} are the measured frequency at node i and node j, respectively. f_d is the desired frequency.

Substituting Equation (3.41) in Equation (3.42) yields

$$J = \frac{1}{2}\left\{\sum_{j\in N_i} p_{ij}\left(T[u_i(t)] - T[u_j(t)]\right) + a_i\left(T[u_i(t)] - f_d(t)\right)\right\}^2 \tag{3.43}$$

The distributed control law for designing the FOPID controller in leader-follower NMG are as follows

$$u_i(t) = K_{pi}\left(f_{mj}(t) - f_{mi}(t)\right)e(t) + K_{ii}\frac{d}{dt}^{-\lambda}\left(f_{mj}(t) - f_{mi}(t)\right)e(t) + K_{di}\frac{d}{dt}^{\mu}\left(f_{mj}(t) - f_{mi}(t)\right)e(t) \tag{3.44}$$

$$u_j(t) = K_{pj}\left(f_{mi}(t) - f_{mj}(t)\right)e(t) + K_{ij}\frac{d}{dt}^{-\lambda}\left(f_{mi}(t) - f_{mj}(t)\right)e(t) + K_{dj}\frac{d}{dt}^{\mu}\left(f_{mi}(t) - f_{mj}(t)\right)e(t) \tag{3.45}$$

where K_{pi}, K_{ii}, and K_{di}, are the gain values of the FOPID controller of leader MG. K_{pj}, K_{ij}, and K_{dj} are the FOPID controller gain values of follower MG. μ and λ are the fractional operators that take the value of non-integer real numbers, on substituting Equation (3.44) and Equation (3.45) in Equation (3.43) results in an objective function to be minimized for determining the gains of the FOPID controller.

Step-3: Design of ZND FOPID control – To ensure the convergence of the error function towards zero, the ZND network is constructed with its change in the dynamics of Equation (3.43) as follows:

$$\frac{dJ}{dt} = -\gamma\left(\frac{\partial J}{\partial x}\right)\times\left(\frac{\partial x}{\partial t}\right) \tag{3.46}$$

where, γ is a positive coefficient used to scale the convergence rate. Equation (3.46) is the dynamics of the ZND with its gradient minimizing monotonically to a steady equilibrium state or zero state. During this case, the activation function is considered a purlin-based linear function. Specifically, the parameter 'x' is the vector of unknown variables such as K_{pi}, K_{ii}, and K_{di} that need to be determined. Also, these parameters are the neurons representing proportional, integral, and derivative gains that are updated using the ZND behaviour. The dynamics of these neurons are described in detail in step-4.

Step-4: Gradient update of ZND FOPID network – The gradients (∇J) are calculated for updating the state of the neurons using

$$\nabla J = \left[\frac{\partial J}{\partial K_{pi}} \cdots \frac{\partial J}{\partial K_{dj}} \right]^T \tag{3.47}$$

The gradients for updating the neurons of the i^{th} leader and j^{th} follower MG-based FOPID controller for DCS are described as follows.

$$\frac{\partial J}{\partial K_{pi}} = \gamma e_i(t) \left[\sum_{j \in N_i} p_{ij} + a_i \right] T\left[u_i(t) \right] e_i(t) \tag{3.48}$$

$$\frac{\partial J}{\partial K_{ii}} = \gamma e_i(t) \left[\sum_{j \in N_i} p_{ij} + a_i \right] T\left[u_i(t) \right] \frac{d}{dt}^{-\lambda} e_i(t) \tag{3.49}$$

$$\frac{\partial J}{\partial K_{di}} = \gamma e_i(t) \left[\sum_{j \in N_i} p_{ij} + a_i \right] T\left[u_i(t) \right] \frac{d}{dt}^{\mu} e_i(t) \tag{3.50}$$

$$\frac{\partial J}{\partial K_{pj}} = -\gamma e_j(t) \sum_{j \in N_i} p_{ij} T\left[u_j(t) \right] e_j(t) \tag{3.51}$$

$$\frac{\partial J}{\partial K_{ij}} = -\gamma e_j(t) \sum_{j \in N_i} p_{ij} T\left[u_j(t) \right] \frac{d}{dt}^{-\lambda} e_j(t) \tag{3.52}$$

$$\frac{\partial J}{\partial K_{dj}} = -\gamma e_j(t) \sum_{j \in N_i} p_{ij} T\left[u_j(t) \right] \frac{d}{dt}^{\mu} e_j(t) \tag{3.53}$$

Initially in this work, a stochastic gradient approach (SGD) approach is employed by calculating the gradient of the energy function with respect to the model parameters, and adjusting it in the direction of negative gradient as:

$$W_{t+1,k} = W_{t,k} - \theta_s \nabla J(W_{t,k}) \tag{3.54}$$

where $W_{t+1,k}$ and $W_{t,k}$ are the current and previous weights of the network. The structure of the h-ZND-tuned FOPID controller for DCS is illustrated in Figure 3.18.

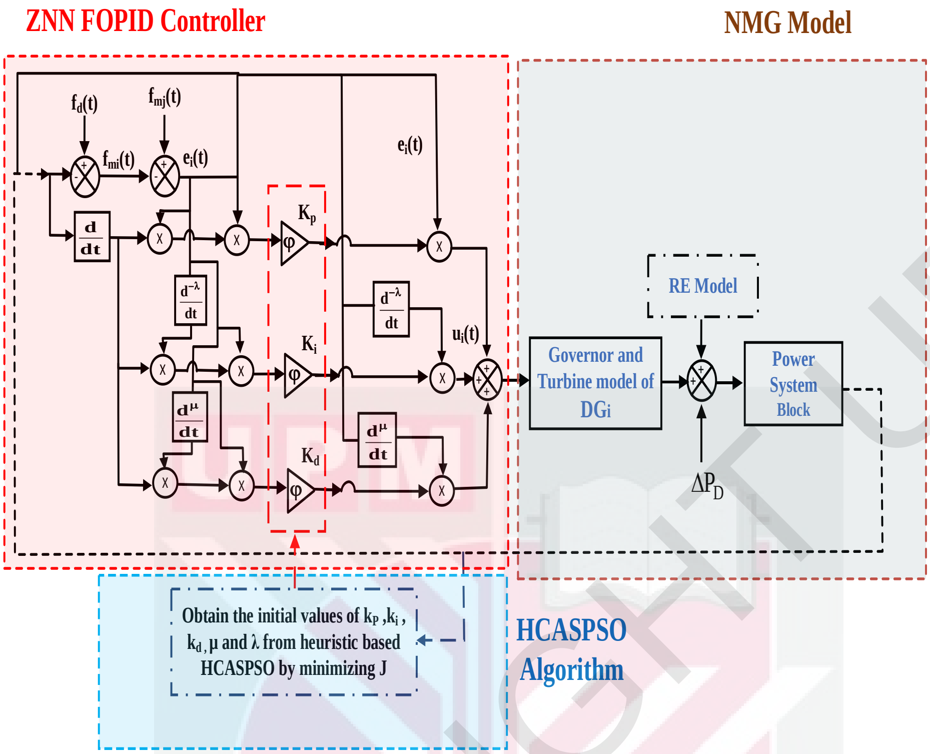

Figure 3.18 : Structure of ZND FOPID controller

3.4.3 The Proposed Consensus-based Federated Average Learning

Generally, the SGD learning of ZND is employed initially which requires local training data, which is limited due to memory constraints. As a result, the SGD-based ZND controller becomes ineffective when dealing with large-scale system dynamics (Pokhrel et al., 2020). To address these issues, this work adopted the concept of federated average learning (FAL). It is a distributed machine learning which cooperatively trains the network models using the data stored in each node's local memory. Then, it aggregates the learned models on a parameter server. This iterative process continues until the network reaches a stable response.

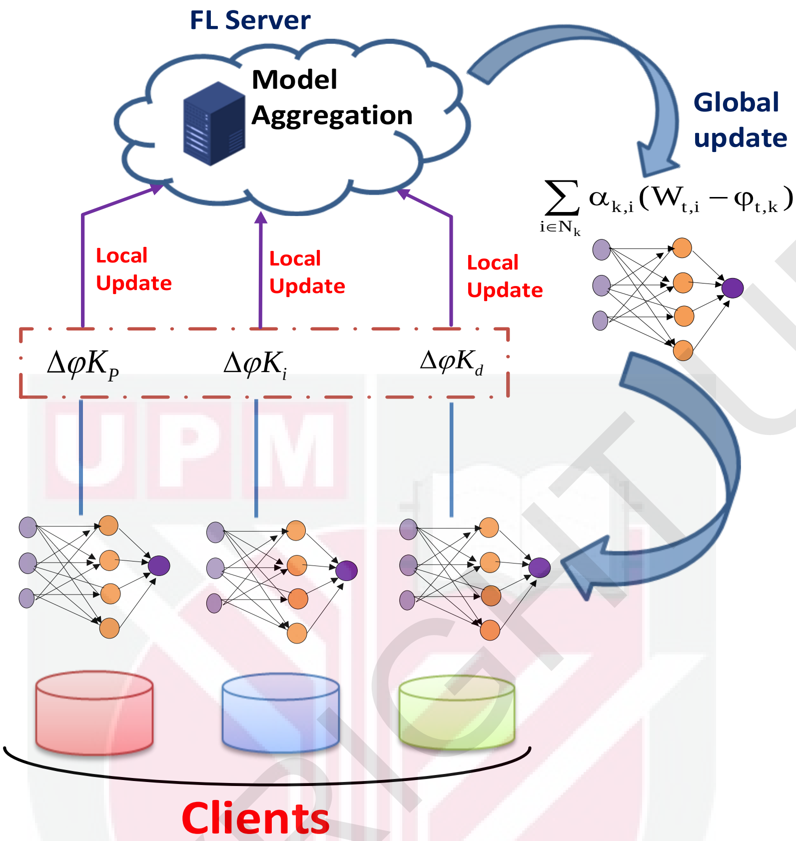

Figure 3.19 : FAL learning of ZND based FOPID control

FAL approach is employed in various domains such as autonomous vehicle control (Pokhrel et al., 2020), identification of anomalies in control systems Truong et al., (2022) and smart grids for energy theft detection Posner et al., (2021). Within FAL, can participate in cooperative model training, store, and analyze input data locally, and share parameters with other nodes. Consequently, an FAL-based controller can effectively operate in diverse scenarios such as real-time P2P electricity markets, despite uncertainties and dynamic environmental conditions. In order to provide a collaborative network architecture for distributed frequency control application while maintaining privacy, an FAL-based approach is employed in this work.

Consensus-based FAL has revolutionized the training of neural networks by harnessing the power of distributed global data from a cooperation of participating neurons while maintaining the privacy and security (Wang et al., 2020). In this approach, each neuron acts as a local learner and trains its own local network using its own data. The local network is then aggregated by a central server to obtain the global model. Then it sent back to the neurons, to update the ZND FOPID controller parameters. This process is repeated until the global model converges. The consensus based FAL technique used in this study is described as

$$\varphi_{t,k} = W_{t,k} + \varepsilon_t \sum_{i \in N_k} \alpha_{k,i} (W_{t,i} - \varphi_{t,k}) \tag{3.55}$$

where ε_t is the consensus step size which controls the consensus stability and is set as (0, Δ), where $\Delta = \max(k)\left(\sum_{i \in N_k} \alpha_{k,i}\right)$ is the graph highest degree representing the topology of the network interaction. The aggregated model $\varphi_{t,k}$ is then used for updating the network.

$$W_{t+1,k} = W_{t,k} - \theta_s \nabla J \varphi_{t,k} \tag{3.56}$$

The step size θ_s is defined further to the consensus step size so that the gradient ∇J decreases with time. Figure 3.19 shows the consensus-based FAL learning approach in updating the neurons of the network to auto-tune the controller parameters in each MG.

3.4.4 Hybrid Adaptive Chaotic Atom Search Particle Swarm Optimization

In this section, the hybrid AS-PSO intelligence technique is further improved by optimizing the convergence parameter through adaptiveness, and the chaos function is added to enhance the global convergence of the method for frequency regulation of NMG application. The proposed method combines the strength of physics-inspired CASO with swarm-inspired PSO to optimize the initial values of the ZND FOPID controller for frequency regulation of distributed NMG system.

a. Adaptive Control of ASO Parameters

As discussed in section 2.6.1, ASO is a population-based stochastic optimization algorithm that uses attraction and repulsion as interaction forces. The constraint force is a significant medium for providing information within the atom population. The interaction force at the t^{th} iteration acting on the i^{th} atom from the j^{th} atom is given as follows.

$$F'_{ij}(t)=-\eta(t)[2(h_{ij}(t))^{13}-(h_{ij}(t))^{7}] \tag{3.57}$$

where $\eta(t)$ is the depth function, $h_{ij}(t)^{13}$and $h_{ij}(t)^{7}$ are the repulsive and attractive interactions. The depth function $\eta(t)=\alpha(1-\frac{t-1}{T})e^{-\frac{20t}{T}}$ adjust the repulsion or attraction region to ensure the algorithm's exploration and exploitation. The depth weight α is the most significant parameter in ASO that directly affects the interaction force. Usually, α is set to be 40 for optimization problems, as seen from the literature (Zhao et al., 2019b, Barshandeh et al., 2021). However, owing to the nonlinear characteristic of ASO, especially for highly nonlinear complex optimization problems like frequency control of power systems where the frequency changes dynamically over time, a nonlinear depth weight is more flexible to balance the exploration and exploitation. In this work, a novel nonlinear method is used to optimize the value of α which can be expressed as follows

$$\alpha=\frac{a}{0.75} \tag{3.58}$$

where a is defined as

$$a=1+0.1\times \mathrm{sqrt}\left(\frac{iter}{iter_{max}}\right) \tag{3.59}$$

where iter is the current iteration number and $iter_{max}$ is defined as the maximum number of iterations. So, the value of α has nonlinear behaviour that encourages the global search during the initial stage of the iterations and improves the local search at the end of the iterations.

Similarly, the constraint force which plays a vital role in atomic motion is defined in Equation (3.10). From the equation, where $\lambda(t)=\beta e^{\frac{-20t}{T}}$ defined as the Lagrangian multiplier, β is the multiplier weight, the best atom found at the t^{th} iteration in the d^{th} position, and $s_i^d(t)$ describes the best atom attained at the t^{th} iteration in the i^{th} position. The multiplier weight β effectively guides the atom to find the optimal solution. Moreover, it directly affects the force constant ($e^{\frac{-20t}{T}}$) value. Therefore, it is important to strengthen the value of β to avoid the atoms trapping of local optima. So, a dynamically adjusting multiplier weight is proposed to guide the atom to find the optimal value. The nonlinear equation for β is given below.

$$\beta=0.2\times\left(\left(1-\frac{iter}{iter_{max}}\right)\times 4.5\right) \tag{3.60}$$

b. Adaptive Control of PSO Parameters

PSO is a probabilistic variant of a global search optimization algorithm and has been applied to many engineering applications (Kennedy et al., 1995, Jin wang chun wei ju et al., 2018), but it still has several shortcomings. In the final stages of evolution, the convergence rate significantly decreases, and it can easily be caught in local optimums. A lack of diversity in the particles is the main cause of premature convergence. To overcome this, the inertia weight ω should be adjusted to increase the diversity. Therefore, a nonlinear adaptive strategy is introduced to train the inertia weights.

$$\omega = \text{iter} \times \left(\frac{\omega_{max} - \omega_{min}}{\text{iter}_{max}} \right) \quad (3.61)$$

where ω_{min} and ω_{max} are the maximum and minimum limits of the inertia weight. In this work, ω_{min} and ω_{max} are set to be 1 and 3. Therefore, a nonlinear varying inertia weight enables the PSO to balance global exploration and local exploitation.

Furthermore, to enhance the self-learning and group learning ability of the particles in search space, the social and cognitive coefficients c_1 and c_2 are changed to nonlinear functions as given below.

$$c_1 = \left(\frac{-2.05}{\text{iter}_{max}} \right) \times \text{iter} + 2.55 \quad (3.62)$$

$$c_2 = \left(\frac{1}{\text{iter}_{max}} \right) * \text{iter} + 1.25 \quad (3.63)$$

As seen from the above equations, during the initial stage of iterations, when ω decreases from 3 to 1, c_1 increases, and c_2 decreases gradually, showing that self-learning ability is enhanced. At the later stages of iterations, when ω decreases further from 2 to 1, c_1 decreases, and c_2 increases indicating that the social learning ability is strong.

3.4.5 CAS-PSO Algorithm for Optimizing ZND FOPID Controller

In addition to the adaptive hybrid AS-PSO strategy, ensuring the ergodicity and diversity of the entire search space of the proposed optimization process is crucial. Therefore, a chaotic tent map ASO is hybridized with PSO to improve the ergodicity of the algorithm. The primary steps to be followed for obtaining the initial gain values of ZND FOPID controller are given below:

Step 1: Initialization of parameters- The parameters of AS-PSO, such as atom population (N) and iter_{max} are initialized. The multiplier weight (β) and depth weight (α) of each atom are calculated using Equation (3.60) and Equation (3.58). Then, initialize the searching area boundary, atom positions and the dimension of the search space D.

Step 2: Calculate the fitness of atoms-The fitness function of each atom is computed using Equation (3.41).

Step 3: Calculate the mass of atoms-The mass of the i^{th} atom, $m_i(t)$, is evaluated using Equation (3.5).

Step 4: Compute the resultant force-The interaction force $F_i^d(t)$ employed by other atoms on an i^{th} atom can be calculated using Equation (3.9) and the constraint force $G_i^d(t)$ is computed as given in Equation (3.10).

Step 5: Update acceleration of atoms-The acceleration of the i^{th} atom defined by newton's law of motion is calculated as specified in Equation (3.12).

Step 6: Chaotic hybrid search-For mathematically imitating the proposed strategy by combining the chaotic ASO and PSO, the atom velocity update is given as follows.

$$v_i^d(t+1) = \omega \cdot x_k \cdot v_i^d(t) + c_1 \cdot a_i^d(t) + c_2 \cdot (r_1 \cdot (p_{best,i} - s_i^d(t)) + r_2 \cdot (g_{best} - s_i^d(t))) \quad (3.64)$$

where r_1 and r_2 are the random number ranging between 0 and 1. The values of ω, c_1, and c_2 are adaptive, and these can be generated using Equation (3.61), (3.62) and (3.63). x_k defines the chaotic tent map. The mathematical definition of the tent map is defined in Equation (2.22). In Equation (3.64), the primary portion of the equation $\{v_i^d(t) + c_1 \cdot a_i^d(t)\}$ depicting the velocity updating equation of ASO, which is predominantly dedicated to exploration; and the second half $c_2 \cdot (r_1 \cdot (p_{best,i} - s_i^d(t)) + r_2 \cdot (g_{best} - s_i^d(t)))$ is similar to PSO, which attracts the atoms in the direction of the resultant force that emphasizes exploitation.

Step 7: Update Position-Once the atom's velocity is updated, and each atom's position is updated using Equation (3.15).

Step 8: Stop or continue the process-The optimum controller parameters gbest are obtained once the required number of iterations has been attained. If not, proceed through steps 2 through 8 until the terminating condition is reached. The detailed steps are also presented as flowchart in Figure 3.20.

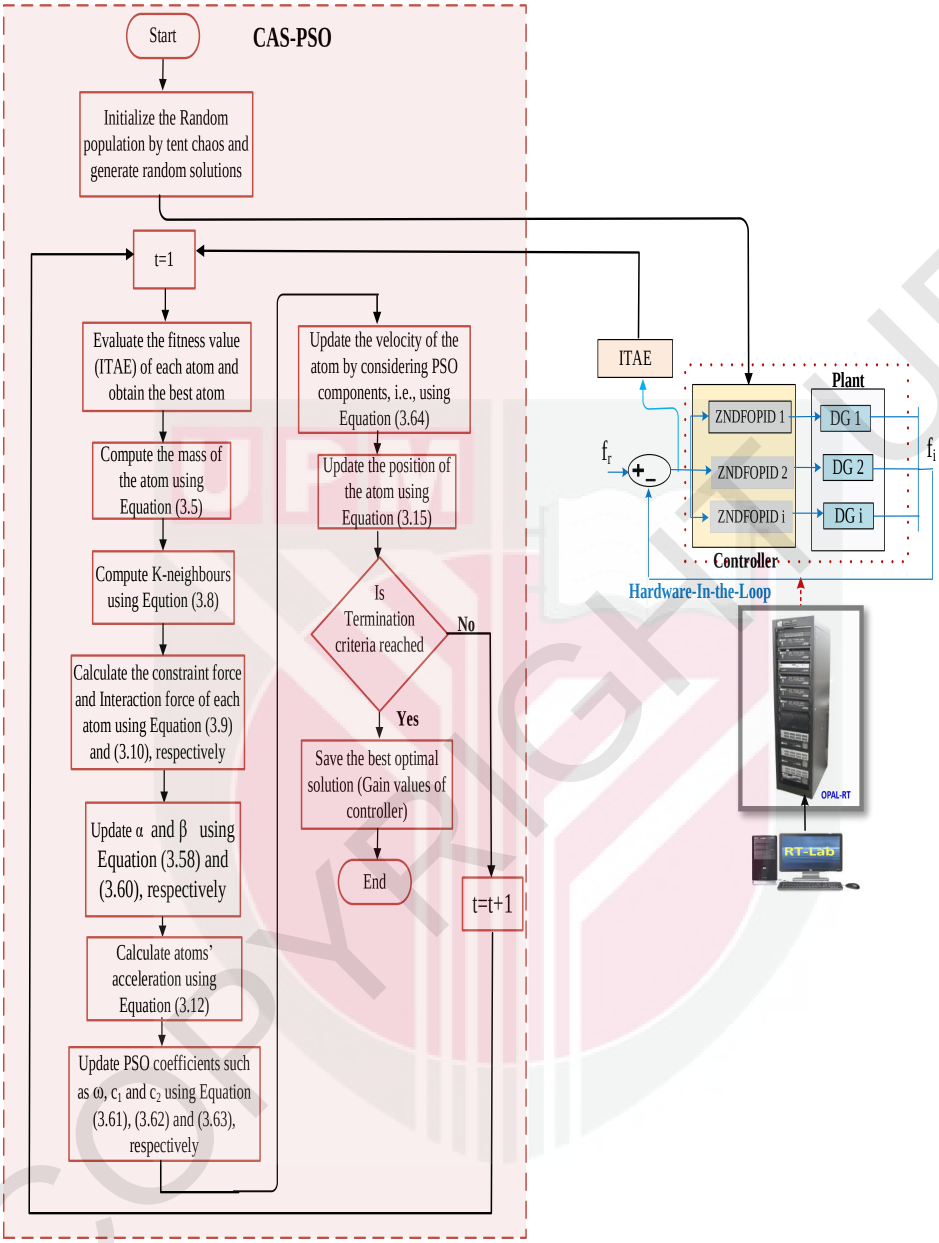

Figure 3.20 : Flowchart of the Proposed CAS-PSO algorithm

3.4.6 LFC Model Studied in Distributed Control Strategy

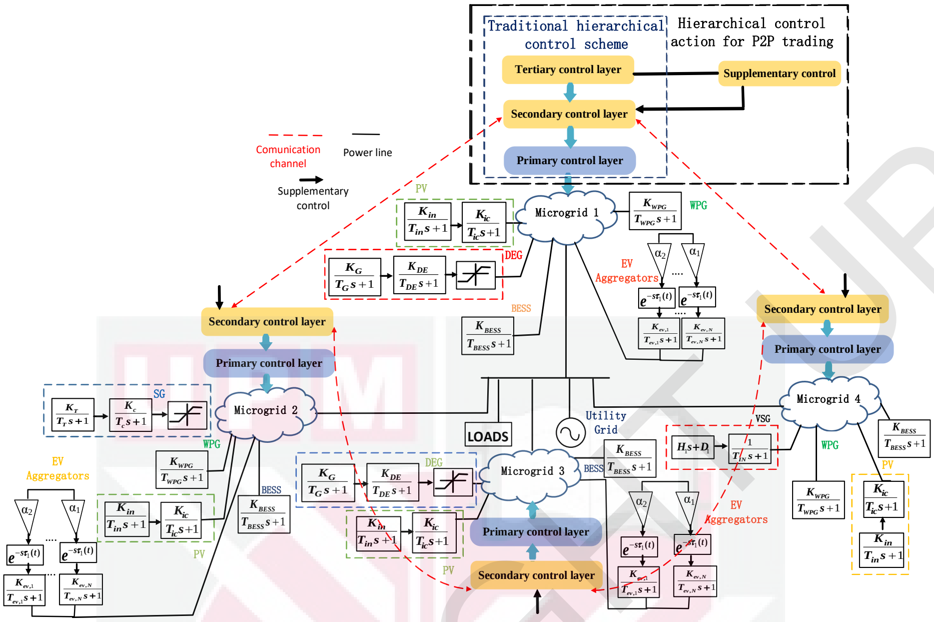

Figure 3.21 : Transfer function model of NMG system

The NMG are formed by interconnecting two or more islanded MGs via a common coupling point, which facilitates power interaction between multiple MGs or with the grid. In NMG the energy sharing between the MGs are carried over tie lines. In this work, we assume that MG network operators act as prosumers and trade the energy between the MG. Figure 3.21 illustrates the schematic representation of the NMG considered in this objective.

The RES, such as PV and WPG units, are connected in all the MGs. However, unpredictable variations associated with RE sources result in frequency instability. To resolve this, inertia support is provided by DEG in MG 1 and 3, synchronous generator (SG) and virtual synchronous generator (VSG) in MG 2 and MG 4. The EV aggregators in the MGs act both as prosumer and consumer based on the market price. The trading method uses a double auction pricing technique (Veerasamy et al., 2023). The primary and secondary control layers are required to govern the system frequency, while the suggested market design operates on the tertiary control layer. In each trading interval, these lower-level control directs guarantee that supply and demand are balanced during RE or load changes. The main objective of the market design is to provide a flexible pricing that enables consumers and prosumers to agree on stable power contracts and works as a supplementary control for frequency regulation applications.

3.4.7 Blockchain Framework for Frequency Regulation

This objective utilizes a real-time digital simulator machine called RT-LAB and incorporates blockchain technology for P2P trading, supplementary and secondary controllers. The proposed framework comprises three layer or module in which layer 1 is a market layer where P2P trading take place with computation of contract participation matrix (CPM). In layer 2, control and optimization which includes the secondary distributed controller. Layer 3 is a physical layer called NMG system, where the MG models has its local primary controller as depicted in Figure 3.22.

Through a double auction method where consumers and prosumers engage, the market is cleared during P2P energy trading at the market layer. By considering the trading price, information on the power shared by prosumers and consumers in the energy market is arranged as CPM. In addition to traditional LFC, the suggested technique includes supplemental control, which reduces frequency oscillations by providing prosumers with additional power commands to meet consumer demands. Low-latency universal datagram protocol (UDP) is then used to transfer the data from the NMG model in RT-LAB to Ethereum blockchain using seven data transmission routes (four prosumers and three consumers). The data is packed and transmitted to the blockchain system using google remote procedure call (gRPC) for authentication and bidirectional streaming.

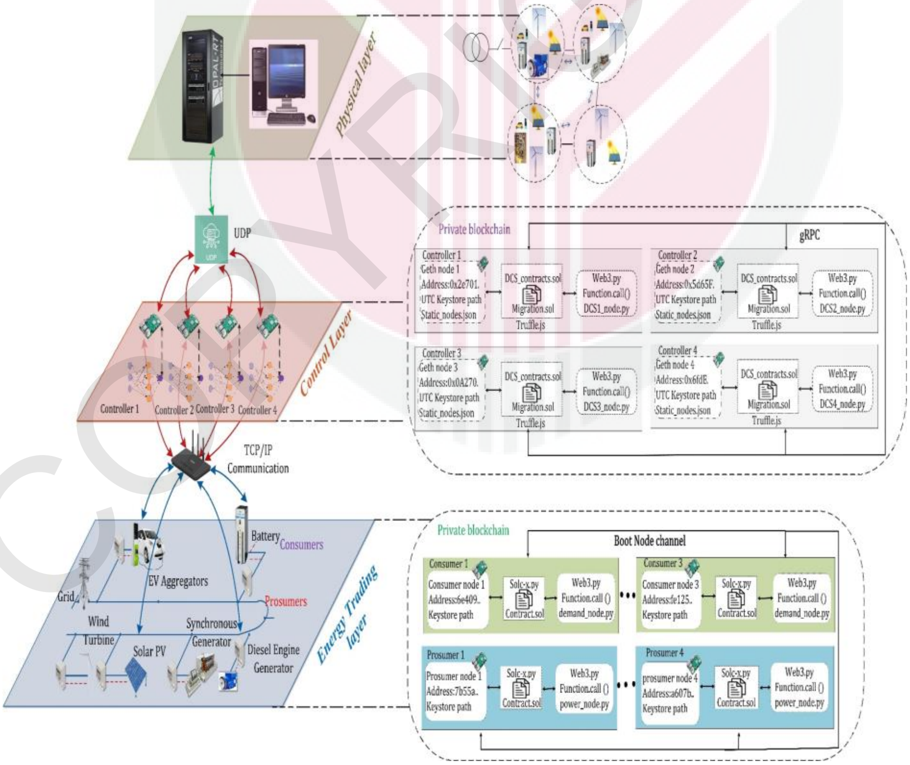

Figure 3.22 : Blockchain Framework for frequency regulation

Finally, in the physical layer, NMG model is implemented in MATLAB/Simulink and integrated to RT-LAB. The secured control command from layer 2 of DCS based federated average learning-based zeroing neural dynamics (FAL-ZND) FOPID controllers is used as secondary controller. In addition, the received power reference data from the prosumers is used as a supplementary control.

a. Implementation of P2P with CPM

In P2P energy market, consumers have the option to select prosumers and create contract as per the bid pricing they want. This is carried out using a double-auction mechanism, as discussed in detail as follows:

Step-1: Place the consumer bids, $c_1\ldots,c_n$, in the descending order in comparison to the price provided by utility grid (UG),

$$c_1 > c_2 >> c_n > b_{FIT} \tag{3.65}$$

where b_{FIT} is the tariff fixed by the UG. In contrast, the trade prices of prosumers, p_1..., pm, are placed in increasing order with respect to the cost submitted by UG,

$$p_1 < p_2 <\ldots. < p_m < a_{UG} \tag{3.66}$$

where a_{UG} represents the UG retail market price. Figure 3.23 shows the market clearing procedure using double auction pricing scheme. In this case, the market clearing is the point of intersection between c_3 and p_3. In the proposed work, the number of prosumer and consumer considered are four and three.

Step-2: In this stage, after the market is cleared and establish the trading among the peers in the network a CPM is developed. The CPM makes the visualization of the contracts easier. The contractual portion of the overall load demanded by a consumer from a prosumer is represented by each entry in the CPM. The CPM entries in each column are always adds up to one, signifying that the demand from consumers is fully satisfied by the prosumers. The CPM is constructed and deployed into the blocks of the blockchain network, guaranteeing safe information exchange throughout the process of energy trading. The detailed description involved in developing the CPM are summarized as follows:

Step-2A: Initialize the CPM as a matrix of zeros with dimensions m × n, where m is the number of prosumers and n is the number of consumers.

$$\mathrm{CPM} = \begin{bmatrix} c_{11} & \cdots & c_{1n} \\ c_{21} & \cdots & c_{2n} \\ \vdots & \ddots & \vdots \\ c_{n1} & c_{n2} & c_{mn} \end{bmatrix} \tag{3.67}$$

Step-2B: Obtain the demanding and selling prices from participating consumers and prosumers. The market clearing process utilizes a double auction-based pricing mechanism. The bidding prices of consumers and the selling prices of prosumers are then sorted accordingly (Veerasamy et al., 2023).

Step-2C: To fulfil consumer demand at an optimal price, calculate every element of each column in the CPM to guarantee that the total of each column equals one.

Step-2D: Check whether the amount of energy generated by a prosumer is equal or greater than the energy required by a consumer. If it is, update the corresponding element in the CPM accordingly. If generation is less than demand, calculate the CPM element using the available generation and update the demand accordingly. Repeat this step until all consumer demands are satisfied.

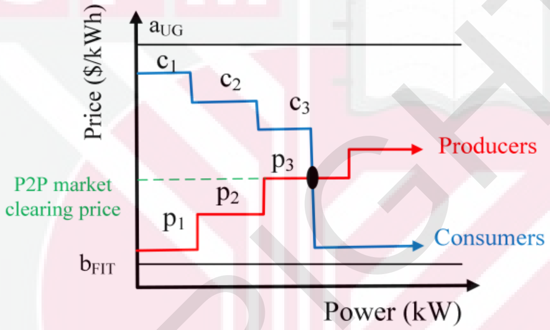

Figure 3.23 : Double auction pricing mechanism

Step-2E: Repeat Step-2D for all consumers to ensure all the demand is satisfied. By implementing these steps, the CPM is created in the P2P energy trading environment.

3.4.8 Proof of Authority-Blockchain based Hierarchical Control

The Proof of Authority (PoA) consensus mechanism is an algorithm that employs Byzantine fault tolerance to determine which nodes are granted permission to validate transactions, considering their reputation (Nazir et al., 2023). PoA blockchains are verified and protected by reputable validators and system administrators, guaranteeing that only they may process transactions and build blocks. This strategy reduces the total weight and expense. PoA has advantages over proof of Work (PoW), such as a cheaper computing cost, the lack of trust problems, and higher transaction throughput (Yang et al., 2022). A distributed energy market has successfully used the PoA-based blockchain, with no gas costs to aid in the growth of the trading platform. The transaction ledger, which keeps track of all blocks containing database transactions, is a crucial part of PoA blockchains. The PoA blockchain, database, and applications are all connected through middleware (Veerasamy et al., 2023).

The P2P energy trading is executed in the tertiary layer of the hierarchical control structure which includes the execution of smart contract that developed considering the double auction mechanism and CPM, then this signal is added up with the distributed controller in the secondary layer. The detailed steps for the implementation are as follows:

Step-1: Install the Raspbian operating system on Raspberry Pi. Install eMEGAsim software for OPAL-RT, including Real-Time Simulation Platform and associated drivers. Connect OPAL-RT hardware interfaces (such as I/O modules) to the Raspberry Pi.

Step-2: The Ethereum is used as a blockchain platform. Geth private blockchain network is setup. The accounts for participants in the P2P energy trading network and for the controller are created.

Step-3: The blockchain is initiated by running the boot node (node-0) and connecting other nodes using the script ("startnode.cmd").

Step-4: The cycle control timer is initiated to commence the cycle loop. To manage the duration of each cycle and handle new data for analysis, a Python file named "timing.py" is generated. This file resets for each cycle, allowing for the storage and analysis of fresh data. When executing "timing.py" in the terminal, a summary of results is displayed. This summary encompasses details such as consumer demands (quantity and price), the maximum capacity of dispatched amounts and power reference values, prices for prosumer generations and the CPM matrix allocation.

Step-5: Within a predetermined range, consumer demands, including quantity and price, are created randomly. By invoking the functions in the smart contract, the values are read from the blockchain and saved there. An exclusive flag on every node becomes true when the information is effectively retrieved. The demands are then arranged according to the bidding price in descending order.

Step-6: Similarly, each prosumer maximum capacity and energy price are randomly created and recorded in the Hyperledger using appropriate functions. The data is sorted in increasing order of selling price after their respective flags become true.

Step-7: The assignment of consumers to prosumers is carried out using the "Power Dispatch" function, which considers the sharing ratio specified in the CPM entries. The description for computing CPM is depicted as flowchart in Figure 3.24.

Step-8: The secondary distributed controller logic is written in Web 3 python scripts on the Raspberry Pi. The node-accounts are created with distinct addresses and private keys to represent the secondary controllers.

Step-9: In this step, a connection has been established with the controller nodes using the 'Enode' addresses recorded in the StaticNode.json file. 'Enode' is a connection port provided by the Ethereum platform.

Step-10: Finally, the control signal $u_i(t)$ is sent back through transfer control protocol/ Internet protocol (TCP/IP) to OPAL-RT, where the plant model is implemented in HIL simulations. Then, the recorded frequency response is passed as input to the secondary distributed controller in the RPis. Thus, the RPis send the power command signal to the OPAL-RT and receive the frequency information of NMG.

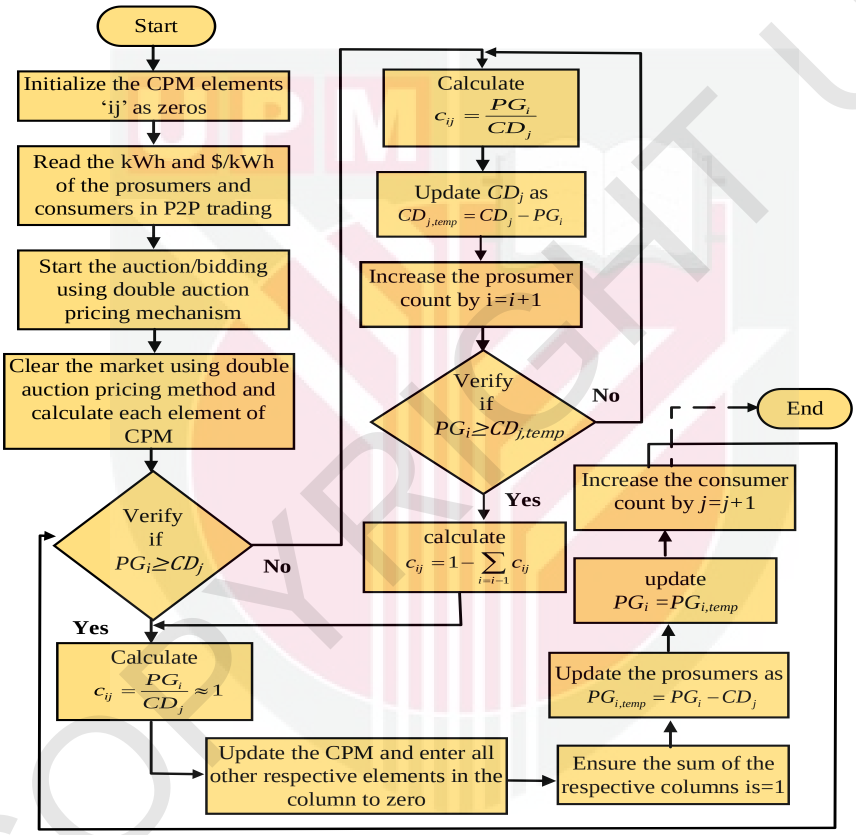

Figure 3.24 : Flowchart for the implementation of CPM

3.5 IEEE New England 39-bus System

To benchmark the proposed distributed FAL-ZND FOPID controller on a real power system, the New England 39-bus network is considered. This system, recognized for its complexity and real-world representation, is widely acknowledged in the literature as a suitable testing ground for evaluating various control strategies (Ramachandran et al., 2021). The new England 39-bus network comprises a total of 10 generators, 34 transmission lines, 12 transformers, and 19 loads with RES as shown in Figure 3.25. To elaborate, buses 1, 2, and 3 host the generator buses (G1, G2, and G3) in area-1, while buses 8, 9, and 10 serve as the generator buses (G8, G9, and G10) for area-2. Furthermore, buses 4, 5, 6, and 7 acts as generator buses (G4, G5, G6, and G7) for area-3. The combined installed capacity for the three areas is 881.2 MW, distributed as follows: 218.96 MW generation and 265.25 MW load in area-1, 232.83 MW generation and load in area-2, and 180.05 MW generation and 124.78 MW load in area-3. Additionally, wind power of 12 MW and STPG of 8 MW are integrated into area-1 and area-3.

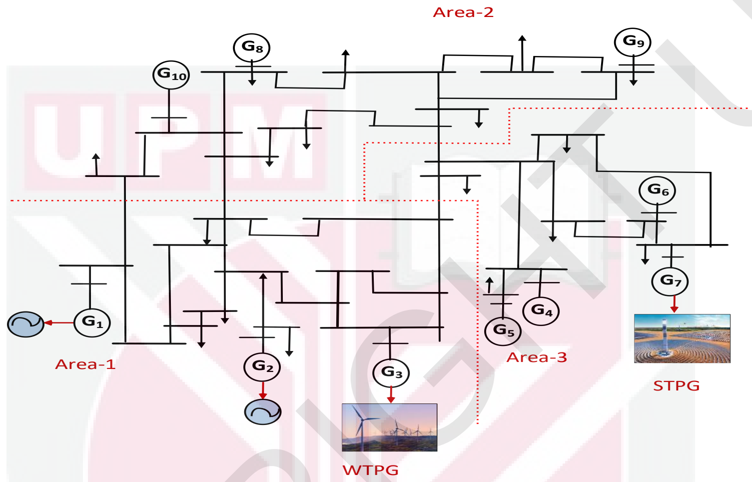

Figure 3.25 : Schematic representation of IEEE new England 39-bus system

3.6 Summary

This chapter outlines the research framework and methodology, consisting of three objectives focusing on control schemes and strategies for LFC problem. The centralized, decentralized, and distributed control strategies are evaluated on a power network. The controller gain values are optimized using various improved versions of ASO algorithm. The research primarily emphasized the utilization of a recurrent fractional order controller employed in a distributed control manner to tackle the LFC challenges, with the aim of achieving the predefined research objectives.

CHAPTER 4

RESULTS AND DISCUSSION

4.1 Introduction

This chapter provides a comprehensive analysis on results from various system model that are studied for the proposed control techniques and schemes. These are essential in achieving the objectives of this research work which are examined critically in this section. Initially, a HPS is considered for the study as shown in Figure 3.5 in Chapter 3. The FOPID controller is designed in a centralized fashion to regulate the frequency of the network. During this case, a CASO technique is proposed to optimize the gain values of the controller. The robustness of the proposed control technique is evaluated particularly concerning its ability to withstand parametric uncertainty in the investigated system. Due to the limitation of single point failure in centralized control scheme and to improve the performance of proposed CASO, an improved form of FOPID controller is designed in a decentralized manner for a multi-area deregulated power network to effectively study the LFC in the open market environment as shown in Figure 3.15 in Chapter 3. In this case, the performance of control technique is improved by hybridization technique called AS-PSO to tune the control parameters. During these cases, the controller gain values are static, and which makes the controller ineffective for large disturbances in the system. Hence, a FAL-based ZND FOPID controller is proposed for distributed frequency control of an NMG system. The system model studied for this is shown in Figure 3.21 in Chapter 3. In order to obtain the initial bias values of the recurrent controller, an adaptive form of CAS-PSO is considered by incorporating the control techniques proposed in objectives 1 and 2. To benchmark the efficacy of the proposed control method on a practical power system a modified New England IEEE 39 bus system is considered. To the end, the performance of various control schemes and the strategies are compared to study its effectiveness in LFC study. From the results, a suitable control strategy with its scheme of operation is suggested as an outcome of this research.

4.2 Simulation Results of CASO Optimized Centralized FOPID Controller

In this section, initially the performance of the proposed CASO is verified by comparing it with the standard ASO algorithm in terms of statistical results by considering the five classical benchmark functions extensively reported in the literature. Furthermore, the proposed CASO tuned centralized FOPID controller is analyzed for multi-area multi-source HPS. The model is developed in MATLAB/Simulink and the simulation results are obtained. The results of CASO (logistic map based chaotic atom search optimization (LM-CASO), sine map based chaotic atom search optimization (SM-CASO) and tent map based chaotic atom search optimization (TM-CASO) tuned FOPID controller are compared with the standard ASO technique. The following section discuss in detail about the results obtained for various benchmark functions and numerous cases of HPS model.

4.2.1 Validation of Benchmark Functions

To validate the performance of the proposed CASO algorithm with ASO algorithm, five classical benchmark functions with diverse set of attributes are considered (Yousri et al., 2021). Table 4.1 depicts the details of benchmark functions used for validation of various forms of chaotic based ASO. The functions F1 and F2 are unimodal separable (US) and unimodal non separable (UN) functions with a single global best as shown in Table 4.1. The unimodal functions are often used in high-dimensional optimization scenarios, and the choice of 30 dimensions is somewhat arbitrary but has become a standard in the literature (Zhao et al., 2019b). The idea is to test the algorithm's ability to handle a relatively high-dimensional search space, which is common in real-world optimization problems. The algorithm exploitation ability is evaluated by the unimodal benchmark functions, indicating that exceptional results require an algorithm with a strong local search capability.

The functions F3-F5 depict multimodal separable (MS) and multimodal non separable (MN) functions. The Kowalik benchmark function is a univariate function with four parameters. When used in optimization, it's common to treat each parameter as a separate dimension, resulting in a four-dimensional search space. The Shekel 5 benchmark function is designed for four-dimensional optimization. The five terms in the function represent different local optima, and the challenge is to find the global optimum among them. In contrast to unimodal functions, multimodal functions have more than one global best and are used to evaluate the algorithm exploration ability (Barshandeh et al., 2021). Further, the chosen range of values for each parameter in the optimization problem defines the feasible solution space that the algorithm explores.

The ranges are often selected based on considerations of the typical scale of the problem or the expected range of parameter values in real-world applications. The selected ranges should be broad enough to encompass a diverse set of potential solutions but not so broad that they include unrealistic or infeasible solutions (hekimoglu et al., 2019). Furthermore, the minimum/optimal values for the benchmark functions are chosen as reference points. In optimization, the goal is often to find the global minimum of a function (or a close approximation). Setting the minimum value to 0 for functions like Sphere, Rosenbrock, and Rastrigin simplifies the interpretation of results. The objective is to minimize the value of these functions and achieving a value of 0 indicates that the global minimum has been found. For Kowalik, the minimum value of 0.0003 is a specific value associated with the global minimum of that function. It represents the optimal solution in that context. Similarly, for Shekel 5, the minimum value of -10.1532 is the known global minimum for that function (Izci et al., 2022).

Table 4.1 : Benchmark functions

Function Name		Type	Formulae	Dimension (d)	Range	Minimum Value
Sphere	F1	US	$f(x)=\sum_{i=1}^{d} x_i^{\,2}$	30	[-100,100]	0
Rosenbrock	F2	UN	$f(x)=\sum_{i=1}^{d-1}[100(x_{i+1}-x_i^2)^2+(x_i-1)^2]$	30	[-30,30]	0
Rastrigin	F3	MS	$f(x)=\sum_{i=1}^{d}[x_i^2-10\cos(2\pi x_i)+(x_i-1)^2]$	30	[-5.12,5.12]	0
Kowalik	F4	MN	$f(x)=\sum_{i=1}^{d}\left(a_i-\frac{x_1(b_i^2+b_i x_2)}{b_i^2+b_i x_3+x_4}\right)$	4	[-5,5]	0.0003
Shekel 5	F5	MN	$f(x)=\sum_{i=1}^{5}\left\|(x_i-a_i)(x_i-a_i)^T+c_i\right\|^{-1}$	4	[0,10]	-10.1532

The statistical results of the algorithms on the classical benchmark functions are presented in Table 4.2. These results are compared in terms of mean and standard deviation (SD) of the best values achieved. Each algorithm is run 30 times independently and the results are recorded. The various benchmark functions are tested using each chaotic and standard ASO technique by considering the atom population of 50 and number of iterations as 100, respectively. The number of iterations in an optimization algorithm is a crucial parameter. It affects the balance between exploration and exploitation. Increasing the number of iterations may allow the algorithm more time to explore the search space thoroughly, but it could also lead to overfitting or spending too much time in certain regions. Therefore, the algorithm iterations should be chosen between 100 to 500 iterations (Zhao et al., 2019b).

The statistical results inferred from Table 4.2 show that the chaotic maps based ASO have significantly improved not only the exploration phase but also the exploitation phase. For both unimodal and multimodal functions, TM-CASO shows lower means and standard deviations when compared with other chaos embedded ASO and standard ASO.

Table 4.2 : Statistical results of benchmark functions

Function	Index	TM-CASO	SM-CASO	LM-CASO	ASO
F1	Best	**4.43e-24**	5.32e-23	0.00015	270.97
	SD	**1.85e-23**	5.74e-22	7.01e-05	290.69
	Mean	**8.40e-21**	3.75e-22	3.14e-05	600.84
F2	Best	86.75	**84.01**	452.18	22815.96
	SD	**30.84**	190.99	127.31	22438.31
	Mean	**45.22**	155.33	165.42	34152.12
F3	Best	66.66	67.65	**56.71**	91.76
	SD	**3.82**	16.13	17.68	34.58
	Mean	**62.07**	63.67	64.08	118.33
F4	Best	**0**	0	0	7.61
	SD	**0**	0.0033	0.0033	17.22
	Mean	**0**	0.0014	0.0015	39.60
F5	Best	**0.001**	0.0013	0.0014	0.0016
	SD	**0.0002**	0.00036	0.0004	0.005
	Mean	**0.0011**	0.0011	0.0013	0.0054

4.2.2 Time Domain Analysis of Interconnected System

In this section, the proposed CASO is further validated for the LFC application of HPS by optimizing the parameters of FOPID controller in each area of interconnected system. The tuned values of FOPID controller using standard and chaotic based ASO for two- and three-area HPS are given in Tables 4.3 and 4.4, respectively.

Table 4.3 : Controller gains for two-area HPS

Proposed control methods to tune FOPID controller	Case 1				
	k_p	k_d	µ	k_i	λ
TM-CASO	-3.3573	-1.2357	0.9895	-4.9961	0.8804
SM-CASO	-3.0573	-1.1610	0.9567	-3.9889	0.8727
LM-CASO	-2.8095	-0.9178	0.9825	-2.9397	0.8864
ASO	-1.9698	-1.5232	0.7980	-2.9807	0.8775

Table 4.4 : Controller gains for three area multi-source power system

Proposed control methods to tune FOPID controller	Case 2					
		k_p	k_d	µ	k_i	λ
TM-CASO	Area-1	-0.9574	-0.8309	0.9880	-2.9986	0.8110
	Area-2	0.4931	-2.5689	0.6257	-2.3836	0.8621
	Area-3	-1.2824	-1.9583	0.8430	-2.4521	0.9028
SM-CASO	Area-1	-0.8773	-0.8744	0.9720	-2.9989	0.8237
	Area-2	0.4927	-2.5338	0.5024	-1.9549	0.8211
	Area-3	-1.8421	-2.1095	0.7579	-1.6505	0.9889
LM-CASO	Area-1	-1.6068	-1.0242	0.9874	-2.9949	0.8064
	Area-2	0.7536	-2.7315	0.6697	-1.7803	0.9721
	Area-3	-1.8873	-1.5059	0.7985	-2.4186	0.9065
ASO	Area-1	-1.5826	-1.0834	0.9868	-2.9907	0.7937
	Area-2	0.8381	-2.5749	0.6792	-2.6118	0.8254
	Area-3	-1.6945	-2.3021	0.6861	-2.5195	0.9748

The effectiveness of the proposed method is examined in various cases of power system operation as described in the following case studies.

a. Case 1: Two-area HPS

In this case, a two-area HPS model that comprises reheat thermal system incorporated with BD, GDB, GRC, and RES like WTPG and STPG combined with energy storage systems of AE and FC were considered. A step load perturbation (SLP) of 50 MW and 30 MW is applied in area-1 and area-2 of interconnected system, respectively. The total power generation of HPS can be expressed as,

$$P_s = P_{Thermal} + P_{Wind} + P_{Solar} - P_{AE} + P_{FC} \tag{4.1}$$

The system dynamic responses (frequency deviation and tie-line power variations) are illustrated in Figure 4.1. It is clear from the response that the FOPID controller tuned by TM-CASO damped out the frequency deviations more rapidly than other methods. In terms of transient specifications as given in Table 4.5, the proposed method (TM-CASO) exhibits minimal ST (4.96 s, 6.4329 s) and P-U (0.0395, 0.0251) in area-1 and area-2, respectively. Further, the tie-line power tends to be smooth and stable for the case of CASO. In addition, the other form of CASO such as SM-CASO (6.1219 s, 6.81 s) and LM-CASO (6.7148 s, 7.4139 s) tuned FOPID controller also have minimum ST than ASO (7.29 s, 7.8381 s) adapted FOPID controller. As the chaotic map embedded in ASO algorithm generates the search agents more dynamically which improves the exploration and exploitation capabilities of standard ASO. The transient performance indices like ST, SE, and P-U are improved by 18% to 32%, 41% to 43%, and 31% to 57%, respectively using TM-CASO than ASO method. On the other hand, the steady-state performance indices like ISE, ITSE, IAE, and ITAE are significantly enhanced by a proportion of 22% to 25%, 25% to 40%, 24% to 28%, and 41% to 44%, respectively by the proffered TM-CASO based FOPID controller than other methods presented in Table 4.5.

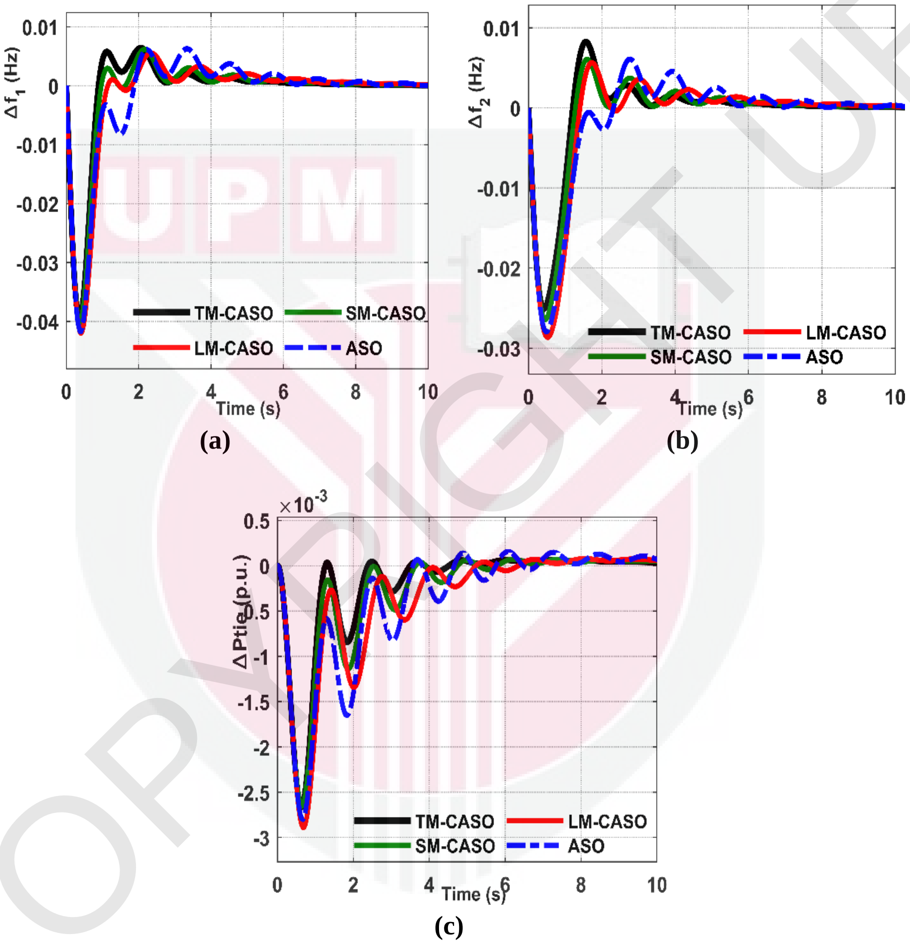

Figure 4.1 : Transient performance response of two-area HPS (a) change in area-1 (b) change in area-2 (c) change in tie-line power deviation

Table 4.5 : Performance Indices of two-area HPS

Case	Performance Indices	Δf1 TM-CASO	SM-CASO	LM-CASO	ASO	Δf2 TM-CASO	SM-CASO	LM-CASO	ASO
Case 1	IAE	0.0333	0.0341	0.0391	0.0445	0.0298	0.0317	0.0372	0.03914
	ITAE	0.068	0.0842	0.1034	0.1212	0.067	0.0827	0.1013	0.1135
	ISE	0.0006	0.0007	0.0008	0.0008	0.0004	0.0004	0.0006	0.0006
	ITSE	0.0003	0.0003	0.0004	0.0005	0.0002	0.0002	0.0004	0.0004
	CE	0.0092	0.0114	0.0147	0.0151	0.0089	0.0114	0.1096	0.0150
	ST (s)	4.96	6.1219	6.7148	7.29	6.4329	6.81	7.4139	7.8381
	SE ($\times 10^{-5}$)	1.324	1.862	2.175	2.246	1.33	1.909	1.391	2.315
	| P-U |	0.0395	0.0403	0.0420	0.0419	0.0251	0.0265	0.0287	0.0361

b. Case 2: Three-area HPS

The robustness of the proposed control technique has been studied for three-area interconnected multi-source power system comprises reheat thermal system with nonlinearities like BD, GRC, and GDB in all areas, hydro generating unit in area-1 and area-3, and gas turbine power plant in all areas of interconnected system. An increased SLP of 60 MW in area-1, 30 MW in area-2, and 50 MW in area-3 were applied, respectively. The dynamic response of the system with optimal values of FOPID controller using TM-CASO is significantly better than LM-CASO, SM-CASO and ASO tuned FOPID controller as shown in Figure 4.2. The proposed method (TM-CASO) has minimum ST with less undershoots compared with other methods presented. The work done by the controller is evaluated in terms of CE and the results exhibits that the TM-CASO optimized FOPID controller achieve low CE even for the large-scale system of three-area compared with standard ASO and other chaotic forms (SM-CASO and LM-CASO). The response of the standard ASO suffers from transient oscillation due to poor exploration and exploitation ability.

Table 4.6 provides the performance indices of IAE, ITAE, ISE, ITSE, CE, ST, SE, and P-U which are enhanced by 7% to 20%, 16% to 25%, 24% to 34%, 35% to 43%, 17% to 22%, 27% to 46%, 7% to 29% and 10% to 15%, respectively for TM-CASO tuned FOPID controller than standard ASO method.

Table 4.6 : Performance Indices of three area multi-source power system

Case		Performance Indices	TM-CASO	SM-CASO	LM-CASO	ASO
		IAE	0.0864	0.1021	0.0914	0.1046
		ITAE	0.283	0.3417	0.2928	0.3504
	Δf1	ISE	0.0025	0.0032	0.0027	0.0033
		ITSE	0.002	0.0029	0.0023	0.0031
		CE	0.0381	0.0431	0.0452	0.0484
		ST (s)	7.25	9.5957	9.7215	9.9842
		SE ($\times 10^{-5}$)	4.75	6.635	6.615	6.691
		| P-U |	0.0606	0.0649	0.0648	0.0697
		IAE	0.0879	0.1093	0.0947	0.1098
		ITAE	0.2952	0.3787	0.3261	0.3916
Case 2		ISE	0.0021	0.0028	0.0024	0.0032
	Δf2	ITSE	0.0025	0.0040	0.0303	0.0044
		CE	0.0439	0.0488	0.0430	0.0529
		ST (s)	6.76	11.2885	11.4213	12.5658
		SE ($\times 10^{-5}$)	4.96	6.309	5.822	7.032
		| P-U |	0.0466	0.0532	0.0510	0.0545
		IAE	0.0891	0.0935	0.1074	0.1096
		ITAE	0.3059	0.3146	0.3421	0.373
		ISE	0.0022	0.0022	0.0024	0.0031
		ITSE	0.0024	0.0026	0.0039	0.0041
	Δf3	CE	0.0420	0.0487	0.0430	0.0540
		ST (s)	7.12	11.4580	10.2467	11.9152
		SE ($\times 10^{-5}$)	4.92	6.08	6.286	6.786
		| P-U |	0.0505	0.0513	0.0531	0.0560

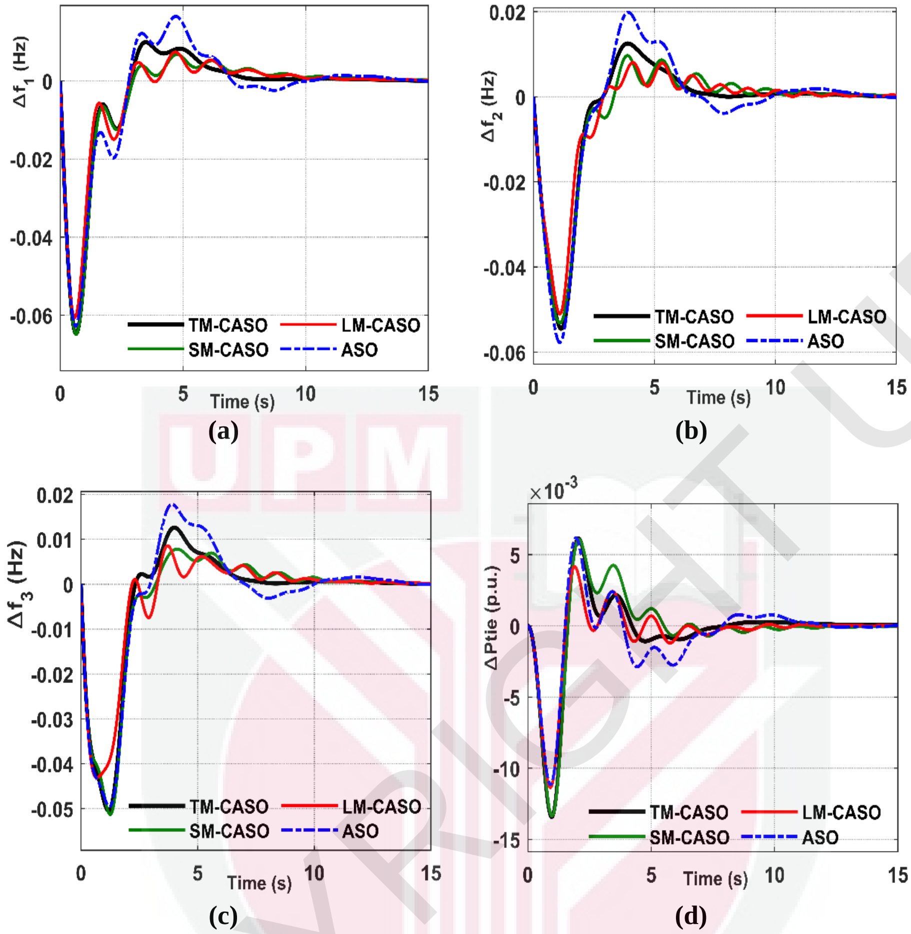

Figure 4.2 : Transient performance response of three-area HPS (a) change in area-1 (b) change in area-2 (c) change in area-3 (d) change in tie-line power deviation

4.2.3 Robustness Analysis

To validate the robustness of the proposed TM-CASO optimized FOPID controller, the two-area HPS model has been tested with real time variation in solar and wind power. Furthermore, to test the adaptability of the proposed technique the two-area HPS has been considered by varying system parameters like inertia constant (H) and system loading (which reflects frequency dependent system loading).

a. Case 1: Real-Time Variation of RES

In this case, the variation in STPG unit output power is considered for real-time monthly-average irradiance data at Universiti Putra Malaysia from Subang meteorological center in Malaysia (Lurwan et al., 2016). The irradiance values are taken from January to

December 2014 for 200-time slots of 0.5 s as given in Figure 4.3. The developed HPS model is tested for this real-time solar power variations and the dynamic response is recorded as given in Figure 4.4 for CASO and ASO method. It is inferred that the TM-CASO tuned FOPID controller shows better and smoother response with minimum overshoot and undershoot than other tuning methods. Similarly, the wind power variation for change in wind speed is obtained in real-time at the Malaysian Meteorological Department in Kuala Terengganu (Ali Kadhem et al., 2019) with latitude= 5°23' N and longitude=103°06' E (considering elevation=5.2m) for a whole year and converted into seconds to assess the reliability of the controller, as depicted in Figure 4.5. The frequency response and tie-line power deviation for this variation in wind power is shown in Figure 4.6. It is observed that the TM-CASO has minimum frequency oscillations with less SE compared to other techniques presented. Thus, overall, it is seen that among the chaotic map that used to improve the performance of the ASO method of tuning FOPID controller the proposed TM-CASO performs remarkably to regulate the system frequency and tie-line power to steady state under step load perturbation and real-time variation in RES.

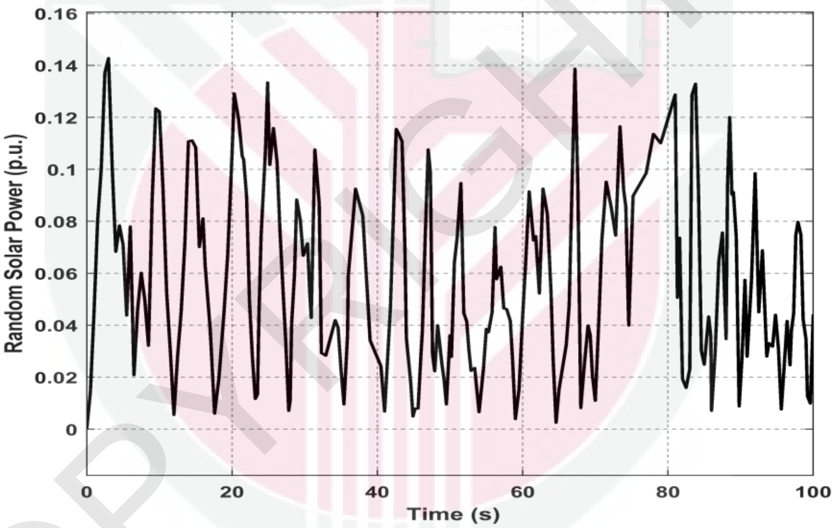

Figure 4.3 : Solar Power Profile

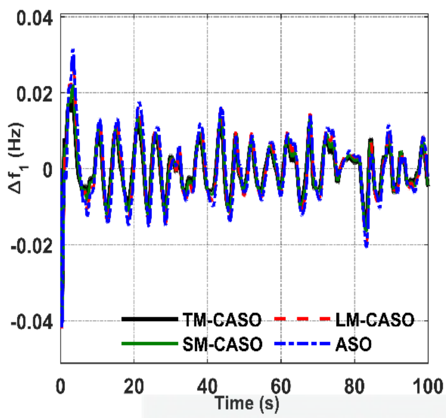

(a)

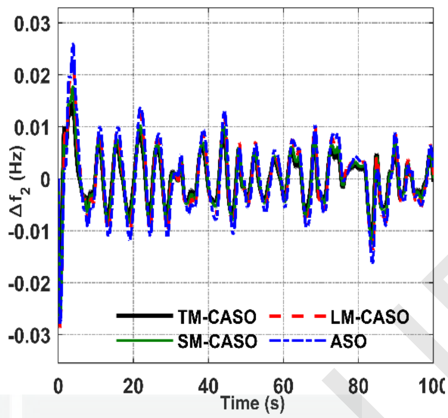

(b)

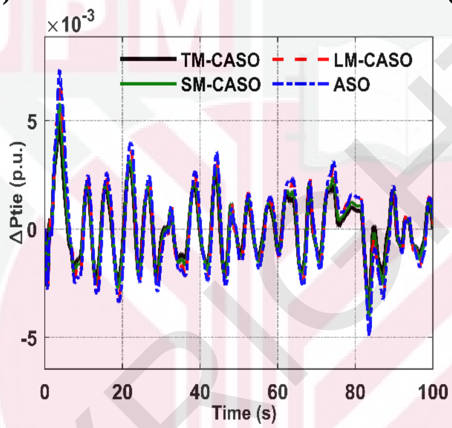

(c)

Figure 4.4 : Dynamic response of two-area HPS during real time solar variation (a) change in area-1 (b) change in area-2 (c) change in tie-lie power

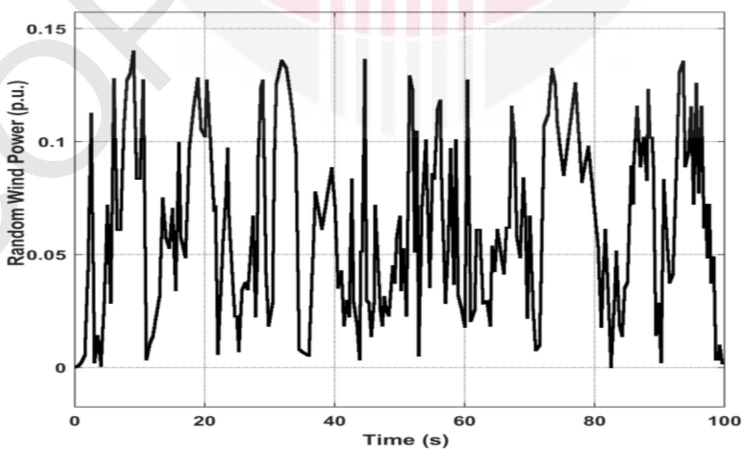

Figure 4.5 : Wind Power Fluctuation

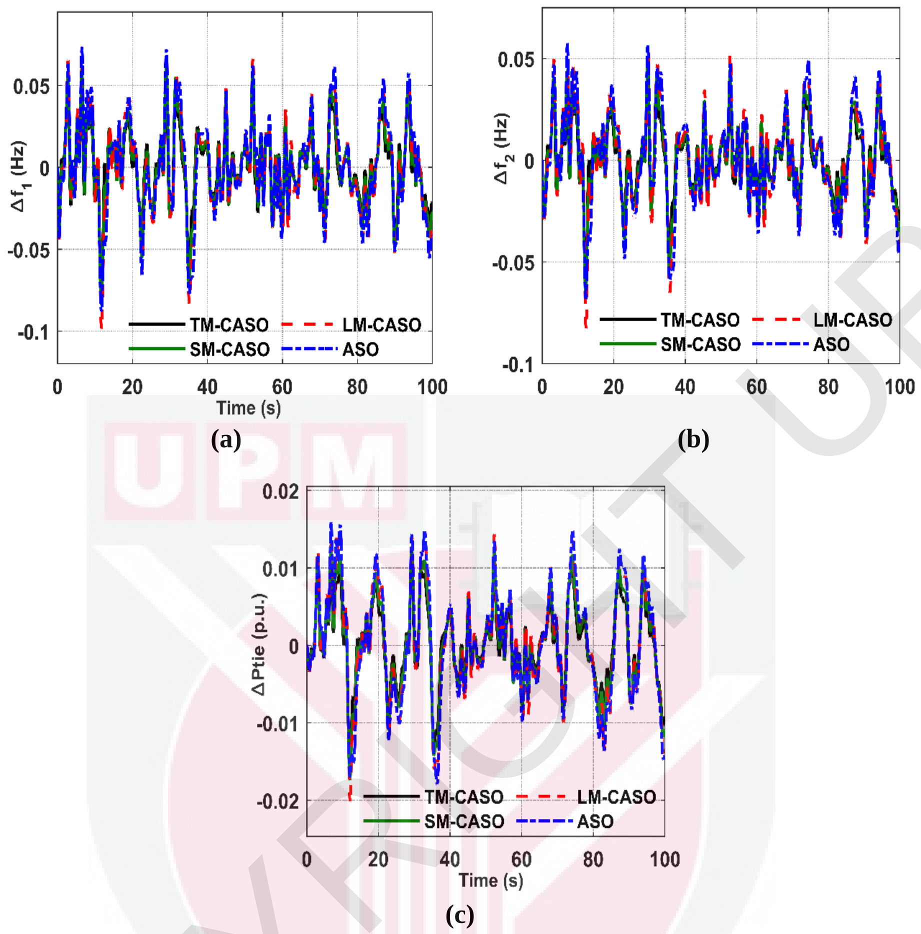

Figure 4.6 : Dynamic response of two-area HPS during real time wind variation (a) change in area-1 (b) change in area-2 (c) change in tie-lie power

b. Case 2: Performance under uncertain variation in loading and inertia

In this case, the system parameter, inertia (H) and loading conditions are varied from their nominal values. The inertia (H) and loading conditions in a power system are crucial for LFC. Variations in these parameters can impact the stability and performance of the system. Several studies have addressed the impact of variable inertia and load damping on frequency control (Ramachandran et al., 2021, Veersamy et al., 2020). The inertia is defined as the ability of a power system to oppose changes in system frequency due to the resistance provided by the system. The decrease in system inertia is due to the integration of RES needs to be restored by the controller. The increase in inertia can affect the stability of the system. Therefore, it is essential to consider the effects of variable inertia and loading conditions on LFC to ensure the stability and reliability of power systems. As per the guidelines given by Elgerd et al., (1983), the nominal value of H is chosen as 5. To test the real time applicability of the proposed control technique, the value of the H is changed by ±25 % (3.75 and 7.25) from its nominal value (H=5) and the tuned values under nominal conditions as given in Table 4.3 is considered. Figure 4.7 shows the frequency and tie line power response obtained for change of H by ±25 % from its nominal value (H=5). From this figure it is observed, the efficacy of the controller tuned using TM-CASO is optimum for wide variation of H.

The work on LFC by Elgerd, (1983) states the importance of nominal system loading. For example, if the power system capacity is 2000 MW the system nominal loading should be chosen as 50 % from its overall capacity to protect the power system from overloading. Therefore, the nominal loading for HPS network considered is chosen as 1000 MW. In case of any change in the load demand from its nominal value (50 %), it will affect the generator's shaft speed to deviate from the pre-set value, leading to a deviation in the system frequency from the standard value. Additionally, the rate of change of frequency increases with load changes, making the frequency of the system respond quicker to power imbalances. Therefore, changes in system loading of ±25 % from the nominal value (50 %) is considered to test the feasibility of the proposed control technique. Figure 4.8 depicts the dynamic response of frequency and tie line power variations for changes in system loading. It can be noted that the system adjusts to changes in system loading more quickly, without any delay in response. Hence, it can be concluded that the controller tuning parameters need not to be re-tuned for parameter changes as the proposed control strategy is adaptive for any change in system parameter or uncertainty.

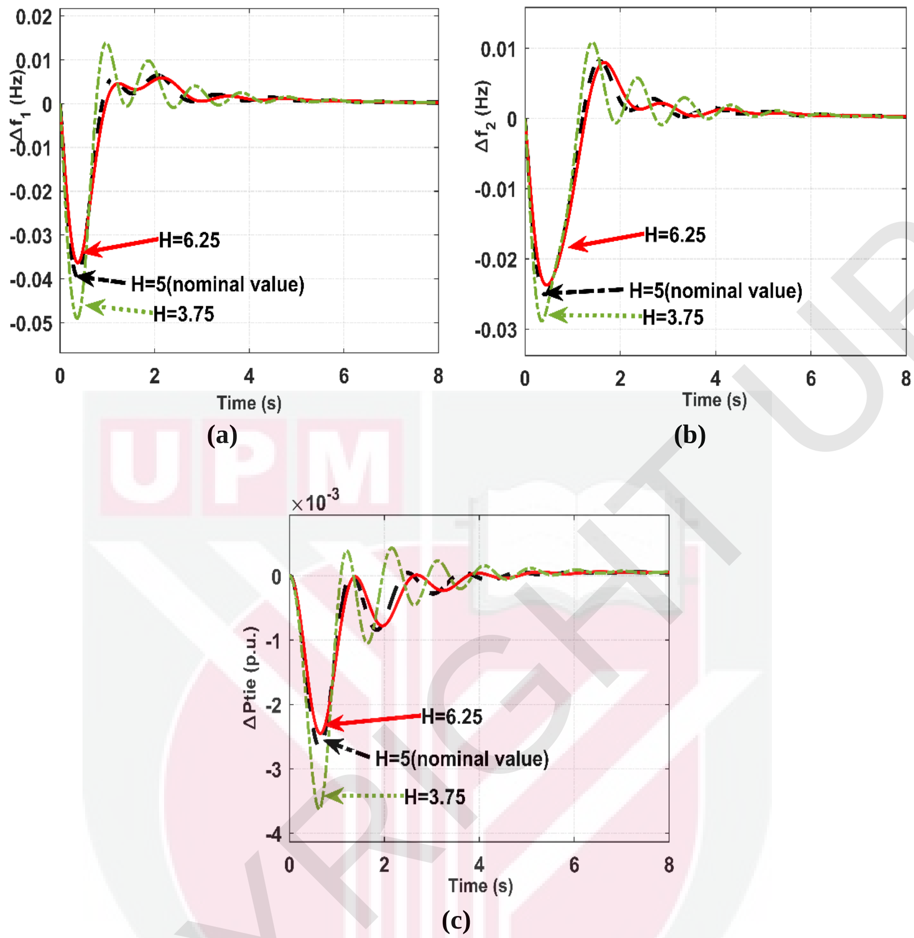

Figure 4.7 : Sensitivity analysis for change in inertia (H) (a) change in area-1 (b) change in area-2 (c) change in tie-lie power

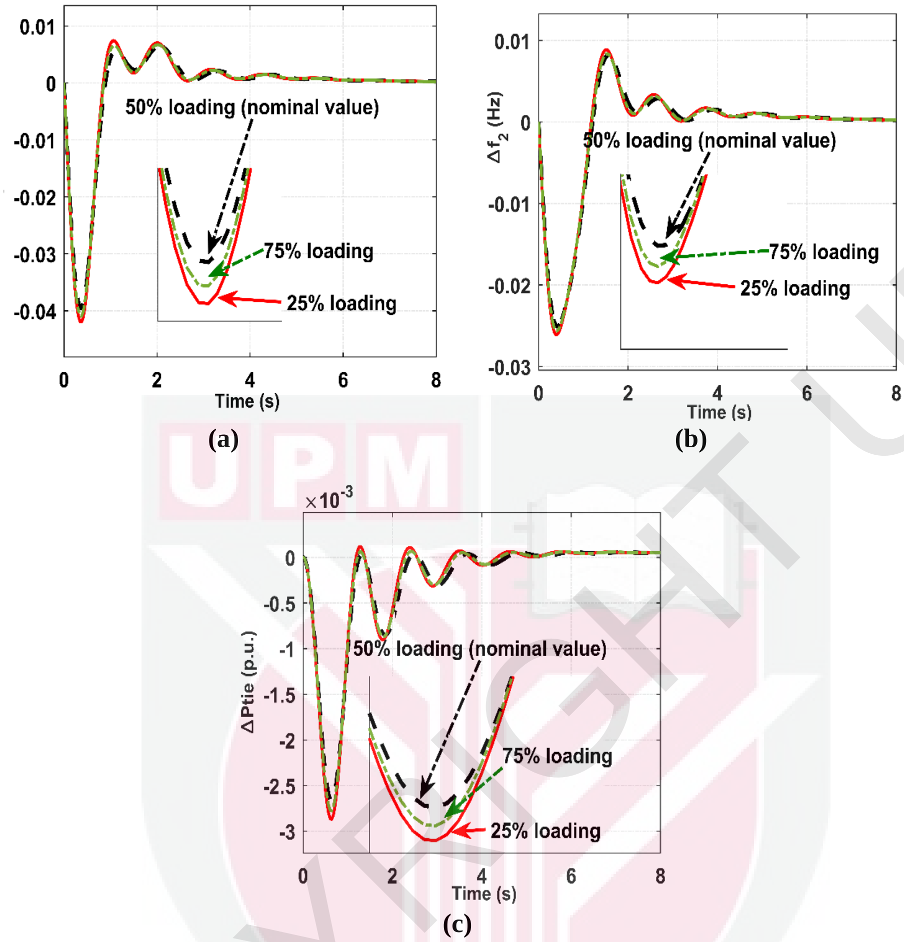

Figure 4.8 : Sensitivity analysis for change in system loading (a) change in area-1 (b) change in area-2 (c) change in tie-lie power

4.2.4 Computational Cost

To investigate the computational complexity of the proposed CASO technique compared to the standard ASO method, this section presents the convergence performance of the proposed algorithm (TM-CASO, LM-CASO and SM-CASO) for tuning the FOPID controller of two-area HPS model. Figure 4.9 shows the convergence curve which depicts the minimization of ITAE of ACE for HPS model considered. It is inferred that the various CASO methods converge faster compared to the standard ASO. However, the TM-CASO algorithm is faster than the LM-CASO and SM-CASO method of tuning the controller. Also, from the results obtained it is seen that the TM-CASO is more reliable in producing superior results with an optimum computation time of 678 seconds with minimum fitness value by avoiding the premature convergence due to its diversification of chaotic sequences compared to the LM-CASO (928 seconds) and SM-CASO (1128 seconds), where the chaotic sequence is appeared for minimum time span.

Thus, the exploration and exploitation capability of the ASO is significantly improved by the tent map compared to other chaotic maps.

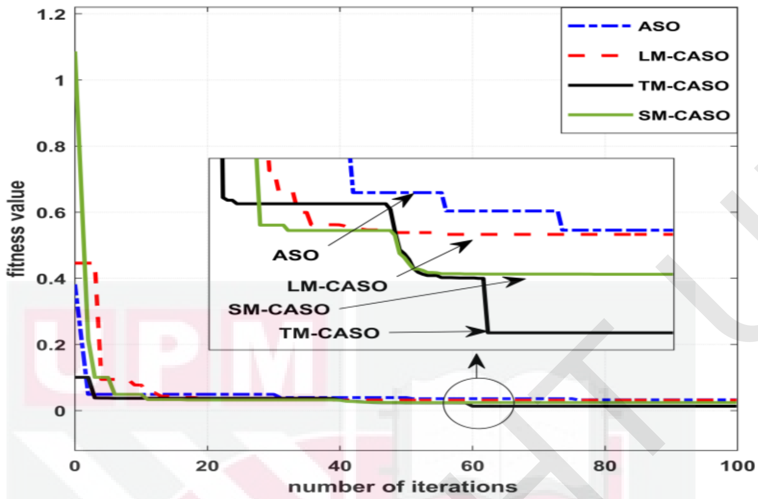

Figure 4.9 : Convergence curve of the algorithms

4.2.5 Stability Analysis

For practical implementation of fractional-order controllers, fractional-order operators are approximated to integer order. In literature, many methods like oustaloup, Carlson, Matsuda, and continued fraction expansion are considered as rational continuous approximations in the frequency domain (Deniz et al., 2020). In this study, the most commonly used oustaloup approximation approach has been used. To analyze the frequency stability of the power system, the two area HPS model is considered with the proposed TM-CASO tuned FOPID controller is considered. As the performance of TM-CASO is predominantly remarkable for several cases considered compared with other chaotic methods (SM-CASO and LM-CASO) of tuning FOPID controller. By applying the oustaloup approximation method for $\omega \in [10^{-2},10^{2}]$ and N=4 to convert the FO transfer function (FOTF) to the integer-order transfer function. The order of transfer function after approximation reaches 48 as given in appendix A and it is difficult to analyse the system stability for high order system. Hence, the higher-order plant transfer function is reduced to a second-order transfer function using the Hankel norm method (Veerasamy et al., 2020). The steps to reduce the higher order system is explained briefly in appendix A. The reduced lower order transfer function obtained using Hankel method for all the control techniques can be expressed as follows:

$$CLTF_{TM\text{-}CASO} = \frac{0.5987s^2+2.103s+4.38}{s^2+9.852s+15.29} \tag{4.2}$$

$$CLTF_{LM\text{-}CASO} = \frac{1.35s^2 + 6.403s + 0.8}{6.23s^2 + 33.02s + 0.84} \tag{4.3}$$

$$CLTF_{SM\text{-}CASO} = \frac{0.583s^2 + 8.35s + 2.86}{8.95s^2 + 0.85s + 85.6} \tag{4.4}$$

Figure 4.10 represents the frequency response plot of two-area HPS model considered. The bode analysis response shows that the closed-loop system is stable for the proposed TM-CASO tuned FOPID controller. Similarly, the stability has been proven for other compared control techniques as shown in Figure 4.10.

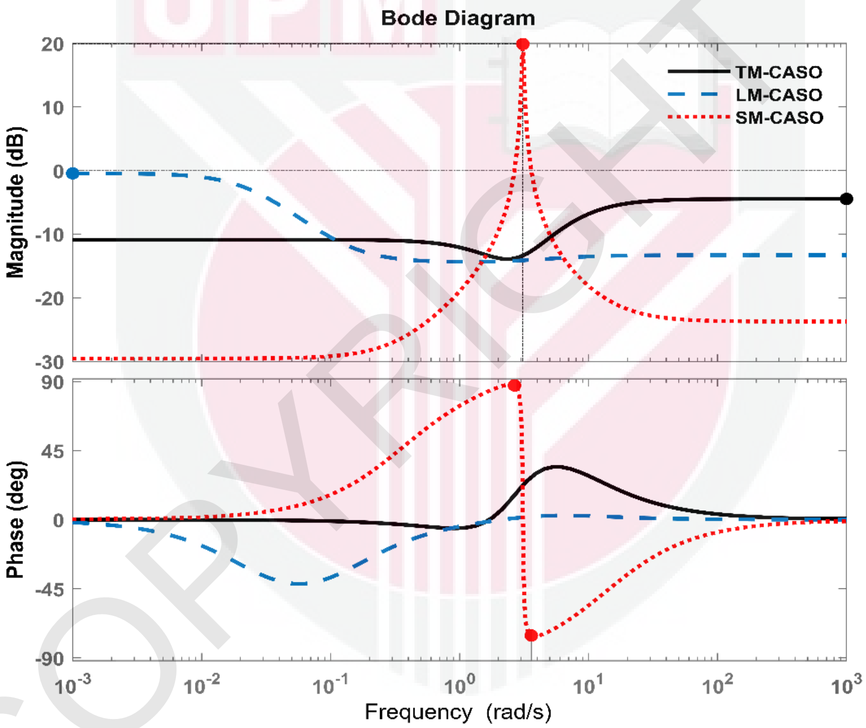

Figure 4.10 : Bode stability analysis

4.3 Simulation Results of AS-PSO Optimized Decentralized Controller

In this section, the performance of the proposed hybrid AS-PSO algorithm performance is initially tested for standard benchmark functions to validate its effectiveness and applicability for real-time optimization problems than the technique presented in the literature. Furthermore, the robustness is examined for the real-time optimization problem of modern energy systems frequency control. To study this, a three unequal area interconnected energy system under the deregulated environment with NLFOPID controller is used to normalize the frequency within the acceptable limit of ± 0.2 Hz. The forthcoming subsections describe the results of the hybrid AS-PSO technique in detail.

4.3.1 Validation of Statistical Functions

This section presents the performance of the AS-PSO technique for general classical benchmark functions, and the results have been compared with the ASO and PSO to provide a fair assessment of its efficiency. The various benchmark functions utilized in this study are Step, Schwefel 2.22, Rastrigin, Griewank, and Kowalik. The descriptions of these benchmark functions, including their mathematical formulation, constraints, and optimal value, can be seen in Table 4.7. Among these five functions (F1 to F5), F1 and F2 are single-peak functions. These functions have a single global optimum solution. On the flip side, F3–F5 are multipeak functions characterized by the presence of many local extremums. The various initialization parameters assumed for testing the optimization technique are as follows: population size is set to be 50, and the maximum number of iterations is set as 500. The code was developed in the MATLAB platform in a PC with the following characteristics: Intel Core i5-4810MQ CPU, 3.20 GHz and 16 GB RAM. Each benchmark function has been run for 30 trial runs, and the statistical findings obtained are shown in Table 4.8, which depicts the best, maximum (max), minimum (min), mean, and standard deviation (Std) values. Figure 4.11 illustrates the convergence curves of the benchmark functions considered. It is inferred from the results that the proposed AS-PSO algorithm minimizes the fitness function optimally with its predominant exploration and exploitation characteristics than the ASO and PSO technique. Furthermore, the minimum value of Std shows that the proposed method for all the benchmark functions provides maximum consistency.

Table 4.7 : Statistical functions considered for experimentation

Name		Function	Dimension (d)	Range	Optimum
Step	F1	$f(x)=\sum_{i=1}^{d}(x_i+0.5)^2$	30	[-100,100]	0
Schwefel 2.22	F2	$f(x)=\sum_{i=1}^{d}\lvert x_i\rvert+\prod_{i=1}^{d}\lvert x_i\rvert$	30	[-10,10]	0
Rastrigin	F3	$f(x)=\sum_{i=1}^{d}[x_i^2-10\cos(2\pi x_i)+(x_i-1)^2]$	30	[-5.12,5.12]	0
Griewank	F4	$f(x)=\sum_{i=1}^{d}\frac{x_i^2}{4000}-\prod_{i=1}^{d}\cos\left(\frac{x_i}{\sqrt{i}}\right)+1$	30	[-600,600]	0
Kowalik	F5	$f(x)=\sum_{i=1}^{d}\left(a_i-\frac{x_1(b_i^2+b_i x_2)}{b_i^2+b_i x_3+x_4}\right)$	4	[-5,5]	0.0003

Table 4.8 : Comparative results of statistical functions

	Value	AS-PSO	ASO	PSO
F1	Best	**-8.93E+03**	-1.19E+04	-1.07E+07
	Mean	**-7.35E+04**	2.80E+02	5.60E+05
	Std	**6.98E+03**	2.81E+02	8.95E+03
	Execution Time	**2.324**	6.89	9.23
F2	Best	**0**	1.25E-3	1.35
	Mean	**6.56E-04**	1.86E-02	2.5
	Std	**3.61E-03**	1.98E-02	3.2
	Execution Time	**4.534**	9.58	9.25
F3	Best	**2.83E-18**	5.98E-05	5.95E-6
	Mean	**1.68E-23**	6.83E-04	6.74E-05
	Std	**6.75E-25**	1.38E-03	2.58E-03
	Execution Time	**5.32**	4.53	4.32
F4	Best	**0**	1.26E-03	0.87
	Mean	**6.86E-25**	1.81E-02	1.04E-02
	Std	**3.62E-03**	1.96E-03	1.85E-03
	Execution Time	**4.47**	4.25	4.18
F5	Best	**0.01**	0.03	0.92
	Mean	**0.014**	0.0160	1.56
	Std	**0.0096**	0.02	5.87
	Execution Time	**0.39**	5.89	9.58

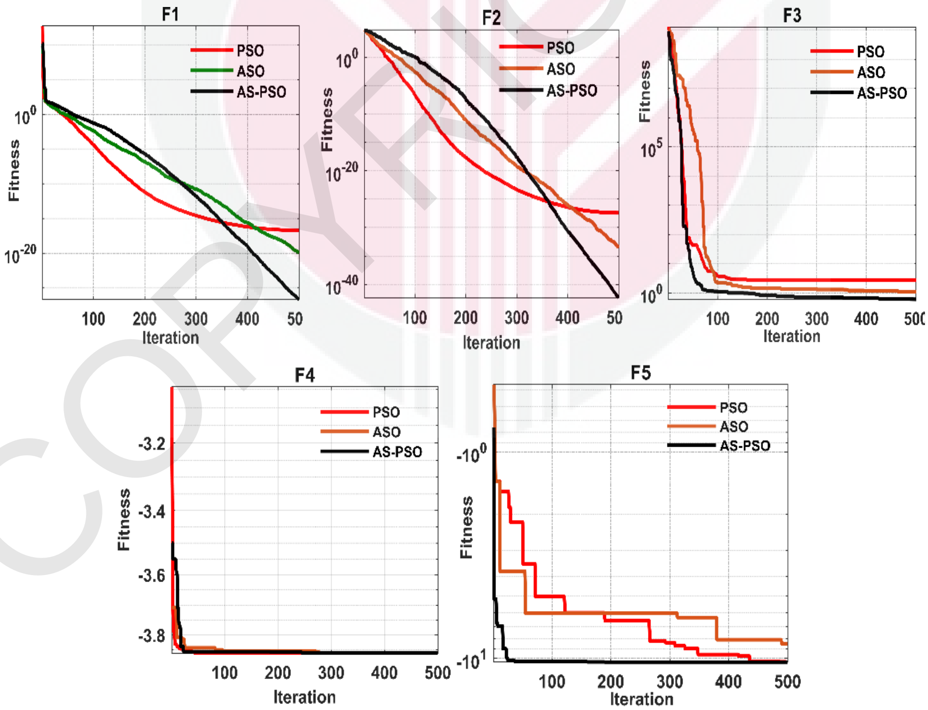

Figure 4.11 : Convergence curves of the benchmark functions

4.3.2 Time Domain Analysis of Deregulated Energy System

In this section, the real-time applicability of proffered AS-PSO technique has been applied for tuning the decentralized NLFOPID controller in the deregulated energy system with different generating sources, as shown in Figure 3.15. The robustness of the AS-PSO technique has been analyzed for various operating cases of an energy system based on contracts made between the consumer (DISCO) and prosumer (GENCO).

a. Case 1: Bilateral Transaction

In this scenario, DISCOs can contract with any GENCO in their or other control areas based on their selling price. In this case, all DISCOs contract for power with all available GENCOs by accepting the contract and this is clearly seen in DPM depicted in Equation (4.5). A large step load change of 0.05 p.u. M.W. is demanded by each DISCOs from GENCOs.

$$DPM_{Bilateral} = \begin{bmatrix} 0.2 & 0.2 & 0.1 & 0.2 & 0.2 & 0.2 \\ 0.2 & 0.2 & 0.1 & 0.1 & 0.2 & 0.1 \\ 0.1 & 0.2 & 0.2 & 0.2 & 0.2 & 0.2 \\ 0.1 & 0.1 & 0.2 & 0.2 & 0.1 & 0.2 \\ 0.2 & 0.1 & 0.2 & 0.2 & 0.1 & 0.2 \\ 0.2 & 0.2 & 0.2 & 0.1 & 0.2 & 0.1 \end{bmatrix} \tag{4.5}$$

For the DPM in Equation (4.5), the actual power to be generated by GENCOs is calculated using Equation (3.32). Rewriting the equation gives,

$$\begin{aligned} \Delta P_{GENCO\text{-}i,bilateral} = & cpf_{i1}\Delta P_{L,1} + cpf_{i2}\Delta P_{L,2} + cpf_{i3}\Delta P_{L,3} \\ & + cpf_{i4}\Delta P_{L,4} + cpf_{i5}\Delta P_{L,5} + cpf_{i6}\Delta P_{L,6} \end{aligned} \tag{4.6}$$

By using the Equation (4.6), the power generation of GENCOs are calculated as follows:

$$\begin{aligned} \Delta P_{GENCO\text{-}1,bilateral} & = (0.2+0.2+0.1+0.2+0.2+0.2)\times 0.05 \\ & = 0.055 \text{ p.u. M.W} \end{aligned} \tag{4.7}$$

Similarly, for GENCO-2 = 0.045 p.u. M.W, GENCO-3 = 0.055 p.u. M.W, GENCO-4 = 0.045 p.u. M.W, GENCO-5= 0.05 p.u. M.W, and GENCO-6= 0.05 p.u. M.W. Also, the change in scheduled tie-line power exchange is calculated using Equation (3.33). Rewriting the equation results in,

$$\begin{aligned} \Delta P_{tie12,scheduled} = & \left(cpf_{13}\Delta P_{L,3} + cpf_{14}\Delta P_{L,4} + cpf_{23}\Delta P_{L,3} + cpf_{24}\Delta P_{L,4}\right) \\ & -\left(cpf_{31}\Delta P_{L,1} + cpf_{32}\Delta P_{L,2} + cpf_{41}\Delta P_{L,1} + cpf_{42}\Delta P_{L,2}\right) \end{aligned} \tag{4.8}$$

$$
\begin{aligned}
\Delta P_{\text{tie12,scheduled}} &= \left(0.1\times 0.05+0.2\times 0.05+0.1\times 0.05+0.1\times 0.05\right) \\
&\quad -\left(0.1\times 0.05+0.2\times 0.05+0.1\times 0.05+0.1\times 0.05\right) \\
&= 0\,\text{p.u.M.W}
\end{aligned}
\tag{4.9}
$$

Similarly, for $\Delta P_{\text{tie23, scheduled}}=\Delta P_{\text{tie13, scheduled}}=0$ p.u. M.W. The apf for each GENCOs is calculated using the procedure given by Parida et al., (2005). The apfs are $apf_{11}=0.55$, $apf_{12}=0.45$, $apf_{21}=0.55$, $apf_{22}=0.45$, $apf_{31}=0.5$ and $apf_{32}=0.5$, respectively.

In this scenario, the proposed AS-PSO optimized the NLFOPID controller of a decentralized deregulated system, and the performance was compared with conventional ASO and PSO algorithms. The gain values obtained while optimizing the control objective of ITAE using the various algorithms are given in Table 4.9. The dynamic response frequency, tie-line power variation and deviation of power in GENCOs of Decentralized Deregulated Energy System (DDES) are recorded and presented in Figure 4.12. It is clearly observed from the results that the initial dynamic oscillations of frequency response are less with minimum ST for NLFOPID than the linear FOPID controller and other methods of tuning NLFOPID controller even though the proffered technique has more PO. Figure 4.13 portrays the steady-state PIs of IAE, ITAE, ISE, ITSE, SE, CE, ST, and PU, which indicates that the proposed controller performs better than the FOPID controller and other control techniques. Moreover, the PIs like ST, CE, and SE are improved by 38.6 % to 75.2 %, 5 % to 36 %, and 7 % to 43 %, using AS-PSO tuned NLFOPID controller than other methods. Similarly, the ITAE, IAE, ITSE and ISE are substantially increased by an amount of 15 % to 35 %, 7 % to 21 %, 12 % to 28 %, and 10 % to 22 %, respectively, by the suggested method than other techniques. However, during real time implementation, when sudden uncertainties happen in the power system, the proposed NLFOPID controller responds with large control actions which leads to undesirable effects, such as instability or oscillations in the power system.

Table 4.9 : Tuned gain values of the controller during the bilateral transaction of the deregulated energy system

Proffered controller and tuning methods		Bilateral transaction					
		k_p	k_d	μ	k_i	λ	A_n
AS-PSO: NLFOPID	Area-1	-1.8986	-1.7428	0.9830	1.2267	0.1749	0.6632
		-6.7359	-7.7695	0.6865	-10	0.9898	0.3252
	Area-2	2.6214	-0.6748	0.8081	-4.8424	0.6188	0.9852
		4.2342	-3.1483	0.7337	-7.8071	0.5091	0.1058
	Area-3	9.1559	-7.6121	0.1453	-4.6193	0.7495	0.6256
		-1.4264	1.2584	0.1575	4.0745	0.4283	0.2361
ASO: NLFOPID	Area-1	-2.2382	-3.8050	0.8494	-3.5732	0.8530	0.4213
		1.1311	-2.3482	0.7074	-3.0796	0.5404	0.6235
	Area-2	0.6603	3.0096	0.5380	0.0783	0.5546	0.114
		0.3714	-1.3265	0.4001	-1.2427	0.5853	0.1575
	Area-3	0.7474	-3.4447	0.6440	-3.3418	0.7103	0.5542
		-3.6618	-3.6150	0.5360	3.8745	0.6234	0.989
PSO: NLFOPID	Area-1	-1.5392	-2.2831	0.8384	-4.3269	0.8687	0.1201
		1.2063	-2.0583	0.6514	-2.8442	0.5380	0.7852
	Area-2	1.6428	-2.7862	0.6195	-3.0451	0.3705	0.8526
		-1.8471	-3.3611	0.9887	-5.7437	0.1030	0.527
	Area-3	1.5010	-3.3925	0.9037	-5.5708	0.8653	0.2532
		-0.2149	-5.1379	0.8963	-5.2342	0.9194	0.9632
AS-PSO: FOPID	Area-1	0.5690	-1.8709	0.8017	-2.9053	0.6278	
		-0.2285	-0.6989	0.5400	-2.8101	0.9214	
	Area-2	0.6707	-1.4210	0.6932	0.0911	0.3626	
		0.3304	-1.3463	0.8198	-1.4852	0.6689	
	Area-3	-0.1087	0.5238	0.2664	-1.0216	0.4384	
		-0.6813	2.0155	0.5030	1.4075	0.1889	

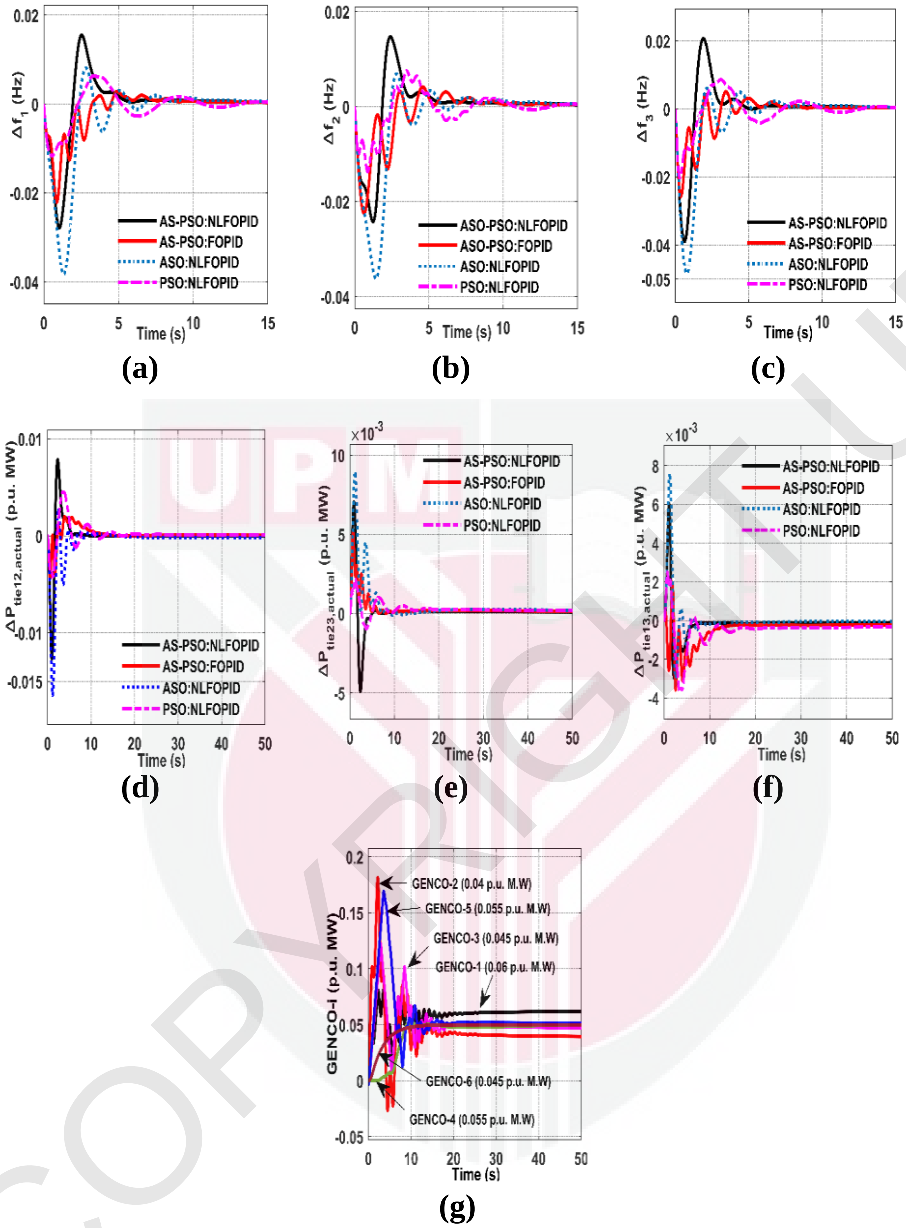

Figure 4.12 : System dynamic response in bilateral-based transaction (a) frequency deviation in area-1 (b) frequency deviation in area-2 (c) frequency deviation in area-3 (d) tie-line power deviation in area-1 (e) tie-line power deviation in area-2 (f) tie-line power deviation in area-3 (g) power generation of GENCOs

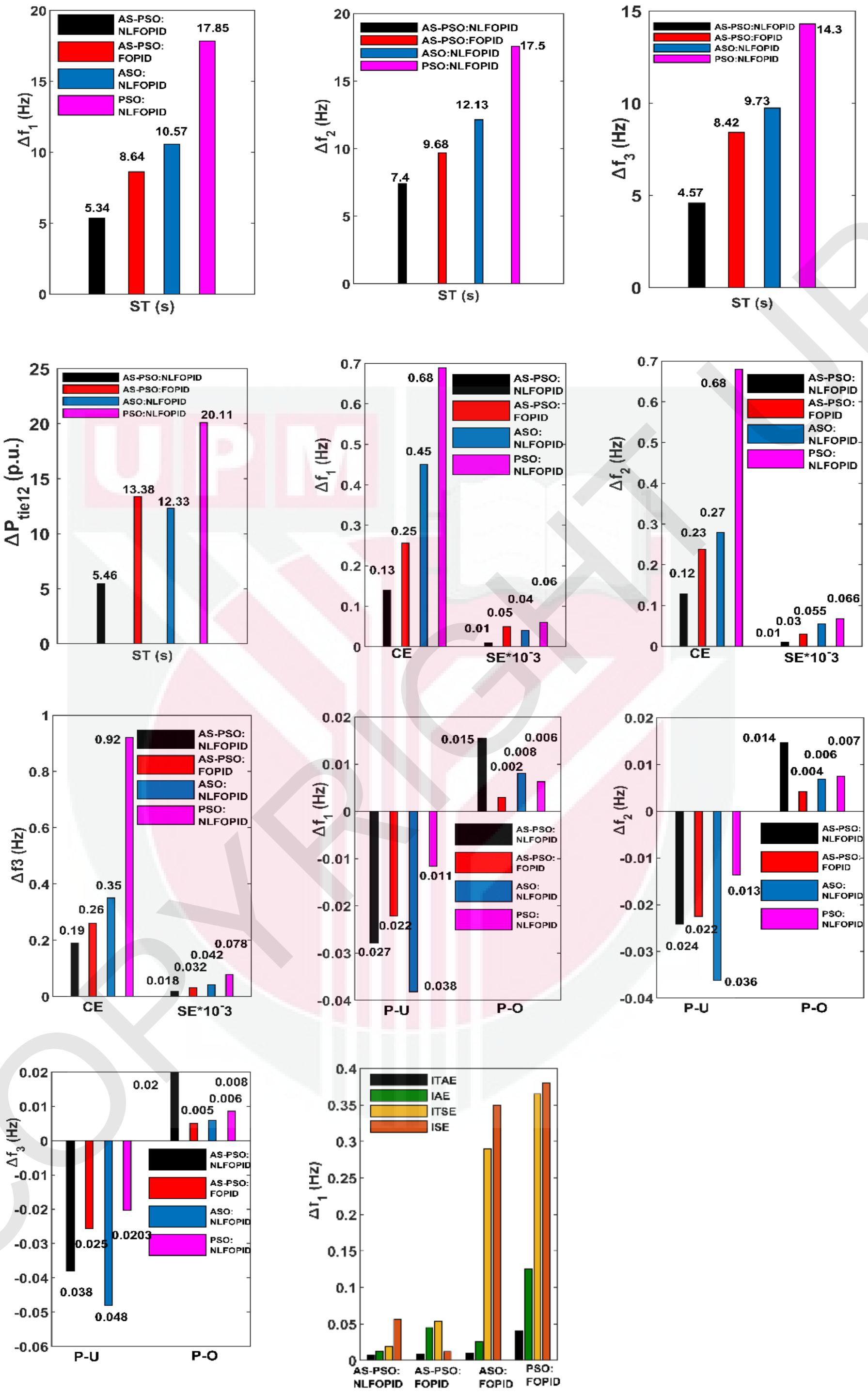

Figure 4.13 : Measured performance indices during bilateral transactions among GENCOs and DISCOs

b. Case 2: Poolco Transaction

In this case, the GENCOs trade the energy within the energy pool, i.e., DISCOs participate in the trading within the same control area. The DPM calculation during this scenario is given in Equation (4.10), depicting the area participation factor (apf) values within the same area as fractional values representing the fraction of power demanded from the generator in the respective area. For instance, area-1 DISCOs only request load from area-1 GENCOs, not from area-2 and area-3. For each DISCOs, a load demand of 0.05 p.u. M.W. is considered.

$$DPM_{Poolco} = \begin{bmatrix} 0.6 & 0.5 & 0 & 0 & 0 & 0 \\ 0.4 & 0.5 & 0 & 0 & 0 & 0 \\ 0 & 0 & 0.4 & 0.5 & 0 & 0 \\ 0 & 0 & 0.6 & 0.5 & 0 & 0 \\ 0 & 0 & 0 & 0 & 0.7 & 0.4 \\ 0 & 0 & 0 & 0 & 0.3 & 0.6 \end{bmatrix} \tag{4.10}$$

The apfs in area-1 apf_{11}=0.6, apf_{12}=0.4, in area-2 apf_{21}=0.45, apf_{22}=0.55, and in area-3 apf_{31}=0.55 and apf_{32}=0.45. Under a steady state, the generation of GENCOs must be sufficient to meet the demand of the DISCOs that have contracted with it. The real power generated by each GENCOs is calculated using Equation (4.6) as follows.

$$\Delta P_{GENCO\text{-}1,Poolco} = (0.6+0.5+0+0+0+0)\times 0.05 \;=\; 0.06 \text{ p.u. M.W} \tag{4.11}$$

Similarly, for GENCO-2 = 0.04 p.u. M.W, GENCO-3 = 0.045 p.u. M.W, GENCO-4 = 0.055 p.u. M.W, GENCO-5 = 0.055 p.u. M.W, and GENCO-6 = 0.045 p.u. M.W. The time-domain response of frequency and tie-line response for the poolco transaction of DDES is shown in Figure 4.14. It is observed that the response of the proposed NLFOPID controller optimized using AS-PSO performs better in damping the initial response faster than other techniques. Moreover, the PIs like ST, CE, and SE is significantly minimized by appropriately tuning the control gain values through optimizing the J_{ITAE} of DDES, as shown in Figure 4.15.

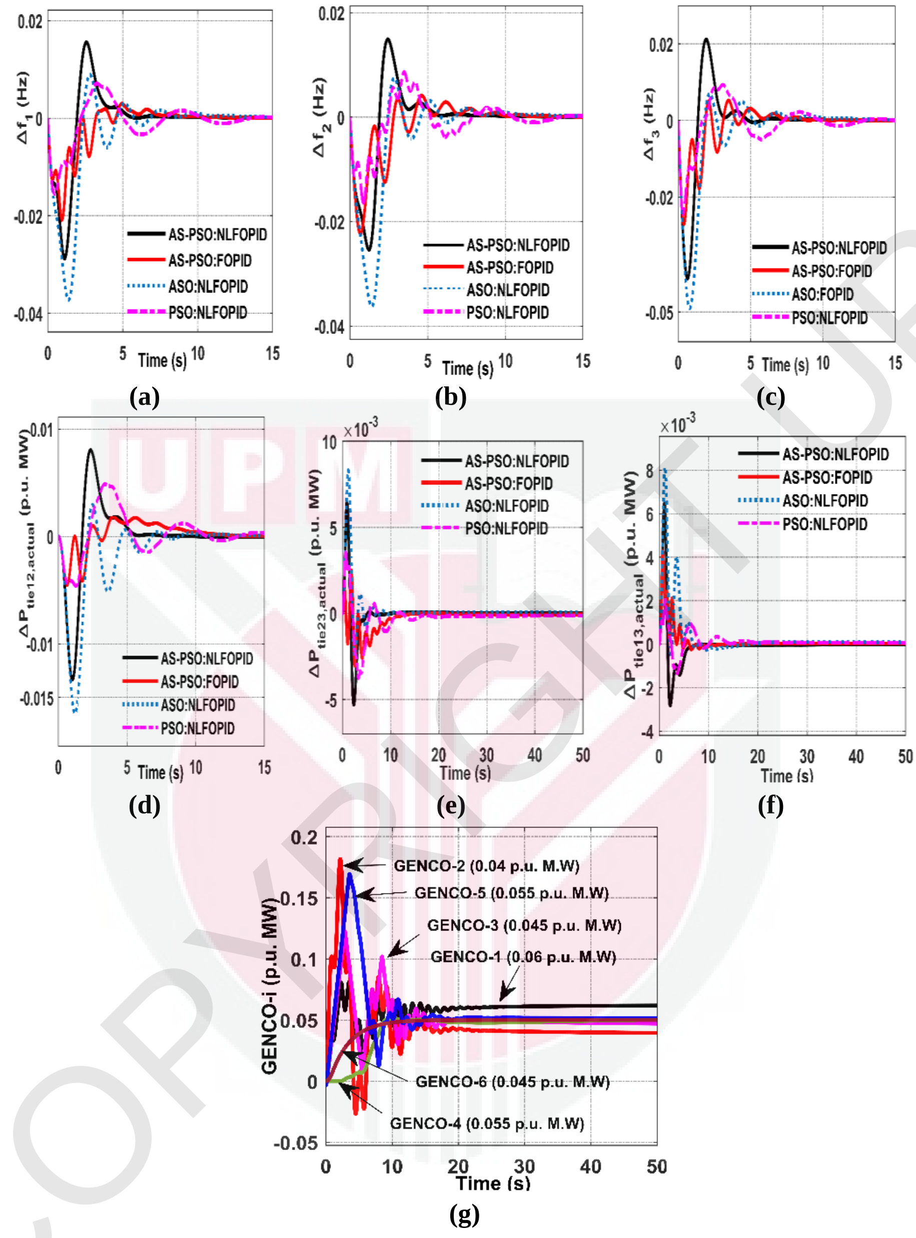

Figure 4.14 : System dynamic response in poolco transaction (a) frequency variation in area-1 (b) frequency variation in area-2 (c) frequency variation in area-3 (d) tie-line power deviation in area-1. (e) tie-line power deviation in area-2 (f) tie-line power deviation in area-3 (g) power generation of GENCOs

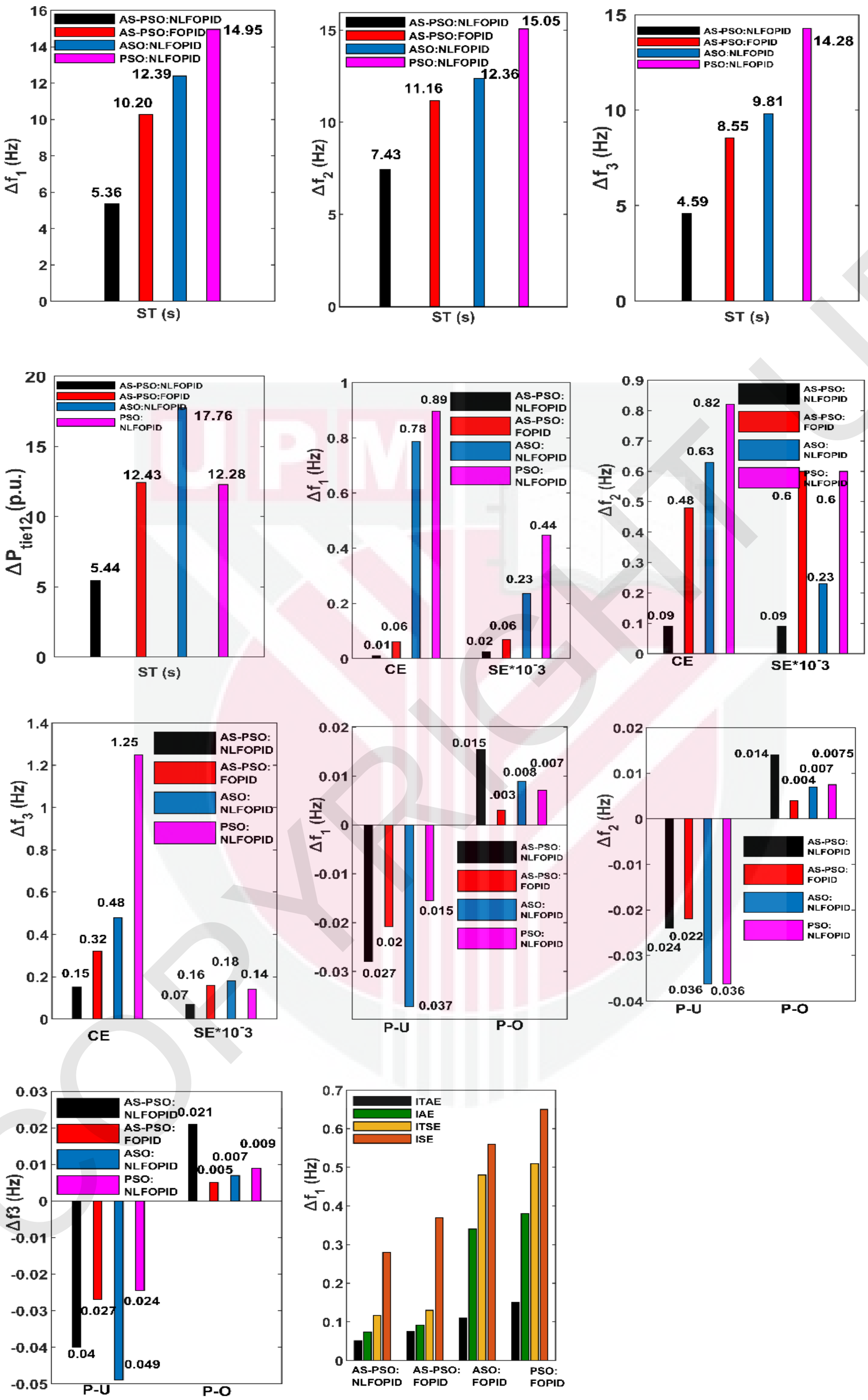

Figure 4.15 : Measured performance indices under poolco transaction

c. Case 3: Contract Violation

In this case, a DISCO participating in energy trading may violate a contract by demanding more power than the one specified in the contract. To study this scenario, the $DPM_{Bilateral}$ given in Equation (4.5) is considered to emulate the contract violation by the DISCOs. For instance, consider the case of DISCO-1 and DISCO-3 breaching a contract by demanding an additional power of 0.01 p.u. MW. This excess energy needs to be traded by the GENCOs in the respective area as the DISCO. This power should be reflected as an area's local demand, not as a contract demand. So, the local load of area-1 and area-2 is calculated using Equation (3.35) is given below,

$$\begin{aligned}\Delta P_{dm} &= \text{load of DISCO-1 (0.05)+load of DISCO-2 (0.05)+0.01} \\ &= 0.11 \text{ p.u. M.W}\end{aligned} \tag{4.12}$$

$$\begin{aligned}\Delta P_{dm} &= \text{load of DISCO-3 (0.05)+load of DISCO-4 (0.05)+0.01} \\ &= 0.11 \text{ p.u. M.W}\end{aligned} \tag{4.13}$$

In this case, the local demand for area-3 remains the same (0.1 p.u.). For the above $DPM_{Bilateral}$, the actual power to be generated by GENCOs for contract violation is calculated using Equation (3.32).

$$\begin{aligned}\Delta P_{\text{GENCO-i,contract violation}} = &\begin{pmatrix} cpf_{i1}\Delta P_{L,1} + cpf_{i2}\Delta P_{L,2} + cpf_{i3}\Delta P_{L,3} + cpf_{i4}\Delta P_{L,4} + \\ cpf_{i5}\Delta P_{L,5} + cpf_{i6}\Delta P_{L,6} \end{pmatrix} \\ &+ \left(apf_{i1} \times \text{uncontracted load demand}\right)\end{aligned} \tag{4.14}$$

By using the above equation, the power generation of GENCOs are calculated as follows**:**

$$\begin{aligned}\Delta P_{\text{GENCO-1,contract violation}} &= \left(0.2+0.2+0.1+0.2+0.2+0.2\right)+\left(0.05\times 0.01\right) \\ &= 0.0605 \text{ p.u. M.W}\end{aligned} \tag{4.15}$$

Similarly, for GENCO-2 = 0.505 p.u. M.W, GENCO-3 = 0.0605 p.u. M.W, GENCO-4 = 0.0495 p.u. M.W, GENCO-5= 0.05 p.u. M.W, and GENCO-6= 0.05 p.u. M.W. Also, the change in scheduled tie-line power exchange is calculated using Equation (3.33).

$$\begin{aligned}\Delta P_{\text{tie12,scheduled}} = &\left(cpf_{13}\Delta P_{L,3} + cpf_{14}\Delta P_{L,4} + cpf_{23}\Delta P_{L,3} + cpf_{24}\Delta P_{L,4}\right) \\ &-\left(cpf_{31}\Delta P_{L,1} + cpf_{32}\Delta P_{L,2} + cpf_{41}\Delta P_{L,1} + cpf_{42}\Delta P_{L,2}\right)\end{aligned} \tag{4.16}$$

$$\begin{aligned}\Delta P_{\text{tie12,scheduled}} &= \left(0.1\times 0.05 + 0.2\times 0.05 + 0.1\times 0.05 + 0.1\times 0.05\right) \\ &-\left(0.1\times 0.05 + 0.2\times 0.05 + 0.1\times 0.05 + 0.1\times 0.05\right) \\ &= 0 \text{ p.u.M.W}\end{aligned} \tag{4.17}$$

Similarly, for $\Delta P_{tie23,\ scheduled}=\Delta P_{tie13,\ scheduled}=0$ p.u. M.W. To examine the efficacy of the proffered hybrid technique, the controller tuned during the bilateral transaction is used for this scenario. The transient response of frequency and tie-line power aberrations are portrayed in Figure 4.16. From the response, the performance of the intended hybrid AS-PSO tuned NLFOPID controller outperforms predominantly than FOPID controller and other tuned techniques. As the contract violation emulated the sudden increase in load demand of area-1 and area-2, which shows a gradual rise in the undershoot of Δf_1 and Δf_2 then compared to the response during the bilateral transaction. Moreover, the transient PIs like CE and SE values are also increased moderately, as shown in Figure 4.17. However, the proposed AS-PSO optimized NLFOPID controller gives optimal transient performance even after an uncertain increase in load demand over FOPID controllers and other tuning methods. It is evident from the various cases that the proffered control approach is robust to any change in load demand or uncertainty, and the controller need not be re-tuned for any changes in the system operating conditions.

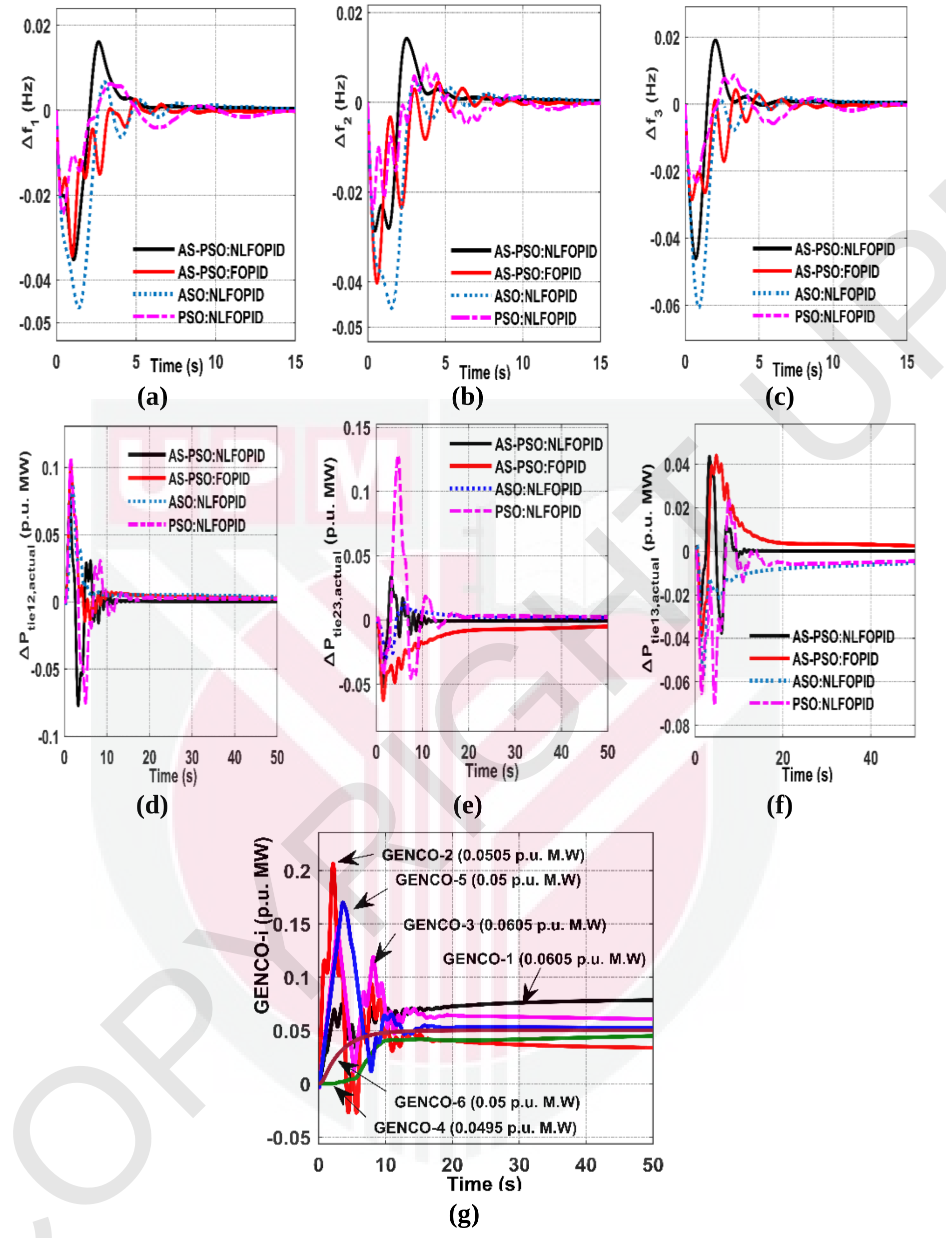

Figure 4.16 : System dynamic response under contract violation (a) frequency deviation in area-1 (b) frequency deviation in area-2 (c) frequency deviation in area-3 (d) tie-line power deviation in area-1 (e) tie-line power deviation in area-2 (f) tie-line power deviation in area-3 (g) power generation of GENCOs

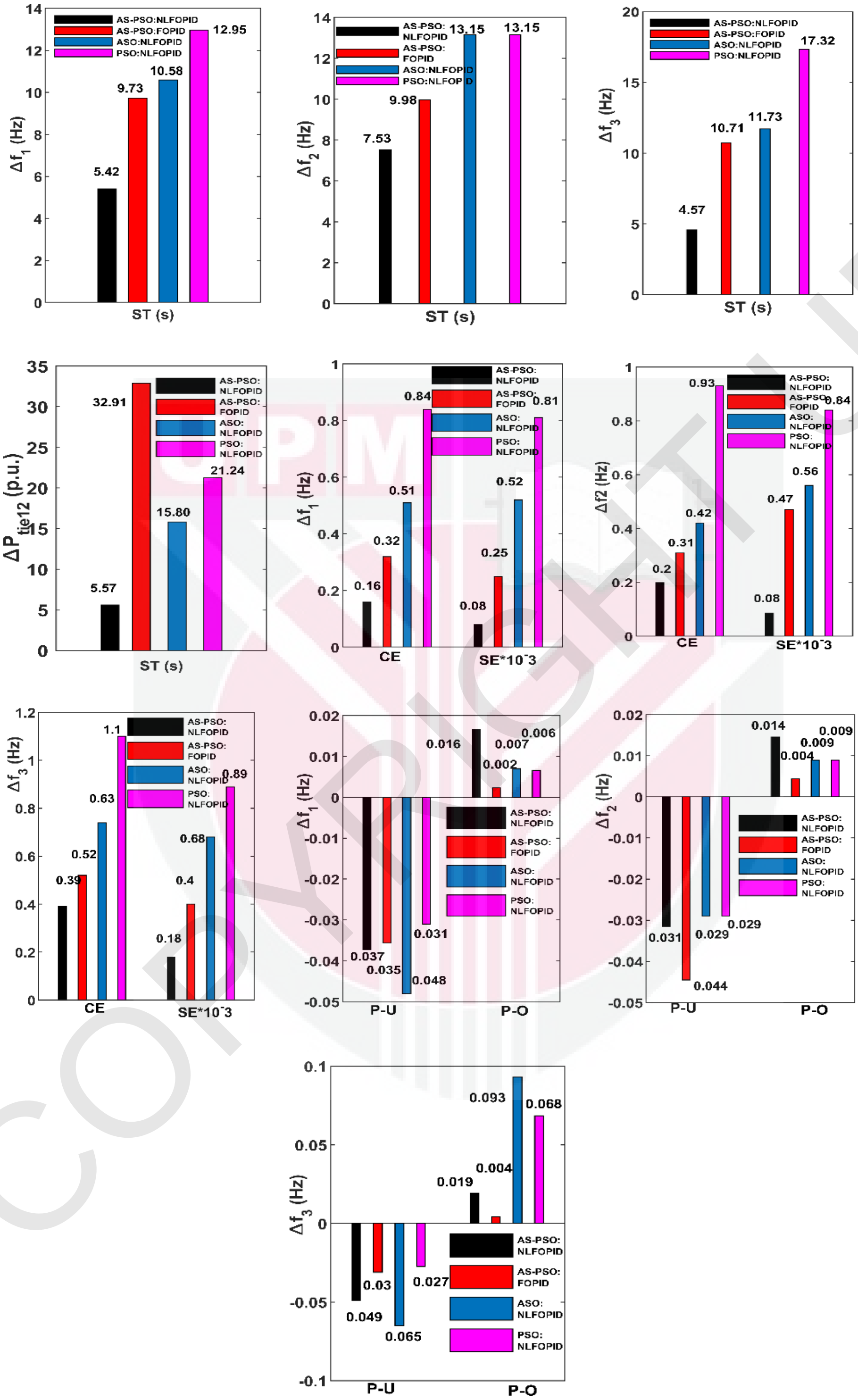

Figure 4.17 : Measured performance indices under contract violation

4.3.3 Robustness Validation under Different Conditions

In this case, the robustness of the proposed NLFOPID controller is examined by applying different types of load patterns and real time variation of RES in the deregulated energy system.

a. Robustness Analysis under Various Load Patterns

A realistic load pattern is developed by combining step load change (e.g., loss of a generating system and rapid switching offload) and ramp load change (e.g., industrial load provides a random shift in the fast load change like the motor pick-up). A combination of high random load change (industrial load), medium random load change (official load), and low random load change (residential load) is therefore considered as a realistic load. The pattern of the realistic load is given in Figure 4.18 (a), with the corresponding dynamic response of $\Delta f1$ is presented in Figure 4.18 (b), (c) and (d). It is interpreted that AS-PSO tuned NLFOPID controller has a better and smoother response with minimum ST. Moreover, a zoomed view of each figure shows that the proposed method has reached the steady-state value before the linear FOPID controller and other control techniques.

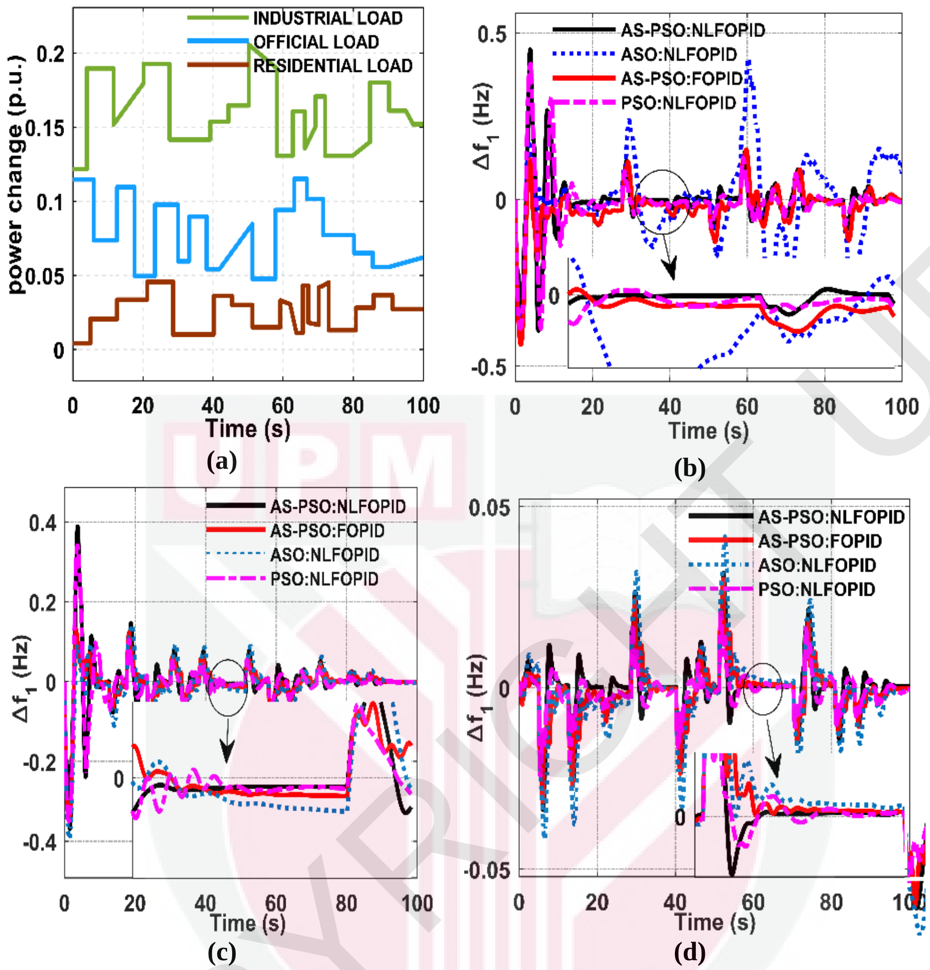

Figure 4.18 : (a) Different realistic load patterns (b) frequency response in area-1 under industrial load (c) frequency response in area-1under official load (d) frequency response in area-1under residential load.

b. Robustness Analysis Against Stochastic Variation Of RES

To further asses the robustness of the proposed AS-PSO optimized NLFOPID controller, variation in STES unit output power is considered for real-time monthly-average irradiance data at Universiti Putra Malaysia (UPM) from Subang meteorological centre in Malaysia (Lurwan et al., 2016). The irradiance values from January to December 2014 for 100-time intervals of 0.3 s is presented in Figure 4.19 (a). The frequency response for the variation in solar irradiance is given in Figure 4.19 (b), (c) and (d). It is observed that AS-PSO optimized NLFOPID has minimum frequency oscillations with less SE compared to other techniques presented. Thus, overall, it is seen that AS-PSO optimized NLFOPID performs remarkably to regulate the system frequency to steady state under real-time variation in STES.

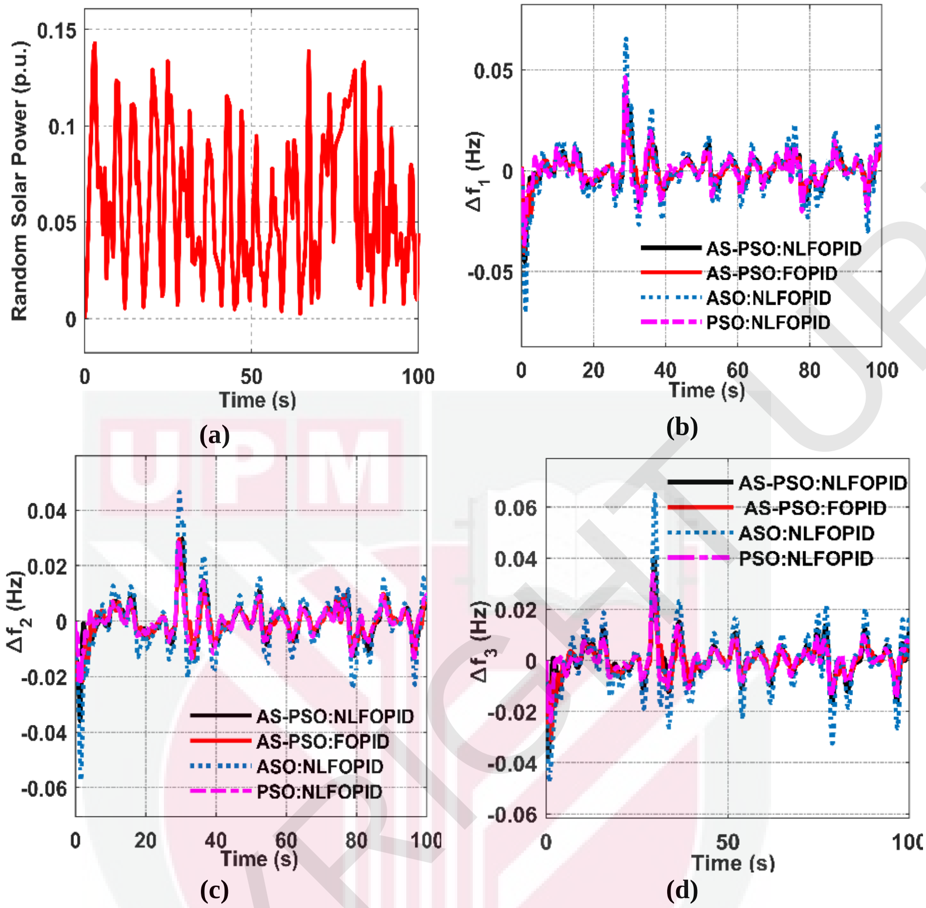

Figure 4.19 : (a) Solar power profile (b) frequency response in area-1 under real time solar variation (c) frequency response in area-2 under real time solar variation (d) frequency response in area-3 under real time solar variation

4.3.4 Convergence Cost

The convergence behavior of the proposed AS-PSO algorithm is compared with the ASO and PSO techniques of tuning the decentralized NLFOPID controller for three unequal area-deregulated systems to assess the computational complexity of the suggested method. Figure 4.20 depicts the convergence curve representing the proposed hybrid strategy converging to a lower cost value with lesser iterations than ASO and PSO. Based on these results, the AS-PSO optimizer outperforms in terms of obtaining a better solution with faster exploitation and attaining an equal tradeoff between exploration and exploitation to avoid being confined to local minima.

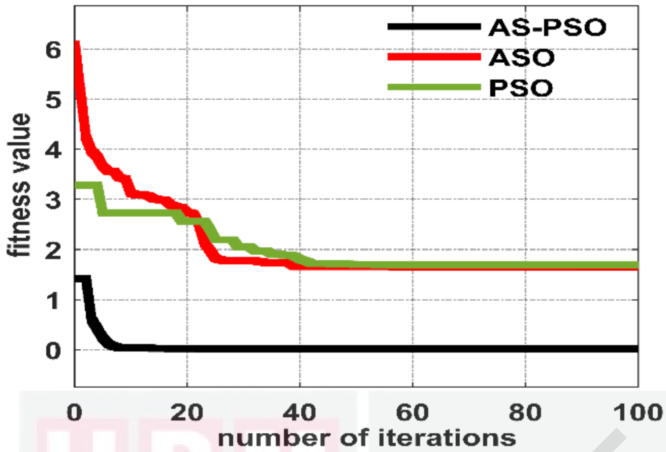

Figure 4.20 : Convergence curve

4.3.5 Proof on Stability

To examine the stability of three unequal DDES models operating in a bilateral transaction scenario is considered. The stability analysis is carried out by applying the improved oustaloup approximation method by selecting $\omega_b = 0.01$, $\omega_h = 1000$, the weight coefficients of b= 10 and d=9 (Kumar et al., 2022). The integer order transfer function, after applying improved oustaloup approximation for the proposed AS-PSO optimized NLFOPID and other compared optimization methods has a transfer function order of 12. However, it is hard to investigate the stability of the system for a much higher-order system. Hence, a model order reduction technique of the Hankel norm approach is used to reduce the higher-order into a second-order transfer function using a detailed procedure discussed in the previous study (Veerasamy et al., 2020). The transfer function obtained using the Hankel approach for the proposed method is given as G_1, the AS-PSO tuned FOPID controller reduced order transfer function is given as G_2, ASO optimized NLFOPID as G_3 and PSO tune NLFOPID as G_4 as illustrated in Equations (4.18) - (4.21):

$$G_1 = \frac{2.1517s + 0.788}{s^2 + 2.13s + 21.2} \tag{4.18}$$

$$G_2 = \frac{0.06768s^2 - 8.918s + 2.535s \times 10^{-13}}{s^2 + 8.885s + 35.49} \tag{4.19}$$

$$G_3 = \frac{-0.0144s^2 - 5.864s + 1.989 \times 10^{-11}}{s^2 + 23.15s + 141} \tag{4.20}$$

$$G_4 = \frac{-0.08989s^2 - 1.696s + 1.38 \times 10^{-12}}{s^2 + 4.75s + 35.99} \tag{4.21}$$

Figure 4.21 shows the frequency response through bode analysis. It is seen in the response that the proposed method has a gain and phase margin of $g_m=\infty$, $p_m=166.50$ degrees. According to the stability theory of control, if the $g_m=\infty$, it means that the system can tolerate any amount of gain without becoming unstable, and this is because the phase margin is sufficient to keep the system stable. Moreover, the proposed method bode plot has a higher phase margin which means it is more stable and have a better ability to reject disturbances.

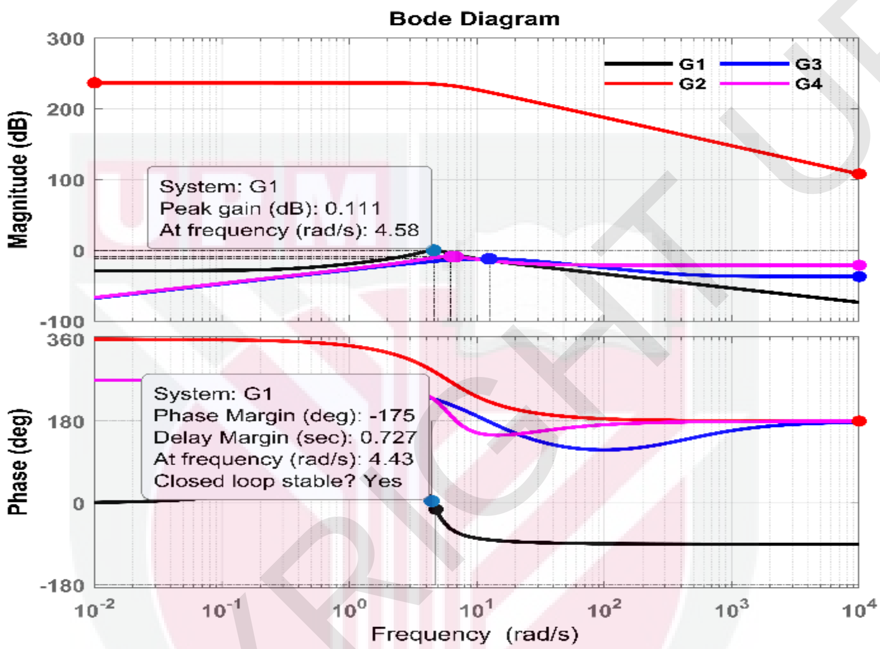

Figure 4.21 : Bode stability analysis

4.3.6 Experimental Validation Using RTDS

Experimental validation of the proposed AS-PSO optimized NLFOPID controller of DDES is implemented in real-time using a real-time digital simulator through hardware-in-the-loop simulation in OPAL-RT. An OP4510 is an entry-level simulator that combines the RT-high-performance LAB's Rapid Control Prototyping and HIL system core features and is used for implementation. It offers 128 fast I/O channels with signal conditioning, extra RS422 channels, and high-speed connection connectors, and it is completely integrated with MATLAB/ SimPower System. Combining upscaled Intel multi-core processors with efficient Kintex 7 FPGA gives more simulation power and sub-microsecond simulation time steps. The three unequal areas of DDES during bilateral transaction scenario is considered for the purpose of validation. Figure 4.22 shows the response of frequency and tie-line power deviations measured using RTDS through an oscilloscope. The result reveals that the frequency deviations of three control areas and tie-line power variation obtained using MATLAB simulation agree with the RTDS response.

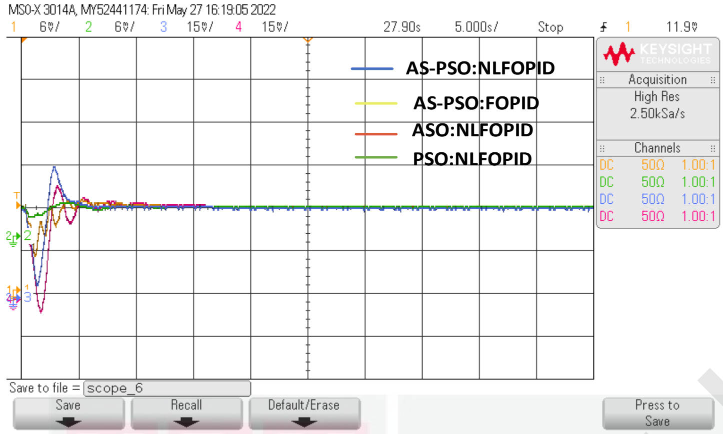

(a)

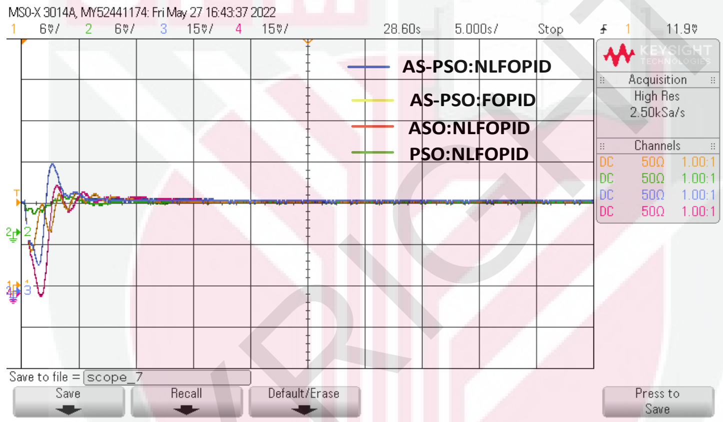

(b)

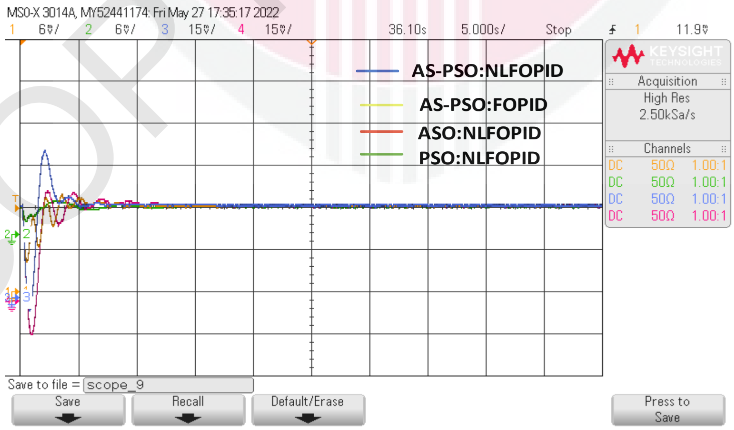

(c)

Figure 4.22 : RTDS output of DDES during bilateral transaction (a) frequency response of area-1 (b) frequency response of area-2 (c) response of area-3

4.4 Simulation Results of CAS-PSO Optimized Distributed ZND Controller

Initially, the effectiveness of the proposed distributed intelligent-based hybrid CAS-PSO algorithm is tested for six well-known standard benchmark functions. Then, the proposed distributed control strategy for NMG illustrated is studied to evaluate the effectiveness of the proposed design method for real-time application. The results are validated through different case studies and compared with other optimization techniques. Further, the considered NMG model with the control strategy is implemented in OPAL-RT OP4150 for HIL validation.

4.4.1 Benchmark Function Validation

Generally, numerous benchmark functions are available in the literature that has been used specifically for evaluating the performance of optimization algorithms. Therefore, any new algorithms proposed must be tested against them. The most standard benchmark functions used to validate the performance of the proposed CAS-PSO algorithm are given in Table 4.10. To measure the efficiency of the proffered algorithm, the authors have considered several measuring indices such as standard deviation (STD), min, execution time and best fit at each run. For the validation of benchmark functions, the population size and number of iterations are set as 50 and 500, respectively, for all the algorithms. The simulation and analyses are carried out in MATLAB platform. Each benchmark function has been run for 30 trial runs, and the benchmark findings obtained are shown in Table 4.11. The findings from the Table indicates that the proposed hybrid CAS-PSO minimizes the fitness function optimally with its predominant diversification and intensification characteristics than AS-PSO, CASO and ASO technique. Moreover, the minimal value of STD proves that the proposed strategy offers maximum consistency for all benchmark functions.

Table 4.10 : Statistical functions

Function		Formulation	Dimension (d)	Range	Global Optimum
Schwefel 2.22	F1	$F(x)=\sum_{i=1}^{d}\lvert x_i\rvert+\prod_{i=1}^{d}\lvert x_i\rvert$	30	[-100,100]	0
Quartic	F2	$F(x)=\sum_{i=1}^{d} ix_i^4+\text{random}[0,1)$	30	[-10,10]	0
Schwefel	F3	$F(x)=-\sum_{i=1}^{d}\left(x_i \sin\sqrt{\lvert x_i\rvert}\right)$	10	[-500,500]	0
Six hump camel-back	F4	$F(x)=4x_1^2-2.1x_1^4+\frac{1}{3}x_1^6+x_1x_2-4x_2^2+4x_2^4$	2	[-5,5]	-1.031
Branin	F5	$F(x)=\left(x_2-\frac{5.1}{4\pi^2}x_1^2+\frac{5}{\pi}x_1-6\right)^2$	2	[-5,5]	0.398

Table 4.11 : Comparative results of statistical functions

	Value	CAS-PSO	AS-PSO	CASO	ASO
F1	Best	0	0.01267	1.17	115.13
	Mean	0	0.0289	1.09	96.12
	STD	0	6E-07	0.016	16.93
	Execution Time	0.79	3.89	5.89	6.19
F2	Best	1.13E-58	39.07	0.00278	0.00279
	Mean	0.2246	43.56	35.77	0.002789
	STD	10.2744	10.68	54.68	4.12E-19
	Execution Time	1.58	5.61	5.72	5.23
F3	Best	0	0	0.000268	0.000275
	Mean	3.58	2.14	1944.54	0.0002718
	STD	41.44	9.95	118.84	4.34E-20
	Execution Time	0.85	1.25	5.89	7.95
F4	Best	3.64E-10	3.73E-10	4950	3549062.1
	Mean	3.64E-10	3.73E-10	133639.5	355896.2
	STD	5.36E-14	5.95E-26	1768776.5	1139708.5
	Execution Time	2.31	4.69	8.12	6.27
F5	Best	0.00024	0.00025	13.253	40.145
	Mean	0.00026	106.65	225.30	57.826
	STD	1.08E-07	235.22	322.07	49.256
	Execution Time	1.56	5.25	5.3	5.10

4.4.2 Implementation of Distributed Frequency Control of NMG System

The proposed distributed frequency control architecture for the NMG system with P2P energy trading is depicted in real time in Figure 4.23. In this work, it is assumed that each MG in the network participates in trading as prosumers, and also the aggregated EV consumers in MG 1, 2 and MG 3 act as a consumer. The prosumers and consumers are generally represented as the nodes in the blockchain network, and the MG controller is also implemented in the RPis. The RPis communicate with the PC connected to the OPAL-RT simulator via TCP/IP. Each RPis are reserved with static IP address in order to participate in the trading and connected to the RT-model of NMG using UDP. The Raspbian Stretch is used as an operating system in RPi. Furthermore, each device running on RPi operates Go Ethereum (Geth) as full authority nodes within a private instance of an Ethereum PoA blockchain. The software includes Geth, Node.js, and Web3 of versions 1.10.6, 6.14.6 and 5.12.0.py with a smart contract developed in solidity incorporating a double-auction mechanism, CPM, and secondary control, deployed on blockchain nodes. The NMG network is simulated in MATLAB/Simulink and executed in RT-LAB, with OPAL-RT handling the primary droop controller and the RPi managing secondary and supplementary control, providing power references to prosumers post-market clearing. The outcomes achieved under various scenarios are discussed as follows:

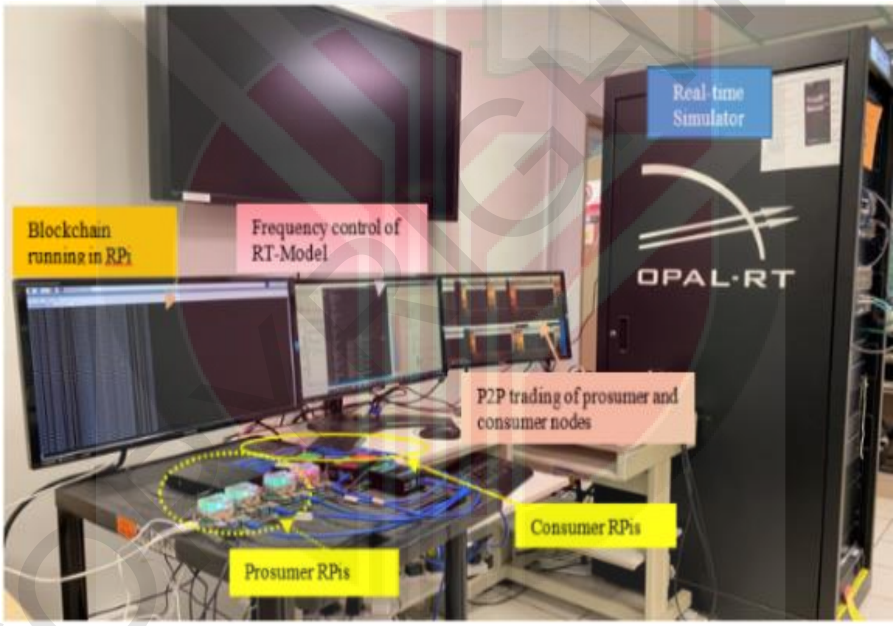

Figure 4.23 : Experimental setup for frequency control of NMG with P2P trading

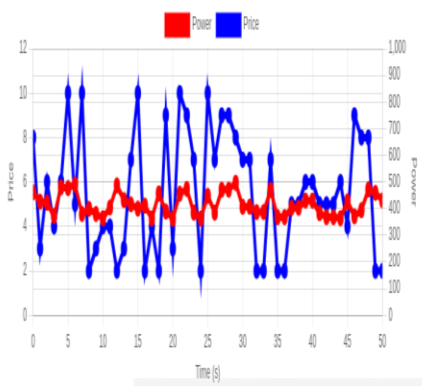

(a)

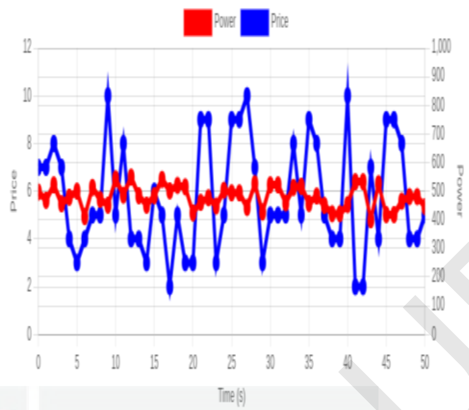

(b)

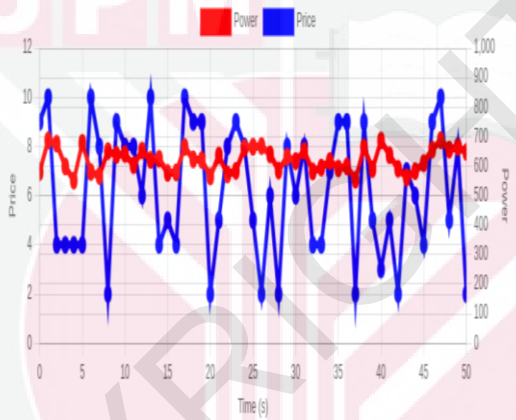

(c)

Figure 4.24 : Aggregated EV Consumers demand power and price (a) Consumer 1 (b) Consumer 2 (c) Consumer 3

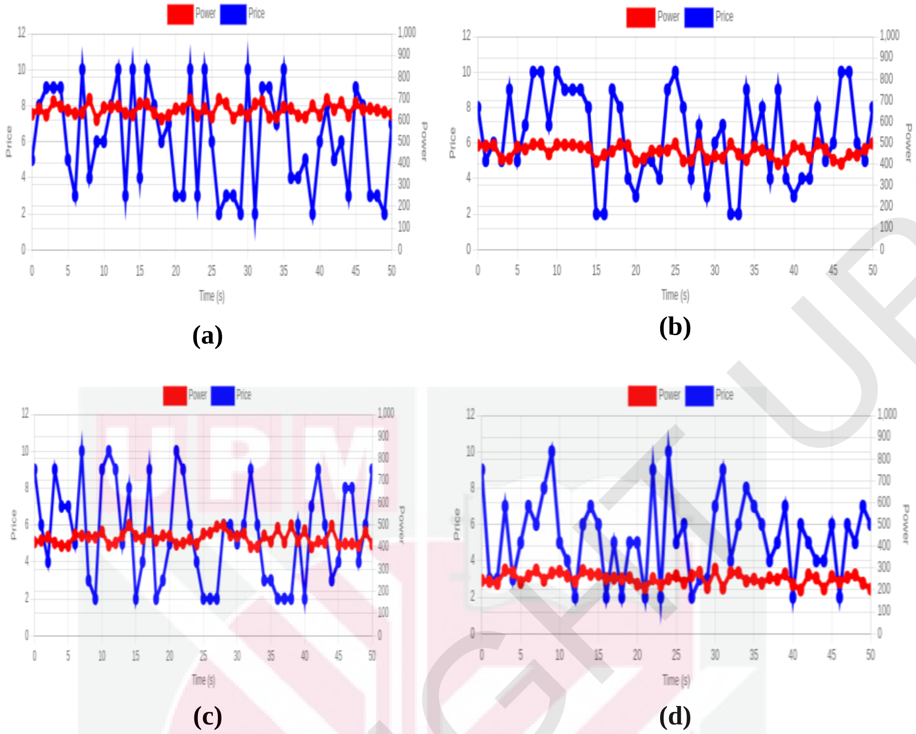

Figure 4.25 : Prosumer generation and selling price (a) MG 1 (b) MG 2 (c) MG 3 (d) MG 4

a. Case 1:P2P trading in Blockchain

A set of randomly generated selling and bidding prices are considered in this scenario to determine how the prosumers and consumers would trade the energy depending on their individual energy capacity. The prosumer and consumer pricing value ranges from 0.1 to 1$/kWh for trade to occur. The range of consumer loads for consumers 1 through 3 is 300 kW to 500 kW, 350 kW to 600 kW, and 550 kW to 720 kW, respectively. In order to satisfy the consumer expectations, the prosumers 1 to 4 generation also ranges between 600 kW to 750 kW, 400 kW to 500 kW, 350 kW to 500 kW and 200 kW to 300 kW, respectively. Figure 4.24 shows the demand requirements and bidding price for aggregated EV consumers 1 to 3. Figure 4.25 displays the MG 1 to 4 selling prices and maximum power dispatching capacities. The prosumers determine the contract and calculate the CPM to satisfy each consumer's demand before trade begin. To satisfy the consumer demand as depicted in Figure 4.24, the CPM is computed, and the power reference is transferred to each prosumer in NMG.

Let's consider a specific scenario of market clearing that occurs at the 1516th cycle within the blockchain, as depicted in Figure 4.26, showing the respective values for consumer demand (CD) and prosumer generation (PG). The demand CD_1 with the highest price, 417 kW for 1$/kWh; CD_2 is 591 kW for 0.8$/kWh and CD_3 is 412 kW for 0.3$/kWh;

while PG_1 with the lowest price, 630 kW for 0.3$/kWh; PG_2 is 489 kW for 0.6$/kWh; PG_3 is 264 kW for 0.8$/kWh and PG_4 is 432 kW for 0.8$/kWh, respectively. As a result, the entry in the CPM starts with the consumer demand at the highest price and with generation at the least expensive value. Now, the computation of CPM is carried as per the flowchart given in Figure 3.24. The CD_1 is 417 kW, while PG_1 is 630 kW. Here $PG_1 \geq CD_1$, then the corresponding element is

$$c_{11} = \frac{PG_1}{CD_1} \approx 1 \tag{4.22}$$

Update the value of c_{11} in CPM while setting the remaining elements in the column to zero as the sum of the first column is equal to one. Now, update PG_1 as $PG_{1,temp} = PG_1 - CD_1 = 630 - 417 = 213$ kW. Then, update $PG_1 = PG_{1,temp}$ and increase the consumer count by 1. In the next step, as shown in Figure 3.27 the control is transferred to the if condition. Here $PG_1 < CD_2$ (213 < 591 kW), the if condition failed and the value of c_{12} is calculated using

$$c_{12} = \frac{PG_1}{CD_2} = \frac{213}{591} \approx 0.36 \tag{4.23}$$

Now, update the value $CD_{2,\ temp} = CD_2 - PG_1 = 591 - 213 = 378$ kW and increase the prosumer count by 1. $PG_2 \geq CD_{2,\ temp}$ (489 > 378), so c_{22} is computed as

$$c_{22} = 1 - \sum_{i=1} C_{12} = 1 - 0.36 \approx 0.64 \tag{4.24}$$

Then, update the value of c_{22} in CPM as the sum of the second column is equal to one, enter all other elements in the column to zero. Now, update PG_2 as $PG_{2,temp} = PG_2 - CD_2 = 489 - 378 = 111$ kW. Then, update $PG_2 = PG_{2,temp}$ and increase the consumer count by 1. Here $PG_2 < CD_3$ (111 < 412 kW), the if condition is failed and the value of c_{23} is calculated using

$$c_{23} = \frac{PG_2}{CD_3} = \frac{111}{412} \approx 0.26 \tag{4.25}$$

Now, update the value $CD_{3,\ temp} = CD_3 - PG_2 = 412 - 111 = 301$ kW and increase the prosumer count by 1. Then, check $PG_3 \geq CD_{3,temp}$ the if-action is not satisfied and the value of c_{33} is computed as

$$c_{33} = \frac{PG_3}{CD_3} = \frac{264}{412} \approx 0.64 \tag{4.26}$$

Now, update the value $CD_{3,\,temp} = CD_3 - PG_3 = 412 - 264 = 148$ kW and increase the prosumer count by 1. Then, check $PG_4 \geq CD_{3,temp}$ the if-action is satisfied and the value of c_{34} is calculated as

$$c_{43} = 1 - \sum_{i=3} c_{43} = 1 - 0.26 - 0.64 \approx 0.1 \tag{4.27}$$

Finally, the resultant CPM is calculated as given in Equation (4.28).

$$CPM = \begin{bmatrix} 1 & 0.36 & 0 \\ 0 & 0.64 & 0.26 \\ 0 & 0 & 0.64 \\ 0 & 0 & 0.1 \end{bmatrix} \tag{4.28}$$

Due to Solidity language limitations, fractional CPM values are converted to integers by multiplying matrix elements and prices by 100. The resulting power reference values as shown in Equation (4.29) indicate consumer requirement met by prosumers, facilitating frequency regulation in the NMG model analyzed in OPAL-RT.

$$CPM = \begin{bmatrix} 100 & 36 & 0 \\ 0 & 64 & 26 \\ 0 & 0 & 64 \\ 0 & 0 & 10 \end{bmatrix} \times \begin{bmatrix} 417 \\ 591 \\ 412 \end{bmatrix} = \begin{bmatrix} 62976 \\ 48536 \\ 26368 \\ 4120 \end{bmatrix} \tag{4.29}$$

In this instance, P2P trading causes a change in the NMG system frequency. In addition to the secondary frequency controller, the supplementary control is used to control the frequency by transmitting the power reference value, and send to the plant model in OPAL-RT. The power instructions and the primary droop control work together to keep the P2P trading system frequency within the allowed tolerance of ±0.2 Hz.

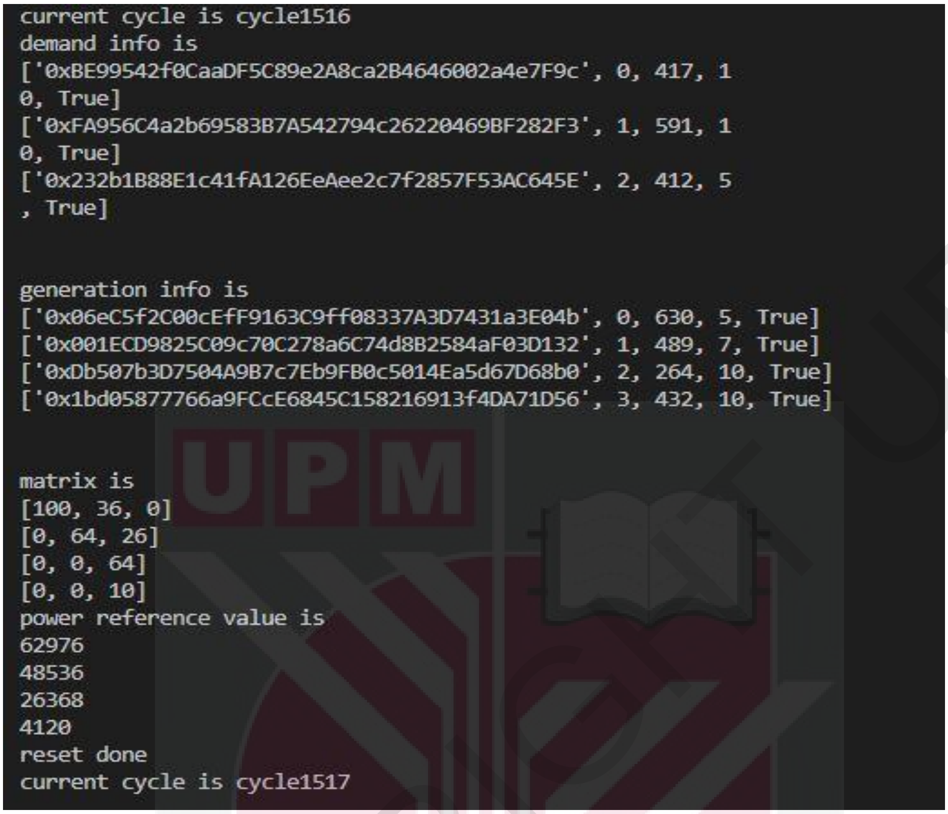

```
current cycle is cycle1516
demand info is
['0xBE99542f0CaaDF5C89e2A8ca2B4646002a4e7F9c', 0, 417, 1
0, True]
['0xFA956C4a2b69583B7A542794c26220469BF282F3', 1, 591, 1
0, True]
['0x232b1B88E1c41fA126EeAee2c7f2857F53AC645E', 2, 412, 5
, True]


generation info is
['0x06eC5f2C00cEfF9163C9ff08337A3D7431a3E04b', 0, 630, 5, True]
['0x001ECD9825C09c70C278a6C74d8B2584aF03D132', 1, 489, 7, True]
['0xDb507b3D7504A9B7c7Eb9FB0c5014Ea5d67D68b0', 2, 264, 10, True]
['0x1bd05877766a9FCcE6845C158216913f4DA71D56', 3, 432, 10, True]


matrix is
[100, 36, 0]
[0, 64, 26]
[0, 0, 64]
[0, 0, 10]
power reference value is
62976
48536
26368
4120
reset done
current cycle is cycle1517
```

Figure 4.26 : 1516th cycle of CPM implementation

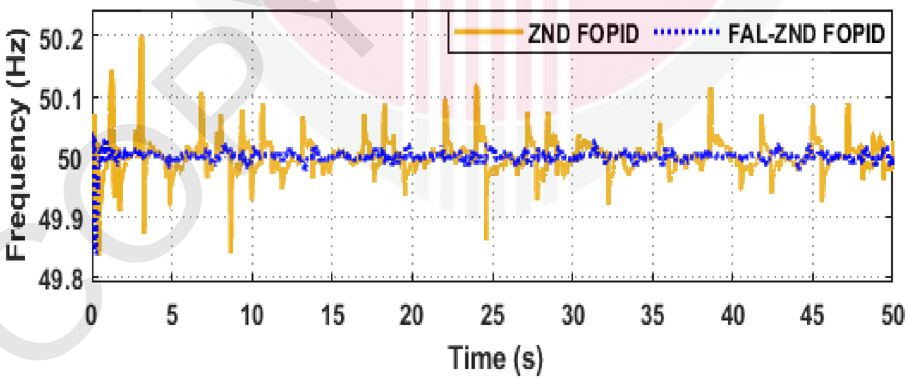

Figure 4.27 : Frequency response of MG 1 in blockchain

For instance, the frequency response of MG 1 is given in Figure 4.27. From the results, it is obvious that the FAL-ZND control has better frequency oscillation regulation than the ZND approach. Additionally, the usage of blockchain enhances security and interest among peers participating in the trading process by ensuring that neither prosumers nor consumers may break the contract.

b. Case 2: Response During FDI Attack

In this case, blockchain based technology is implemented on the controller to secure the control signals from the attacker who manipulates or injects false data into the control signals in order to change the dynamics of the power grid. To prove its reliability, an FDI attack is investigated by infusing a random signal in MG 1 that changes by 80 % with plant frequency information. Figure 4.28 (a) depicts the frequency response of an intruder's FDI assault started at 3 s without and with blockchain enabled controller, whereas Figure 4.28 (b) depicts the consensus error during FDI assault.

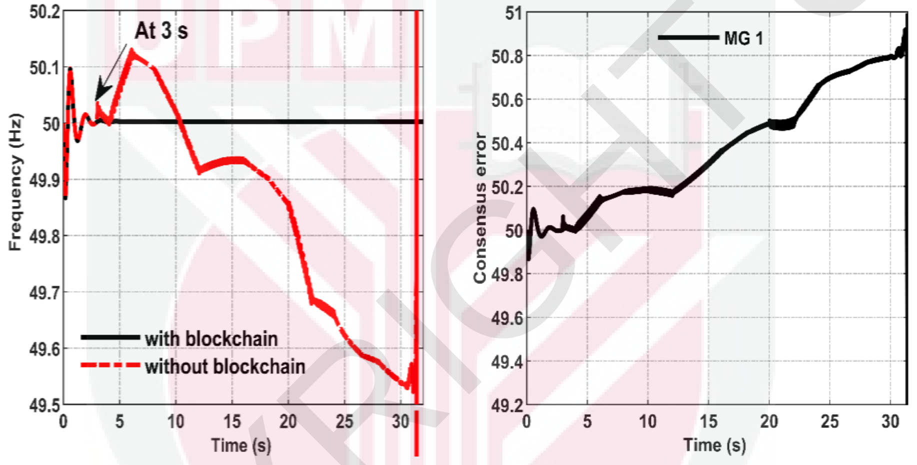

(a) (b)

Figure 4.28 : Response during FDI attack on control (a) Frequency of MG 1 (b) Consensus error of MG 1

As a result of the attack at 3 s, the proffered controller response considered without blockchain oscillates around the permissible range of 50.1 Hz to 49.8 Hz till 22 s, it means the proffered controller tries to maintain the frequency within the allowable limit, however the response reaches unstable state after 30 s whereas the blockchain enabled controller response is intended to maintain system stability in the event of an FDI assault.

c. Case 3: Performance During Communication Delay

In a practical NMG system, the information exchange between the MG is usually prone to delays due to unreliable communication channels. In this case, the performance of the proposed control is validated using various communication delays. Figure 4.29 depicts the frequency deviation plot of MG 1, 2, and 3. It is seen that a communication delay of 15 ms is activated at 20 s with a load change of 0.14 p.u. in MG 2. Due to the delay, the frequency data between MG 2 and MG1 and between MG 2 and MG 3 are delayed, which results in small oscillations in the frequency profile. To further prove the robustness of the proposed control, a large delay of 30 ms is given at 30 s in MG 2, the performance of the frequency deviation is still under the nominal value. Therefore, the proposed distributed controller guarantees the system's robustness under different communication delays.

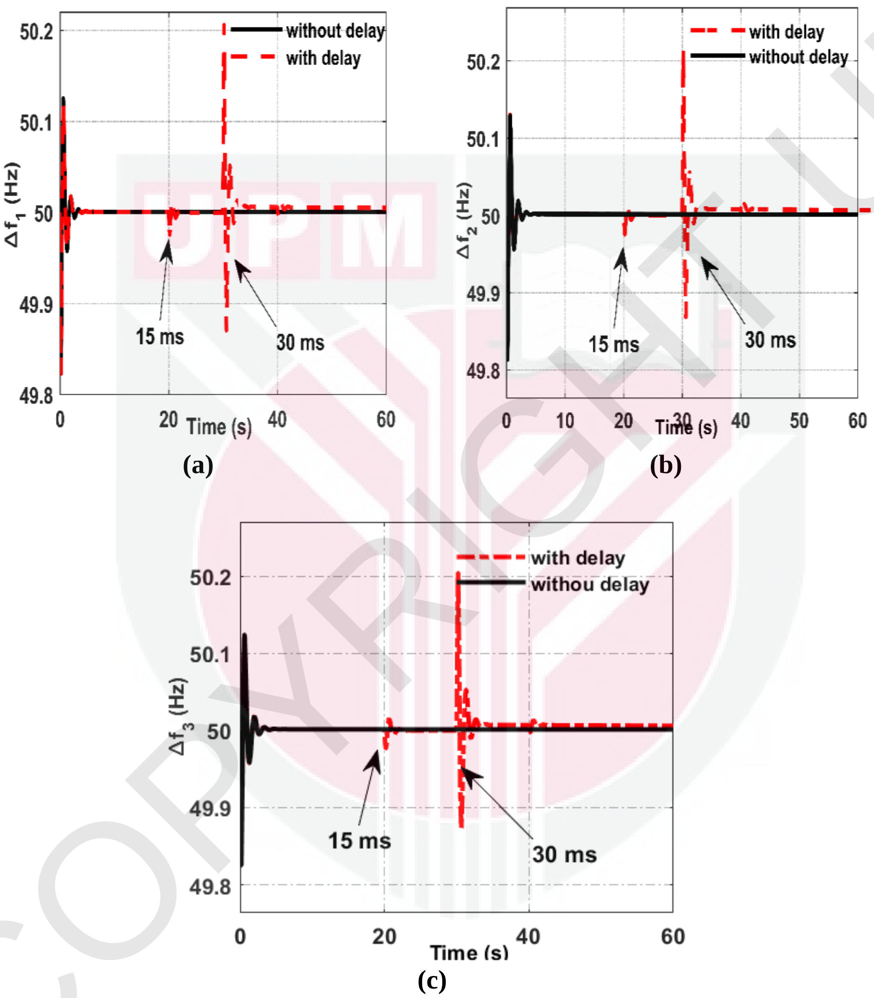

Figure 4.29 : Frequency response during delay (a) MG 1, (b) MG 2 and (c) MG 3

d. Case 4: Performance During Communication Failure

In a distribution system, the MGs may be far apart, affecting the communication services, such as communication delays, communication link loss, etc. Therefore, communication link failures may affect the control performance, leading to system instability. Hence, to show the performance of the proposed control, a communication failure test is conducted in this case. To assess, the communication link between MG 2 to MG 3 and MG 2 to MG 1 are disconnected at 20 s and gets restored at 35 s. Figure 4.30 illustrates the frequency response plot of the MMG system under this scenario. Despite the loss of communication link, it is clearly seen that the communication network is still connected and has a balanced Laplacian matrix.

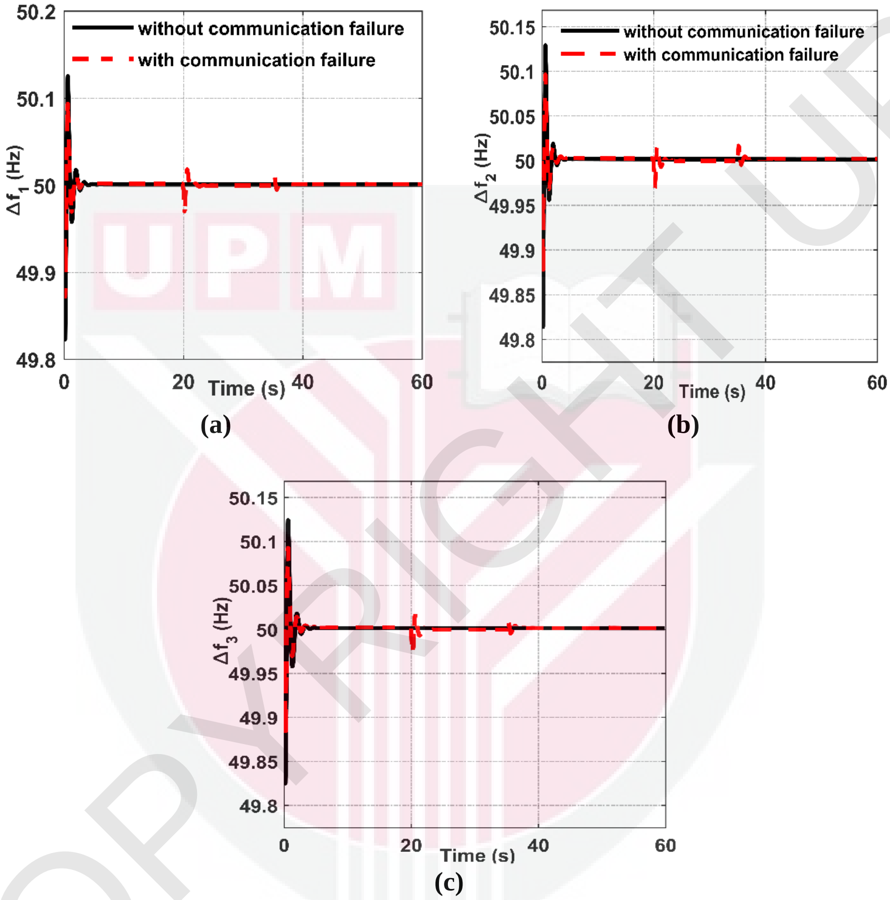

Figure 4.30 : Frequency response during failure (a) MG 1, (b) MG 2 and (c) MG 3

4.4.3 Comparative Study

To validate the robustness of the proposed controller, the performance of the proposed controller is compared with other state-of-the-art controllers. The performance analysis is carried out with four prosumers generating constant power at fixed prices to satisfy consumer demand. The prosumers 1 to 4 trade energy at rates of \$ 0.4, \$ 0.6, \$ 0.7, and \$ 0.8 per kWh with dispatching powers of 600 kW, 400 kW, 225 kW and 400 kW. Consumers 1 to 3 are bidding at \$ 0.5, \$ 0.3, and \$ 0.2 per kWh with demand capacities of 450 kW, 600 kW, and 400 kW. In this instance of P2P energy trading, the CPM is obtained in order to provide the power reference for DG as stated in Equation (4.30).

$$CPM=\begin{pmatrix} 100 & 25 & 0 \\ 0 & 66 & 0 \\ 0 & 9 & 43 \\ 0 & 0 & 57 \end{pmatrix} \tag{4.30}$$

The frequency response, depicted in Figure 4.31, demonstrates the dynamic change in NMG system. It is inferred from the figure that the FAL-ZND FOPID approach settles at 5.64 s at steady state (50 Hz) in the shortest time, followed by ZND FOPID at 10.25 s, NLFOPID at 15.1 s, and FOPID technique at 22.5 s. This is also inferred from the consensus error, for instance shown in Figure 4.32. The magnitude of the error is small in the case of proposed control, and it reaches to zero steady state faster compared to those of other techniques. Additionally, the computational burden can be evaluated by examining the convergence of the Lyapunov-based energy function, defined in Equation (3.39) and illustrated in Figure 4.33. Moreover, the steady state performance indices like IAE, ITAE, ISE and ITSE are significantly enhanced by a proportion of 18 % to 35 %, 15 % to 41 %, 28 % to 48 % and 35 % to 54 %, respectively by the proposed FAL-ZND FOPID controller. Further, the transient performance indices like ST, RT, |P-O| and CE are improved by 23 % to 83 %, 10 % to 25 %, 36 % to 62 % and 23 % to 81 %, respectively by the proposed control technique. The energy profile reaches the global minima faster using the proposed FAL-ZND FOPID technique, with a minimum computational time (4 seconds), compared to ZND FOPID (8 seconds) approach, effectively minimizing the dynamics of the network, and attaining stable equilibrium state as shown in Table 4.12.

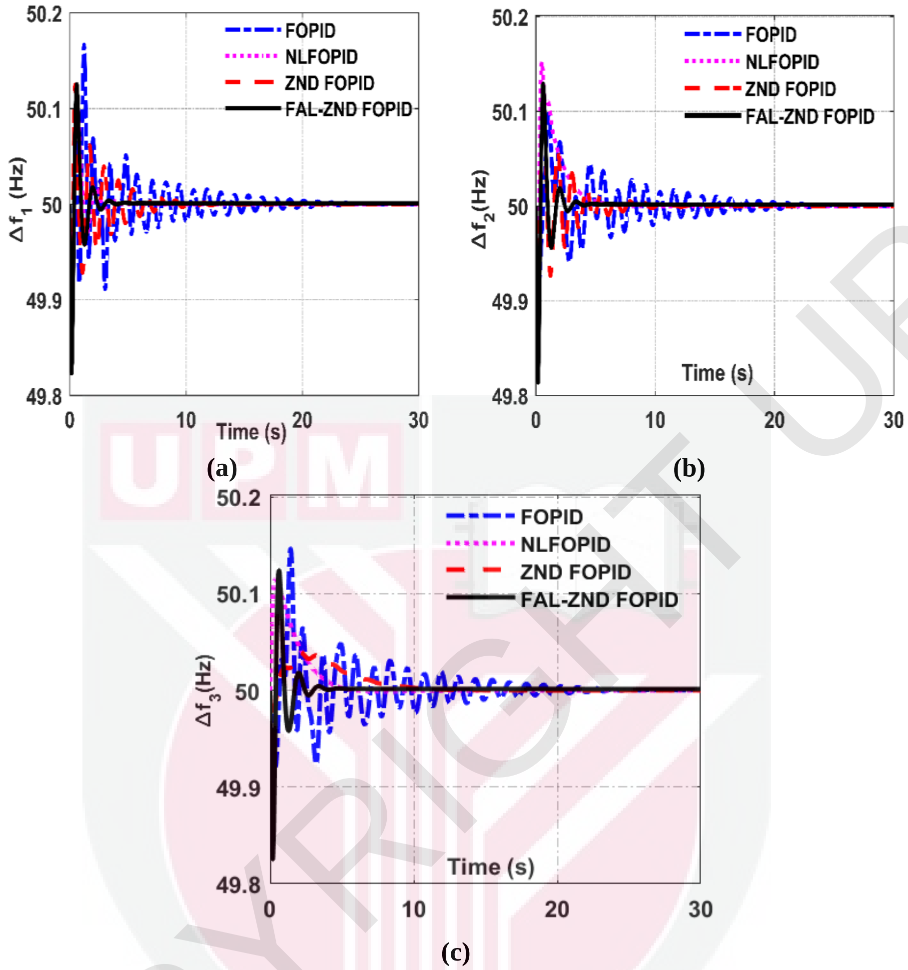

Figure 4.31 : Dynamic frequency response in (a) MG 1, (b) MG 2 and (c) MG 3

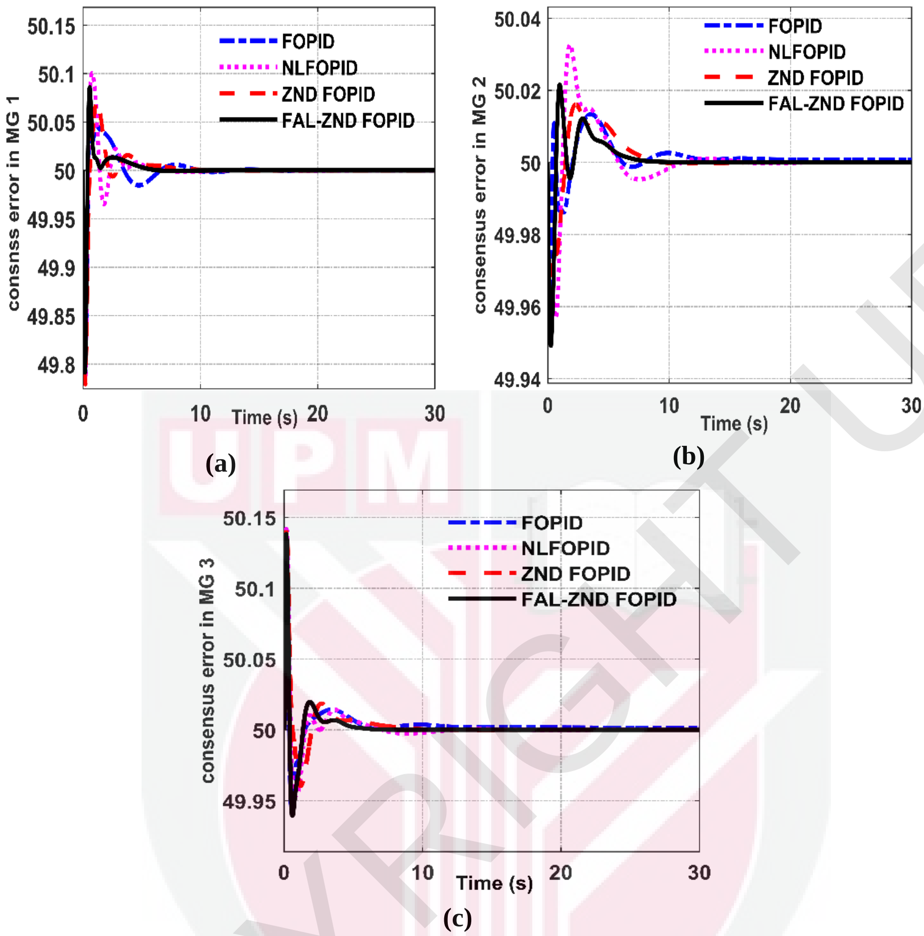

Figure 4.32 : Consensus error dynamics in (a) MG 1, (b) MG 2 and (c) MG 3

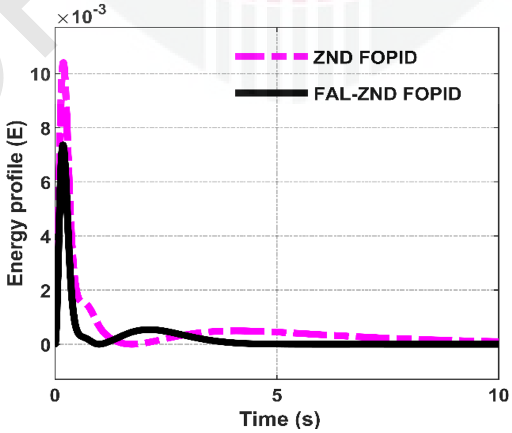

Figure 4.33 : Energy profile

Table 4.12 : Performance indices for MG 1, MG 2 and MG3

Performance parameters	MG 1				MG 2				MG 3			
	FOPID	**NLFOPID**	**ZND FOPID**	**FAL-ZND FOPID**	**FOPID**	**NLFOPID**	**ZND FOPID**	**FAL-ZND FOPID**	**FOPID**	**NLFOPID**	**ZND FOPID**	**FAL-ZND FOPID**
ST (s)	22.5	15.1	10.25	5.64	21.23	14.56	9.39	6.75	25.32	15.83	10.22	7.17
RT x10^-6 (s)	214.51	3.69	2.376	2.095	360.21	4.62	4.88	4.58	0.03	46.8	7.60	4.07
|P-O| (Hz)	50.8	50.15	50.12	50.08	50.19	50.18	50.13	50.1	50.15	50.12	50.1	50.09
CE (Joules)	0.34	0.23	0.16	0.11	0.33	0.23	0.16	0.11	0.52	0.36	0.23	0.08
IAE	0.01	0.006	0.007	0.004	0.008	0.009	0.009	0.004	0.007	0.009	0.007	0.04
ITAE	0.07	0.012	0.20	0.12	0.024	0.25	0.25	0.12	0.29	0.256	0.024	0.15
ISE	0.22	0.186	0.025	0.006	0.28	0.024	0.025	0.006	0.025	0.024	0.22	0.06
ITSE	1.56	0.72	0.66	0.335	2.16	1.031	0.88	0.335	2.31	1.031	0.86	0.43

4.4.4 Analysis on Large Scale System

To prove the real time applicability of the proposed controller, the New England 39-bus network is considered. In addition to the distributed control, a comparison of the proposed FAL-ZND based FOPID controller in both the centralised and decentralised control is considered with the supplementary control is investigated in this system. An increase in load demand by 3.283 MW, 0.233 MW, and 3.601 MW is imposed in Area-1, Area-2, and Area-3, respectively.

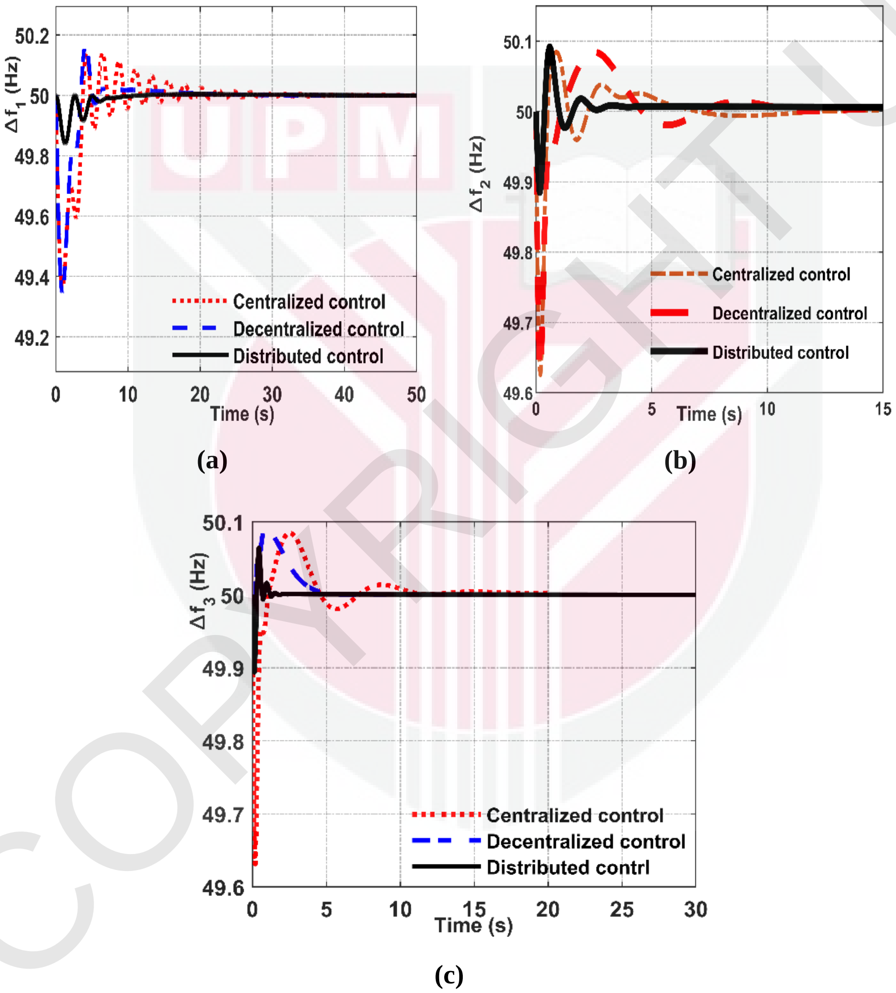

Figure 4.34 : Frequency response of NMG for New England 39-bus system

In the context of LFC, only a single generator within each area is crucial for the frequency control task. The specified generators for this responsibility are G1 in Area-1, G9 in Area-2, and G4 in Area-3. Figure 4.34 visually represents the frequency response acquired from the 39-bus test system. It is evident that the proposed distributed controller highlights a quicker ST of 11 seconds in area-1, 6.35 seconds in area-2 and 4.56 seconds in area-3. Further, the PO and PU of the proposed distributed control technique is also minimal compared to other control strategies. Moreover, the transient performance indices such as ST, PO, PU and CE are improved by a percentage of 23 % to 69 %, 5 % to 23 %, 10 % to 42 % and 32 % to 45 %, respectively.

4.5 Summary

This section provides a comprehensive summary of proposed control techniques implementation for frequency control in the thesis. The results are obtained to fulfil the three key objectives of the thesis. A centralized FOPID controller is initially designed to regulate the power network frequency, and a CASO control technique is proposed to optimize the controller's gain values. The proposed control technique's robustness is evaluated, particularly its ability to handle parametric uncertainty in the system under study. Then, a decentralized control scheme is developed for a deregulated power network, focusing on effective LFC in a market environment. The control technique's performance is further enhanced through hybridization of PSO with ASO. Finally, a control technique is proposed by incorporating the control techniques in objectives 1 and 2. A federated learning-based recurrent adaptive FOPID controller is proposed for distributed frequency control of NMG system. The initial bias values of the recurrent controller are obtained through the propounded hybrid CAS-PSO technique. The modified New England IEEE 39 bus system is chosen to validate the proposed FAL-ZND FOPID control in different control schemes.

CHAPTER 5

CONCLUSIONS AND RECOMMENDATIONS FOR FUTURE RESEARCH

5.1 Conclusions

This section sums up the conclusions derived from each objective and provides a summary of the significant findings obtained through this research. Additionally, the contributions to the field and recommendations for future research are discussed to further advance our comprehension in the ongoing research. Several fractional order secondary frequency controls were designed based on various control schemes to maintain the frequency within ±0.2 Hz in different testbed systems. In order to achieve the best possible dynamic performance of the control, numerous intelligence-based control techniques were utilised to find the optimum values of the controller.

In this research, a centralized control scheme is initially implemented for a multi-area renewable energy (RE) integrated power network using a fractional order proportional integral derivative (FOPID) controller. The gain values of the controller were optimized using a proposed chaotic atom search optimization (CASO) algorithm. Then, to enhance the robustness of the FOPID controller and to overcome the drawbacks of centralized control scheme, a nonlinear FOPID (NLFOPID) controller is designed and implemented in a decentralized fashion on a complex RE integrated deregulated power network. A new hybrid atom search particle swarm optimization (AS-PSO) algorithm is developed to optimize the parameters of NLFOPID controller. Further, to coordinate the operations of various areas of microgrids (MGs) in the network, a distributed control scheme is studied based on a leader-follower framework.

Furthermore, the robustness and adaptive features of the FOPID controller is improved by a federated average learning of recurrent zeroing neural dynamics designed self-adaptive fractional order proportional integral derivative (FAL-ZND FOPID) controller for distributed frequency control of NMG system. The initial bias values of the propounded controller are obtained using an hybrid chaotic AS-PSO algorithm. To conclude, the performance of the proposed distributed leader-follower based adaptive consensus control is tested in a New England 39-bus system and the results obtained reveal that the distributed control scheme is more robust compared to other schemes. The conclusions attained from specific research objectives are as follows:

Objective 1: Design of Centralized FOPID controller optimized using CASO

The specific conclusions attained from the first objective is as follows:

- An improved form of ASO algorithm called CASO by embedding the characteristics of tent map is proposed to tune the parameters of centralized FOPID controller for multi-area multi-source HPS that consisting of both conventional and RE sources.

- Initially, to establish the competence of CASO over ASO, five classical benchmark functions have been evaluated. The output results in terms of mean, best and standard deviation values clearly substantiate the competence of TM-CASO over SM-CASO, LM-CASO and ASO algorithms.
- Further, to prove the efficacy of chaotic version of ASO they are used to optimize the FOPID controller for two and three-area power system and the performance is compared with standard ASO by minimizing ITAE of ACE. The results of frequency deviation and tie-line power variation obtained for different cases reveal that the CASO method outperforms significantly compared to standard ASO.
- This claim has been verified by measuring the steady state and transient performance indices, it is seen that the CASO has improvement of 24 % to 95 % in terms of ST, PO, and CE, respectively.
- The robustness of the controller has been tested by considering ±25 % variation in system parameters and its real-time applicability has been validated for uncertain variation in solar thermal and wind power variations as per the Metrological data obtained from Malaysia.

Objective 2: Design of Decentralized NLFOPID controller optimized using AS-PSO

The conclusions attained from second objective are as follows:

- A decentralized NLFOPID controller is designed and analyzed for LFC of the restructured energy system. The study considers various energy transaction scenarios through a contract via DPM among DISCOs and GENCOs for frequency control application.
- A local decentralized NLFOPID controller is developed in each control area to regulate the frequency and tie-line power of three unequal area energy systems comprising renewable and conventional sources. A hybrid AS-PSO technique is proposed to tune the parameters of the NLFOPID controller.
- The effectiveness is validated for different energy trading scenarios and standard benchmark functions. The results from later clearly demonstrate the superiority of the AS-PSO algorithm over the ASO and PSO for benchmark functions considered. Furthermore, the simulation results for frequency control applications by optimizing the NLFOPID controller for the DDES model considered revealed that the area frequency and tie-line power oscillations are well regulated within the standard limits.
- This claim is validated by evaluating the steady-state and transient PIs. The result proves that the AS-PSO tuned NLFOPID controller has an improvement of 75.2 % of ST, 36 % of CE, and 43 % of SE to FOPID controller and other optimization techniques, respectively. The robustness of the controller has been tested under various real-time load patterns.

Objective 3: Design of an adaptive distributed frequency control of NMG

The conclusions obtained from third objective is,

- For a direct P2P energy market in NMG, this study presents a cyber-secure distributed controller for frequency regulation. To enable prosumers to trade energy with appropriate consumers a CPM is implemented on a PoA-based private blockchain.
- To effectively control the system frequency, a federated average learning based ZND FOPID controller has been proposed. The HIL simulation environment, the robustness of the proposed FAL-ZND FOPID controller is compared with ZND FOPID controller together with blockchain implementation.
- An AS-PSO algorithm is proposed to obtain the initial bias values of the FAL-ZND FOPID controller. The controller resiliency is tested against FDI attack, communication failure and delays. The findings demonstrate that the proposed distributed control scheme regulates the frequency with the least amount of steady-state error.
- A comparative analysis of the proposed control scheme is made with the conventional centralized and decentralized scheme and with the state-of-the-art to validate the performance of the proposed FAL-ZND FOPID controller.

5.2 Contributions of the Research

The significant contributions and findings from the thesis can be summarized as follows:

- An improved form of ASO algorithm called CASO algorithm is proposed for the first time to optimize the gain values of the centralized FOPID controller. A considerable contribution is performed in improving the efficacy of the proposed control technique by avoiding the premature convergence due to its diversification of chaotic sequences compared to the standard ASO algorithm.
- An NLFOPID controller is proposed for the first time to regulate the frequency of a complex deregulated power network through decentralized control. Then, a maiden attempt has been made to hybridize ASO with PSO to optimize the parameters of NLFOPID controller.
- Finally, a comprehensive design of distributed frequency control using FAL-ZND based FOPID controller for NMG system is proposed for the first time. Then, a maiden effort has been performed by hybridizing the control techniques proposed in contribution one and two i.e., CASO algorithm is hybridized with PSO algorithm. Further, to improve the performance of the algorithm, the constant parameters in algorithm are modified into an adaptive value by incorporating nonlinear equations. The initial bias values of the adaptive controller are attained using the proffered CAS-PSO algorithm.

5.3 Recommendations for Future Research

Based on the results and findings obtained from the research work, several recommendations for future research endeavours are identified to further advance the field of LFC study:

- The proposed hybrid metaheuristic algorithms can be further hybridized with deep learning algorithms to leverage the strengths of both approaches to improve the optimization performance.
- Advanced ZNDs, including networks of higher order or fractional order, can be explored to boost the effectiveness of ZNDs and utilized in addressing contemporary challenges and problems within power systems.
- The practical applicability of the proffered FAL-ZND controller for frequency regulation of NMG system can be studied in real-time by considering demand side management.

REFERENCES

Abazari, A., Monsef, H., & Wu, B. (2019). Coordination strategies of distributed energy resources including FESS, DEG, FC and WTG in load frequency control (LFC) scheme of hybrid isolated micro-grid. *International Journal of Electrical Power & Energy Systems*, *109*, 535–547. https://doi.org/https://doi.org/10.1016/j.ijepes.2019.02.029

Abd-Elazim, S. M., & Ali, E. S. (2018). Firefly algorithm-based load frequency controller design of a two area system composing of PV grid and thermal generator. *Electrical Engineering*, *100*(2), 1253–1262. https://doi.org/10.1007/s00202-017-0576-5

Abou El-Ela, A. A., El-Sehiemy, R. A., Shaheen, A. M., & Diab, A. E.-G. (2022). Design of cascaded controller based on coyote optimizer for load frequency control in multi-area power systems with renewable sources. *Control Engineering Practice*, *121*, 105058. https://doi.org/https://doi.org/10.1016/j.conengprac.2021.105058

Ali Kadhem, A., Abdul Wahab, N. I., & N. Abdalla, A. (2019). Wind Energy Generation Assessment at Specific Sites in a Peninsula in Malaysia Based on Reliability Indices. *Processes*, *7*(7). https://doi.org/10.3390/pr7070399

Ali, L., Azim, M. I., Peters, J., Bhandari, V., Menon, A., Tiwari, V., Green, J., & Muyeen, S. M. (2023). Application of a Community Battery-Integrated Microgrid in a Blockchain-Based Local Energy Market Accommodating P2P Trading. *IEEE Access*, *11*, 29635–29649. https://doi.org/10.1109/ACCESS.2023.3260253

Almasalma, H., Engels, J., & Deconinck, G. (2017). Peer-to-Peer Control of Microgrids. *ArXiv Preprint ArXiv:1711.04070*.

Aly, M., Mohamed, E. A., Noman, A. M., Ahmed, E. M., El-Sousy, F. F. M., & Watanabe, M. (2023). Optimized Non-Integer Load Frequency Control Scheme for Interconnected Microgrids in Remote Areas with High Renewable Energy and Electric Vehicle Penetrations. *Mathematics*, *11*(9). https://doi.org/10.3390/math11092080

An, J., Lee, M., Yeom, S., & Hong, T. (2020). Determining the Peer-to-Peer electricity trading price and strategy for energy prosumers and consumers within a microgrid. *Applied Energy*, *261*, 114335. https://doi.org/https://doi.org/10.1016/j.apenergy.2019.114335

Andrade, D. M., Gamboa, S., & Torres, J. A. (2020). Distributed Load-Frequency Control in Power Systems. *2020 IEEE ANDESCON*, 1–6. https://doi.org/10.1109/ANDESCON50619.2020.9272070

Arya, Y. (2017a). AGC performance enrichment of multi-source hydrothermal gas power systems using new optimized FOFPID controller and redox flow batteries. *Energy*, *127*, 704–715. https://doi.org/https://doi.org/10.1016/j.energy.2017.03.129

Arya, Y. (2023). ICA assisted FTIλDN controller for AGC performance enrichment of interconnected reheat thermal power systems. *Journal of Ambient Intelligence and Humanized Computing*, *14*(3), 1919–1935. https://doi.org/10.1007/s12652-021-03403-6

Arya, Y., Dahiya, P., Çelik, E., Sharma, G., Gözde, H., & Nasiruddin, I. (2021). AGC performance amelioration in multi-area interconnected thermal and thermal-hydro-gas power systems using a novel controller. *Engineering Science and Technology, an International Journal*, *24*(2), 384–396. https://doi.org/https://doi.org/10.1016/j.jestch.2020.08.015

Arya, Y., & Kumar, N. (2017b). Design and analysis of BFOA-optimized fuzzy PI/PID controller for AGC of multi-area traditional/restructured electrical power systems. *Soft Computing*, *21*(21), 6435–6452. https://doi.org/10.1007/s00500-016-2202-2

Athira, S., & Aneesh, V. (2023). FOPID controller tuning: A comparative study of optimization techniques for an automatic voltage regulator. AIP Conference Proceedings, 2904(1), 060002. https://doi.org/10.1063/5.0170829

Babu, N. R., & Saikia, L. C. (2022). Optimal location of accurate HVDC and energy storage devices in a deregulated AGC integrated with PWTS considering HPA-ISE as performance index. *Engineering Science and Technology, an International Journal*, *33*, 101072. https://doi.org/https://doi.org/10.1016/j.jestch.2021.10.004

Bandeiras, F., Pinheiro, E., Gomes, M., Coelho, P., & Fernandes, J. (2020). Review of the cooperation and operation of microgrid clusters. *Renewable and Sustainable Energy Reviews*, *133*, 110311. https://doi.org/https://doi.org/10.1016/j.rser.2020.110311

Baranowski, J., Bauer, W., Zagórowska, M., Dziwiński, T., & Piątek, P. (2015). Time-domain Oustaloup approximation. *2015 20th International Conference on Methods and Models in Automation and Robotics (MMAR)*, 116–120. https://doi.org/10.1109/MMAR.2015.7283857

Barshandeh, S., & Haghzadeh, M. (2021). A new hybrid chaotic atom search optimization based on tree-seed algorithm and Levy flight for solving optimization problems. *Engineering with Computers*, *37*(4), 3079–3122. https://doi.org/10.1007/s00366-020-00994-0

Bevrani, H. (2014). *Robust Power System Frequency Control* (J. H. Chow, A. M. Stankovic, & D. Hil, Eds.; 2nd ed., Vol. 4). Springer. https://doi.org/10.1007/978-3-319-07278-4

Bevrani, H., Hiyama, T., & Bevrani, H. (2011). Robust PID based power system stabiliser: Design and real-time implementation. *International Journal of Electrical Power & Energy Systems*, *33*(2), 179–188. https://doi.org/https://doi.org/10.1016/j.ijepes.2010.08.013

Bidram, A., Davoudi, A., Lewis, F. L., & Guerrero, J. M. (2013). Distributed Cooperative Secondary Control of Microgrids Using Feedback Linearization. *IEEE Transactions on Power Systems*, *28*(3), 3462–3470. https://doi.org/10.1109/TPWRS.2013.2247071

Boretti, A. (2021). Integration of solar thermal and photovoltaic, wind, and battery energy storage through AI in NEOM city. *Energy and AI*, *3*, 100038. https://doi.org/https://doi.org/10.1016/j.egyai.2020.100038

Cam, E., Gorel, G., & Mamur, H. (2017). Use of the Genetic Algorithm-Based Fuzzy Logic Controller for Load-Frequency Control in a Two Area Interconnected Power System. *Applied Sciences*, *7*(3). https://doi.org/10.3390/app7030308

Cao, J.-Y., Liang, J., & Cao, B.-G. (2005). Optimization of fractional order PID controllers based on genetic algorithms. *2005 International Conference on Machine Learning and Cybernetics*, *9*, 5686-5689 Vol. 9. https://doi.org/10.1109/ICMLC.2005.1527950

Çelik, E., Öztürk, N., Arya, Y., & Ocak, C. (2021). (1 + PD)-PID cascade controller design for performance betterment of load frequency control in diverse electric power systems. *Neural Computing and Applications*, *33*(22), 15433–15456. https://doi.org/10.1007/s00521-021-06168-3

Çelik, V., Özdemir, M. T., & Lee, K. Y. (2019). Effects of fractional-order PI controller on delay margin in single-area delayed load frequency control systems. *Journal of Modern Power Systems and Clean Energy*, *7*(2), 380–389. https://doi.org/10.1007/s40565-018-0458-5

Christie, R. D., & Bose, A. (1996). Load frequency control issues in power system operations after deregulation. *IEEE Transactions on Power Systems*, *11*(3), 1191–1200. https://doi.org/10.1109/59.535590

Daneshfar, F., & Bevrani, H. (2012). Multiobjective design of load frequency control using genetic algorithms. *International Journal of Electrical Power & Energy Systems*, *42*(1), 257–263. https://doi.org/https://doi.org/10.1016/j.ijepes.2012.04.024

Daraz, A., Malik, S. A., Basit, A., Aslam, S., & Zhang, G. (2023). Modified FOPID Controller for Frequency Regulation of a Hybrid Interconnected System of Conventional and Renewable Energy Sources. Fractal and Fractional, 7(1). https://doi.org/10.3390/fractalfract7010089

Das, D. C., Sinha, N., & Roy, A. (2014). Automatic generation control of an organic rankine cycle solar–thermal/wind–diesel hybrid energy system. *Energy Technology*, *2*(8), 721–731.

Das, M. K., Bera, P., & Sarkar, P. P. (2021). PID-RLNN controllers for discrete mode LFC of a three-area hydrothermal hybrid distributed generation deregulated power system. *International Transactions on Electrical Energy Systems*, *31*(5), e12837.

Delassi, A., Arif, S., & Mokrani, L. (2018). Load frequency control problem in interconnected power systems using robust fractional PIλD controller. *Ain Shams Engineering Journal*, *9*(1), 77–88. https://doi.org/https://doi.org/10.1016/j.asej.2015.10.004

Demir, F. B., Tuncer, T., Kocamaz, A. F., & Ertam, F. (2020). A survival classification method for hepatocellular carcinoma patients with chaotic Darcy optimization method based feature selection. *Medical Hypotheses*, *139*, 109626. https://doi.org/https://doi.org/10.1016/j.mehy.2020.109626

Deniz, F. N., Alagoz, B. B., Tan, N., & Koseoglu, M. (2020). Revisiting four approximation methods for fractional order transfer function implementations: Stability preservation, time and frequency response matching analyses. *Annual Reviews in Control*, *49*, 239–257. https://doi.org/https://doi.org/10.1016/j.arcontrol.2020.03.003

Dinesha, D. L., & Balachandra, P. (2022). Conceptualization of blockchain enabled interconnected smart microgrids. *Renewable and Sustainable Energy Reviews*, *168*, 112848. https://doi.org/https://doi.org/10.1016/j.rser.2022.112848

Ding, L., Han, Q.-L., & Zhang, X.-M. (2019). Distributed Secondary Control for Active Power Sharing and Frequency Regulation in Islanded Microgrids Using an Event-Triggered Communication Mechanism. *IEEE Transactions on Industrial Informatics*, *15*(7), 3910–3922. https://doi.org/10.1109/TII.2018.2884494

Donde, V., Pai, M. A., & Hiskens, I. A. (2001). Simulation and optimization in an AGC system after deregulation. *IEEE Transactions on Power Systems*, *16*(3), 481–489. https://doi.org/10.1109/59.932285

Doolla, S., & Bhatti, T. S. (2006). Load Frequency Control of an Isolated Small-Hydro Power Plant With Reduced Dump Load. *IEEE Transactions on Power Systems*, *21*(4), 1912–1919. https://doi.org/10.1109/TPWRS.2006.881157

Du, P., Mago, N. V, Li, W., Sharma, S., Hu, Q., & Ding, T. (2020). New Ancillary Service Market for ERCOT. *IEEE Access*, *8*, 178391–178401. https://doi.org/10.1109/ACCESS.2020.3027722

Ebrahim, M. A., Mostafa, H. E., Gawish, Saied. A., & Bendary, F. M. (2009). Design of decentralized load frequency Based-PID Controller using Stochastic Particle Swarm optimization technique. *2009 International Conference on Electric Power and Energy Conversion Systems, (EPECS)*, 1–6.

El Haj Assad, M., Ahmadi, M. H., Sadeghzadeh, M., Yassin, A., & Issakhov, A. (2021). Renewable hybrid energy systems using geothermal energy: hybrid solar thermal–geothermal power plant. *International Journal of Low-Carbon Technologies*, *16*(2), 518–530. https://doi.org/10.1093/ijlct/ctaa084

El-Sehiemy, R., Shaheen, A., Ginidi, A., & Al-Gahtani, S. F. (2023). Proportional-Integral-Derivative Controller Based-Artificial Rabbits Algorithm for Load Frequency Control in Multi-Area Power Systems. Fractal and Fractional, 7(1). https://doi.org/10.3390/fractalfract7010097

Elyaalaoui, K., Labbadi, M., Ouassaid, M., & Cherkaoui, M. (2021). A Continuous Nonlinear Fractional-Order PI Controller for Primary Frequency Control Application. Mathematical Problems in Engineering, 2021, 9953828. https://doi.org/10.1155/2021/9953828

El Yakine Kouba, N., Menaa, M., Hasni, M., & Boudour, M. (2015). Optimal load frequency control based on artificial bee colony optimization applied to single, two and multi-area interconnected power systems. *2015 3rd International Conference on Control, Engineering & Information Technology (CEIT)*, 1–6. https://doi.org/10.1109/CEIT.2015.7233027

Elgerd, O. I. (1982). *Electric energy systems theory: an introduction*. McGraw-Hill Book Company. https://www.osti.gov/biblio/5599996

Fan, H., Zhou, K., Zhang, E., Wen, W., & Li, M. (2020). Subdata image encryption scheme based on compressive sensing and vector quantization. *Neural Computing and Applications*, *32*(16), 12771–12787. https://doi.org/10.1007/s00521-020-04724-x

Fan, P., Ke, S., Yang, J., Li, R., Li, Y., Yang, S., Liang, J., Fan, H., & Li, T. (2023). A load frequency coordinated control strategy for multimicrogrids with V2G based on improved MA-DDPG. *International Journal of Electrical Power & Energy Systems*, *146*, 108765. https://doi.org/https://doi.org/10.1016/j.ijepes.2022.108765

Farahani, M., Ganjefar, S., & Alizadeh, M. (2012). PID controller adjustment using chaotic optimisation algorithm for multi-area load frequency control. *IET Control Theory & Applications*, *6*(13), 1984–1992. https://doi.org/10.1049/iet-cta.2011.0405

Fathy, A., Kassem, A. M., & Abdelaziz, A. Y. (2020). Optimal design of fuzzy PID controller for deregulated LFC of multi-area power system via mine blast algorithm. *Neural Computing and Applications*, *32*(9), 4531–4551. https://doi.org/10.1007/s00521-018-3720-x

Fathy, A., Yousri, D., Rezk, H., Thanikanti, S. B., & Hasanien, H. M. (2022). A Robust Fractional-Order PID Controller Based Load Frequency Control Using Modified Hunger Games Search Optimizer. Energies, 15(1). https://doi.org/10.3390/en15010361

Fu, C., & Tan, W. (2018). Decentralised load frequency control for power systems with communication delays via active disturbance rejection. *IET Generation, Transmission & Distribution*, *12*(6), 1397–1403. https://doi.org/https://doi.org/10.1049/iet-gtd.2017.0852

Gao, Z., & Liao, X. (2012). Improved Oustaloup approximation of fractional-order operators using adaptive chaotic particle swarm optimization. *Journal of Systems Engineering and Electronics*, *23*(1), 145–153. https://doi.org/10.1109/JSEE.2012.00018

Glover, J. D., Sarma, M. S., & Overbye, T. (2007). Power System Analysis and Design,(4th). *CL Engineering*, *534548849*.

Guha, D., Roy, P. K., & Banerjee, S. (2016b). Load frequency control of large scale power system using quasi-oppositional grey wolf optimization algorithm. *Engineering Science and Technology, an International Journal*, *19*(4), 1693–1713. https://doi.org/https://doi.org/10.1016/j.jestch.2016.07.004

Guha, D., Roy, P. K., & Banerjee, S. (2018). Optimal tuning of 3 degree-of-freedom proportional-integral-derivative controller for hybrid distributed power system using dragonfly algorithm. *Computers & Electrical Engineering*, *72*, 137–153. https://doi.org/https://doi.org/10.1016/j.compeleceng.2018.09.003

Guo, J. (2021). Application of a novel adaptive sliding mode control method to the load frequency control. *European Journal of Control*, *57*, 172–178. https://doi.org/https://doi.org/10.1016/j.ejcon.2020.03.007

Gupta, S. K., Ghose, T., & Chatterjee, K. (2022). Coordinated control of Incentive-Based Demand Response Program and BESS for frequency regulation in low inertia isolated grid. *Electric Power Systems Research*, *209*, 108037. https://doi.org/https://doi.org/10.1016/j.epsr.2022.108037

Hasan, M. W., & Abbas, N. H. (2020). An improved swarm intelligence algorithms-based nonlinear fractional order-PID controller for a trajectory tracking of underwater vehicles. *TELKOMNIKA (Telecommunication Computing Electronics and Control)*, *18*(6), 3173–3183.

Hekimoğlu, B. (2019). Optimal Tuning of Fractional Order PID Controller for DC Motor Speed Control via Chaotic Atom Search Optimization Algorithm. *IEEE Access*, *7*, 38100–38114. https://doi.org/10.1109/ACCESS.2019.2905961

Honarvar Nazari, M., Costello, Z., Feizollahi, M. J., Grijalva, S., & Egerstedt, M. (2014). Distributed Frequency Control of Prosumer-Based Electric Energy Systems. *IEEE Transactions on Power Systems*, *29*(6), 2934–2942. https://doi.org/10.1109/TPWRS.2014.2310176

Hu, Q., Zhu, Z., Bu, S., Wing Chan, K., & Li, F. (2021). A multi-market nanogrid P2P energy and ancillary service trading paradigm: Mechanisms and implementations. *Applied Energy*, *293*, 116938. https://doi.org/https://doi.org/10.1016/j.apenergy.2021.116938

Hussein, T., & Shamekh, A. (2019). Design of PI Fuzzy Logic Gain Scheduling Load Frequency Control in Two-Area Power Systems. *Designs*, *3*(2). https://doi.org/10.3390/designs3020026

Izci, D. (2022). A novel improved atom search optimization algorithm for designing power system stabilizer. Evolutionary Intelligence, 15(3), 2089–2103. https://doi.org/10.1007/s12065-021-00615-9

Jalali, N., Razmi, H., & Doagou-Mojarrad, H. (2020). Optimized fuzzy self-tuning PID controller design based on Tribe-DE optimization algorithm and rule weight adjustment method for load frequency control of interconnected multi-area power systems. *Applied Soft Computing*, *93*, 106424. https://doi.org/https://doi.org/10.1016/j.asoc.2020.106424

Jayachandran, M., & Ravi, G. (2019). Decentralized model predictive hierarchical control strategy for islanded AC microgrids. *Electric Power Systems Research*, *170*, 92–100. https://doi.org/https://doi.org/10.1016/j.epsr.2019.01.010

Jin, L., He, Y., Zhang, C.-K., Shangguan, X.-C., Jiang, L., & Wu, M. (2022). Robust Delay-Dependent Load Frequency Control of Wind Power System Based on a Novel Reconstructed Model. *IEEE Transactions on Cybernetics*, *52*(8), 7825–7836. https://doi.org/10.1109/TCYB.2021.3051160

Jin Wang Chunwei Ju, Y. G. A. K. S. G. K. (2018). A PSO based Energy Efficient Coverage Control Algorithm for Wireless Sensor Networks. *Computers, Materials & Continua*, *56*(3), 433–446. https://doi.org/10.3970/cmc.2018.04132

Jood, P., Aggarwal, S. K., & Chopra, V. (2019). Performance assessment of a neuro-fuzzy load frequency controller in the presence of system non-linearities and renewable penetration. *Computers & Electrical Engineering*, *74*, 362–378. https://doi.org/https://doi.org/10.1016/j.compeleceng.2019.02.009

Kamal, F., & Chowdhury, B. (2022). Model predictive control and optimization of networked microgrids. *International Journal of Electrical Power & Energy Systems*, *138*, 107804. https://doi.org/https://doi.org/10.1016/j.ijepes.2021.107804

Kayalvizhi, S., & Vinod Kumar, D. M. (2017). Load Frequency Control of an Isolated Micro Grid Using Fuzzy Adaptive Model Predictive Control. *IEEE Access*, *5*, 16241–16251. https://doi.org/10.1109/ACCESS.2017.2735545

Kennedy, J., & Eberhart, R. (1995). Particle swarm optimization. *Proceedings of ICNN'95 - International Conference on Neural Networks*, *4*, 1942–1948 vol.4. https://doi.org/10.1109/ICNN.1995.488968

Khaleel, M., Yusupov, Z., Yasser, N., & J. El-Khozondar, H. (2023). Enhancing Microgrid Performance through Hybrid Energy Storage System Integration: ANFIS and GA Approaches. *International Journal of Electrical Engineering and Sustainability (IJEES)*, *1*(2), 38–48. https://ijees.org/index.php/ijees/article/view/34

Khalghani, M. R., Khooban, M. H., Mahboubi-Moghaddam, E., Vafamand, N., & Goodarzi, M. (2016). A self-tuning load frequency control strategy for microgrids: Human brain emotional learning. *International Journal of Electrical Power & Energy Systems*, *75*, 311–319. https://doi.org/https://doi.org/10.1016/j.ijepes.2015.08.026

Khokhar, B., Dahiya, S., & Singh Parmar, K. P. (2020). Atom search optimization-based study of frequency deviation response of a hybrid power system. 2020 IEEE 9th Power India International Conference (PIICON), 1–5. https://doi.org/10.1109/PIICON49524.2020.9112932

Khooban, M. H., & Niknam, T. (2015). A new intelligent online fuzzy tuning approach for multi-area load frequency control: Self Adaptive Modified Bat Algorithm.

International Journal of Electrical Power & Energy Systems, *71*, 254–261. https://doi.org/https://doi.org/10.1016/j.ijepes.2015.03.017

Khooban, M. H., Niknam, T., Blaabjerg, F., & Dragičević, T. (2017). A new load frequency control strategy for micro-grids with considering electrical vehicles. *Electric Power Systems Research*, *143*, 585–598. https://doi.org/https://doi.org/10.1016/j.epsr.2016.10.057

Khooban, M.-H., Dragicevic, T., Blaabjerg, F., & Delimar, M. (2018). Shipboard Microgrids: A Novel Approach to Load Frequency Control. *IEEE Transactions on Sustainable Energy*, *9*(2), 843–852. https://doi.org/10.1109/TSTE.2017.2763605

Kler, D., Kumar, V., & Rana, K. P. S. (2019). Optimal integral minus proportional derivative controller design by evolutionary algorithm for thermal-renewable energy-hybrid power systems. *IET Renewable Power Generation*, *13*(11), 2000–2012. https://doi.org/https://doi.org/10.1049/iet-rpg.2018.5745

Kozák, Š. (2014). State-of-the-art in control engineering. *Journal of Electrical Systems and Information Technology*, *1*(1), 1–9. https://doi.org/https://doi.org/10.1016/j.jesit.2014.03.002

Kumar, A., Gaidhane, P. J., & Kumar, V. (2017). A nonlinear fractional order PID controller applied to redundant robot manipulator. *2017 6th International Conference on Computer Applications In Electrical Engineering-Recent Advances (CERA)*, 527–532. https://doi.org/10.1109/CERA.2017.8343385

Kumar, N., Alotaibi, M. A., Singh, A., Malik, H., & Nassar, M. E. (2022). Application of Fractional Order-PID Control Scheme in Automatic Generation Control of a Deregulated Power System in the Presence of SMES Unit. *Mathematics*, *10*(3). https://doi.org/10.3390/math10030521

Kumar, N., Kumar, J., Chaurasia, R., & Sharma, H. (2021). Comparison of Various Load Frequency Control Schemes in Restructured Power System Environment. *Journal of Physics: Conference Series, 3rd International Conference on Computational & Experimental Methods in Mechanical Engineering ICCEMME (2021)*, 1–9.

Kumar, P. K. A., Uthirasamy, R., Saravanan, G., & Ibrahim, A. M. (2016). AGC performance enhancement using ANN. *2016 2nd International Conference on Contemporary Computing and Informatics (IC3I)*, 452–456. https://doi.org/10.1109/IC3I.2016.7918007

Kumar, V., Sharma, V., & Naresh, R. (2023). Leader Harris Hawks algorithm based optimal controller for automatic generation control in PV-hydro-wind integrated power network. *Electric Power Systems Research*, *214*, 108924. https://doi.org/https://doi.org/10.1016/j.epsr.2022.108924

Kumari, D., Chattopadhyay, S. K., & Verma, A. (2020). Improvement of Power Flow Capability By Using An Alternative Power Flow Controller. *IEEE Transactions on Power Delivery*, *35*(5), 2353–2362. https://doi.org/10.1109/TPWRD.2020.2966579

Kumari, N., Malik, N., Jha, A. N., & Mallesham, G. (2017). Design of PI Controller for Automatic Generation Control of Multi Area Interconnected Power System using Bacterial Foraging Optimization. *CoRR*, *abs/1701.08081*. http://arxiv.org/abs/1701.08081

Kumari, R., & Kumar, A. (2023). Power system stabilizer design for ideal AVR using local measurements. *International Journal of Electrical Power & Energy Systems*, *150*, 109061. https://doi.org/https://doi.org/10.1016/j.ijepes.2023.109061

Kundur, P., Balu, N. J., & Lauby, M. G. (1994). Sub-synchronous resonance. In *Power system stability and control* (Vol. 7, pp. 1025–1105). McGraw-hill.

Kundur, P., Paserba, J., Ajjarapu, V., Andersson, G., Bose, A., Canizares, C., Hatziargyriou, N., Hill, D., Stankovic, A., Taylor, C., Van Cutsem, T., & Vittal, V. (2004). Definition and classification of power system stability IEEE/CIGRE joint task force on stability terms and definitions. *IEEE Transactions on Power Systems*, *19*(3), 1387–1401. https://doi.org/10.1109/TPWRS.2004.825981

Latif, A., Das, D. C., Barik, A. K., & Ranjan, S. (2019). Maiden coordinated load frequency control strategy for ST-AWEC-GEC-BDDG-based independent three-area interconnected microgrid system with the combined effect of diverse energy storage and DC link using BOA-optimised PFOID controller. *IET Renewable Power Generation*, *13*(14), 2634–2646. https://doi.org/https://doi.org/10.1049/iet-rpg.2019.0199

Lee, D.-J., & Wang, L. (2008). Small-Signal Stability Analysis of an Autonomous Hybrid Renewable Energy Power Generation/Energy Storage System Part I: Time-Domain Simulations. *IEEE Transactions on Energy Conversion*, *23*(1), 311–320. https://doi.org/10.1109/TEC.2007.914309

Li, H., Hua, Z., Bao, H., Zhu, L., Chen, M., & Bao, B. (2021). Two-Dimensional Memristive Hyperchaotic Maps and Application in Secure Communication. *IEEE Transactions on Industrial Electronics*, *68*(10), 9931–9940. https://doi.org/10.1109/TIE.2020.3022539

Li, H., Wang, X., & Xiao, J. (2019). Adaptive Event-Triggered Load Frequency Control for Interconnected Microgrids by Observer-Based Sliding Mode Control. *IEEE Access*, *7*, 68271–68280. https://doi.org/10.1109/ACCESS.2019.2915954

Li, S., Oshnoei, A., Blaabjerg, F., & Anvari-Moghaddam, A. (2023). Hierarchical Control for Microgrids: A Survey on Classical and Machine Learning-Based Methods. *Sustainability*, *15*(11). https://doi.org/10.3390/su15118952

Li, Z., Shahidehpour, M., Aminifar, F., Alabdulwahab, A., & Al-Turki, Y. (2017). Networked Microgrids for Enhancing the Power System Resilience. *Proceedings of the IEEE*, *105*(7), 1289–1310. https://doi.org/10.1109/JPROC.2017.2685558

Liu, N., Cheng, M., Yu, X., Zhong, J., & Lei, J. (2018a). Energy-Sharing Provider for PV Prosumer Clusters: A Hybrid Approach Using Stochastic Programming and

Stackelberg Game. *IEEE Transactions on Industrial Electronics*, *65*(8), 6740–6750. https://doi.org/10.1109/TIE.2018.2793181

Liu, W., Gu, W., Wang, J., Yu, W., & Xi, X. (2018b). Game Theoretic Non-Cooperative Distributed Coordination Control for Multi-Microgrids. *IEEE Transactions on Smart Grid*, *9*(6), 6986–6997. https://doi.org/10.1109/TSG.2018.2846732

Liu, X., Chen, X., Jin, T., Liu, Z., Liu, Y., Su, M., Li, C., & Wu, Q. (2023). Network-Constrained Peer-to-Peer energy trading for multiple microgrids considering zoning pricing. *International Journal of Electrical Power & Energy Systems*, *147*, 108837. https://doi.org/https://doi.org/10.1016/j.ijepes.2022.108837

Long, C., Wu, J., Zhou, Y., & Jenkins, N. (2018). Peer-to-peer energy sharing through a two-stage aggregated battery control in a community Microgrid. *Applied Energy*, *226*, 261–276. https://doi.org/https://doi.org/10.1016/j.apenergy.2018.05.097

Luo, L., Abdulkareem, S. S., Rezvani, A., Miveh, M. R., Samad, S., Aljojo, N., & Pazhoohesh, M. (2020). Optimal scheduling of a renewable based microgrid considering photovoltaic system and battery energy storage under uncertainty. *Journal of Energy Storage*, *28*, 101306. https://doi.org/https://doi.org/10.1016/j.est.2020.101306

Lurwan, S. M., Mariun, N., Hizam, H., Radzi, M. A. M., & Zakaria, A. (2014). Predicting power output of photovoltaic systems with solar radiation model. *2014 IEEE International Conference on Power and Energy (PECon)*, 304–308. https://doi.org/10.1109/PECON.2014.7062461

Machowski, J., Lubosny, Z., Bialek, J. W., & Bumby, J. R. (2020). *Power system dynamics: stability and control* (3rd ed.). John Wiley & Sons.

Magdy, G., Shabib, G., Elbaset, A. A., Kerdphol, T., Qudaih, Y., Bevrani, H., & Mitani, Y. (2019). Tustin's technique based digital decentralized load frequency control in a realistic multi power system considering wind farms and communications delays. *Ain Shams Engineering Journal*, *10*(2), 327–341. https://doi.org/https://doi.org/10.1016/j.asej.2019.01.004

Malik, O. P., Kumar, A., & Hope, G. S. (1988). A load frequency control algorithm based on a generalized approach. *IEEE Transactions on Power Systems*, *3*(2), 375–382. https://doi.org/10.1109/59.192887

Mansour, S., Badr, A. O., Attia, M. A., Sameh, M. A., Kotb, H., Elgamli, E., & Shouran, M. (2022). Fuzzy Logic Controller Equilibrium Base to Enhance AGC System Performance with Renewable Energy Disturbances. *Energies*, *15*(18). https://doi.org/10.3390/en15186709

Mi, Y., Fu, Y., Wang, C., & Wang, P. (2013). Decentralized Sliding Mode Load Frequency Control for Multi-Area Power Systems. *IEEE Transactions on Power Systems*, *28*(4), 4301–4309. https://doi.org/10.1109/TPWRS.2013.2277131

Mishra, A. K., Mishra, P., & Mathur, H. D. (2022). Enhancing the performance of a deregulated nonlinear integrated power system utilizing a redox flow battery with a self-tuning fractional-order fuzzy controller. *ISA Transactions*, *121*, 284–305. https://doi.org/https://doi.org/10.1016/j.isatra.2021.04.002

Mohamed Mostafa Elsaied Mahmoud Abdallah Attia, M. A. M., & Mekhamer, S. F. (2018). Application of Different Optimization Techniques to Load Frequency Control with WECS in a Multi-Area System. *Electric Power Components and Systems*, *46*(7), 739–756. https://doi.org/10.1080/15325008.2018.1509913

Mohanty, B. (2020). Hybrid flower pollination and pattern search algorithm optimized sliding mode controller for deregulated AGC system. *Journal of Ambient Intelligence and Humanized Computing*, *11*(2), 763–776. https://doi.org/10.1007/s12652-019-01348-5

Mohanty, B., Hota, P. K., & Paikray, A. (2014). Performance evaluation of differential evolution algorithm on automatic generation control. *2014 International Conference on Circuits, Power and Computing Technologies [ICCPCT-2014]*, 763–768. https://doi.org/10.1109/ICCPCT.2014.7054840

Morsali, J., Zare, K., & Tarafdar Hagh, M. (2014). Appropriate generation rate constraint (GRC) modeling method for reheat thermal units to obtain optimal load frequency controller (LFC). *2014 5th Conference on Thermal Power Plants (CTPP)*, 29–34. https://doi.org/10.1109/CTPP.2014.7040611

Mossa, M. A., Kamel, O. M., Sultan, H. M., & Diab, A. A. Z. (2021). Parameter estimation of PEMFC model based on Harris Hawks' optimization and atom search optimization algorithms. Neural Computing and Applications, 33(11), 5555–5570. https://doi.org/10.1007/s00521-020-05333-4

Mu, C., Zhang, Y., Jia, H., & He, H. (2020). Energy-Storage-Based Intelligent Frequency Control of Microgrid With Stochastic Model Uncertainties. *IEEE Transactions on Smart Grid*, *11*(2), 1748–1758. https://doi.org/10.1109/TSG.2019.2942770

Mundra, P., Arya, A., & Gawre, S. K. (2023). An Efficient Model for Forecasting Renewable Energy Using Ensemble LSTM Based Hybrid Chaotic Atom Search Optimization. *Neural Processing Letters*, *55*(2), 1625–1647. https://doi.org/10.1007/s11063-022-10954-y

Naderi, M., Khayat, Y., Shafiee, Q., Blaabjerg, F., & Bevrani, H. (2023). Dynamic modeling, stability analysis and control of interconnected microgrids: A review. *Applied Energy*, *334*, 120647. https://doi.org/https://doi.org/10.1016/j.apenergy.2023.120647

Naderipour, A., Abdul-Malek, Z., Davoodkhani, I. F., Kamyab, H., & Ali, R. R. (2023). Load-frequency control in an islanded microgrid PV/WT/FC/ESS using an optimal self-tuning fractional-order fuzzy controller. *Environmental Science and Pollution Research*, *30*(28), 71677–71688. https://doi.org/10.1007/s11356-021-14799-1

Nasiri, N., Zeynali, S., & Ravadanegh, S. N. (2022). A tactical transactive energy scheduling for the electric vehicle-integrated networked microgrids. *Sustainable Cities and Society*, *83*, 103943. https://doi.org/https://doi.org/10.1016/j.scs.2022.103943

Nazir, A., Singh, M., Destefanis, G., Memon, J., Neykova, R., Kassab, M., & Tonelli, R. (2023). An Optimized Concurrent Proof of Authority Consensus Protocol. *2023 IEEE International Conference on Software Analysis, Evolution and Reengineering (SANER)*, 874–877. https://doi.org/10.1109/SANER56733.2023.00105

Obaid, Z. A., Cipcigan, L. M., & Muhssin, M. T. (2016). Fuzzy hierarchal approach-based optimal frequency control in the Great Britain power system. *Electric Power Systems Research*, *141*, 529–537. https://doi.org/https://doi.org/10.1016/j.epsr.2016.08.032

Pandey, S. K., Mohanty, S. R., Kishor, N., & Payasi, R. P. (2013). Iterative linear matrix inequality algorithm based decentralized controller for load frequency control of two-area thermal power systems. *2013 International Conference on Power, Energy and Control (ICPEC)*, 431–436. https://doi.org/10.1109/ICPEC.2013.6527695

Parmar, K. P. S., Majhi, S., & Kothari, D. P. (2014). LFC of an interconnected power system with multi-source power generation in deregulated power environment. *International Journal of Electrical Power & Energy Systems*, *57*, 277–286. https://doi.org/https://doi.org/10.1016/j.ijepes.2013.11.058

Pathak, D., Bhati, S., & Gaur, P. (2020). Fractional-order nonlinear PID controller based maximum power extraction method for a direct-driven wind energy system. *International Transactions on Electrical Energy Systems*, *30*(12), e12641.

Peng, C., Zhang, J., & Yan, H. (2018). Adaptive Event-Triggering H_ Load Frequency Control for Network-Based Power Systems. *IEEE Transactions on Industrial Electronics*, *65*(2), 1685–1694. https://doi.org/10.1109/TIE.2017.2726965

Podlubny, I. (1999). Fractional-order systems and PI/sup /spl lambda//D/sup /spl mu//-controllers. *IEEE Transactions on Automatic Control*, *44*(1), 208–214. https://doi.org/10.1109/9.739144

Pokhrel, S. R., & Choi, J. (2020). Federated Learning With Blockchain for Autonomous Vehicles: Analysis and Design Challenges. *IEEE Transactions on Communications*, *68*(8), 4734–4746. https://doi.org/10.1109/TCOMM.2020.2990686

Posner, J., Tseng, L., Aloqaily, M., & Jararweh, Y. (2021). Federated Learning in Vehicular Networks: Opportunities and Solutions. *IEEE Network*, *35*(2), 152–159. https://doi.org/10.1109/MNET.011.2000430

Prajapati, Y. R., Kamat, V. N., & Patel, J. (2020). Load Frequency Control Under Restructured Power System Using Electrical Vehicle as Distributed Energy Source. *Journal of The Institution of Engineers (India): Series B*, *101*(4), 379–387. https://doi.org/10.1007/s40031-020-00458-5

Prasad, S., & Ansari, M. R. (2020). Frequency regulation using neural network observer based controller in power system. *Control Engineering Practice*, *102*, 104571. https://doi.org/https://doi.org/10.1016/j.conengprac.2020.104571

Rahim, S. A., Ahmed, S., & Nawari, M. (2018). A Study of Load Frequency Control for Two Area Power System Using Two Controllers. *2018 International Conference on Computer, Control, Electrical, and Electronics Engineering (ICCCEEE)*, 1–6. https://doi.org/10.1109/ICCCEEE.2018.8515892

Rahman, A., Farrok, O., & Haque, M. M. (2022). Environmental impact of renewable energy source based electrical power plants: Solar, wind, hydroelectric, biomass, geothermal, tidal, ocean, and osmotic. *Renewable and Sustainable Energy Reviews*, *161*, 112279. https://doi.org/https://doi.org/10.1016/j.rser.2022.112279

Rai, A., & Das, D. K. (2020). Optimal PID Controller Design by Enhanced Class Topper Optimization Algorithm for Load Frequency Control of Interconnected Power Systems. *Smart Science*, *8*(3), 125–151. https://doi.org/10.1080/23080477.2020.1805540

Rajesh, K. S., & Dash, S. S. (2019a). Load frequency control of autonomous power system using adaptive fuzzy based PID controller optimized on improved sine cosine algorithm. *Journal of Ambient Intelligence and Humanized Computing*, *10*(6), 2361–2373. https://doi.org/10.1007/s12652-018-0834-z

Rajesh, K. S., Dash, S. S., & Rajagopal, R. (2019b). Hybrid improved firefly-pattern search optimized fuzzy aided PID controller for automatic generation control of power systems with multi-type generations. *Swarm and Evolutionary Computation*, *44*, 200–211. https://doi.org/https://doi.org/10.1016/j.swevo.2018.03.005

Raju, M., Saikia, L. C., Sinha, N., & Saha, D. (2017). Application of antlion optimizer technique in restructured automatic generation control of two-area hydro-thermal system considering governor dead band. *2017 Innovations in Power and Advanced Computing Technologies (i-PACT)*, 1–6. https://doi.org/10.1109/IPACT.2017.8245099

Raju More and Sarma, U. and S. L. C. (2020). Application of Firefly Algorithm Optimized Fuzzy 2DOFPID Controller for Diverse-Sourced Multi-area LFC. In N. K. and P. R. K. and S. V. P. Giri V. K. and Verma (Ed.), *Computing Algorithms with Applications in Engineering* (pp. 261–267). Springer Singapore.

Ramachandran, R., Madasamy, B., Veerasamy, V., & Saravanan, L. (2018). Load frequency control of a dynamic interconnected power system using generalised Hopfield neural network based self-adaptive PID controller. *IET Generation, Transmission & Distribution*, *12*(21), 5713–5722. https://doi.org/https://doi.org/10.1049/iet-gtd.2018.5622

Ramachandran, R., Satheesh Kumar, J., Madasamy, B., & Veerasamy, V. (2021). A hybrid MFO-GHNN tuned self-adaptive FOPID controller for ALFC of renewable energy integrated hybrid power system. *IET Renewable Power Generation*, *15*(7), 1582–1595. https://doi.org/https://doi.org/10.1049/rpg2.12134

Rayati, M., Sheikhi, A., & Ranjbar, A. M. (2019). Optimal Contract Design for Purchasing From Frequency Regulation Service Providers With Private Information. *IEEE Transactions on Power Systems*, *34*(3), 2445–2448. https://doi.org/10.1109/TPWRS.2019.2895561

Sahu, B. K., Pati, T. K., Nayak, J. R., Panda, S., & Kar, S. K. (2016). A novel hybrid LUS–TLBO optimized fuzzy-PID controller for load frequency control of multi-source power system. *International Journal of Electrical Power & Energy Systems*, *74*, 58–69. https://doi.org/https://doi.org/10.1016/j.ijepes.2015.07.020

Sahu, R. K., Chandra Sekhar, G. T., & Panda, S. (2015). DE optimized fuzzy PID controller with derivative filter for LFC of multi source power system in deregulated environment. *Ain Shams Engineering Journal*, *6*(2), 511–530. https://doi.org/https://doi.org/10.1016/j.asej.2014.12.009

Saikia, L. C., Paul, A., Dash, P., & Dev Choudhury, N. B. (2014). AGC of an interconnected multi-area hydrothermal system using a neuro-fuzzy controller. *Proceedings of The 2014 International Conference on Control, Instrumentation, Energy and Communication (CIEC)*, 407–411. https://doi.org/10.1109/CIEC.2014.6959120

Sasaki, T., & Enomoto, K. (2002). Statistical and dynamic analysis of generation control performance standards. *IEEE Transactions on Power Systems*, *17*(2), 476–481. https://doi.org/10.1109/TPWRS.2002.1007921

Sasaki, T., & Enomoto, K. (2003). Closure on “Statistical and dynamic analysis of generation control performance standards.” *IEEE Transactions on Power Systems*, *18*(1), 410–413. https://doi.org/10.1109/TPWRS.2002.807057

Saurabh, K., Gupta, N. K., & Singh, A. K. (2020). Fractional Order Controller Design for Load Frequency Control of Single Area and Two Area System. *2020 7th International Conference on Signal Processing and Integrated Networks (SPIN)*, 531–536. https://doi.org/10.1109/SPIN48934.2020.9070993

Saxena, S., & Hote, Y. V. (2018). PI Controller Based Load Frequency Control Approach for Single-Area Power System Having Communication Delay. *IFAC-PapersOnLine*, *51*(4), 622–626. https://doi.org/https://doi.org/10.1016/j.ifacol.2018.06.165

Schiffer, J., Dörfler, F., & Fridman, E. (2017). Robustness of distributed averaging control in power systems: Time delays & dynamic communication topology. *Automatica*, *80*, 261–271. https://doi.org/https://doi.org/10.1016/j.automatica.2017.02.040

Shangguan, X.-C., He, Y., Zhang, C.-K., Jin, L., Yao, W., Jiang, L., & Wu, M. (2022). Control Performance Standards-Oriented Event-Triggered Load Frequency Control for Power Systems Under Limited Communication Bandwidth. *IEEE*

Transactions on Control Systems Technology, *30*(2), 860–868. https://doi.org/10.1109/TCST.2021.3070861

Sharma, G., Panwar, A., Arya, Y., & Kumawat, M. (2020). Integrating layered recurrent ANN with robust control strategy for diverse operating conditions of AGC of the power system. *IET Generation, Transmission & Distribution*, *14*(18), 3886–3895. https://doi.org/https://doi.org/10.1049/iet-gtd.2019.0935

Shayeghi, H., Rahnama, A., & Alhelou, H. H. (2021). Frequency control of fully-renewable interconnected microgrid using fuzzy cascade controller with demand response program considering. *Energy Reports*, *7*, 6077–6094. https://doi.org/https://doi.org/10.1016/j.egyr.2021.09.027

Shiroei, M., Toulabi, M. R., & Ranjbar, A. M. (2013). Robust multivariable predictive based load frequency control considering generation rate constraint. *International Journal of Electrical Power & Energy Systems*, *46*, 405–413. https://doi.org/https://doi.org/10.1016/j.ijepes.2012.10.039

Shojaee, M., Mohammadi Shakiba, F., & Azizi, S. M. (2022). Decentralized Model-Predictive Control of a Coupled Wind Turbine and Diesel Engine Generator System. *Energies*, *15*(9). https://doi.org/10.3390/en15093349

Siano, P., & Mohammad, D. (2021). MILP Optimization model for assessing the participation of distributed residential PV-battery systems in ancillary services market. *CSEE Journal of Power and Energy Systems*, *7*(2), 348–357. https://doi.org/10.17775/CSEEJPES.2020.01170

Singh, T. (2022). Chaotic slime mould algorithm for economic load dispatch problems. *Applied Intelligence*, *52*(13), 15325–15344. https://doi.org/10.1007/s10489-022-03179-y

Siti, M. W., Mbungu, N. T., Tungadio, D. H., Banza, B. B., & Ngoma, L. (2022). Application of load frequency control method to a multi-microgrid with energy storage system. *Journal of Energy Storage*, *52*, 104629. https://doi.org/https://doi.org/10.1016/j.est.2022.104629

Sondhi, S., & Hote, Y. V. (2014b). Stability testing and IMC based fractional order PID controller design for heating furnace system. *2014 Annual IEEE India Conference (INDICON)*, 1–5. https://doi.org/10.1109/INDICON.2014.7030379

Song, J., Wang, L., Cai, G., & Qi, X. (2015). Nonlinear fractional order proportion-integral-derivative active disturbance rejection control method design for hypersonic vehicle attitude control. *Acta Astronautica*, *111*, 160–169. https://doi.org/https://doi.org/10.1016/j.actaastro.2015.02.026

Sudha, K. R., & Vijaya Santhi, R. (2011). Robust decentralized load frequency control of interconnected power system with Generation Rate Constraint using Type-2 fuzzy approach. *International Journal of Electrical Power & Energy Systems*, *33*(3), 699–707. https://doi.org/https://doi.org/10.1016/j.ijepes.2010.12.027

Sun, P., Liu, H., Zhang, Y., Tu, L., & Meng, Q. (2021). An intensify atom search optimization for engineering design problems. Applied Mathematical Modelling, 89, 837–859. https://doi.org/https://doi.org/10.1016/j.apm.2020.07.052

Taghizadegan, N., Babaei, F., & Safari, A. (2023). A linear active disturbance rejection control technique for frequency control of networked microgrids. *Energy Systems*. https://doi.org/10.1007/s12667-023-00563-6

Tan, W. (2011). Decentralized load frequency controller analysis and tuning for multi-area power systems. *Energy Conversion and Management*, *52*(5), 2015–2023. https://doi.org/https://doi.org/10.1016/j.enconman.2010.12.011

Tasnin, W., Saikia, L. C., & Raju, M. (2018). Deregulated AGC of multi-area system incorporating dish-Stirling solar thermal and geothermal power plants using fractional order cascade controller. *International Journal of Electrical Power & Energy Systems*, *101*, 60–74. https://doi.org/https://doi.org/10.1016/j.ijepes.2018.03.015

Tian, Y., & Lu, Z. (2017). Chaotic S-Box: Intertwining Logistic Map and Bacterial Foraging Optimization. *Mathematical Problems in Engineering*, *2017*, 6969312. https://doi.org/10.1155/2017/6969312

Too, J., & Abdullah, A. R. (2020). Binary atom search optimisation approaches for feature selection. Connection Science, 32(4), 406–430. https://doi.org/10.1080/09540091.2020.1741515

Tripathy, S. C., Balasubramanian, R., & Nair, P. S. C. (1992). Effect of superconducting magnetic energy storage on automatic generation control considering governor deadband and boiler dynamics. *IEEE Transactions on Power Systems*, *7*(3), 1266–1273. https://doi.org/10.1109/59.207343

Truong, H. T., Ta, B. P., Le, Q. A., Nguyen, D. M., Le, C. T., Nguyen, H. X., Do, H. T., Nguyen, H. T., & Tran, K. P. (2022). Light-weight federated learning-based anomaly detection for time-series data in industrial control systems. *Computers in Industry*, *140*, 103692. https://doi.org/https://doi.org/10.1016/j.compind.2022.103692

Tushar, W., Saha, T. K., Yuen, C., Morstyn, T., McCulloch, M. D., Poor, H. V., & Wood, K. L. (2019). A motivational game-theoretic approach for peer-to-peer energy trading in the smart grid. *Applied Energy*, *243*, 10–20. https://doi.org/https://doi.org/10.1016/j.apenergy.2019.03.111

Vedady Moghadam, M. R., Ma, R. T. B., & Zhang, R. (2014). Distributed Frequency Control in Smart Grids via Randomized Demand Response. *IEEE Transactions on Smart Grid*, *5*(6), 2798–2809. https://doi.org/10.1109/TSG.2014.2316913

Veerasamy, V., Abdul Wahab, N. I., Ramachandran, R., Othman, M. L., Hizam, H., Satheesh Kumar, J., & Irudayaraj, A. X. R. (2022). Design of single- and multi-loop self-adaptive PID controller using heuristic based recurrent neural network for ALFC of hybrid power system. *Expert Systems with Applications*, *192*, 116402. https://doi.org/https://doi.org/10.1016/j.eswa.2021.116402

Veerasamy, V., Abdul Wahab, N. I., Ramachandran, R., Vinayagam, A., Othman, M. L., Hizam, H., & Satheeshkumar, J. (2019). Automatic Load Frequency Control of a Multi-Area Dynamic Interconnected Power System Using a Hybrid PSO-GSA-Tuned PID Controller. *Sustainability*, *11*(24). https://doi.org/10.3390/su11246908

Veerasamy, V., Sampath, L. P. M. I., Singh, S., Nguyen, H. D., & Gooi, H. B. (2023). Blockchain-based Decentralized Frequency Control of Microgrids using Federated Learning Fractional-Order Recurrent Neural Network. *IEEE Transactions on Smart Grid*, 1. https://doi.org/10.1109/TSG.2023.3267503

Veerasamy, V., Wahab, N. I. A., Ramachandran, R., Othman, M. L., Hizam, H., Irudayaraj, A. X. R., Guerrero, J. M., & Kumar, J. S. (2020). A Hankel Matrix Based Reduced Order Model for Stability Analysis of Hybrid Power System Using PSO-GSA Optimized Cascade PI-PD Controller for Automatic Load Frequency Control. *IEEE Access*, *8*, 71422–71446. https://doi.org/10.1109/ACCESS.2020.2987387

Wang, L., & Huang, C.-B. (2010). Dynamic Stability Analysis of a Grid-Connected Solar-Concentrated Ocean Thermal Energy Conversion System. *IEEE Transactions on Sustainable Energy*, *1*(1), 10–18. https://doi.org/10.1109/TSTE.2010.2046189

Wang, X., Wang, C., Li, X., Leung, V. C. M., & Taleb, T. (2020). Federated Deep Reinforcement Learning for Internet of Things With Decentralized Cooperative Edge Caching. *IEEE Internet of Things Journal*, *7*(10), 9441–9455. https://doi.org/10.1109/JIOT.2020.2986803

Weedy, B. M., Cory, B. J., Jenkins, N., Ekanayake, J. B., & Strbac, G. (2012). *Electric power systems* (5th ed.). John Wiley & Sons.

Wen, G.-X., Chen, C. L. P., Liu, Y.-J., & Liu, Z. (2015). Neural-network-based adaptive leader-following consensus control for second-order non-linear multi-agent systems. *IET Control Theory & Applications*, *9*(13), 1927–1934. https://doi.org/https://doi.org/10.1049/iet-cta.2014.1319

Xia, Y., Xu, Y., Wang, Y., Mondal, S., Dasgupta, S., Gupta, A. K., & Gupta, G. M. (2022). A Safe Policy Learning-Based Method for Decentralized and Economic Frequency Control in Isolated Networked-Microgrid Systems. *IEEE Transactions on Sustainable Energy*, *13*(4), 1982–1993. https://doi.org/10.1109/TSTE.2022.3178415

Yang, D., Li, G., & Cheng, G. (2007). On the efficiency of chaos optimization algorithms for global optimization. *Chaos, Solitons & Fractals*, *34*(4), 1366–1375. https://doi.org/https://doi.org/10.1016/j.chaos.2006.04.057

Yang, F., Yu, S., Zhao, J., Li, D., & Lin, S. (2023). Distributed reconfigurable model predictive control based load frequency control of microgrid clusters with dynamic topology. *Electric Power Systems Research*, *221*, 109445. https://doi.org/https://doi.org/10.1016/j.epsr.2023.109445

Yang, J., Dai, J., Gooi, H. B., Nguyen, H. D., & Paudel, A. (2022a). A Proof-of-Authority Blockchain-Based Distributed Control System for Islanded Microgrids. *IEEE Transactions on Industrial Informatics*, *18*(11), 8287–8297. https://doi.org/10.1109/TII.2022.3142755

Yang, M.-H., & Yeh, R.-H. (2022b). Investigation of the potential of R717 blends as working fluids in the organic Rankine cycle (ORC) for ocean thermal energy conversion (OTEC). *Energy*, *245*, 123317. https://doi.org/https://doi.org/10.1016/j.energy.2022.123317

Yousri, D., Mirjalili, S., Machado, J. A. T., Thanikanti, S. B., elbaksawi, O., & Fathy, A. (2021). Efficient fractional-order modified Harris hawks optimizer for proton exchange membrane fuel cell modeling. *Engineering Applications of Artificial Intelligence*, *100*, 104193. https://doi.org/https://doi.org/10.1016/j.engappai.2021.104193

Yu, X., & Tomsovic, K. (2004). Application of linear matrix inequalities for load frequency control with communication delays. *IEEE Transactions on Power Systems*, *19*(3), 1508–1515. https://doi.org/10.1109/TPWRS.2004.831670

Zamee, M. A., Islam, K. K., Ahmed, A., & Zafreen, K. R. (2016). Differential evolution algorithm based load frequency control in a two-area conventional and renewable energy based nonlinear power system. *2016 4th International Conference on the Development in the in Renewable Energy Technology (ICDRET)*, 1–6. https://doi.org/10.1109/ICDRET.2016.7421476

Zhang, B., Rahmatullah, B., Wang, S. L., & Liu, Z. (2023a). A plain-image correlative semi-selective medical image encryption algorithm using enhanced 2D-logistic map. *Multimedia Tools and Applications*, *82*(10), 15735–15762. https://doi.org/10.1007/s11042-022-13744-9

Zhang, H., Liu, J., & Xu, S. (2020a). H-Infinity Load Frequency Control of Networked Power Systems via an Event-Triggered Scheme. *IEEE Transactions on Industrial Electronics*, *67*(8), 7104–7113. https://doi.org/10.1109/TIE.2019.2939994

Zhang, H., Liu, T., Ye, X., Heidari, A. A., Liang, G., Chen, H., & Pan, Z. (2023b). Differential evolution-assisted salp swarm algorithm with chaotic structure for real-world problems. *Engineering with Computers*, *39*(3), 1735–1769. https://doi.org/10.1007/s00366-021-01545-x

Zhang, K., Troitzsch, S., Hanif, S., & Hamacher, T. (2020b). Coordinated Market Design for Peer-to-Peer Energy Trade and Ancillary Services in Distribution Grids. *IEEE Transactions on Smart Grid*, *11*(4), 2929–2941. https://doi.org/10.1109/TSG.2020.2966216

Zhang, Y., & Yang, T. (2020c). Decentralized Switching Control Strategy for Load Frequency Control in Multi-Area Power Systems With Time Delay and Packet Losses. *IEEE Access*, *8*, 15838–15850. https://doi.org/10.1109/ACCESS.2020.2967455

Zhao, W., Shi, T., Wang, L., Cao, Q., & Zhang, H. (2021). An adaptive hybrid atom search optimization with particle swarm optimization and its application to optimal no-load PID design of hydro-turbine governor. *Journal of Computational Design and Engineering*, *8*(5), 1204–1233. https://doi.org/10.1093/jcde/qwab041

Zhao, W., Wang, L., & Zhang, Z. (2019a). Atom search optimization and its application to solve a hydrogeologic parameter estimation problem. *Knowledge-Based Systems*, *163*, 283–304. https://doi.org/https://doi.org/10.1016/j.knosys.2018.08.030

Zhao, W., Wang, L., & Zhang, Z. (2019b). A novel atom search optimization for dispersion coefficient estimation in groundwater. Future Generation Computer Systems, 91, 601–610. https://doi.org/https://doi.org/10.1016/j.future.2018.05.037

Zhou, Y., Wei, Z., Sun, G., Cheung, K. W., Zang, H., & Chen, S. (2018). A robust optimization approach for integrated community energy system in energy and ancillary service markets. *Energy*, *148*, 1–15. https://doi.org/https://doi.org/10.1016/j.energy.2018.01.078

Ziegler, J. G., & Nichols, N. B. (1942). Optimum Settings for Automatic Controllers. *Transactions of the American Society of Mechanical Engineers*, *64*(8), 759–765. https://doi.org/10.1115/1.4019264

APPENDICES

Appendix A

In chapter 5, in section 4.2.5, The 48th order of transfer function obtained after approximation is given below

Numerator=

$$
\begin{aligned}
&-6s^{47}-690.5s^{46}-3.034\times10^{4}s^{40}-6.791\times10^{5}s^{39}-8.593\times10^{6}s^{35}-6.338\times10^{7}s^{33}-2.682\times10^{8}s^{32}\\
&-6.212\times10^{8}s^{30}-7.668\times10^{8}s^{29}-4.839\times10^{8}s^{28}-1.384\times10^{8}s^{27}-1.376\times10^{7}s^{26}-3.995\times10^{5}s^{25}\\
&-4.18\times10^{8}s^{22}-2.8\times10^{8}s^{21}-12.89\times10^{8}s^{20}-16.25\times10^{8}s^{19}-2.8\times10^{7}s^{15}-3.995\times10^{5}s^{14}\\
&-4\times10^{5}s^{13}-8.252\times10^{8}s^{22}-12.89\times10^{8}s^{10}-16.25\times10^{8}s^{11}-2.8\times10^{7}s^{9}-3.995\times10^{5}s^{8}\\
&8.1\times10^{8}s^{7}-2.5\times10^{8}s^{5}-25\times10^{8}s^{3}-2.22\times10^{7}s^{2}-9.995\times10^{5}s
\end{aligned}
$$

Denominator=

$$
\begin{aligned}
&s^{48}+115.1s^{47}+5302s^{45}+1.387\times10^{5}s^{44}+2.406\times10^{6}s^{43}+2.841\times10^{7}s^{42}+2.173\times10^{8}s^{41}+9.974\times10^{8}s^{40}\\
&+2.553\times10^{9}s^{39}+3.671\times10^{9}s^{38}+2.985\times10^{9}s^{37}+1.372\times10^{9}s^{36}+3.348\times10^{8}s^{35}+3.036\times10^{7}s^{34}+7.708\times10^{30}\\
&+0.25\times10^{9}s^{29}+3.85\times10^{9}s^{28}+18.2\times10^{9}s^{27}+5.20\times10^{9}s^{26}+3.12\times10^{8}s^{25}+9.03\times10^{7}s^{24}+9.25\times10^{20}\\
&+6.25\times10^{9}s^{19}+15.23\times10^{9}s^{18}+0.25\times10^{9}s^{17}+5.36\times10^{9}s^{11}+9.25\times10^{8}s^{10}+8.25\times10^{7}s^{9}+0.89\times10^{8}\\
&+0.753\times10^{9}s^{7}+8.32\times10^{9}s^{6}+12.85\times10^{9}s^{5}+89.2\times10^{9}s^{4}+46.8\times10^{8}s^{2}+89.25\times10^{7}s+8.21
\end{aligned}
\tag{A.1}
$$

To assess the stability of the proposed work, the higher-order plant transfer function given above should be reduced to a second-order transfer function. This reduction was achieved by preserving the dominant poles of the system through the utilization of the Hankel matrix method. The state space matrix (A, B, C, and D) for the Closed-Loop Transfer Function (CLTF) given in Equation (A.1) is given below.

$$
A=\begin{bmatrix}
1.5 & 0 & -0.55 & 0 & 0 & 1 & -0.98 & -646.23 & 0 & 0 & 0 & 1 & 0 & 0 \\
-756.7 & -0.05 & 0.45 & 0 & 0 & -646.56 & -0.85 & 0 & 0 & 0 & 1 & 0 & 0 & 0 \\
-0.5 & 0.55 & -858.5 & 0 & 0 & 1 & 1 & 0 & 0 & 0 & 1 & 0 & 0 & 1 \\
-12.62 & 0.98 & 8.25 & 0 & 0 & 0 & 0 & 1 & 1 & 1 & 0 & 0 & 0 & 0 \\
-0.58 & 1.5 & 2.98 & 0 & 0 & 0 & 0 & 1 & 0 & 0 & 1 & 1 & 0 & 0 \\
7.58 & -0.45 & 3.85 & -745.12 & 1 & 1 & 1 & 0 & 1 & 0 & 1 & 0 & 1 & 0 \\
0 & 0 & -12.52 & 0 & 1 & 0 & -12.63 & -9.25 & -80 & 0.12 & 0 & 0 & 0 & 0 \\
0 & 0 & -8.95 & 0 & 8.5 & 0 & -1.58 & 8.87 & -1.585 & -5.6 & 0 & 1 & 0 & 0 \\
0 & 0 & 9.78 & 0 & -2.56 & 0 & 3.56 & 0 & -3.6 & -1.58 & 0 & 0 & 0 & -2.3 \\
0 & 0 & 1.25 & 0 & -756.85 & 0 & 347.62 & 0 & 100 & 0 & -10.215 & 0 & 0 & -15.85 \\
0 & -12.62 & 0 & 0 & 0 & 1 & 0 & 0 & 678.52 & 1 & 0 & 0 & 0 & 0 \\
0 & 1.5 & 0 & 1 & 0 & 1 & 0 & 0 & 0 & 0 & -100 & -1.25 & 0 & 0 \\
-725.21 & 352.85 & 0 & -18.52 & 0 & 0 & 0 & 0 & 0 & 0 & 0 & 0 & 0 & 0 \\
-9.87 & -1.258 & 0 & -646.28 & 0 & 0 & 1 & 1 & 1 & 0 & 1 & 0 & 785.32 & 1
\end{bmatrix} \tag{A.2}
$$

$$
B=\begin{bmatrix}
0 & 0 & 0 & 0.15 & 0 & 0 & 0 & 0 & 0 & 0 & 0 & 0 & 0 & 0 \\
0 & 0 & 0 & 0 & 18.5 & 0 & 0 & 0 & 0 & 0 & 0 & 0 & 0 & 0
\end{bmatrix}^{T} \tag{A.3}
$$

$$
C=\begin{bmatrix} 1 & 0 & 1 & 0 & 0 & 0 & 0 & 0 & 0 & 0 & 0 & 0 & 1 & 0 \end{bmatrix}^{T} \tag{A.4}
$$

The Hankel matrix is derived from the state space matrix in a general form as outlined below.

$$
H_{nn}^{(0)}=\begin{bmatrix}
CB & CA^{-1}B & \dots & \dots & CA^{-n+1}B \\
CA^{-1}B & CA^{-2}B & \dots & \dots & CA^{-n}B \\
\dots & \dots & \dots & \dots & \dots \\
CA^{-n+2}B & CA^{-n+1}B & \dots & \dots & CA^{-2n+3}B \\
CA^{-n+1}B & CA^{-n}B & \dots & \dots & CA^{-2n+2}B
\end{bmatrix} \tag{A.5}
$$

As given in Equation (A.1) the transfer function's order is 48 (n=48), the matrix Equation (A.2) mentioned above can be represented in Hankel form as follows:

$$
H_{4848}^{(0)}=\begin{bmatrix}
e_{11} & e_{12} & e_{13} & \dots & e_{1n} \\
e_{21} & e_{22} & e_{23} & \dots & e_{2n} \\
e_{31} & e_{32} & e_{34} & \dots & e_{3n} \\
\dots & \dots & \dots & \dots & \dots \\
e_{n1} & e_{n2} & e_{n3} & \dots & e_{nn}
\end{bmatrix} \tag{A.6}
$$

The simplified form of Equation (A.3) is represented as

$$H_{4848}^{(0)} = \left[H_1^{(0)} \quad H_2^{(0)} \right] \tag{A.7}$$

The Hankel matrices in Hermite normal form are represented as follows

$$\mathrm{H}_1^{(0)} = \begin{bmatrix} 6.12\times10^{-12} & 3.0\times10^{02} & 2.98\times10^{-03} & 6.32\times10^{01} & 5.23\times10^{04} & -7.12\times10^{06} & 5.36\times10^{08} \\ -8.3\times10^{01} & 2.98\times10^{-01} & 3.19\times10^{01} & 5.25\times10^{02} & -3.25\times10^{06} & 8.15\times10^{08} & -5.89\times10^{10} \\ 3.00\times10^{-01} & 1.59\times10^{01} & 8.08\times10^{04} & -9.05\times10^{06} & 9.17\times10^{08} & -9.29\times10^{10} & 9.43\times10^{12} \\ 1.59\times10^{01} & 8.08\times10^{04} & -9.05\times10^{06} & 9.17\times10^{08} & -9.29\times10^{10} & 9.43\times10^{12} & -9.57\times10^{14} \\ 8.08\times10^{04} & -9.05\times10^{06} & 9.17\times10^{08} & -9.29\times10^{10} & 9.43\times10^{12} & -9.57\times10^{14} & 9.71\times10^{16} \\ -9.05\times10^{06} & 9.1704\times10^{08} & -9.29\times10^{10} & 9.43\times10^{12} & -9.57\times10^{14} & 9.71\times10^{16} & -9.85\times10^{18} \\ 9.17\times10^{08} & -9.29\times10^{10} & 9.43\times10^{12} & -9.57\times10^{14} & 9.71\times10^{16} & -9.85\times10^{18} & 1.00\times10^{21} \\ -9.29\times10^{10} & 9.43\times10^{12} & -9.57\times10^{14} & 9.71\times10^{16} & -9.85\times10^{18} & 1.00\times10^{21} & -1.01\times10^{23} \\ 9.43\times10^{12} & -9.57\times10^{14} & 9.71\times10^{16} & -9.85\times10^{18} & 1.00\times10^{21} & -1.01\times10^{23} & 1.03\times10^{25} \\ -9.57\times10^{14} & 9.71\times10^{16} & -9.85\times10^{18} & 1.00\times10^{21} & -1.01\times10^{23} & 1.03\times10^{25} & -1.04\times10^{27} \\ 9.71\times10^{16} & -9.85\times10^{18} & 1.00\times10^{21} & -1.01\times10^{23} & 1.03\times10^{25} & -1.04\times10^{27} & 1.06\times10^{29} \\ -9.85\times10^{18} & 1.00\times10^{21} & -1.01\times10^{23} & 1.03\times10^{25} & -1.04\times10^{27} & 1.06\times10^{29} & -1.07\times10^{31} \\ 1.59\times10^{01} & -9.29\times10^{10} & -9.57\times10^{14} & 1.00\times10^{21} & 1.03\times10^{25} & 5.36\times10^{08} & 9.17\times10^{08} \\ 9.43\times10^{12} & -9.29\times10^{10} & 1.59\times10^{01} & 9.05\times10^{06} & 5.25\times10^{02} & 9.17\times10^{08} & 9.43\times10^{12} \end{bmatrix}$$

$$\mathrm{H}_2^{(0)} = \begin{bmatrix} -9.29\times10^{10} & 9.43\times10^{12} & -9.57\times10^{14} & 9.71\times10^{16} & -9.85\times10^{18} & 1.00\times10^{21} \\ 9.43\times10^{12} & -9.57\times10^{14} & 9.71\times10^{16} & -9.85\times10^{18} & 1.00\times10^{21} & -1.01\times10^{23} \\ -9.57\times10^{14} & 9.71\times10^{16} & -9.85\times10^{18} & 1.00\times10^{21} & -1.01\times10^{23} & 1.03\times10^{25} \\ 9.71\times10^{16} & -9.85\times10^{18} & 1.00\times10^{21} & -1.01\times10^{23} & 1.03\times10^{25} & -1.04\times10^{27} \\ -9.85\times10^{18} & 1.00\times10^{21} & -1.01\times10^{23} & 1.03\times10^{25} & -1.04\times10^{27} & 1.06\times10^{29} \\ 1.00\times10^{21} & -1.01\times10^{23} & 1.03\times10^{25} & -1.04\times10^{27} & 1.06\times10^{29} & -1.07\times10^{31} \\ -1.01\times10^{23} & 1.03\times10^{25} & -1.04\times10^{27} & 1.06\times10^{29} & -1.07\times10^{31} & 1.09\times10^{33} \\ 1.03\times10^{25} & -1.04\times10^{27} & 1.06\times10^{29} & -1.07\times10^{31} & 1.09\times10^{33} & -1.10\times10^{35} \\ -1.04\times10^{27} & 1.06\times10^{29} & -1.07\times10^{31} & 1.09\times10^{33} & -1.10\times10^{35} & 1.12\times10^{37} \\ 1.06\times10^{29} & -1.07\times10^{31} & 1.09\times10^{33} & -1.10\times10^{35} & 1.12\times10^{37} & -1.14\times10^{39} \\ -1.07\times10^{31} & 1.09\times10^{33} & -1.10\times10^{35} & 1.12\times10^{37} & -1.14\times10^{39} & 1.15\times10^{41} \\ 1.09\times10^{33} & -1.10\times10^{35} & 1.12\times10^{37} & -1.14\times10^{39} & 1.159\times10^{41} & -1.17\times10^{43} \\ -1.10\times10^{35} & 1.12\times10^{37} & -1.14\times10^{39} & 1.15\times10^{41} & -1.17\times10^{43} & 1.193\times10^{45} \\ 1.09\times10^{33} & 1.00\times10^{21} & 1.21\times10^{15} & 3.85\times10^{16} & 9.71\times10^{16} & -1.89\times10^{33} \end{bmatrix}$$

Thus, the reduced-order function can be derived by solving the state space parameters using the elements of the Hermite form as follows

$$\mathrm{A}_2 = \begin{bmatrix} -8.885 & -35.49 \\ 1 & 0 \end{bmatrix}$$

$$\mathrm{B}_2 = \begin{bmatrix} 1 \\ 0 \end{bmatrix}$$

$$\mathrm{C}_2\mathrm{A}_2^{-1} = \begin{bmatrix} 0.0677 & -8.918 \end{bmatrix}$$

Appendix B

In chapter 5, in section 4.3.5, The 12th order of transfer function obtained after approximation is given below

$$\begin{aligned}\text{num} = & -6s^{12} - 1392s^{11} - (1.004\times10^{5})s^{10} - (2.418\times10^{6})s^{9} \\ & -(3.218\times10^{7})s^{8} - (2.636\times10^{8})s^{7} - (1.132\times10^{9})s^{6} \\ & -(2.653\times10^{9})s^{5} - (3.511\times10^{9})s^{4} - (2.116\times10^{9})s^{3} \\ & -(4.302\times10^{8})s^{2} - (2.512\times10^{7})s\end{aligned}$$

$$\begin{aligned}\text{den} = & s^{12} + 1.932s^{11} + \left(8.674\times10^{4}\right)s^{10} + \left(9.26\times10^{5}\right)s^{19} \\ & +\left(18.044\times10^{4}\right)s^{8} + (6..383\times10^{7})s^{7} + \left(36.23\times10^{7}\right)s^{6} \\ & +\left(1.5821\times10^{9}\right)s^{5} + \left(7.486\times10^{4}\right)s^{4} + \left(1.449\times10^{10}\right)s^{3} \\ & +\left(1.621\times10^{20}\right)s^{2} + \left(9.87\times10^{3}\right)s^{1} + \left(9.88\times10^{5}\right)s\end{aligned} \tag{A.8}$$

To assess the stability of the proposed work, the higher-order plant transfer function given above should be reduced to a second-order transfer function. This reduction was achieved by preserving the dominant poles of the system through the utilization of the Hankel matrix method. The state space matrix (A, B, C, and D) for the Closed-Loop Transfer Function (CLTF) given in Equation (A.8) is given below

$$A = \begin{bmatrix} 0 & -0.44 & 0 & 0 & 1 & 0 & 0 & 0 & 0 & 0 & 0 & 0 \\ -0.05 & 0.44 & 0 & 0 & 0 & 0 & 0 & 1 & 0 & 0 & 0 & 0 \\ -6 & 0 & 0 & 0 & 0 & 0 & 0 & 0 & 0 & 0 & 0 & 0 \\ 0 & 10.24 & -12.5 & 0 & 0 & 0 & 0 & 0 & 282.1 & -80 & 0 & 0 \\ 0 & 0 & 12.5 & -0.1 & 0 & 0 & 0 & 0 & 0 & 0 & 0 & 0 \\ 0 & 0 & 20.83 & 0.17 & -3.33 & 0 & 0 & 0 & 0 & 0 & 0 & 0 \\ -646.47 & -10.24 & 0 & 0 & 0 & -12.5 & 0 & 0 & 0 & 0 & 282.1 & -80 \\ 0 & 0 & 0 & 0 & 0 & 12.5 & -0.1 & 0 & 0 & 0 & 0 & 0 \\ 0 & 0 & 0 & 0 & 0 & 20.83 & 0.17 & -3.33 & 0 & 0 & 0 & 0 \\ 0 & -1.01 & 0 & 0 & 0 & 0 & 0 & 0 & 0 & 0 & 0 & 0 \\ 0 & 12.62 & 0 & 0 & 0 & 0 & 0 & 0 & 347.62 & -100 & 0 & 0 \\ -5.77 & 1.01 & 0 & 0 & 0 & 0 & 0 & 0 & 0 & 0 & 0 & 0 \\ -796.64 & -12.62 & 0 & 0 & 0 & 0 & 0 & 0 & 0 & 0 & 347.62 & -100 \end{bmatrix} \tag{A.9}$$

$$B = \begin{bmatrix} 0 & 0 & 0.1 & 0 & 0 & 0 & 0 & 0 & 0 & 0 & 0 & 0 & 0 \\ 0 & 0 & 0 & 12.5 & 0 & 0 & 0 & 0 & 0 & 0 & 0 & 0 & 0 \end{bmatrix}^{T} \tag{A.10}$$

$$C = [1 \quad 1 \quad 0 \quad 0 \quad 0 \quad 0 \quad 0 \quad 0 \quad 0 \quad 0 \quad 0 \quad 0 \quad 1]^{T} \tag{A.11}$$

By following the steps for the Hankel norm reduction as given in appendix A, the reduced-order function can be derived by solving the state space parameters as given below

$$A_2 = \begin{bmatrix} -2.13 & -21.2 \\ 1 & 0 \end{bmatrix}$$

$$B_2 = \begin{bmatrix} 1 \\ 0 \end{bmatrix}$$

$$C_2 A_2^{-1} = \begin{bmatrix} 2.1517 & 1 \end{bmatrix}$$

The data for simulating the HPS model presented in Figure 3.8 is as follows

Case 1: Two-area HPS - Synchronizing coefficients: $T_{12} = T_{21}$=0.08674 p.u.MW/rad.Hz, Power system block gain and time constant: K_{pi} = 200 Hz/(p.u. MW), T_{pi} = 20 s, Reheat gain and time constant: K_{ri}= 0.5, T_{ri} = 10 s, Governor time constant: T_{gi}= 0.08 s, Steam turbine time constant: T_{ti} =0.3 s, Frequency bias coefficient: B_i = 0.425 p.u. MW/Hz, Governor speed regulation: R_i= 2.4 p.u. MW/Hz, Change in step load perturbation with frequency: D_i=8.33 × 10−3 p.u. MW/Hz, System inertia: H_i = 5 s. Solar collector gain and time constant: K_S = 1.8,T_S = 1.8 s, Solar thermal steam turbine gain and time constant: K_T = 1, T_T = 0.3 s, Wind turbine gain and time constant: K_{WTG} = 1, T_{WTG} = 1.5 s, Aqua Electrolyzer gain and time constant: K_{AE} = 0.002, T_{AE} = 0.5 s, Fuel cell gain and time constant: K_{FC} = 0.01, T_{FC} = 4 s, area capacity ratio: a_{12} = −1, constant for renewable power sharing K_n = 0.6 and loading = 50%.

Case 2: Three-area HPS - Hydro turbine model parameters: T_H =28.75 s, T_{RS} = 1 s, T_{RH} = 0.3, Tw =3.06 s, K_H = 0.5747 and Gas Turbine model parameters: C_g=1, b_g =0.05 s, X_c = 0.6 s, Y_c =1 s, T_{CR} = 0.01 s, T_F =0.23 s, T_{CD} = 0.2 s, K_G = 0.1304. Synchronizing coefficients: $T_{12} = T_{21}$=0.08674 p.u.MW/rad.Hz, Power system block gain and time constant: K_{pi} = 120 Hz/(p.u. MW), T_{pi} = 20 s, Reheat gain and time constant: K_{ri}= 0.8, T_{ri} = 20 s, Governor time constant: T_{gi}= 0.06 s, Steam turbine time constant: T_{ti} =0.5 s, Frequency bias coefficient: B_i = 0.425 p.u. MW/Hz, Governor speed regulation: R_i= 4.8 p.u. MW/Hz, Change in step load perturbation with frequency: D_i=4.33 × 10−3 p.u. MW/Hz, System inertia: H_i = 3.75 s.

The data for simulating the deregulated model presented in Figure 3.18 is as follows

RTES data: $T_{12} = T_{23} = T_{13}$ = 0.08674 p.u.MW/rad.Hz (tie-line power synchronization coefficient), $K_{p1} = K_{p2} = K_{p3}$ = 120 Hz/(p.u. MW) (power system block transfer function gain), $T_{p1} = T_{p2} = T_{p3}$ = 20 s (power system block transfer function time constant), $K_{T1} = K_{T2} = K_{T3}$ = 0.5 (reheat transfer function gain constant), $T_{r1} = T_{r2} = T_{r3}$ = 10 s (reheat transfer function time constant), $D_1 = D_2 = D_3$ = 8.33 × 10−3 p.u. MW/Hz (area damping coefficient), $R_1 = R_2 = R_3$ = 2.4 p.u. MW/Hz (governor speed regulation), $H_1 = H_2 = H_3$ = 5 s (inertia constant), $T_{g1} = T_{g2} = T_{g3}$ = 0.08 s (governor time constant), $T_{t1} = T_{t2} = T_{t3}$ = 0.3 s (steam turbine time constant), $B_1 = B_2 = B_3$ = 0.425 p.u. MW/Hz (Frequency bias coefficient).

STES data: Solar field gain constant K_{SS} = 1.8, solar field time constant T_{SS} = 1.8 s, Governor time constant T_{GS} = 1 s, Turbine gain constant K_{TS} = 1 s, Turbine time constant T_{TS} = 3 s.

GES data: Governor gains constant K_{GGE} = 1 s, Governor time constant T_{GGE} = 0.2 s, Turbine gain constant K_{TGE} = 1 s, Turbine time constant T_{TGE} = 0.5 s.

OTEC data: Speed droop and gain constant of the governor and turbine: K =20, K_{OT} = 1 s. Time delay T_{OG2} =1 s, T_1 = 0.1 s. Turbine time constant T_{OT} = 3 s, Net power P_{net} = 87 W.

The data for simulating the NMG model presented in Figure 3.22 is as follows

MG 1: $T_{12} = T_{23} = T_{13}$ = 0.08674 p.u.MW/rad.Hz (tie-line power synchronization coefficient), K_{p1} = 120 Hz/(p.u. MW) (MG block transfer function gain), T_{p1} = 20 s (MG block transfer function time constant), K_V = 1, T_V = 2 s (valve actuator gain and time constant), K_{DE} = 1, T_{DE} = 1.8 s (diesel engine gain and time constant), R_1= 2.4 p.u. MW/Hz (governor speed regulation), B_1 = 0.425 p.u. MW/Hz (Frequency bias coefficient), WPG gain and time constant: K_{WPG} = 1, T_{WPG} = 1.5 s, PV input k_{ic}= 1, T_{ic} =0.8 s, , K_{BESs}= 1, T_{BEsS}=0.1 s (BESS gain and time constant).

MG 2: K_{p2} = 120 Hz/(p.u. MW) (MG system block transfer function gain), T_{p2} = 20 s (MG system block transfer function time constant), K_G = 0.5, T_G = 0.5 s (governor transfer function gain and time constant), K_T = 0.5, T_T=0.3 s (turbine transfer function gain and time constant), R_2= 2.4 p.u. MW/Hz (governor speed regulation), B_2 = 0.425 p.u. MW/Hz (Frequency bias coefficient), Solar collector gain and time constant: K_S = 1.8, T_S = 1.8 s, K_{BES}= 1, T_{BES}=0.1 s (BES gain and time constant).

MG 3: K_{p3} = 120 Hz/(p.u. MW) (MG system block transfer function gain), T_{p3} = 20 s (MG system block transfer function time constant), H_i = 5s (inertia constant of VSG), D_i = 0.5 s (damping constant of VSG), R_3= 2.4 p.u. MW/Hz (governor speed regulation), B_3 = 0.425 p.u. MW/Hz (Frequency bias coefficient), Solar collector gain and time constant: K_S = 1.8, T_S = 1.8 s, Solar thermal steam turbine gain and time constant: K_T = 1, T_T = 0.3 s, Wind turbine gain and time constant: K_{WPG} = 1, T_{WPG} = 1.5 s, Aqua Electrolyzer gain and time constant: K_{AE} = 0.002, T_{AE} = 0.5 s, Fuel cell gain and time constant: K_{FC} = 0.01, T_{FC} = 4 s, Solar thermal input P_{solar}= 0.15 and wind input P_{wind}=0.1, K_{BES}= 1, T_{BES}=0.1 s (BES gain and time constant).

MG 4: Contribution factor, α_1= 1.8, delay, $e^{-s\tau(t)}$=0.5, Gain and time constant of EV battery, $K_{ev} = 0.1, T_{ev} = 0.5$ s. K_{p4} = 120 Hz/ (p.u. MW) (MG system block transfer function gain), T_{p4} = 20 s (MG system block transfer function time constant), H_i = 5s (inertia constant), D_i = 0.5 s (damping constant), R_4= 2.4 p.u. MW/Hz (governor speed regulation), B_4 = 0.425 p.u. MW/Hz (Frequency bias coefficient).

LIST OF PUBLICATIONS

Journal Articles

Andrew Xavier Raj Irudayaraj, Noor Izzri Abdul Wahab, Veerapandiyan Veerasamy, Manoharan Premkumar, Mohd Amran Mohd Radzi, Nasri Bin Sulaiman, "Distributed Intelligent for Consensus-based Frequency Control of Multi-Microgrid System" in Journal of Energy Storage, (Q1, IF=8.95, Published).

Andrew Xavier Raj Irudayaraj, Noor Izzri Abdul Wahab, Veerapandiyan Veerasamy, Manoharan Premkumar, Mohd Amran Mohd Radzi, Nasri Bin Sulaiman, "Decentralized Frequency Control of Restructured Energy System using Hybrid Intelligent Algorithm and Nonlinear Fractional Order Proportional Integral Derivative Controller" in IET Renewable Power Generation, 2023 (Q2, IF=3.48, Published).

Andrew Xavier Raj Irudayaraj, Noor Izzri Abdul Wahab, Manoharan Premkumar, Mohd Amran Mohd Radzi, Nasri Bin Sulaiman, Veerapandiyan Veerasamy, Rizwan A. Farade, and Mohammad Zohrul Islam, "An Improved Atom Search Optimized FOPID controller for Automatic Load Frequency Control of Hybrid Power System", in Applied Soft Computing, 2022 (Q1, IF-6.725, Published).

Andrew Xavier Raj Irudayaraj, Noor Izzri Abdul Wahab, Mallapu Gopinath Umamaheswari, Mohd Amran Mohd Radzi, Nasri Bin Sulaiman, Veerapandiyan Veerasamy, S C Prasana, and Rajeswari Ramachandran. "A Matignon's Theorem Based Stability Analysis of Hybrid Power System for Automatic Load Frequency Control Using Atom Search Optimized FOPID Controller," in IEEE Access, 2020 (Q1, IF-3.745, Published).

Andrew Xavier Raj Irudayaraj, Noor Izzri Abdul Wahab, Veerapandiyan Veerasamy, Manoharan Premkumar, "Block Chain based distributed frequency control of sustainable networked microgrid system with P2P energy trading" in IEEE Transactions on Sustainable Energy, (Q1, IF=8.75, Major Revision)

Proceedings /Conference

Andrew Xavier Raj Irudayaraj, Noor Izzri Abdul Wahab, Veerapandiyan Veerasamy, Prem Kumar Manoharan and Hoay Beng Gooi, "An adaptive Zeroing Neural Network controller for Frequency Control of Multi Microgrid system", 2023 IEEE IAS GlobConET.

Andrew Xavier Raj Irudayaraj, Noor Izzri Abdul Wahab, Veerapandiyan Veerasamy, Sailendra Singh, Mohammed Lutfi Othman and Hoay Beng Gooi "An adaptive Zhang Neural Network controller for Frequency Control of Renewable Energy Integrated System" IEEE 10th Power India International Conference (PIICON 2022) in 2022 held at NIT, Delhi, India.